PHASE-FIELD MODELS FOR SOLIDIFICATION AND SOLID/LIQUID INTERACTIONS

A Dissertation

by

MIN SOO PARK

Submitted to the Office of Graduate Studies of
Texas A&M University
in partial fulfillment of the requirements for the degree of

DOCTOR OF PHILOSOPHY

December 2009

Major Subject: Mechanical Engineering

PHASE-FIELD MODELS FOR SOLIDIFICATION AND SOLID/LIQUID INTERACTIONS

A Dissertation

by

MIN SOO PARK

Submitted to the Office of Graduate Studies of
Texas A&M University
in partial fulfillment of the requirements for the degree of

DOCTOR OF PHILOSOPHY

Approved by:

Chair of Committee,	Raymundo Arróyave
Committee Members,	Miladin Radovic
	Xinghang Zhang
	Amine Benzerga
Head of Department,	Dennis O'Neal

December 2009

Major Subject: Mechanical Engineering

ABSTRACT

Phase-field Models for Solidification and Solid/liquid Interactions. (December 2009)

Min Soo Park, B. En., M. S., Yeungnam University, Korea

Chair of Advisory Committee: Dr. Raymundo Arróyave

The microstructure resulting from the solidification of alloys can greatly affect their properties, making the prediction of solidification phenomena under arbitrary conditions a very important tool in the field of computer-aided design of materials. Although considerable attention has been allocated to the understanding of this phenomenon in cases in which the solidification front advances freely into the liquid, the actual microstructure of solidification is strongly dependent of interfacial interactions. Over the past decade, the phase-field approach has been proved to be a quite effective tool for the simulation of solidification processes. In phase-field models, one or more phase fields ϕ (conserved and/or non-conserved) are introduced to describe the microstructure of a complex system. The behavior of a given microstructure over time is then simulated by solving evolution equations written in terms of the minimization of the free energy of the entire system, which is written as functional of the field variables as well as their gradients and materials' constitutive equations. With the given free energy functional, the governing equations (phase-field equation, diffusion equation, heat equation and so on) are solved throughout the entire space domain without having to track each of the interfaces formed or abrupt changes in the topology of the microstructure. In this work I will present phase-field models for solidification processes, solid/liquid interactions as well as their applications.

To So Young, Mom and Dad

ACKNOWLEDGMENTS

Most of the calculations were carried out on the CAT cluster in Department of Chemical Engineering at Texas A&M University. Author would also like to thank the advisor, Raymundo Arróyave in Department of Mechanical Engineering at Texas A&M University and NSF Grant No. CMMI-0758298 that supported me during graduate study.

TABLE OF CONTENTS

CHAPTER Page

CHAPTER Page

LIST OF FIGURES

FIGURE Page

FIGURE Page

FIGURE Page

FIGURE Page

FIGURE Page

FIGURE Page

FIGURE Page

FIGURE Page

FIGURE Page

FIGURE Page

CHAPTER I

MOTIVATION

Over the past decades, there has been considerable interest in finding efficient methods for simulating solidification phenomena [1, 2, 3, 4, 5, 6, 7, 8]. Recently, the phase-field method has emerged as a very robust approach to investigating complex microstructural evolution phenomena in a wide range of materials systems, involving an equally wider range of physical phenomena. These models are able to describe phase transformations in a system with a set of equations written in terms of conserved and non-conserved field variables that are continuous and smooth across the interfacial regions, while allowing for highly localized variations at the interfaces. The evolution equations of the field variables are determined, through variational principles, by letting the system relax in a path that most efficiently minimizes the total free energy of the system. This free energy is a functional of the field variables, their gradients as well as constitutive equations and couplings involving thermal, chemical, electrical, magnetic (and many more) contributions to the total free energy. The simplest phase-field models (for binary systems) consist of a nonlinear diffusion equation and a phase field equation. These models attempt to simulate phase transformations involving mass transport across interfaces. With the use of the fundamental thermodynamic and kinetic information as input, the phase-field method can be used to investigate the evolution of arbitrary morphologies and complex microstructures without explicitly tracking the positions of interfaces.

Phase field modeling has been widely used to investigate many important solidification problems including solute trapping during rapid solidification, dendritic

---

The journal model is *IEEE Transactions on Automatic Control.*

growth in pure and binary materials, eutectic solidification in a binary alloys, and so on. In this chapter, I will motivate the research objectives of this work by briefly describing some key developments in the phase-field descriptions of phase transitions involving solid/liquid interactions. A more detailed mathematical description of the fundamental phase-field models will be provided in Chapter II.

A. Introduction

The complexities of the pattern evolution of a moving solid-liquid interface have been solved by many different mathematical methods. Among the different approaches developed, phase-field models are known to be simple and powerful from the numerical perspective because the governing equations are defined throughout the whole system, without having to identify internal interfaces or changes in topology as well as the formation of new phases. Additionally, the interface position does not need to be tracked during numerical calculation. Over the past decade, fairly robust phase field models have been introduced for describing solidification phenomena in unary systems [9, 10, 11], binary systems involving a single solid phase [3, 12], as well as solidification phenomena involving two solid phases [4, 13, 14]–namely, eutectic and peritectic reactions [15, 16].

Phase-field models are used for calculating morphology of solid-liquid interface as well as solute redistribution during the solidification of a material system. Parameters used in phase-field models can be obtained by matching classical balance equations across a zero-thickness interface with approximate solutions to the phase-field equations across the interfaces. In classical models in solidification, each phase has their own governing equations and conservation equations (mass, energy) to be solved for. Additionally, supplemental conditions are also required to couple with neighboring

phases. If there is a system that have more than 4 phases, for example, 8 governing equations for each phase and 6 supplemental conditions are demanded to solve the solidification behaviors of the system.

Realistic simulations involving multiple phases and components involve the coupling of dynamic and conservation equations within and between phase interfaces, making the simulation of complex systems undergoing extensive topological changes in their microstructure a very challenging problem. Contrary to the classical models, phase field models are free from those restrictions by introducing the concept of conserved or non-conserved field variables ϕ which are smooth and continuous throughout the simulation domain. However, implementation of realistic phase-field descriptions of phase transformation phenomena involve the consideration of problems not present in alternative models, such as the dimensions and structures of interfaces separating neighboring domains with different values of a particular conserved or non-conserved field variables [17].

As mentioned above, the development of phase-field models starts with the description of the total free energy of a system in terms of conserved (e. g. concentration) or non-conserved (e. g. order parameter) field variables, their gradients and constitutive relations that are used to introduce different energy contributions to the total free energy of a system. The phase-field approach consists of formulating dynamic equations for all the field variables used to describe the state of the system at any point in space and moment in time. The actual dynamical behavior of the relaxation equations depends on the nature of the field variables (conserved vs. non-conserved), but ultimately is related to the maximization of the rate at which a system minimizes its free energy [3]. For further developments of this powerful approach, several technical issues have needed to be solved, while other important issues still remain.

In classical models, the thickness of interface does not need to be specified or can be considered to be sharp because supplemental conditions involving conservations equations can be used to couple dynamic equations across neighboring phase domains. However, phase-field models of a collection of integrated governing equations valid for all phases and regions of the computational domain. Therefore, when considering regions in which field variables change rapidly (i.e. phase interfaces), the field variable profiles should be continuous and differentiable. In order to ensure a continuous and smooth change in the field variables defining the microstructure of a system, it is necessary to impose a minimum thickness for the interfaces considered in implementations. These interfaces do not correspond to physical interfaces but are rather numerical representations of rapid changes in the topology of the distribution of field variables. To develop more realistic phase-field descriptions, it is necessary to define phase-field interfaces through sound physical understanding. Recently, Karma and Rappel [18] have provided some guidelines for the determination of parameters necessary for describing finite thickness interfaces in the phase-field equation in a unary solidification system.

With the aspect of phase field modeling, phase field models, WBM model [3] and KKS model [5] are introduced and widely used so far. The two models are developed with the Landau-Ginzberg free energy functional associated with the Helmholtz free energy and the concept of minimizing free energy in a system [19]. However, they took different definition of the structure of the interface which is one of the key aspects of phase-field modeling. In real physical systems, interfaces have very specific structures which are fundamentally different from the bulk. Interfaces in the context of phase-field modeling are simply mathematical constructs that need to be properly defined in order to represent realistic microstructural features. One school of thought [3] postulates that at the interface there is a combination of coexisting phases that have

identical compositions even though they are different in nature. An example would be a phase-field solidification model in which the liquid and solid phases are assumed to coexist at the solid/liquid interfaces and to have equal compositions.

While this approach has been proven to be quite useful in many cases, implementation of this description imposes very stringent constraints on the thickness of the numerical interfaces used in phase-field simulations. To resolve this issue, Kim *et al.* [5] proposed a new concept for a phase field model that has a different definition of solid and liquid composition at a interface. They justified the new approach by demonstrating that the assumption of coexisting phases with equal compositions resulting in artificial contributions to the chemical free energy of the system which were greatly amplified as the thickness of the numerical interfaces was increased. To resolve this issue they proposed that across the interface local chemical equilibrium conditions be imposed. These thermodynamic constraints and mass conservation were then used to fix the compositions of coexisting phases. This approach was shown to be successful at eliminating artificial contributions to the free energy, consequently relaxing the constraints on the maximum interface thickness which could be used in phase-field modeling.

The phase field models described above are only single phase field model. A phase field model that can handle with multiple phases is required. A multi-phase field model developed by Steinbach *et al.* [6] and Tiaden *et al.* [20] was a milestone for modeling solidification problems through the phase-field approach. The multi-phase field model was originally derived from a single phase field model, but they defined that each phase has a discrete phase variable and that each phase coexists with other phases at a interfacial region. The free energy functional was the defined in terms of pair-wise differences in field variables at interfacial regions and conventional homogeneous contributions to the free energies in regions away from interfaces. The

multi-phase field dynamic (relaxation) equations were thus defined only within interfacial regions by summing (pair-wise) contributions of each existing phase-field at the interface. Problems involving the formation of multiple grains of the same phase but with well defined grain boundaries separating them involved the definition of multiple phase-field variables corresponding to different variants (with different orientations, for example) of the same structural phase. While this approach is rather unphysical, it has been shown to be quite effective at modeling complex phase transformations.

A more physical approach to the simulation of multiple coexisting grains of the same structural phase would be to consider the changes orientation of each grain with respect to a frame of reference as a way for defining grain boundaries between these grains. Recently, several researchers [8, 21, 22, 23] have attempted to introduce crystal orientation as an additional field-variable to be relaxed during phase-field formulations. The crystallographic model had been developed to treat at least two-dimensional configurations that considerably simplifies the description of a grain boundary where one can expect that the grain boundary has two geometrical degrees of freedom. one is the inclination angle of the boundary plane between two crystals Ψ, and the crystallographic misorientation $\Delta\theta$, which is discontinuous across the boundary. Two more degrees of freedom (two more misorientations) should be required in three dimensions and its implementation is conceptually straightforward. The introduction of the orientation field effectively reduces the number of field variables to solve for during the evolution of complex multi-phase phenomena. Unfortunately, this comes with the cost of adding at least an additional dynamical equation to solve.

Based on the phase field models above, there are many investigations that have been done in many interesting applications. Phase field model for dendrite growth is developed initially in undercooled pure melt [1, 9, 10, 19, 24, 25] and extended to binary or ternary alloy system [26]. Kim *et al.* [27] investigated eutectic solidification

in organic alloy system. They presented a variety of numerical results based on the tilt of the eutectic growth, lamellar spacing and compositions under isotropic and anisotropic effect. Modeling and simulation of soldering reactions in electronic materials is also a good example for use of phase field approaches in order to investigate the microstructural evolution of intermetallic compounds and the reliability of solder interconnections [28, 29, 30, 31, 32]. Interfacial interactions–including crystal formation and growth–occurring at the interface of two substances is also can be solved by the phase field approaches [33, 34, 35, 36].

There are also experimental investigations about the solidification process which can have been motivated by phase-field simulations or that can be used to refine phase-field descriptions of solidification phenomena. Mergy *et al.* [37] worked on the experimental investigation of the eutectic growth pattern of CBr_4-C_2Cl_6 system considering physical parameters such as interfacial energies and diffusion coefficients. Ginibre *et al.* [38] investigated the instability of lamellar growing pattern under the directional solidification by controlling lamellar spacing, concentration and solidification velocity with the same organic alloy. The experimental characterization of the instability of eutectic growth was found to be in very good agreement with instability diagrams previously computed by Karma [4, 18]. A better understanding of the conditions that drive the (in)stability of eutectic patterns have provided researchers with the fundamental inspiration to control lamellar growth pattern [39]. Investigations of the intermetallic compound growth are of great importance for the preliminary researches [40, 41, 42, 43, 44, 45, 46]. In soldering reactions between Sn-based solders and Cu substrate, Cu_6Sn_5 is formed as scallop-type grains with liquid solder penetrating between them and Cu_3Sn is formed under Cu_6Sn_5 scallops. Many research results found the rapid intermetallic compound growth with growth rates on the order of several microns per minute during the reaction, grains coarsening with decreased

number of grains.

In Chapter II, I will motivate the use of phase-field modeling for solidification by describing existing models developed over the past decade as well as computational investigations and experimental results used to corroborate (and in some instances inspire) phase-field simulations. In Chapter III, I will introduce a recent modification to the description of the interface structure in phase-field modeling. The approach in question is based on imposing a thermodynamic equilibrium constraint though regions of space occupied by more than one phase (i. e. interfaces). Examples of the usage of this formalism to describe one and two-dimensional solidification phenomena will be provided. In Chapter IV, the multi-phase-field formalism will be introduced and will be used to describe solidification phenomena involving more than two co-existing phases. Specifically, eutectic solidification of organic alloys will be simulated. Furthermore the influence of insoluble particles on the stability of eutectic solidification fronts will be investigated through multi-phase field simulations. This later mathematical model is inspired by recent attempts to improve mechanical properties of electronic solder alloys through eutectic refinement and synthesis of nano-composite alloys. In Chapter V, the multi-phase-field approach introduced in Chapter IV will be used to describe the morphological evolution of intermetallic compound (IMC) layers formed through liquid/solder chemical interactions during electronic soldering. Specifically, the morphological evolution of a single IMC (Cu_6Sn_5 only) phase and two IMCs (coexistence of Cu_6Sn_5 and Cu_3Sn_5)in Cu-Sn system will be studied. Chapter VI describes further refinements of the mathematical models presented in Chapter V through the incorporation of nucleation. This refinement allows the investigation of the early stages of soldering reactions. In Chapter VII, the multi-phase-field method used throughout most of this thesis will be replaced with a novel formalism based on the addition of a non-conserved field variable representing

the orientation of a particular solid phase formed through the interaction between solid and liquid. This new formalism will be applied to the problem of soldering in the Cu-Sn binary system. The thesis concludes with a summary of the work presented.

CHAPTER II

LITERATURE REVIEW

This chapter provides readers with background knowledge and reviews of the key literature in the field of simulation of microstructural evolution of materials, specifically with regards to phase-field modeling of solidification and microstructure evolution involving solid/liquid interactions. This review is not meant to be exhaustive on the topic but to provide readers with a basic framework within which the basic physical and computational principles are presented.

We start with a discussion of a classical solidification model for unary and binary systems by using heat equation and concentration equation. The goal of introducing the classical solidification model is to show the difficulty of acquisition of governing and coupling equations in computational investigations of phase transformations involving complex topological changes.

Secondly, we provide a detailed discussion of solidification models based on the phase-field approach. Contrary to the classical model, it turns out that only two types of governing equations describing the dynamics of conserved (concentration) and non-conserved (phase parameter) field variables are required. To obtain the governing equation of a phase-field variable (hereafter, phase-field equation), a definition of phase stability should be required based on entropy-approached points of view [47] or free-energy-approached points of view [3, 5], depending on whether non-isothermal or isothermal conditions are imposed on the system, respectively. For the free-energy-approach points of view, two different models are introduced. While these models are not the only ones that have been developed to tackle this problem, they represent two very different views on how to represent the structure of the interface, which ultimately constitutes the basis of the phase-field approach (which in some instances

is known as diffuse-interface model).

Wheeler *et al.* [3] defined a interface where solid and liquid composition are equal while Kim *et al.* [5] defined a interface where solid and liquid composition are different, but chemical potentials are equal. Steinbach *et al.* [6] extended the classical two-phase-field description by introducing a phase-field model that considers the existence of multiple phases (hereafter, a multi-phase field model). The dynamics of this later approach are defined in terms of pairwise energy difference between the coexisting phases at an interface. With these models, there have been many computational efforts aimed at reproducing experimental investigations of microstructure formation and evolution during solidification and other phenomena involving solid/liquid interactions. I will introduce some important computational results that come from use of the phase field models and provide key experimental results for reference.

Finally, I will introduce the intermetallic compound formation and growth during lead-free soldering, which has also been simulated by the phase-field approach. Before showing the examples of the experimental researches, I will briefly introduce the motivation for the use of lead-free soldering which is important in the microelectronics industry, prospectives of using lead-free solder, selection of lead-free solder and the characteristic of materials that are used for lead-free solders. This section would not be directly relevant to phase-field modeling of current works, but rather provide readers with appropriate backgrounds necessary to understand the importance of using lead-free solder, as well as the relevance of the work presented in the second half of this thesis. Contributions of this work provide a better understanding of interfacial interactions during soldering and will be discussed in the later parts of this thesis.

All sections represent the state-of-the-art of current works for phase-field modeling and solid-liquid interactions accompanying with interesting applications.

A. Classical solidification models

In this section I will briefly introduce a mathematical overview of a classical solidification model. Consider first a physical one-component system that is in thermal equilibrium with uniform temperature. A part of the system is in the liquid state while the other part is solid. In the region that has two phases, if solid-liquid interface would be planar and the substance would be pure, the temperature of the interface must correspond with the equilibrium melting temperature, and the melting temperature may depends on pressure. During the process of phase change, the amount of latent heat (L) of the substance evolved during the solid/liquid transformation needs to be considered. Per unit volume, this latent heat is expressed as $\rho^S L$. Now, consider a new system that has a temperature gradient and heat flux, and then we can get a heat balance given by

$$\frac{\mathrm{d}}{\mathrm{d}t}\int_V \rho c_p T \mathrm{d}V = -\int_{\partial V} \mathbf{q}\cdot\mathbf{n}\mathrm{d}V, \tag{2.1}$$

where ρ is density, $\mathbf{q}$ is heat flux, and $\mathbf{n}$ is the normal vector on the system boundary (∂V). Using the transport theorem applied into Gauss's theorem leads to the heat balance as

$$\int_V \left[\frac{\partial}{\partial t}(\rho c_p T) + \nabla\cdot(\rho c_p T\mathbf{v})\right]\mathrm{d}V = -\int_V \nabla\cdot\mathbf{q}\mathrm{d}V, \tag{2.2}$$

and the differential form is

$$\frac{\mathrm{d}}{\mathrm{d}t}(\rho c_p T) + \rho c_p T\nabla\cdot\mathbf{v} = -\nabla\cdot\mathbf{q}, \tag{2.3}$$

where the material derivative is given by

$$\frac{\mathrm{d}}{\mathrm{d}t} = \frac{\partial}{\partial t} + \mathbf{v}\cdot\nabla. \tag{2.4}$$

The constitutive equation for the heat flux is required and it can be obtained from the Fourier law of heat conduction as

$$\mathbf{q} = -k_T \nabla T, \tag{2.5}$$

where k_T is the thermal conductivity. Thus the final equation for the heat balance is given by

$$\frac{\mathrm{d}}{\mathrm{d}t}(\rho c_p T) + \rho c_p T \nabla \cdot \mathbf{v} = \nabla \cdot k_T \nabla T. \tag{2.6}$$

If there is no fluid flow and ρ, c_p and k_T are constant, the heat balance becomes the standard heat conduction equation.

Because the interface moves, another constitutive equation involving interface velocity is required as [48]

$$\rho^S L V_n \delta t = (\mathbf{q_l} - \mathbf{q_s}) \cdot \mathbf{n} \delta t, \tag{2.7}$$

and it becomes

$$\rho^S L V_n = \left[k_T^s \nabla T^s - k_T^l \nabla T^l\right] \cdot \mathbf{n}, \tag{2.8}$$

which indicates that interface velocity V_n depends on the heat entering the interface. In addition, the continuous temperature across the interface should be obeyed as

$$T_s = T_l = T_m. \tag{2.9}$$

Now consider a binary system that is undergoing solidification. Due to the fact that in most cases the solid phase dissolves much less solute than the liquid, this phase transformation usually involves the rejection of solute from the solid into the liquid as more solid is formed. The degree of rejection can be obtained from the equilibrium phase diagram of the binary system. Because the rejected solute into the liquid will diffuse far away from the interface, the variations of temperature and

concentration have to be tracked in the binary system, as opposed to what happens in a unary system.

The heat conduction in the liquid and solid is

$$\frac{\partial T}{\partial t} = \kappa \nabla^2 T, \tag{2.10}$$

where κ is the thermal conductivity.

If the solute is dilute, the solute diffusion equation in both solid and liquid is

$$\frac{\partial C}{\partial t} = D \nabla^2 C, \tag{2.11}$$

where D is the solute diffusivity.

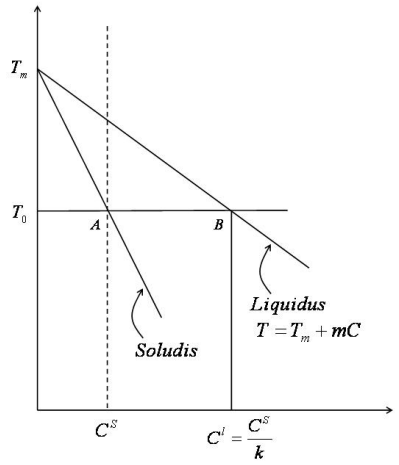

Fig. 1. A linearized phase diagram with the constitutional undercooling profile in small solute concentration.

Because the solute is assumed to be dilute, it is valid to define that the liquidus and solidus lines in the phase diagram as linear. The interface region is located between two lines in given temperature as seen in Fig. 1. The solid concentration is C^s, and the liquid concentration is equal to C^l. In addition, we can get the

liquid concentration at the interface from the solid concentration by using segregation coefficient ($k = C^s/C^l$) at constant temperature and pressure. If the thickness of interface is zero. there is a concentration jump across the interface, which is given by

$$\triangle C_0 = \left(C^l - C^s\right)^I = \frac{1-k}{k} C^s. \tag{2.12}$$

With the equation of the liquidus, the temperature difference with the corresponding concentration represents the undercooling situation as

$$\triangle T_0 = -m \triangle C_0, \tag{2.13}$$

where the Gibbs-Thompson equation on the interface can be obtained including capillary and kinetic undercooling effects as [49]

$$T^s = T^l = T^I = T_m \left(1 + 2H\frac{\gamma}{L}\right) + mC - \mu^{-1} V_n, \tag{2.14}$$

where μ^{-1} is the kinetic coefficient, γ is the interfacial energy, and H is the mean curvature.

The heat balance including the Gibbs-Thompson equation is given by

$$\left(L + 2H\gamma\right) V_n = \left[k_T^s \nabla T^s - k_T^l \nabla T^l\right] \cdot \mathbf{n}, \tag{2.15}$$

and the solute balance is

$$\left(C - C^s\right) V_n = \left[D^s \nabla C^s - D^l \nabla C^l\right] \cdot \mathbf{n}. \tag{2.16}$$

As studied above, a classical model is associated with many governing equations and their corresponding supplements. A classical model , for example, may be good for solving solidification problem if a system is simple like the above case. However, if a given system is complicated, for example the existence of multiple phases, a classical solidification model requires more equations and their corresponding supplements

resulting in difficulties in terms of mathematical and computational works. To avoid problems, a integrated formulation is needed. Phase-field models are a good solution (although not the only one) of this problem.

B. Phase-field models

Phase-field models can be classified into several categories. One that involves a single order parameter, another that is based on a thermodynamic formulation, another that involves multiple order parameters, and one that is derived from geometrical considerations. There are also formulations that are derived for systems with large deviations from local equilibrium. There are order parameters that can easily be measurable for quantities such as a long-range chemical order parameter and a displacing order parameter in solids as well as order (or phase field) parameters that are not easily measurable (or that represent a physical quantity at all) in solidification. In some cases, the method might represent real physical phenomena while in other occasions the phase-field method might be better thought of as a computational technique.

1. Entropy vs. free energy functional

Many papers have used approaches to construct phase-field models [3, 5, 47] and to develop the evolution equations from a few basic concepts, such as irreversible thermodynamics.

Because the entropy always increases locally in a system conserving internal energy and concentration, we can obtain relationships between internal energy and concentration which represents the generalization of the laws of diffusion. The total entropy of the system should include contributions associated with gradients (interfaces), terms for energy (heat) diffusion, solute diffusion and phase field evolution so

that the function of the entropy can be broadly written as [47]

$$\begin{aligned} S &= \int_V [s(e,c,\phi)]\,\mathrm{d}V - \int_V \left[\frac{\epsilon_e^2}{2}|\nabla e|^2\right]\mathrm{d}V \\ &\quad - \int_V \left[\frac{\epsilon_c^2}{2}|\nabla c|^2\right]\mathrm{d}V - \int_V \left[\frac{\epsilon_\phi^2}{2}|\nabla \phi|^2\right]\mathrm{d}V, \end{aligned} \tag{2.17}$$

where s is the entropy density, e is the internal energy density, c is the concentration and ϕ is the phase field. ϵ_e, ϵ_c and ϵ_ϕ are the corresponding gradient entropy coefficients. The variable ϕ distinguishes the liquid and solid, and should be involved in the entropy density s for a double well. The equation is a very general formulation for an entropy functional with all three gradient energy contributions.

In an isothermal case, the enthalpy density can be expressed from the entropy formulation with $\epsilon_e = 0$ as $h = h_0 + C_p T + L\phi$. A formulation for thermal diffusion with a source term from the enthalpy equation as

$$C_p \frac{\partial T}{\partial t} + L\frac{\partial \phi}{\partial t} = \nabla \cdot (k \nabla T), \tag{2.18}$$

where T, C_p, L and k are temperature, heat capacity per unit volume, latent heat per unit volume and thermal conductivity, respectively. The equation tells us that the latent heat evolves when ϕ is changing with time near a moving interface.

On the other side, an isothermal consideration can use a free energy functional F defined as

$$F = \int_V \left[f(\phi,c,T) + \frac{\epsilon_c^2}{2}|\nabla c|^2 + \frac{\epsilon_\phi^2}{2}|\nabla \phi|^2\right]\mathrm{d}V \tag{2.19}$$

where $f(\phi, c, T)$ is the free energy density.

In equilibrium state, the derivative of the free energy functional with respect to ϕ is equal to zero because locally system is located in a stable state and there is no other state lower in energy to relax to. The derivative of the free energy functional

with respect to c is equal to constant because of mass conservation in a whole system. The equation can be expressed as

$$\frac{\delta F}{\delta \phi} = \frac{\partial f}{\partial \phi} - \epsilon_\phi^2 \nabla^2 \phi = 0, \tag{2.20}$$

$$\frac{\delta F}{\delta c} = \frac{\partial f}{\partial c} - \epsilon_c^2 \nabla^2 c = constant. \tag{2.21}$$

In the case that an isothermal system is not in an equilibrium state, we can make the assumption that the system will relax towards the final equilibrium state by finding the fastest path for the minimization of the local (and total) free energy. For conserved parameters, their local changes driving minimization of the free energy involve fluxes (i.e. diffusive fluxes due to concentration and chemical potential gradients). On the other hand, non-conserved field parameters do not require macroscopic fluxes to change the local free energy. For these two cases, the most simple equations that can be written are given by [50]:

$$\frac{\partial \phi}{\partial t} = -M_\phi \left[\frac{\partial f}{\partial \phi} - \epsilon_\phi^2 \nabla^2 \phi \right] \tag{2.22}$$

$$\frac{\partial c}{\partial t} = \left[M_C c(c-1) \nabla \left(\frac{\partial f}{\partial c} - \epsilon_c^2 \nabla^2 c \right) \right] \tag{2.23}$$

The parameters M_ϕ is related to the interface kinetic coefficient, and M_C is from solute diffusion coefficient. Equation (2.22) is called the Allen-Cahn equation and equation (2.23) is known as the Cahn-Hilliard equation [50]. Having described the different dynamic equations relevant for relaxations involving conserved and non-conserved field-variables, we now describe different models depending on how the interface structure is considered.

2. WBM model vs. KKS model

The WBM model represents the model introduced in Wheeler *et al.* [3] while KKS model presents the model introduced in Kim *et al.* [5]. The two models are formulated by considering that the system relaxes along a path that minimizes the free energy of the system in the fastest manner. The free energy density in the two models used different kinds of functional relationships to express the energetic cost associated with the phase transformation. Some models, for example, considered the existence of a double-well contribution to the free energy functional, such as $g(\phi) = \phi^2(1-\phi)^2$ and the other is an interpolating type, such as $p(\phi) = \phi^3(10 - 15\phi + 6\phi^2)$ ensuring that derivative of free energy density is equal to zero when $\phi = 0$ and $\phi = 1$ in all temperatures as seen in Fig. 2. In this case $\phi = 1$ and $\phi = 0$ represent solid and liquid, respectively. As seen below, the fundamental difference between the WBM and KKS models is the assumption regarding the structure of the interface.

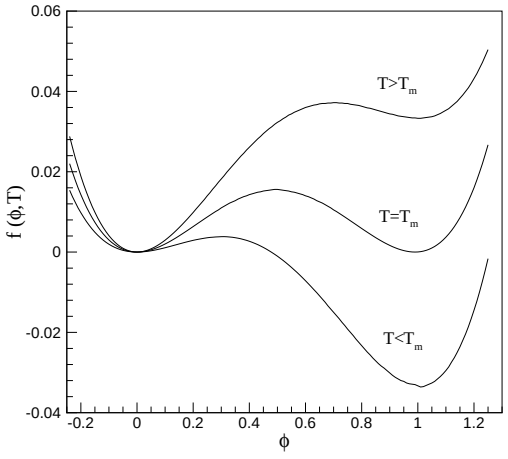

Fig. 2. Free energy density as a function of ϕ with three different temperature.

When Wheeler *et al.* [3] were seeking a form of free energy density, they selected the form from Kobayashi (private communication) instead of from [51]. If there are A and B components, we can write free energy density for component A and B as

$$f_A(\phi, T) = W_A \int p(p-1)\left[p - \frac{1}{2} - \beta_A(T)\right] \mathrm{d}p \tag{2.24}$$

and

$$f_B(\phi, T) = W_B \int p(p-1)\left[p - \frac{1}{2} - \beta_B(T)\right] \mathrm{d}p, \tag{2.25}$$

and free energy density of solution including concentrations, without regular solution parameters $(c(1-c)\left[\Omega_S(1-p(\phi)) + \Omega_L p(\phi)\right])$, as

$$\begin{aligned} f(\phi, c, T) &= (1-c)f_A(\phi, T) + c f_B(\phi, T) \\ &\quad + RT\left[(1-c)\ln(1-c) + c(\ln c)\right], \end{aligned} \tag{2.26}$$

where W is the height of energy hump. β is a constant $(-0.5 < \beta_A(T) < 0 < \beta_B < 0.5)$.

Wheeler *et al.* [3] obtained a governing equation for phase field and concentration, respectively, as

$$\frac{\partial \phi}{\partial t} = -M_\phi \left[\frac{\partial F}{\partial \phi}\right] \tag{2.27}$$

and

$$\frac{\partial c}{\partial t} = M_c \nabla \left[c(c-1)\nabla \frac{\partial F}{\partial c}\right] \tag{2.28}$$

with the defined free energy functional:

$$F(\phi, c, T) = \int^V \left[f(\phi, c; T) + \frac{\epsilon^2}{2}|\nabla \phi|^2\right] \mathrm{d}V. \tag{2.29}$$

The WBM model contains, as we can see, model parameters which can be obtained from the following. For getting the coefficients in the two governing equation to simulation solidification, we need to know, at first, the difference in free energy

between solid and liquid with the assumption that the difference is often obtained by a linear function of temperature near the melting temperature. This can be written as:

$$f_S^A(T) - f_L^A(T) = \frac{L_A(T - T_M^A)}{T_M^A} \tag{2.30}$$

which yield with the function of free energy density

$$f_A(\phi, T) = W_A g(\phi) - L_A \frac{T - T_M^A}{T_M^A} p(\phi). \tag{2.31}$$

The excess free energy of the interface region can be obtained from the definition of the interfacial energy as

$$\sigma_A = \epsilon_\phi \sqrt{2} \int_0^1 \sqrt{f_A(\phi, T)} \mathrm{d}\phi = \frac{\epsilon_\phi \sqrt{W_A}}{3\sqrt{2}}. \tag{2.32}$$

In equilibrium, a one-dimensional solution for a flat steady-state interface under a pure material exists at melting point of component A in a transition zone between liquid and solid can be obtained as

$$\phi(x) = \frac{1}{2}\left[1 + \tanh\left(\frac{x}{2\delta_A}\right)\right], \tag{2.33}$$

where δ_A is the interface thickness given by $\delta_A = \epsilon_\phi / \sqrt{2W_A}$. The value of the thickness should be optimized by the fact that the interface should be sharp enough to minimize the volume of material occupied by the interface and be diffuse enough to reduce the energy associated with the gradient of ϕ according to the computational techniques.

To investigate a moving interface, the mathematical transformation should be taken care of to a coordinate frame moving at a constant velocity v under one dimensional system. Changing $\partial\phi/\partial t$ into $-v(\partial\phi/\partial x)$ leads to a solution in small interface thickness when the temperature is given by

$$T = T_M^A - \frac{v}{\mu_A} \quad \text{where} \quad \mu_A = \frac{6 M_\phi \epsilon_\phi L_A}{T_M^A \sqrt{2W_A}}. \tag{2.34}$$

The classical approach to linear interface kinetics is identical to an interface velocity for corresponding temperature. The above equation can be used to determine a value of M_ϕ when μ is known.

Although the WBM model has been recently used [52, 53, 54], it appeared to have a problem. In numerical simulation where a finite interface thickness is assumed, model parameters actually are mainly functions of the interface thickness. Due to chemical energy contribution with respect to interfacial energy, a certain limit of the interface thickness arises, which is not only restricted by the interface energy but also the difference between the equilibrium liquid and solid compositions. As mentioned above, the fundamental characteristic of the WBM is to consider the interface as a combination of co-existing phases with equal composition. This assumption eventually results in discontinuities in the chemical potentials of the constituent elements at the interface. These energetic contributions to the free energy functional of the system may become very important as soon as the interface thickness is increased.

Tiaden *et al.* [20] proposed that the interface should be assumed to be a mixture of solid and liquid with different compositions, but constant in ratio. This assumption resulted in chemical potential equilibrium constraint which in turn helped to define a more thermodynamically-consistent interface structure for cases in which the interface is considered as a mixture of two co-existing phases at an interface. The adoption of chemical potential equilibrium makes elimination of extra potential that is included in the WBM model [3]. The existence of the extra potential under the condition of the some composition of liquid and solid restricts the interface energy and interface width because the extra potential is a function of temperature, the height of the extra potential increases according to the increasing temperature. It can be said that the temperature variation causes the variation of the interface energy and interface width which tend to be material properties that are not mainly functions of

temperature. To eliminate this unphysical situation, Kim *et al.* [5] adapted chemical potential equilibrium at a interface region as

$$f_{c_S}^S \left[c_S(x,t)\right] = f_{c_L}^L \left[c_L(x,t)\right], \tag{2.35}$$

where $f_{c_S}^S$ is the derivative of free energy density of solid phase with respect to solid composition, which is called as chemical potential of solid phase, and follows the definition of free energy density [20], and free energies for liquid and solid are obtained from thermodynamics modeling from CALPHAD. The free energy density that Kim *et al.* [5] used is

$$f(c,\phi) = h(\phi) f^S(c_S) + [1 - h(\phi)] f^L(c_L) + w g(\phi), \tag{2.36}$$

where $f^S(c_S)$ is the free energy density of solid composition that can be obtained from thermodynamics modeling.

The governing equations they introduced are

$$\frac{\partial \phi}{\partial t} = M \left(\epsilon^2 \nabla^2 \phi - f_\phi \right), \tag{2.37}$$

$$\frac{\partial c}{\partial t} = \nabla \left(\frac{D(\phi)}{f_{cc}} \nabla f_c \right), \tag{2.38}$$

with

$$c = h(\phi) c_S + [1 - h(\phi)] c_L, \tag{2.39}$$

$$f_{c_S}^S [c_S(x,t)] = f_{c_L}^L [c_L(x,t)], \tag{2.40}$$

$$f(c,\phi) = h(\phi) f^S(c_S) + [1 - h(\phi)] f^L(c_L) + \omega g(\phi), \tag{2.41}$$

where $D(\phi) = h(\phi)D_S + (1 - h(\phi))D_L$ is the diffusivity. $h(\phi) = \phi^3 (6\phi^2 - 15\phi + 10)$ and $g(\phi) = \phi^2 (1 - \phi)^2$. To get model parameters, ϵ and ω, Kim *et al.* [5] used a equilibrium state solution of phase field model adopting a definite of interface energy and choose a interface thickness that is relevant to phase field continuity. With WBM model, This model is also widely used by many researches [55, 56, 57, 58].

3. Multi-phase field models

The WBM and KKS models were developed to understand phase transitions involving only two phases. Steinbach *et al.* [6] developed multiphase-field approach that describes the interaction between an arbitrary number of individual phase fields with individual characteristics by the use of interface fields. The first concept of the multiphase-field modeling was from his previous work [14]. The order parameter ϕ is not a characteristics of a single phase, but can be distinguished between two different phases. For example, in case of the three different phases (α, β and L) in a system, phase α may be transformed into phase L, and phase L may be again transformed into phase β. Thereby we may consider a position that might have two or three different coexisting phases (in a binary system). Steinbach *et al.* defined the set of phase fields, $(0 \leq \phi_i \leq 1)$, by local traction of a phase, i, that is a certain value, but constrained by the summation of the existing ϕ_i at a point is equal to 1. For the definition of free energy, they adopted the interpretation given by [59], set up the free energy density functional F of a system in its dependence on a local phase field variable ϕ_i and the partial derivatives $\nabla\phi_i$ as

$$F\left[\phi_1,\ \phi_2,\ \phi_3, ..., \nabla\phi_1,\ \nabla\phi_2,\ \nabla\phi_3...\right] = \int_V f\left[\phi_1,\ \phi_2,\ \phi_3, ..., \nabla\phi_1,\ \nabla\phi_2,\ \nabla\phi_3...\right] \mathrm{d}V. \tag{2.42}$$

For the free energy density f, they distinguished a free energy density for each

single phase, for a region of two coexisting phases, and a region of triple phase coexisting and so forth as pairwise difference. Therefore, they introduced

$$f = f^0 + \sum_i f_i^1 + \sum_{i,j(i\neq j)} f_{ij}^2 + \sum_{i,j,k(i\neq k\neq k)} f_{i,j,k}^1 + ... \tag{2.43}$$

With the free energy density, they applied the Euler-Lagrangian formulation to get the minimization of the local free energy density of a system, resulting in a relaxation ansatz [6]

$$\frac{\partial \phi_i}{\partial t} = \left(\nabla \frac{\partial}{\partial \nabla \phi_i} - \frac{\partial}{\partial \phi_i} \right) f(\phi_i), \tag{2.44}$$

which can be transformed, in terms of F, into

$$\frac{\partial \phi i}{\partial t} = -M_{ij} \frac{1}{N} \sum_{i\neq j} \left(\frac{\partial}{\partial \phi_i} - \frac{\partial}{\partial \phi_j} \right) F. \tag{2.45}$$

Their introduction of multi-phase field model became an important feature not only to engineering applications but also to scientific reasons to develop multi-phase field solidification methods involving one liquid and one or more solid phases. Extending the number of phases, such as eutectic/peritectic solidification can be achieved by several methods. One is to introduce three phase fields to define each phase, another is to introduce two phase fields where one is used to discriminate between the solid and liquid phases, another is to discriminate between two different solid phases, and the other is to couple the phase field model with the spinodal decomposition model where two solids phases are distinguished by two different compositions. Each approach shows its own benefit for producing useful information to understand solidification pattern.

With the establishment of multiphase field concept [14, 20, 59], Kim *et al.* [27]

developed a conventional multiphase field model as

$$\frac{\partial \phi_i}{\partial t} = -\frac{2}{N}\sum_{i \neq j} M_{ij} s_i s_j \left[\frac{\partial F}{\partial \phi_i} - \frac{\partial F}{\partial \phi_j}\right]. \tag{2.46}$$

and

$$\frac{\partial F}{\partial \phi_i} = \sum_{i \neq j}\left[\frac{\epsilon_{ij}^2}{2}\nabla^2\phi_j + \omega_{ij}\phi_j\right] + f^i(c_i) - f_c c_i, \tag{2.47}$$

where M_{ij} is the mobility. N is the number of coexisting phases. It is noted that the derivative of the free energy functional $\partial F/\partial \phi_i$ is the sum of $\partial F_P/\partial \phi_i$ and $\partial F_T/\partial \phi_i$. $\epsilon(\epsilon_{ij} = \epsilon_{ji})$ is the gradient energy coefficient and $\omega(\omega_{ij} = \omega_{ji})$ is the height of double well potential.

The phase-field models can be extended to the multi-component system by using the equal composition (WBM) [3] or equal chemical potential conditions (KKS) [5]. However, the model involving equal chemical composition condition creates the advantage of reducing extra computational cost to find the compositions of coexisting solid and liquid phase comparing with that involving equal chemical potential condition. Unfortunately, setting the compositions of coexisting phases as equal introduced extraneous contributions to the free energy functional. The dilute solution approximation reduces the computational cost of the KKS approach because of the constant partition coefficients for a reference phase (liquid phase) [5]. The multi-component phase-field models is still used as a tool for qualitative simulation because the mapping of the models onto the classical sharp interface model has not been completely done although multi-component phase-field models have been developed with the constant partition coefficients [18].

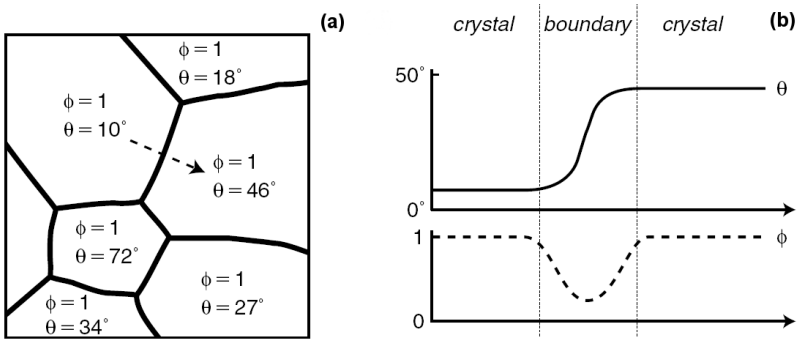

Fig. 3. Phase-field configurations of polycrystalline microstructure. (a) Continuous-orientation model: Each grains are specified by an order parameter for orientations Θ, and an order parameter for phase field ϕ. (b) Two order parameters are continuously lined through the boundary. The figures come from [8]. (Reprinted with Permission of Elsevier.)

4. Crystallographic field models

The treatment of the formation and growth of crystals of the same phase but with different crystallographic orientation have been treated in the past by resorting to a multi-phase field description. However, this approach results in several undesirable consequences as this approach [60] implies that the free energy functional is not invariant with respect to orientation measured from a frame of reference. Given these limitations, some researchers had attempted to express field equations in terms of continuous crystal orientations [8, 21, 22]. In two dimensions, the orientation of a given grain can be specified completely by a single continuous parameter Θ indicating the angle between the normal to a particular set of atomic planes and a fixed direction in the reference frame as shown in Fig. 3(a).

It is sure that grain orientations are freely chosen from arbitrary manners, which means that the grain orientations are independent of bulk free energy in systems.

Because of this independence, the energy penalty caused by misorientation can not be established for growth simulations. So, it is necessary to build an additional phase field that is coupled between the width of the interfacial region and bulk free energy. The order parameter ϕ indicating the degree of crystallinity at each point in the calculation domain can be defined with unit values differentiating perfect crystalline order, such as inner grains, (ϕ=1) with overlapped crystalline order, such as grains boundaries ($0 < \phi < 1$). As shown in Fig. 3(b), both ϕ and Θ have their distinct gradients in the interface regions, but only the value of the orientational coordinate distinguishes a given grain from its neighbors.

A static, one-dimensional boundary between two semi-infinite grains (a bicrystal) of orientations, 0 and $\Delta\Theta$, with interface normal in the x-direction. We impose $\phi(\pm\infty) = 1$. The equations governing the one-dimensional spatial dependence of a bicrystal [8] are

$$\frac{1}{M_\phi}\frac{\partial\phi}{\partial t} = \alpha^2\phi_{xx} - \frac{\partial f}{\partial\phi} - \frac{\partial g}{\partial\phi}s|\Theta_x| - \frac{\partial h}{\partial\phi}\frac{\epsilon^2}{2}|\Theta_x|^2 \tag{2.48}$$

and

$$\frac{1}{M_\Theta}\frac{\partial\Theta}{\partial t} = \left[h\epsilon^2\Theta_x + gs\frac{\Theta_x}{|\Theta_x|}\right]_x. \tag{2.49}$$

5. Review of computational researches

The analysis of dendrite solidification is widely used in the phase field simulations, and there are lots of applications for pure materials, pure materials with convection, binary alloys and ternary alloys [18, 25, 61, 62, 63, 64, 65, 66, 67, 68].

Models for dendrite growth were developed initially in undercooled pure melt [1, 9, 10, 19, 24, 25] and then extended to binary alloy system. The first model for alloy solidification was from Wheeler *et al.* [3]. The model is still used by many researchers in many solidification problems [4, 5, 69] under thermodynamic considerations. In

this model, it is assumed that a mixture of solid and liquid have a same composition any point within the interfacial region. A sharp interface condition and a finite interface thickness condition are applied for determining phase field parameters. In order to illustrate the successive growth of arms from parents arms under dendritic solidification, anisotropy was introduced in gradient term coefficient as

$$\epsilon(\theta) = \epsilon_0 \left\{1 + \nu \cos(4\theta)\right\}, \tag{2.50}$$

where ν is the anisotropic coefficient. θ is the angle between normal direction of interface and x-axis, which can be given by

$$\theta = \tan^{-1} \frac{(\phi_i)_y}{(\phi_i)_x}. \tag{2.51}$$

Fig. 4 is a good example of the single dendrite growth by using phase-field model. It shows the effect of the anisotropy coefficient in the shape of the dendrite tip and the number of secondary and tertiary arms qualitatively by varying the value of the model parameters arbitrary. Wheeler *et al.* [10] adopted the phase-field parameters which were determined from physical properties and studied the dendrite tip shape more quantitatively. They also pointed out the calculation result changed depending on the interface thickness because of the sharp interface limit. The prediction of the solvability theory adopting by phase-field simulation was successful by Karma and Rappel [4]. A phase-field model is also useful to numerically study a cellular/dendritic pattern formation in the directional solidification. Fig. 5 shows transition procedure of cellular/dendritic growth pattern in directional solidification under temperature gradient in Al-Cu alloy. In this example, phase-field models turn out to be computationally efficient, and provide one with quantitative predictions of the microstructure evolution.

Ode *et al.* [70] focused on the growth and mergence of secondary arm in Fe-base

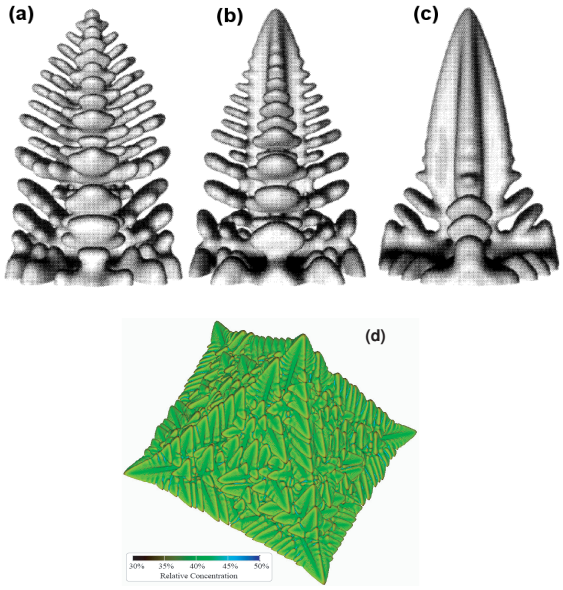

Fig. 4. The phase-field simulation of dendrite solidification in 3D. The anisotropy is introduced in the driving force for the interface. The anisotropic coefficient ν is (a) 0.2 (b) 0.3 (c) 0.5 respectively. The effect of the anisotropy and the competitive growth of the side branches are nicely reproduced. (d) A dendrite simulation with grid of size $500 \times 500 \times 500$ and mirrored along the x and y axes. Figs. 4(a)-(c) come from [71]. Fig. 4(d) comes from [72]. (Reprinted with Permission of Elsevier.)

and Al-base alloys and produced numerical simulations using a phase-field model. They calculated arm spacing and the exponent of the local solidification time and compared with experimental data. They examined the change in the arm spacing and the exponent which depend on physical properties (interface energy, solute diffusivity, liquidus slope and so on). They found that interface energy and solute diffusivity in liquid change the arm spacing while liquidus slope and partition coefficient change both the arm spacing and the exponent. Fig. 6 shows the growth and merge of the secondary arms for Fe-0.1wt%C alloy. The difference size of triangular solid seeds are

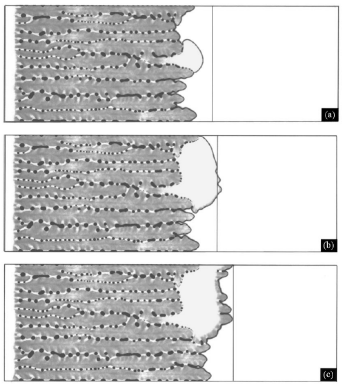

Fig. 5. Cellular/dendritic growth pattern in directional solidification under temperature gradient in Al-Cu alloy. The temperature gradient is 1.11×10^7(K/m). The figures come from [73]. (Reprinted with Permission of Elsevier.)

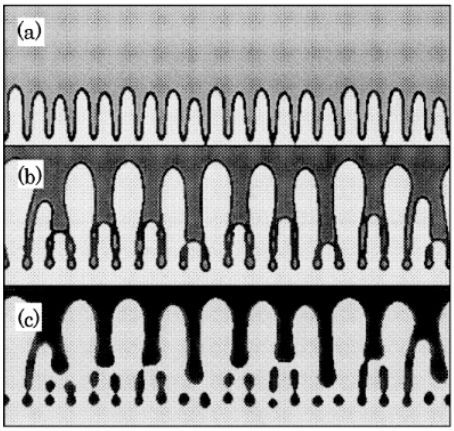

Fig. 6. Evolution of secondary arms for Fe-0.1wt%C. (a) early stage of arm growth, (b) arm growth and selection, (c) arm coarsening. The large size of initial seeds in Fig. 6(a) grow preferably and other arms stop or melt back due to the curvature effect [Fig. 6(b)]. The small secondary arms coarsen in Fig. 6(c). The figures come from [70]. (Reprinted with Permission of Elsevier.)

initially located at the bottom of the calculation domain and grow upward according to the anisotropy.

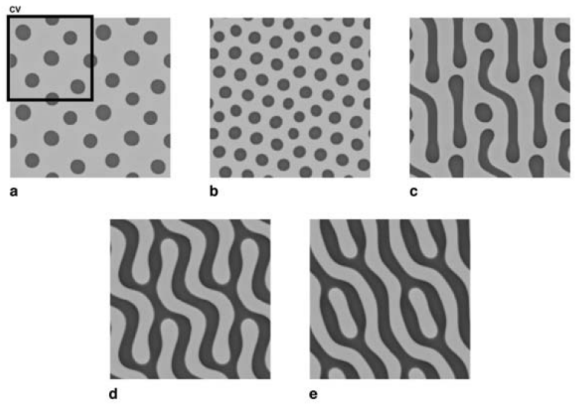

Fig. 7. Two dimensional results of eutectic solidification simulation for different volume fractions of the two phases in computational domain (200×200 μm). The minor phase volume fractions are (a) 0.178, (b) 0.305, (c) 0.379, (d) 0.485, and (e) 0.499. It is calculated in the computational volume (CV), and four pieces of CV are put together due to the periodicity. The figures come from [74]. (Reprinted with Permission of Elsevier.)

Eutectic solidification is also computed by multi-phase field model [74] that is based on the work by [6, 20]. The multi-phase field model is well described in Appendix B. Fig. 7 shows two-dimensional results of eutectic solidification simulation for different volume fractions of the two phases in computational domain (200×200μm). The minor phase volume fractions are (a) 0.178, (b) 0.305, (c) 0.379, (d) 0.485, and (e) 0.499. It is calculated in the computational volume (CV), and four pieces of CV are put together due to the periodicity. A. Parisi *et al.* [75] reported stability of lamellar eutectic growth in three dimension. They found that Jackson-hunt stability limit is agreeable when low solidification front velocity (V) and temperature gradients, and the zigzag shape of lamellae the instability is a classical transverse phase diffusion

instability similar to those observed in many other non-equilibrium systems [76].

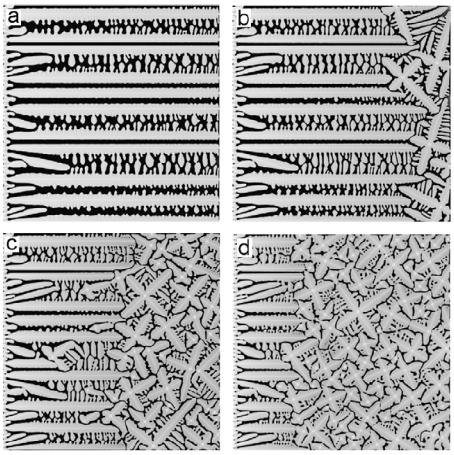

Fig. 8. Microstructure for a Ni-0.369mol% Cu alloy solidified under different cooling rates: (a) 30, (b) 75, (c) 150, (d) 300 K/s. The figures come from [56]. (Reprinted with Permission of Elsevier.)

A method for incorporating nucleation into phase-field simulations relies on explicitly incorporating nuclei throughout the simulation time by relying on classical nucleation theory and stochastic approaches [33, 34, 56]. In this approach, the probability for the nucleation of a new phase at an arbitrary point in space and time is determined and the microstructure is 'seeded' accordingly. This approach assumes that the time necessary for the new phase to nucleate is much smaller than the time interval of the simulation. Furthermore, the expectation value of the number of nuclei that form during a time interval Δt corresponds to the nucleation rate, J, which can be calculated from classical nucleation theory. This approach further assumes that once the nuclei forms, it occupies a definite volume of space which in turn yields a "zero event probability" for the formation of subsequent nuclei [33, 34, 56]. The detail explanation of a "zero event probability" will be addressed in another chapter. It is

interesting to know that they performed microstructures that involves many physical phenomenon mentioned in previous paragraphs, such as dendrite solidification, nucleation by using phase-field model including the effect of polycrystalline as seen in Fig. 8.

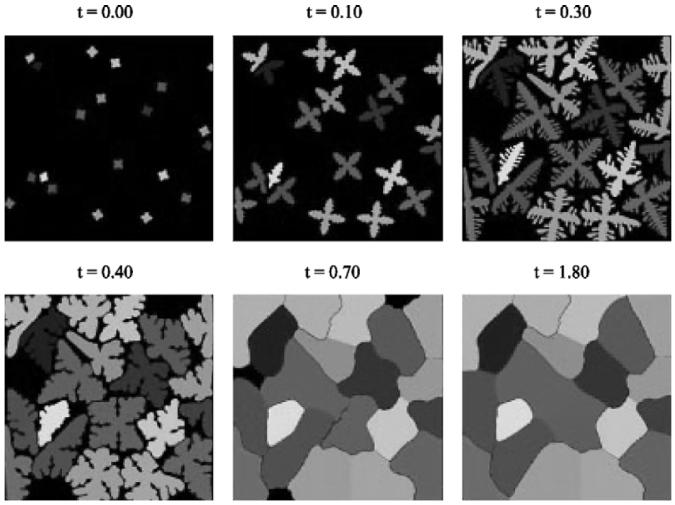

Fig. 9. Evolution of crystal growth under the effect of ploycrystalline in materials. Dendritic microstructure forms in early stages, and crystals impinge and coarsen each other in late stages. The box is initially cooled under the freezing temperature, and then a constant rate of heat sink is imposed to make the entire box freezing. The figures come from [8]. (Reprinted with Permission of Elsevier.)

Recently, phase-field model has been extended to investigate the orientation of crystals as introduced in Eqs. (2.50) and (2.50). Warren *et al.* [8] is one of the leading researches in this field. Their model can easily be extended to include alloy effects like Fig. 9 and encourages one to be interested in studying grain coalescence in thin films as well as grain boundary migration. However, in spite of being widely applicable, the model is necessary to extend to three dimensional simulation. In principle, this

extension is straightforward once the addition of two more angle variables is well established. Warren *et al.* [8] briefly introduced the analysis to couple with two more angle variables, but it is still a challenging area of research.

6. Review of experimental researches

Dendrite researches in experimental investigation have been done in several decades ago. However, many researches are still interested in dendrite solidification which is a common phenomenon in solidification of materials, and industrial fields are still suffering from the formation and growth of dendritic microstructure because dendrites usually form before (or after) desired microstructure.

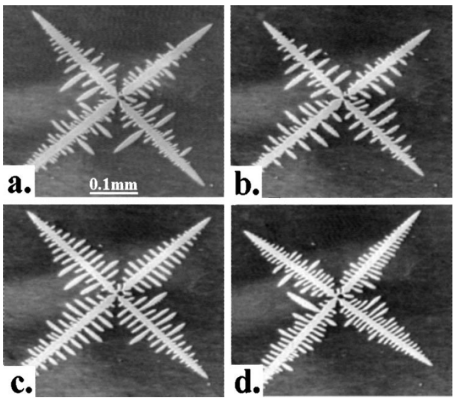

Fig. 10. Snapshots demonstrating the effect of modulated pressure on the dendrite growing into undercooled condition. Higher frequency of modulated pressure is applied at (d), and frequency of modulated pressure is applied at (b). (a) is not applied with oscillatory pressure. The figures come from [77]. (Reprinted with Permission of American Physical Society.)

Borzsonyi *et al.* [77] performed computational simulations and experiments in order to demonstrate dendritic formation pattern under the effect of modulated pressure

and heat flux that result in an fluctuated velocity of the dendrite tip, and eventually yield secondary arms on primary arms. By using the high frequency of pressure variation in the dendrite solidification, they tried to create more seeds that will grow as secondary arms on the primary arms as shown in Fig. 10, and they found that high variation of imposed conditions, such as modulated pressure and heat flux, on the system creates more secondary arms, and they revealed that the imposed condition is related to the anisotropic coefficient of a phase field model that is used to confront with experimental results.

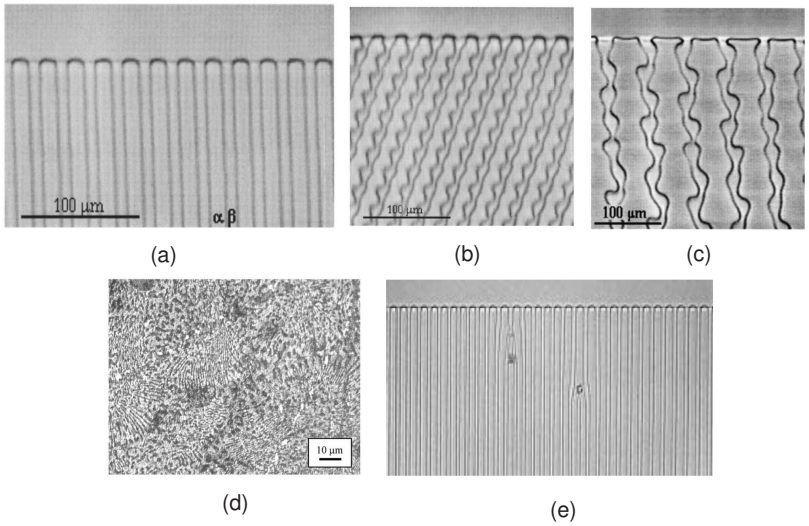

Fig. 11. Experimental results for eutectic solidification: (a) Directionally solidified thin sample of the eutectic alloy CBr_4-C_2Cl_6 in a basic state, (b) tilted, period-preserving oscillatory pattern, (c) the transition from the basic state to oscillatory pattern, (d) microstructure change of composite solders containing TiO_2 nanopowder, and (e) the decay of lamellae due to the existence of glass particles. The figures come from [38] for (a)-(c), [78] for (d), and [76] for (e). (Reprinted with permission from the American Physical Society and Elsevier.)

Mergy *et al.* [37] worked on the experimental investigation of the eutectic growth pattern considering physical parameters such as interfacial energies and diffusion coefficients. The value of the parameters for the transparent organic alloy (CBr_4-C_2Cl_6) was determined by experiments under directional solidification. Ginibre *et al.* [38] investigated the instability of lamellar growing pattern under the directional solidification by controlling lamellar spacing, concentration and solidification velocity with the same organic alloy [see Fig. 11(a)-(c)]. The experimental characterization of the instability of eutectic growth was found to be in very good agreement with instability diagrams previously computed by Karma [4, 18]. A better understanding of the conditions that drive the (in)stability of eutectic patterns have provided researchers with the fundamental inspiration to control lamellar growth pattern [39]. More experimental results can be seen in [37, 38].

Akamatsu *et al.* [76] accidentally observed the decay of eutectic lamellae by glass particles [see Fig. 11(e)]. Although it happens accidentally, the evolution of eutectic lamellae is worthy of note . One of the researches to look into the effect of particles was performed by Lin *et al.* [78] who showed an experimental study of the solidification kinetics and microstructure development in tin/lead solders by mechanically mixing nanopowders of either copper or TiO_2 with tin/lead powders [see Fig. 11(d)]. They found that the solidified composite solder results in the reduction of grain size and spacing of the eutectic lamellae. They concluded that nanopowders increase hardness of microstructure.

C. Lead-free soldering in microelectronics

1. Environmental and health issues with lead

The Environmental Protection Agency (EPA) announced lead and its compounds as one of the 17 chemical poisons that threat human life and environment [79]. When lead accumulates in the body for a long time, it will produce adverse health effects because lead combines strongly to proteins in the body and prohibits normal functions of proteins in the human body, which causes disorder of nervous and reproductive system resulting in delaying neurological and physical development [80]. Those effects are some of the adverse effects of lead on human health. When the level of lead in the blood exceeds 50 mg/dl of blood, lead poisoning is considerable enough to occur the adverse effects [81]. Lead level even below the official threshold causes hazardous situation to humane neurological and physical development, especially for children.

The usage of lead in the electronics industry exposes to occupations, such as the waste from the manufacturing process and the disposal of electronic assemblies. Although the consumption of lead in the electronics industry appears tiny [80], the potential due to lead exposure should not be negligible. Soldering process is one of occupational exposure in electronics, especially the wave soldering operation. Researches have addressed that there is little danger of exposure to lead in hand during soldering and tinning because of non-volatileness under normal temperatures [82].

However, lead vapors or dust formed by dross during the wave soldering operation increase to expose them to workers. Wave soldering generates dross from surface oxidation at the surface of the molten solder. About 90 percent of dross generated during wave soldering is refined to pure metal for reuse [83], but the remaining stays out of the refining process, which means that 10 percent of lead would move into the human body when workers breath close to the lead source. The Resource Conservation

and Recovery Act classified this remaining as hazardous substance to human health and regulate special handling and disposal in a law.

The Occupational Safety and Health Administration regulates no more than 50 mg/dl of lead accumulation in worker's blood [84]. This accumulation limit is related to maintaining lead levels in blood below 40 mg/dl, which level is believed to prohibit adverse health effects from exposure to lead in a working lifetime. Therefore, it is very important to develop possibly alternative lead-free solders for electronic assemblies keeping existing soldering characteristics. In initial stage to make the world legislation, some companies did not follow the ban of lead-using legislation, but almost all companies have begun to respond to this by announcing their own plans for shifting to lead-free solders because a lot of reports about the hazard of using lead in the industry.

2. Lead-free alloy selection

The descried issues forced one to perform examining and understanding of the implications for lead-free alternatives to tin-lead eutectic solder. The Department of Trade and Industry (DTI) developed a progressive report on the selection of lead-free solder [85]. DTI first tasked the introducing a possible lead free solder alternatives. Once a material is selected, DTI manufactured a sample with the selected material on the same procedure of manufacturing lead-based alloys, and tested the sample to see the performance which should be equivalent to the lead-based alloys. The criteria of selecting lead-free alternatives to tin-lead eutectic solder are follows [30]:

1. The lead-free alloy stays with at most ternary alloys if possible.
   Quaternary alloys may make control difficult.
2. The lead-free alloy should be located in near the eutectic point. If it

would be far away from the point, the solder have large pasty range during cool-down.

3. The lead-free alloy should be have similar melting point comparing with tin-lead alloy in order to use existing manufacturing equipments.
4. The lead-free alloy should be equal or better characteristics than tin-lead alloy in reliability when it is used in electronics assembly.
5. The lead-free alloy should create equal or less cost comparing with tin-lead alloy.
6. If possible, the lead-free solder should be free from the existing patents.
7. The information of lead-free solder should be well known in the industry.
8. The lead free solder should be free from the health and environment issues.

3. Candidate alloy compositions

The second task to select the alternatives is to find a lead free solder that is free from patents of alloys because more than 30 companies have already achieved the patent about technologies and components related to lead-free alloy. Based on the criteria for selecting new lead-free alloys, the International Electronics Manufacturing Initiative evaluated more than 79 solder alloys, and then selected the solder alloy in the following [85]:

1. Sn-Bi alloy
2. Sn-Zn (or Sn-Zn-Bi) alloy
3. Sn-Ag (or Sn-Ag-Bi) alloy

4. Sn-Ag-Cu alloy
5. Sn-Ag eutectic alloy
6. Sn-Cu eutectic alloy

a. Sn

Sn is the principal component in most solder alloys for electronic applications in terms of wetting and spreading on a wide range of substrates. Melting point of Sn is 504 K. Tin has two different forms with two different crystal structures in solid state. β-tin that is stable at room temperature has a body-centered tetragonal crystal structure. α-tin has a diamond cubic crystal structure and is thermodynamically stable below 286 K. β-tin transforms to α-tin when the temperature is below 286 K resulting in increasing volume, which lead to cracking in the tin structure. Tin pest induces problems for applications that are performed at low temperature and can be partially problematic for equipments across the 286 K. The thermal expansion of tin is also anisotropic because of the body centered tetragonal crystal structure [86]. Therefore, when tin repeats thermal plastic deformation, cracking on grain boundaries eventually occurs. Thermal cycling over a range as 303-448 K allows one to observe [87]. Thus, even though there is no external mechanical strain, thermal fatigue appears considerable in tin or tin-rich phases of solder alloys.

Tin also leads to whisker growth that represents single-crystal growth like fine wire extending up to 0.64 mm high [88]. The whiskers are tetragonal β-tin growing associated with internal stress or external loads of the material. The quick growth in tin occurs at about 424 K, which is influenced by substrate property and plating conditions. Although solderability and deterioration of the tin coatings is free from the whiskers, it is interesting to know that longer whiskers may lead to electrical shorts in PCB boards. In order to avoid whisker growth Pb is usually used.

b. Sn-Bi

The Sn-Bi alloy has a eutectic composition of 42Sn-58Bi at the temperature of 512K. Equilibrium phases of Bi and Sn are about 4 wt.% Bi in solid solution at room temperature [89]. Although Bi has maximum solubility (21 wt.%) in Sn, the Bi phase is essentially pure Bi because tin has low solubility in Bi at 512K. Bi precipitates in the Sn phase during cool-down. When cooling rate is moderate, the lamellar growth of Sn-Bi occurs. When the cooling rate is low, cracks can be observed in eutectic Sn-Bi solder joints resulting in large grain formation [90]. However, cracking is not observed in rapid cooling. Tin precipitates from the solder matrix along the boundaries of these large grains through which cracking occurs. Recrystallization of the alloy produced an expansion was also observed resulting that the crystal may be brittle because of strain hardening caused by deformation from the expansion [86, 90].

c. Sn-Zn

The melting temperature (471K), close to eutectic Sn-Pb, of the Sn-9wt.%Zn alloy appears to be an attractive alternative. The eutectic structure has two phases. one is a body centered tetragonal Sn matrix phase, and the other is a secondary phase of hexagonal Zn containing less than 1% Sn in solid solution. The microstructure is reported to show large grains with a fine uniform two-phase eutectic pattern. Sn-9 wt.% Zn is the eutectic composition for the Sn-Zn family, and the microstructure appears to be lamellar, containing alternating Sn-rich and Zn rich phases. In the Sn-Zn family, intermetallic phases are formed by both Sn and Zn interacting with Cu.

The solid solubility of Sn is less than 0.05 wt.% in Zn. The maximum solid solubility of Zn in Sn has been reported as 2 wt.% [91]. Intermetallic compounds of

Zn-Cu can be expected to form when Sn-Zn solders are used on copper substrates because the Zn-rich phase is essentially pure Zn.

d. Sn-Ag

The eutectic solidification occurs at 494K with Sn-3.5Ag in the Sn-Ag binary system. The microstructure consists of Sn and the intermetallic Ag_3Sn in the form of thin plates. The solidified microstructure of the binary eutectic Sn-3.5%Ag consists of a β-Sn phase with dendritic globules and inter-dendritic regions with a eutectic dispersion of Ag_3Sn precipitates within a β-Sn matrix. Additional 1% Zn was reported to improve the solidification microstructure of this alloy by removing the large β-Sn dendritic globules and producing a finer and more uniform two-phase distribution throughout the alloy [92]. The addition of Zn suppresses the formation of b-Sn dendrites resulting in a uniform dispersion of Ag_3Sn. This solder is likely susceptible to whisker growth due to its high tin composition. The similar phenomenon happens to the Sn-0.07Cu alloy.

As described above this system exhibits eutectic behavior on the Sn-rich side with a eutectic composition of Sn-3.5Ag at 494K. The Sn-enriched intermetallic phase (ϵ) has a nominal composition of Ag_3Sn. The concentration of Sn may vary between 25.5 and 26 wt.%. The solid solubility of Ag in Sn is less than 0.1 wt.%.

e. Sn-Cu

A eutectic solidification occurs at 500K with Sn-0.7 wt%Cu in the Sn-Cu binary alloy. The solidification reaction has Cu that is precipitated in the form of hollow rods as the intermetallic Cu_6Sn_5. Data for the property of this alloy hardly exists. However it may be likely that whisker growth or transformation to gray tin may occur because of the high concentration of tin in this alloy. The additional Cu causes tin whisker

growth, or the $\beta \rightarrow \alpha$ transformation is not clear at this time.

From the Sn-Cu phase diagram, the intermetallic phases becomes stable below 573K, and they are η and ϵ phases. Sn concentration in the η phase is between 44.8 and 45.5 wt.% corresponding to Cu_6Sn_5. Sn concentration in the ϵ phase is between 25.7 and 27.1 wt.% corresponding closely to Cu_3Sn. It is important to know that both phases are identified in investigations of Pb-Sn solder-Cu substrate interactions [93, 94]. The growth of these phases were addressed to follow the relationship that the activation energy for Cu_6Sn_5 is between 0.41 and 0.5 eV, and that for Cu_3Sn is between 1.06 and 1.27 eV at 363-443K range [95], which means that the growth of Cu_6Sn_5 would be faster than Cu3Sn under the temperature conditions. These data can be obtained from reaction of a 60%Sn-40%Pb solder paste on single crystal Cu substrate. In microelectronics, copper is normally used in one of the three following forms. One is a rolled copper for lead frames, another is a rolled copper foil for lead traces, and the other is electroplated copper traces or pads. According to the formation and growth of the Cu_6Sn_5 and Cu_3Sn on these types of copper, the activation energies appears being different forms of single crystal copper.

Based on the candidates, there have been many researchers who tried to investigate the characteristic of the materials during soldering reaction in experimental methods. Important features are shown in follows.

4. Review of experimental researches

Experimental investigations on IMC growth during soldering previously published by other groups have provided important insights into the nature of these complex interfacial reactions [41, 43, 44, 45, 46, 96]. They reported that a Cu_6Sn_5 layer is formed as scallop-type grains in contact with liquid solder, while Cu_3Sn is formed as a reactive diffusion layer between Cu_6Sn_5 and the solid substrate. They also mentioned

on the influence of IMC morphology on the solid-state microstructural processes that affect reliability of interconnects during normal operation. Although many groups have observed the morphological change of IMC layers, it is still unclear how kinetics of the soldering process is related to IMC growth.

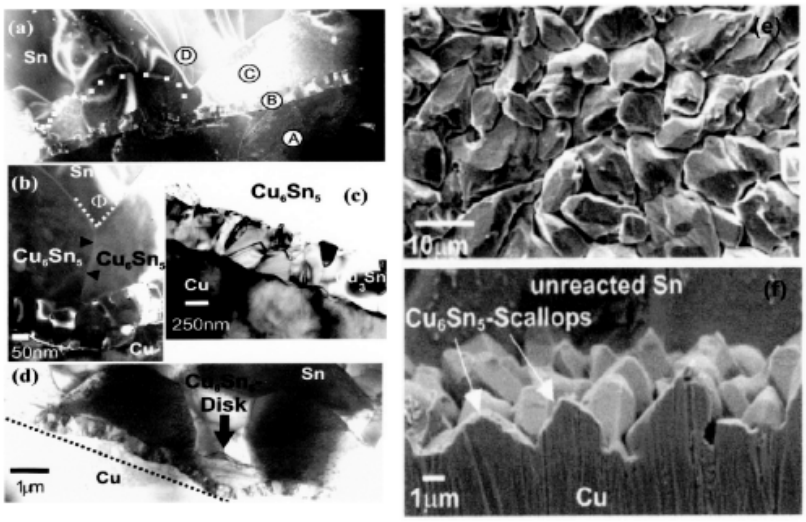

Fig. 12. Micrographs of a Cu-Sn specimen. The figures come from [45]. (Reprinted with Permission of Elsevier.)

In Fig. 12(a) a binary reaction couple is shown. Four different regions are easily distinguished: the Cu-substrate (ⓐ), the Cu_3Sn layer (ⓑ), the Cu_6Sn_5 grains/scallops (ⓒ), and the unreacted Sn (ⓓ). Most remarkable channels between individual scallops reveal sharpness down to about 1 nm in Fig. 12(b). Furthermore, a clearly defined triple joint with wetting angle is seen in Fig. 12(b). Since the appearance of the triple joints does not depend on the reflow time and thus on the scallop size, it is suggested that the observed wetting angle is an equilibrium feature at the reaction temperature instead of being formed at quenching. In consequence, those channels must be interpreted as ordinary grain boundaries separating two grains of Cu_6Sn_5.

Between the scallops and the Cu substrate a polycrystalline Cu_3Sn layer has formed, 300 nm in thickness in Fig. 12(c). This layer seems to form just at the beginning of the reaction. The dense Cu_3Sn layer consists of a row of columnar grown grains. However, with its high density of grain boundaries it is probably not the rate limiting factor for the Cu supply to the reactive solid/liquid interface. During the reaction the substrate develops a certain waviness in correspondence to the scallop structure. The onset of this process is already noticed in the presented pictures in Fig. 12(d). That confirms that Cu is predominantly transported along the Cu_6Sn_5 grain boundaries. The outflow of Cu cannot be compensated by volume diffusion inside the Cu substrate or by diffusion along the interfaces to the Cu_3Sn layer. In consequence the region closed to the Cu_6Sn_5 shifts into the Cu substrate. The reaction zone of the binary system in the figure is shown in plane (viewing direction normal to the interface) and cross-section view (viewing direction along original interface) in Fig. 12(e) and (f). It is clearly seen that also the binary system develops a non-planar morphology of the Cu_6Sn_5 product, with channels of solder apparently extending to the Cu substrate.

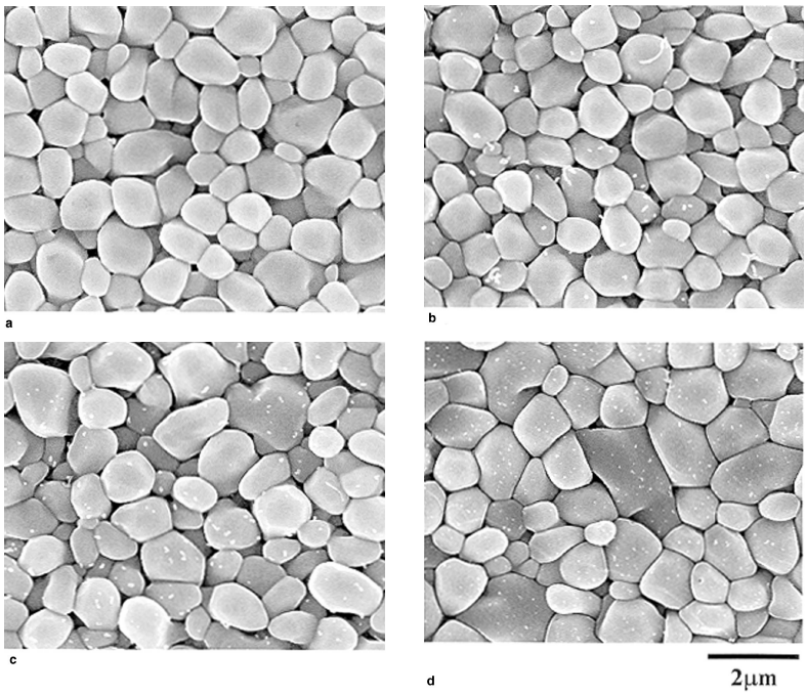

Fig. 13. Micrographs of Cu_6Sn_5 interface formed by hot dipping in molten tin with copper substrate for 1 sec at different temperatures: (a) 513K, (b) 533K, (c) 553K and 575K. Gagliano *et al.* [97] investigates the heterogeneous nucleation of the Cu_6Sn_5 phase in liquid tin/solid copper couples. They carried out to determine (a) the effective rate of nucleation of Cu_6Sn_5 in the temperature range from 513K to 575K, (b) the effect of surface finish for the nucleation rate, and (c) the average radius of Cu_6Sn_5 grains at each temperatures and surface finishes. The figures come from [97]. Similar experimental researches can be found at Load *et al.* [98]. (Reprinted with Permission of Elsevier.)

CHAPTER III

PHASE TRANSITION FOR ISOTHERMAL SOLIDIFICATION IN BINARY ALLOYS

A. Introduction

The complexity of the pattern evolution of the solid-liquid interface on a nonequilibrium state has been solved by many mathematical methods. Among the methods phase field models are known to be simple and powerful in numerical treatments because governing equations are expressed in integrated formula in the whole system regardless distinguishing the interface from old phases and new phases. Plus, interface positions don't need to be tracked during numerical calculation. Currently, some phase field models have been introduced for a unary solidification system [9, 10, 11] and meanwhile they have been developed to a binary solidification system with a single solid phase [3, 12] or with two solid phases [4, 14, 99]. Parameters used in the phase-field models can be represented by material parameters with relationships which are usually obtained from the approximation solutions of the phase-field equation in zero interface thickness in classical techniques.

To physically verify phase field models with respect to classical models, production of solute trapping is required. If the liquid have solute, there is preferential equilibrium compositions in both solid composition and liquid composition at a interface. Because of that, preferential rejection or incorporation of solute happens. According to solubility, the rejection composition will be diffused away from the interface through the solid phase, liquid phase, or both phases resulting in concentration gradient at the interface. The performance of the solute trapping by using phase-field models had been done by Wheeler *et al.* [3, 69].

Meanwhile, Kim *et al.* [5] proposed a new concept for the phase field model that has a different definition of solid and liquid composition at a interface. The model reported by Wheeler [3] is postulated under the consistency of thermodynamics and assumed the same composition of solid and liquid at the interface. However, Kim *et al.* [5] found a certain limitation in the interface thickness that is not free from the interface energy and the difference between the same composition of solid and liquid due to the chemical energy distribution in the interface. They introduced a new concept regarding the chemical energy distribution in the interface. It is that the chemical potential is equal at the interface. The composition of the solid and liquid at the interface can be obtained from the chemical potential equilibrium, and then each composition will be different. To verify their phase field model, they also simulated the common phenomenon, and it was successful.

Another common phenomenon in solidification process is dendrite growth. So, simulations of dendrite growth are required for effectiveness of a model. For the dendrite growth, one should know that the most important factor of internal characteristic is physically the anisotropy at the solid-liquid interface, and it is a key parameter affecting the evolution of crystal morphology. Adaption of anisotropy effect in the phase-field model is a key issue in computational work [1, 10, 19, 70, 100]. Therefore, simulation of dendrite solidification is one of the common works in computational work. Once a phase-field model is introduced, the model is handled to obtain the verification from simulations compared with results of classical models. The models of dendrite solidification have been developed initially in undercooled pure melt [1, 9, 10, 19, 24, 25] and extended to binary alloy system [70, 100].

In this chapter, before moving to complicated applications, we will present discussions on phase transition in 1-D and dendrite growth in 2-D using the phase field model by Kim *et al.* [5] in Al-2mole%Si alloy at 870 K. We will show the composi-

tion and phase-field profile at a interface for verification. I will show the variation of composition of solid and liquid at interface with different interface velocities and mobilities in one dimensional calculation. Additionally, we will introduce an anisotropic phase field model and simulate dendrite solidification in 2-D.

B. Governing equations

1. An isotropic model

Based on the theory [3], we need free energy density of the solid-liquid mixture that can be written as

$$f(c,\phi) = h(\phi)f^S(c) + [1-h(\phi)]\, f^L(c) + wg(\phi), \tag{3.1}$$

where f^S is the free energy density of solid, and f^S is the free energy density of liquid. ϕ is phase field. $\phi = 0$ and $\phi = 1$ correspond liquid phase and solid phase, respectively. Therefore $0 < \phi < 1$ indicates solid-liquid interface. h and g are a constitutive equation for free energy density of solid-liquid mixture and double well potential, respectively. The two functions vary according to numerical techniques. However, h should have the similar shape of the predicted phase-field according to ϕ , and g should be 'w' formation with respect to ϕ and has two minima at $\phi = 0$ and $\phi = 1$. The preferential form of h and g are

$$h(\phi) = \phi^3\left(6\phi^2 - 15\phi + 10\right) \tag{3.2}$$

and

$$g(\phi) = \phi^2\left(1-\phi\right)^2, \tag{3.3}$$

where w is the barrier height of double-well potential. The value w can be taken with a constant value because of independence of composition in the case with finite

interface thickness, which means that it does not indicate that the interface energy is independent of the temperature. The interface energy is mostly dependent on the shapes of the free energy curves of interfacial phases that vary with respect to temperature and equilibrium concentration at the interface. Because the form of free energy density at the solid-liquid interface is only a function of phase filed, any solution model or thermodynamic data can be applied.

Time dependent equations of substances for enthalpy and phase field are given by [5]:

$$\frac{\partial H}{\partial t} = \nabla \left[k \nabla T \right] \tag{3.4}$$

$$\frac{\partial \phi}{\partial t} = M \left(\epsilon^2 \nabla^2 \phi - f_\phi \right), \tag{3.5}$$

$$H = h(\phi) H_S + \left[1 - h(\phi) \right] H_L, \tag{3.6}$$

$$T_S(x,t) = T_L(x,t) = T(x,t), \tag{3.7}$$

$$f(H,\phi) = h(\phi) f^S(H_S) + \left[1 - h(\phi) \right] f^L(H_L) + w g(\phi). \tag{3.8}$$

Eqs. (3.4)-(3.8) can be reduced with two equations as

$$c_p \frac{\partial T}{\partial t} - L \frac{\partial h}{\partial \phi} \frac{\partial \phi}{\partial t} = \nabla \left[k \nabla T \right], \tag{3.9}$$

$$\frac{\partial \phi}{\partial t} = M \left[\epsilon^2 \nabla^2 \phi + \frac{\partial h}{\partial \phi} \left(f^L - f^S \right) - w \frac{\partial g}{\partial \phi} \right]. \tag{3.10}$$

Replacing H for c and T for f_c in Eqs. (3.9)-(3.10) yields the phase field equation and diffusion equation as

$$\frac{\partial \phi}{\partial t} = M \left(\epsilon^2 \nabla^2 \phi - f_\phi \right), \tag{3.11}$$

$$\frac{\partial c}{\partial t} = \nabla \left(\frac{D(\phi)}{f_{cc}} \nabla f_c \right) \tag{3.12}$$

with

$$c = h(\phi) c_S + \left[1 - h(\phi) \right] c_L, \tag{3.13}$$

$$f^S_{c_S}[c_S(x,t)] = f^L_{c_L}[c_L(x,t)], \tag{3.14}$$

$$f(c,\phi) = h(\phi)f^S(c_S) + [1-h(\phi)]f^L(c_L) + wg(\phi), \tag{3.15}$$

where $D(\phi) = h(\phi)D_S + (1-h(\phi))D_L$ is the diffusivity.

The model parameters, ϵ and ω, obtained from the definition of the interface energy [5], are functions of phase field and interface width, and the interface width is analytically obtained from finite interface limit condition, where the model parameters are required only in the interface region and the interface region in this chapter is $0.1 < \phi < 0.9$. Mobility M is related to the kinetic coefficient β [5]. They are given, under the dilute solute approximation [5], as

$$\sigma = \frac{\epsilon\sqrt{w}}{\sqrt{18}}, \tag{3.16}$$

$$\lambda = 1.55\frac{\epsilon}{\sqrt{w}}, \tag{3.17}$$

$$\beta = \frac{v_m}{RT}\frac{m^e}{1-k^e}\left[\frac{\sigma}{M\epsilon^2} - \frac{\epsilon}{D_i\sqrt{2w}}\zeta^e\right]. \tag{3.18}$$

$$\begin{aligned}\zeta^e &= \frac{RT}{v_m}\left(c^e_L - c^e_S\right)^2 \\ &\times \int_0^1 \frac{1}{\phi(1-\phi)}\frac{h[1-h]}{[1-h]\frac{1}{c^e_S} + h\frac{1}{c^e_L}}\mathrm{d}\phi.\end{aligned} \tag{3.19}$$

where m^e is the equilibrium slope of liquidus from phase diagram, k^e is the equilibrium partition coefficient, and D_i is the diffusion coefficient at the interface [see Appendix A].

2. An anisotropic model

The phase field equation should be modified in order to include the anisotropy of interface. The four-fold anisotropy is introduced by putting the coefficient in the phase-field parameter [70] as

$$\epsilon(\theta) = \epsilon_0 \left\{1 + \nu \cos(4\theta)\right\}, \tag{3.20}$$

where ν is the anisotropic coefficient. θ is the angle between normal direction of interface and x-axis, which can be given by

$$\theta = \tan^{-1} \frac{(\phi_i)_y}{(\phi_i)_x}. \tag{3.21}$$

In order to modify the phase-field equation ϵ^2 should be located inside the divergence in equation (3.10). The following terms

$$\frac{\partial}{\partial x}\left[\epsilon\epsilon' \frac{\partial \phi}{\partial y}\right] - \frac{\partial}{\partial y}\left[\epsilon\epsilon' \frac{\partial \phi}{\partial x}\right] \tag{3.22}$$

should be added in the phase field equation [12], so that the phase field equation becomes

$$\begin{aligned}\frac{1}{M}\frac{\partial \phi}{\partial t} = \nabla \cdot (\epsilon^2 \nabla \phi) + \frac{\partial}{\partial x}\left[\epsilon\epsilon' \frac{\partial \phi}{\partial y}\right] - \frac{\partial}{\partial y}\left[\epsilon\epsilon' \frac{\partial \phi}{\partial x}\right] \\ + \frac{\partial h}{\partial \phi}\left(f^L - f^S\right) - w g'(\phi).\end{aligned} \tag{3.23}$$

The phase-field and diffusion equations are discretized on uniform grids using an explicit finite difference scheme. During the calculation, a stochastic noise on the liquid composition in the vicinity of interface is imposed in order to simulate the fluctuations, which give the well-developed secondary arms. Note that the free energy densities are obtained by using the thermodynamic data for binary alloys under the assumption of a dilute solution approximation.

C. Numerical analysis and discussions

1. Phase transition simulation in 1-D

Eqs. (3.11) and (3.12) are discretized by finite difference method for spatial derivatives and a simple explicit Euler scheme for temporal derivative, considering mass conservation. Phase dependent diffusivity in Eq. (3.12) is imposed as $D(\phi) = h(\phi)D_S + [1 - h(\phi)]\, D_L$. Initial liquid composition is uniform with 2.0 silicon mole % and the temperature of the system is uniformly fixed as 870 K. The phase diagram of the system can be given by Fig. 14. In order to guarantee existence of stationary solution at long time, we put a moving solute sink point in liquid, keeping a given distance from the interface. In every time step, the solute sink is moved by just the interface migration distance and enforced to put the initial bulk composition. The system initially states in transition and then reaches a steady state. The interface velocity at the steady state could be varied by changing the given distance between solute sink and interface.

We impose a initial condition in calculation as an undercooled state with a given temperature in the system, and then a solid phase with the same composition as the bulk liquid nucleates and starts to grow. After a long time, the interface velocity decreases monotonically and finally stops at an equilibrium state due to the solute trapping behavior as shown in Fig. 15(a).

The material parameters we selected for Al-2mole%Si alloy at 870 K are the followings; diffusivity of solid (D_S) and liquid (D_L) are 1×10^{-12} and $1 \times 10^{-9} m^2/s$. Moral volume (v_m) and interface energy (σ) are $1.06 \times 10^{-5} m^3/mole$ and $0.093 J/m^2$. Melting point (T_m) is 993.6K. Equilibrium composition of solid and liquid in at 870 K are 0.006387 and 0.79. Equilibrium partition coefficient (k^e) and equilibrium liquidus slop in phase diagram m_e are 0.08 and 939.0. The free energy density for solid and

liquid are

$$f^S = \frac{1}{v_m}\left[G^0_{Al}(1-c) + G^0_{Si}c + RT\left[c\ln c + (1-c)\ln(1-c)\right] + A_S c(1-c)\right], \quad (3.24)$$

$$\begin{aligned} f^L &= \frac{1}{v_m}RT\left[c\ln c + (1-c)\ln(1-c)\right] \\ &\quad + c(1-c)\left[A_L + B_L(1-2c) + C_L(1-6c-6c^2)\right], \end{aligned} \quad (3.25)$$

where

$$G^0_{Al} = -10792 + 11.56T,\ G^0_{Al} = 12.12T, A_S = -220 - 7.594T,$$

$$A_L = -107.4 - 1.82T,\ B_L = -4274.5 - 3.0T,\ C_L = 670.7 - 0.46T.$$

The grid size Δx is taken as 0.5 nm, and the interface thickness 2λ is imposed as 3 nm, which will give w and ϵ from Eqs. (3.16) and (3.17) as $2.10 \times 10^8 J/m^3$ and $1.91 \times 10^{-5}(J/m)^{1/2}$, respectively. The total grid number was fixed to be 1000. The phase field mobility M and the corresponding interface kinetics coefficient β are variables related to the compositions of solid and liquid at interface. Eqs. (3.18) and (3.19) allow to evaluate M and β under assumption of dilute solution approximation.

Fig. 15(a) shows stationary composition profiles with three different fixed distances when $M = 44m^3/Js$, where the distance is taken from the position of $\phi = 0.5$ and the solute sink point in liquid phase. The solute sink position that is set to be the initial bulk composition can be seen in each profile. The interface velocities can be measured according to the figure. They are $0.060m/s$ for solid line, $0.20m/s$ for dashed line and $0.50m/s$ for dotted line. We can found that the maximum and the minimum compositions are different with different interface velocity resulting from different the distances.

Because different interface velocities resulted from the different distances of solute sink point cause different maximum and minimum compositions for solid and liquid,

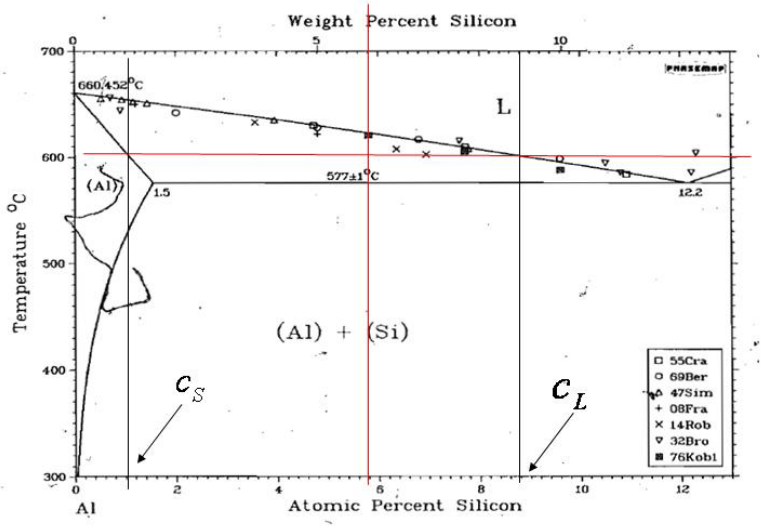

Fig. 14. Phase diagram for Al-2mole%Si alloy at 870 K.

we can compare the solid and liquid compositions at the interface considering high/low interface velocity condition. According to the increase of velocity the effect of solute trapping decreases because high velocity can not drag less solute composition to solid phase during solidification process. Thus, lower solid composition appears in high interface velocity than in low velocity. Because of less solute composition is dragged into the solid phase, large amount of solute composition diffuse to the liquid phase, thus higher composition appears in low interface velocity than in high velocity.

The mobility also affects solute trapping during solidification process. Two cases ($M = 44$ & 2.2) are taken in order to investigate solute trapping. $M = 2.2$ and $M = 44$ corresponds interface kinetics coefficients which are calculated as $0.0165m/Ks$ and

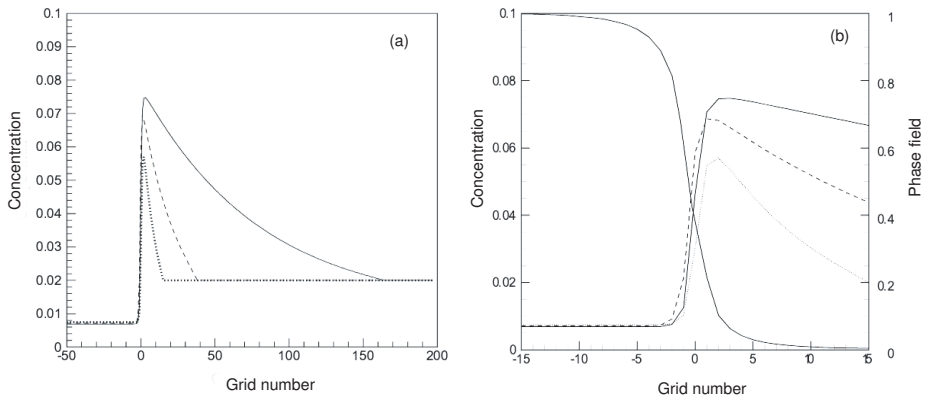

Fig. 15. Steady-state concentration profiles (a) with M=44 m^3/Js for Al-2mole%Si alloy at 870 K. The origin was taken as the position with ϕ=0.5. The interface velocities are 0.060 m/s for solid line, 0.20 m/s for dashed line, and 0.50 m/s for dotted line. (b) Zoom-in profiles of interface corresponding to Fig. 15(a).

$0.0043m/Ks$, respectively, [5] under the dilute solute approximation. Fig. 16 shows variations of the liquid and solid composition dependent of interface velocities at the interface, respectively. In the figures, filled circles ($M = 44m^3/Js$) and open circles ($M = 2.2m^3/Js$) are the results obtained by numerical simulation, and solid curves ($M = 44m^3/Js$) and dashed curves ($M = 2.2m^3/Js$) are from the analytical solution based on low interface velocity limit. From Fig. 16, small M causes both solid and liquid compositions decreased with respect to the increasing interface velocity while large M causes the increase of solid composition and decrease of liquid composition. We can find that high mobility affects the degree of solute drag to the solid phase, which means that large amount of solute composition associates with solid composition because phase transformation occurs faster.

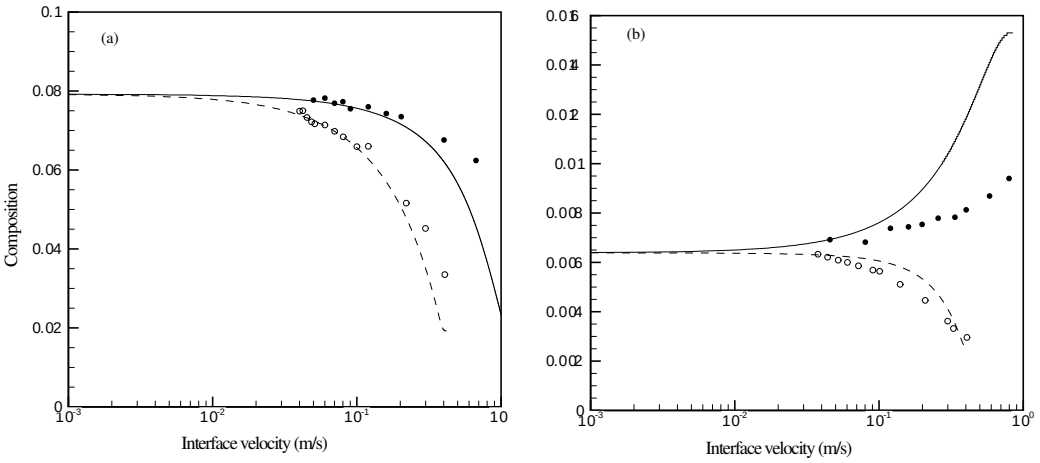

Fig. 16. Variations of the (a) liquid composition and (b) solid composition at the interface with the interface velocity. The solid (M=44 m^3/J s) and dashed curves (M=2.2 m^3/J s) are the predictions with low interface velocity limit condition, and the filled circles (M=44 m^3/J s) and open circles (M=2.2 m^3/J s) are the results obtained from numerical simulations with the same parameters.

2. Dendrite solidification simulations

Eqs. (3.11) and (3.23) are discretized by finite difference method for spatial derivatives and a simple explicit Euler scheme for time derivative, considering mass conservation. Phase dependent diffusivity in Eq. (3.11) is imposed as $D(\phi) = h(\phi)D_S + [1 - h(\phi)]\, D_L$. Initial liquid composition is uniform with 2.0% silicon mole and the temperature of the system is uniformly fixed as 870 K. The phase diagram of the system is given in Fig. 14.

The grid size Δx is taken as 0.03μm, and the interface thickness 2λ is imposed

as 0.12μm, which will give w and ϵ from Eqs. (3.16) and (3.17) as $2.10 \times 10^8 J/m^3$ and $1.91 \times 10^{-5}(J/m)^{1/2}$, respectively. The grid number is fixed to be 2000 by 2000. The phase field mobility M and the corresponding interface kinetics coefficient β are variables related to the compositions of solid and liquid at interface. Eqs. (3.18) and (3.19) allow to evaluate M and β under the assumption of dilute solution approximation. As shown in Eq. (3.20), four-fold dendrite solidification will be performed with a reference angle (45^o). The free energy density for solid and liquid are Eqs. (3.24) and (3.25).

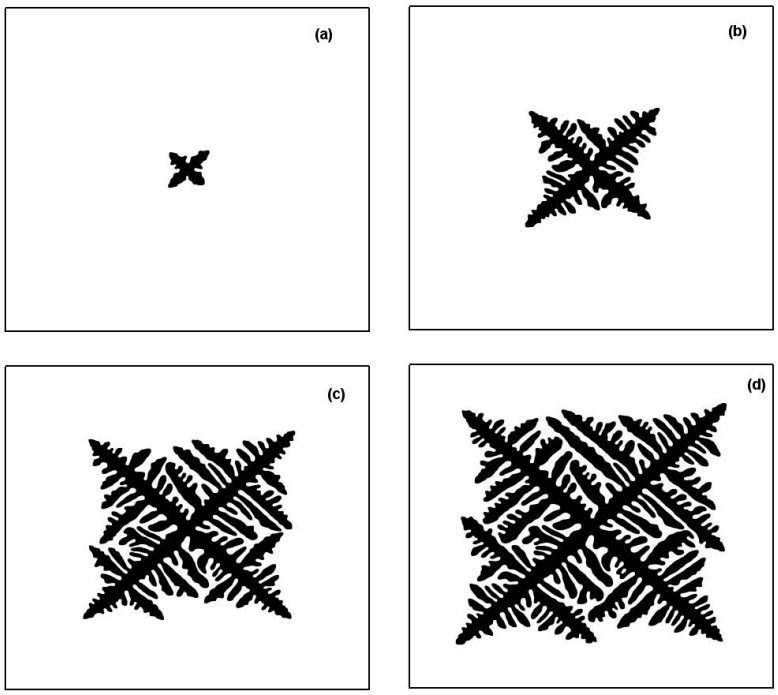

Fig. 17. Dendrite solidification under Al-2mole%Si alloy at 870 K (ν=0.02). (a)t=0.00045(sec), (b)=0.0012(sec), (c)t=0.0021(sec) and (d)t=0.003(sec).

,

The morphologies of dendrite growth will be performed with different anisotropic

coefficients which lead to changing the growth of the primary arms and secondary arms during the dendrite solidification. Noise of the phase on the solid/liquid interface is employed to produce well-developed secondary arms and added into the governing equation.

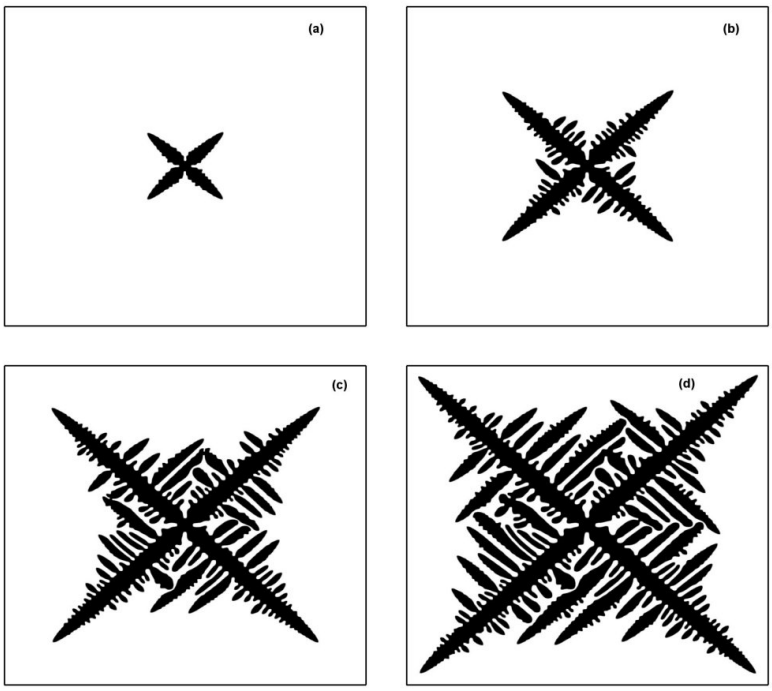

Fig. 18. Dendrite solidification under Al-2mole%Si alloy at 870 K (ν=0.04).

Figs. (17)-(19) show the dendritic morphology with different anisotropic coefficients (ν=0.02, 0.04, 0.08). A dendrite is initially seeded in the center of the calculation domain. According to the figures, we can find that the each arm grows forming parabolic tip at the leading edge according to the preferred directions, and secondary and tertiary arms grows well until they are blocked by other arms. Although the growth of primary arms initially start at the same time, the shape of the primary arms and secondary arms branching from the primary arm are independently differ-

ent because of the imposed noise on the interface. It is clear to see that the thickness of secondary arm in figures increases with the distance behind the primary dendrite tip. Growth procedure inbetween arms can be classified with two successive stages. At first, near the primary arm, the small secondary arms compete with each other and some over-grown secondary arms survive. In second, the competition between the survived arms is rather weak due to large spacing and can grow until further growth are screened by the tertiary arms. Only a few secondary arm can outgrow the neighboring tertiary arms.

The primary arms in the figures grow preferably and other arms stop advancing or slightly melt back. After melt between the primary and secondary arms, they start solidifying again resulting in the coarsening of the primary arms and secondary arms. This melt back process was experimentally observed by [101, 102]. It is interesting to know that the coarsening is observed in high anisotropic coefficient as shown in Figs. (17)-(19). High anisotropic coefficient leads to high difference of interface kinetics according to the orientation (see Eq. (3.20)), resulting in increasing the change of arms' birth, their competition, and the sharpness of dendrite tip.

Asymmetry branching is found for the secondary and tertiary arms. The side branching occurs only at one side of the arms, which has been observed in experiments [35, 102]. It is noted that the asymmetry is related with the thermal field distribution. The side branching prefers to the direction to release the latent heat. One-side branching of tertiary arm is found on the secondary arm. The tertiary branching depends on the liquid-layer thickness between secondary arms, rather than the length of the secondary arm. Also, there seems to be a critical thickness of the liquid-layer between secondary arms for the growth of tertiary arms. Although it is unclear that the same criterion for tertiary branching in real experiments can operate, the large-scale evolution of well-developed tertiary branches in a thermal dendrite promises the

computational development of the dendrite solidification.

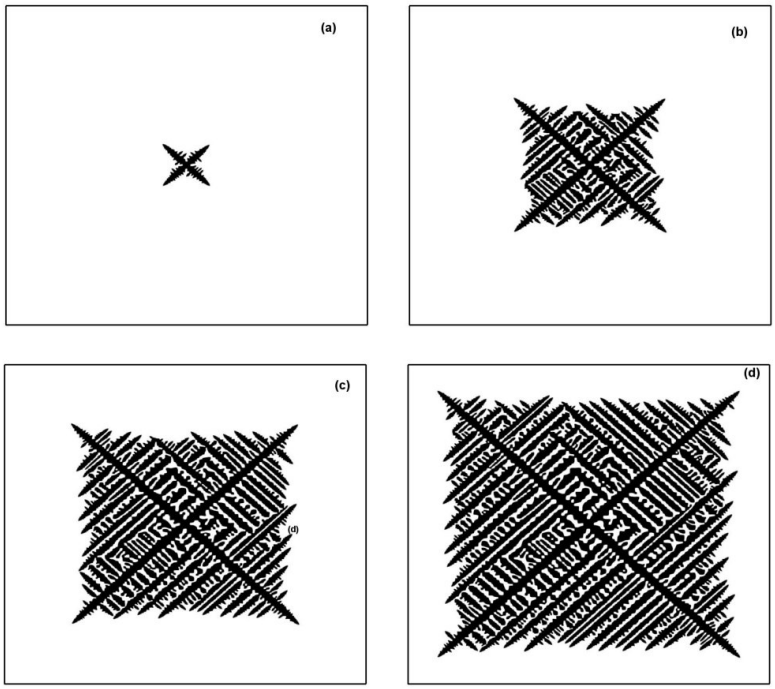

Fig. 19. Dendrite solidification of Al-2mole%Si alloy at 870 K (ν=0.08).

D. Conclusions

We introduced a phase-field model for solidification of an alloy and presented isothermal solidification of Al-2mole%Si alloy at 870 K performed by a numerical method under one and two dimensions. The interfacial compositions of solid and liquid based on a low interface velocity limit were in good agreement with those from the numerical simulations when interface velocity is especially less than $0.2m/s$. we can find that the interface kinetics coefficients vary according to the thermophysical properties of alloys.

For 2-D we simulate the patten of dendrite solidification in the same solidification

system by using an anisotropic phase field model. The simulated dendrite showed similar microstructure observed in experimental researches [35, 102]. There were many interesting phenomenon to know. They are the follows: (1) the each arms grows forming parabolic tip at the leading edge, (2) the primary arms in the figures grow preferably and other arms stop advancing or slightly melt back. After melt between the primary and secondary arms, they start solidifying again resulting in the coarsening of the primary arms and secondary arms, and the coarsening rate is related to the anisotropic coefficient, (3) asymmetry branching is found for the secondary and tertiary arms, and (4) one-side branching of tertiary arm is found on the secondary arm. All phenomena shown in conclusion can be observed in experimental researches [35, 102].

CHAPTER IV

EUTECTIC SOLIDIFICATION

A. Introduction

Understanding the evolution of eutectic patterns during solidification has been a very interesting and difficult problem in materials processing for a long time. Although considerable attention has been allocated to the understanding of this phenomenon in cases in which the solidification front advances freely into the liquid, the actual microstructure of eutectic solidification is strongly dependent of interfacial interactions. If there would be extraneous secondary insoluble impurities, predicting the actual microstructure of eutectic solidification and interfacial interactions becomes more difficult. Several researches reported the beneficial aspects of adding insoluble nanoparticles to solidifying alloys [78, 103, 104, 105].

Mergy *et al.* [37] worked on the experimental investigation of the eutectic growth pattern considering factors such as interfacial energies and diffusion coefficients. The value of the parameters for the transparent organic alloy (CBr_4-C_2Cl_6) was determined by experiments under directional solidification. Ginibre *et al.* [38] investigated the instability of lamellar growing pattern under directional solidification by controlling lamellar spacing, concentration and solidification velocity with the same organic alloy. The experimental characterization of the instability of eutectic growth was found to be in very good agreement with stability diagrams previously computed by Karma [4, 18]. A better understanding of the conditions that drive the (in)stability of eutectic patterns have provided researchers with the fundamental inspiration to control lamellar growth pattern [39], which in turn can provide significant enhancements to the structural properties of eutectic structures.

Chernov *et al.* [106] studied interactions between an impurity and a solidification front governed by van der Waals interactions and viscous lubrication force. They derived an approximate analytical expression for the impurity behavior as a function of its size, temperature gradient and interfacial energy. Similar treatment of the problem proposed by Uhlmann *et al.* [107] was based on the change of chemical potential. The effect of impurities on the structure and stability of the impinging solidification front is determined by an interplay among van der Waals interactions, thermal conductivity differences between the impurity and the melt, interfacial energy and the density change during phase transition [108, 109]. Experimental observations have corroborated that all these factors affect the stability of solidification fronts interacting with insoluble particles [110]. Ode *et al.* [111] investigated the evolution of solid-liquid interface shape with an insoluble impurity using a phase field model with different initial solute concentrations and solidification front velocities in the Fe-C system. The solid-solid interface shape change produced by impurities considered as a second phase field was reported by Moelans *et al.* [112, 113, 114].

Akamatsu *et al.* [76] accidentally observed the decay of eutectic lamellae through interaction with glass particles. Although it happened accidentally, the evolution of eutectic lamellae is worthy of note. One of the first investigations to look into the effect of particles was performed by Lin *et al.* [78] who showed an experimental study of the solidification kinetics and microstructure development in tin/lead solders by mechanically mixing nanopowders of either copper or TiO_2 with tin/lead powders. They found that the solidified composite solder results in the reduction of grain size and spacing of the eutectic lamellae. They concluded that nanopowders increase hardness of microstructure.

In the first section in this chapter, isotropic (and anisotropic) multi-phase field and diffusion equations for eutectic solidification will be derived. The relationships

between thermodynamic variables and parameters in eutectic phase diagram and the relationship between the phase-field mobility and interface kinetics coefficient are derived. Computation methods will be described in detail. 2D simulation results on the lamella eutectic patterns in directional solidification of a organic alloy (CBr_4-C_2Cl_6) will be shown under the same physical parameters and conditions with experimental result [37, 38].

In the second section, we address the problem by employing a relative simple phase-field formulation that will enable us to understand the behavior of a solidifying eutectic front encountering an insoluble particle. We build on already developed descriptions for phenomena associated with the problem at hand, namely, eutectic solidification, the interaction between interfaces and insoluble, secondary particles as well as the encapsulation of impurities by a solidification front. By combining all these different models within a coherent, self-consistent mathematical description, we have been able to address this complex phenomenon in a systematic manner. We then proceed to formulate the model, and then we present the results from an extensive numerical experimentation that had the objective of mapping the behavior of the system as a function of controlled parameters, such as particle size, lamella spacing, temperature gradient at the solid/liquid interface as well as the velocity of the solidification front. In the third section, we add the term of particle conductivity on the calculation based on the description of second section. By combining all these different models as done in the second section, we address this complex phenomenon including system conductivity. We then proceed to formulate the model and then we present and compare results with the second section by mapping the behavior of the system as a function of controllable parameters, such as particle size, temperature gradient, the velocity of the solidification front as well as conductivity difference between a system and a particle.

B. Phase field model for eutectic solidification

1. Free energy functional

During eutectic solidification in a binary system, two solid phases—in this mathematical model represented as α-phase (ϕ_1) and β-phase (ϕ_2)—and a liquid phase—L-phases (ϕ_3)— coexist at equilibrium. Within the context of multi-phase field modeling already described in previous chapters, it is assumed the unitarity of the phase-fields sums at any point in the computational domain, i. e.:

$$\sum_{i=1}^{3} \phi_i = 1. \tag{4.1}$$

It is also assumed that the composition at any point and time interval is given by a simple rule of mixtures, taking into account the contribution of any phase with non-zero phase-field parameter:

$$c(x,t) = \sum_{i=1}^{3} \phi_i c_i. \tag{4.2}$$

The free energy functional for a system of given volume V can be defined as [6]:

$$F = \int_V \left[f_P + f_T \right] \mathrm{d}V \tag{4.3}$$

with f_p being defined as

$$f_P = \sum_{j>i} \sum_{i} \left[-\frac{\epsilon_{ij}}{2} \nabla\phi_i \cdot \nabla\phi_j + \omega_{ij} \left(\phi_i \phi_j \right) \right], \tag{4.4}$$

where ϵ is the gradient energy coefficient and ω is the double well potential representing the energy barrier separating two phases ϕ_i and ϕ_j.

The thermodynamic potential can be obtained from the mixture rule as

$$f_T = \sum_{i} \phi_i f^i \left(c_i \right), \tag{4.5}$$

where $f^i\left(c_i\right)$ is the free energy density of i phase as a function of composition c_i. At any point in the computational grid, when multiple phases coexist, their composition can be determined by assuming a condition of local thermodynamic equilibrium [5], which can be defined as:

$$f_{c_1}^1\left[c_1\right] = f_{c_2}^2\left[c_2\right] = f_{c_3}^3\left[c_3\right] \tag{4.6}$$

Local thermodynamic equilibrium enforces continuity in the chemical potential of all the species across the interfaces, eliminating the extra chemical potential that introduces additional interfacial energetic contributions to the total free energy of a system. This approach in turn relaxes the restrictions on the width of the numerical interfaces during the simulations [6], as mentioned in previous chapters.

The composition can be obtained from a function of ϕ_i and c_i at any point in the computational domain:

$$c(x,t) = \sum_{i=1}^{3} \phi_i c_i. \tag{4.7}$$

2. Phase field and diffusion equations

From [6] the number of phases coexisting in a given point can be obtained as

$$N(x,t) = \sum_{i}^{3} \chi_i(x,t). \tag{4.8}$$

According to [20] and [6], we can get a phase field description for coexisting phases at interfaces as:

$$\Psi_{ij} = \phi_i - \phi_j. \tag{4.9}$$

With Eq. (4.9) we can obtain a description of the kinetics of the evolution of the phase-field as a function of time through the use of the so-called Allen-Cahn evolution equation:

$$\frac{\partial \phi_i}{\partial t} = \frac{1}{N}\left(\sum_{i \neq j} \chi_i \chi_j \frac{\partial \Psi_{ij}}{\partial t}\right), \tag{4.10}$$

where χ_i is equal 1 when corresponding phase exists, otherwise 0, and N presents the number of the coexisting phases. This equation is only valid on the phase interfaces since the presence of only on phase in any point of the calculation domain would make χ_i or χ_j zero, resulting in the cancelation of the whole equation.

Eqs. (4.9) and (4.10) lead to the ansatz of the phase field [6, 27] as [see Appendix B]

$$\frac{\partial \phi_i}{\partial t} - \frac{\partial \phi_j}{\partial t} = -2M_{ij}\left[\frac{\partial F}{\partial \phi_i} - \frac{\partial F}{\partial \phi_j}\right], \tag{4.11}$$

where M_{ij} is mobility. It is noted that the derivative of the free energy functional $\partial F/\partial \phi_i$ is

$$\frac{\partial F}{\partial \phi_i} = \frac{\partial F_P}{\partial \phi_i} + \frac{\partial F_T}{\partial \phi_i}. \tag{4.12}$$

The functional derivatives can be obtained from Eqs. (4.4) and (4.5) by differentiation with respect to ϕ_i as

$$\frac{\partial F_P}{\partial \phi_i} = \sum_{i \neq j}\left[\frac{\epsilon_{ij}^2}{2}\nabla^2 \phi_j\right] \tag{4.13}$$

and

$$\frac{\partial F_T}{\partial \phi_i} = f^i(c_i) - f_c c_i, \tag{4.14}$$

so that Eq. (4.12)

$$\frac{\partial F}{\partial \phi_i} = \sum_{i \neq j}\left[\frac{\epsilon_{ij}^2}{2}\nabla^2 \phi_j + \omega_{ij}\phi_j\right] + f^i(c_i) - f_c c_i, \tag{4.15}$$

where $\epsilon(\epsilon_{ij} = \epsilon_{ji})$ is gradient energy coefficient and ω $(\omega_{ij} = \omega_{ji})$ is the height of double well potential. Finding these two parameters will be explained in the next section. Thus the phase field equation can be obtained from the combination of Eqs. (4.10) and (4.11) as

$$\frac{\partial \phi_i}{\partial t} = -\frac{2}{N}\sum_{i \neq j} M_{ij}\chi_i\chi_j\left[\frac{\partial F}{\partial \phi_i} - \frac{\partial F}{\partial \phi_j}\right]. \tag{4.16}$$

In order to get a diffusion equation, we can set a formulation consisting of diffusion coefficient and the derivative of free energy functional with respect to composition. The diffusion equation with diffusivity that remains constant in a bulk phase can be written as:

$$\frac{\partial c}{\partial t} = \nabla \left(\frac{D(\phi)}{f_{cc}} \nabla f_c \right). \tag{4.17}$$

Eq. (4.17) can be modified with the consideration of multiphase field as

$$\frac{\partial c}{\partial t} = \nabla D \nabla c + \nabla \frac{D}{f_{cc}} \sum_i f_{c\phi_i} \nabla \phi_i. \tag{4.18}$$

With $f_{c\phi_i}/f_{cc} = -c_i$ we can modify Eq. (4.19) again as

$$\frac{\partial c}{\partial t} = \nabla \cdot [D \nabla c] + \nabla \cdot \left[D \sum_i c_i \nabla \phi_i \right]. \tag{4.19}$$

Because each phase has different diffusion coefficient (D), the formulation can be modified depending on phase-field by inserting Eq. (4.2) into Eq. (4.19), resulting in an equivalent diffusion equation under dilute solute approximation [5, 27, 39] as

$$\frac{\partial c}{\partial t} = \nabla \cdot \left(D \sum_{i=1}^{3} \phi_i \nabla c_i \right). \tag{4.20}$$

3. Evaluation of model parameters

In order to get model parameters in the phase field equation, we should obtain a stationary solution of the phase field equation in a planar interface. For example of α phase and L phase, 1-dimensional stationary equation of the phase field and diffusion equation can be changed as

$$\epsilon_{\alpha L}^2 \frac{\mathrm{d}\phi_\alpha}{\mathrm{d}x^2} - \omega_{\alpha L}(1 - 2\phi_\alpha) - \left[f^\alpha - f^L - (c_\alpha - c_L) f_c \right] = 0 \tag{4.21}$$

and

$$\frac{\mathrm{d}}{\mathrm{d}x} D \left[\phi_\alpha \frac{\mathrm{d}c_\alpha}{\mathrm{d}x} + (1-\phi_\alpha) \frac{\mathrm{d}c_L}{\mathrm{d}x} \right] = 0 \tag{4.22}$$

with

$$f_c^\alpha \left[c_\alpha \right] = f_c^L \left[c_L \right] = f_c \tag{4.23}$$

and

$$c = \phi_\alpha c_\alpha + \phi_L c_L. \tag{4.24}$$

From Eq. (4.23) the phase field equation (4.21) will be change as a function of equilibrium composition of each phases. Combining this equation with Eq. (4.23) leads to

$$\epsilon_{\alpha L}^2 \frac{\mathrm{d}\phi_\alpha}{\mathrm{d}x^2} = \omega_{\alpha L}(1-2\phi_\alpha), \tag{4.25}$$

and then integrating this equation yields

$$\phi_\alpha \frac{1}{2} \left(1 - \sin \frac{\sqrt{2\omega_{\alpha L}}}{\epsilon_{\alpha L}} \right). \tag{4.26}$$

The solution will then be associated with interfacial energy and interfacial width. According to the definition of the interface energy as a function of gradient energy coefficient and phase field with a referred interface width, we can get two relationships between model parameters and material parameters, as shown in [5]:

$$\xi = \frac{1}{\sqrt{8}} \frac{\pi \epsilon_{\alpha L}}{\sqrt{\omega_{\alpha L}}} \quad \text{and} \quad \sigma_{\alpha L} = \frac{\pi \epsilon_{\alpha L} \sqrt{\omega_{\alpha L}}}{4\sqrt{2}}, \tag{4.27}$$

In the same manner, we can get a general forms of the model parameter as

$$\xi = \frac{1}{\sqrt{8}} \frac{\pi \epsilon_{ij}}{\sqrt{\omega_{ij}}} \quad \text{and} \quad \sigma_{ij} = \frac{\pi \epsilon_{ij} \sqrt{\omega_{ij}}}{4\sqrt{2}}, \tag{4.28}$$

where ξ is the half width of the interface, and σ_{ij} is the interface energy for the corresponding phases. Based on the approximation of the interface thickness [27], ξ has a fixed value for interfaces.

The phase field mobility M can be determined according to the solution of kinetic coefficient in the previous chapter. It is

$$M_{iL} = \frac{v_m}{RT}\frac{\sigma_{iL}}{(1-k_i)^2}\frac{\sqrt{2\omega_{iL}}}{c_{L\{i\}}\epsilon_{iL}^3\zeta_{iL}}, \tag{4.29}$$

where

$$\zeta_{iL} = \int_0^1 \frac{p(\phi)[1-h(\phi)]}{D\sqrt{g(\phi)}\,[1-(1-k_i)h(\phi)]}\mathrm{d}\phi \tag{4.30}$$

and i can be either α and β. The functions $p(\phi)$, $h(\phi)$ and $g(\phi)$ are referred from the equations in the previous chapter.

4. An anisotropic phase field model

We can extend it for the anisotropic model by changing two model parameters: interface energy σ_{ij} and kinetic coefficient β_{ij}. These parameters are a function of an angle between the x-axis and the directions normal to the $\phi_i = constant$ and $\phi_j = constant$ lines. It is

$$\theta_i = \tan^{-1}\frac{(\phi_i)_y}{(\phi_i)_x}. \tag{4.31}$$

Because mobility M, σ, ω are a function of ϵ, all model parameters can be regarded as a function of θ so that we should focus on the gradient coefficient. It is denoted that

$$\epsilon_{ij} = \epsilon(\theta_{ij}), \quad \text{and} \quad M_{ij} = M(\theta_{ij}) \tag{4.32}$$

and

$$\theta_{ij} = \frac{1}{2}(\theta_i + \theta_j), \tag{4.33}$$

which follows

$$(\epsilon_{ij})_{\theta_i} = \frac{1}{2}\epsilon'_{ij}, \tag{4.34}$$

$$(\epsilon_{ij})_{\theta_i\theta_i} = \frac{1}{4}\epsilon''_{ij}. \tag{4.35}$$

For simplicity, we consider the free energy functional

$$F = \int_V \left[-\frac{\epsilon_{ij}^2(\theta_{ij})}{2} \nabla\phi_i \nabla\phi_j \right] \mathrm{d}V. \tag{4.36}$$

The variation $\delta\phi_i$ in ϕ_i results in the variation of the functional

$$\delta F = -\int_V \left[\epsilon_{ij} \delta\epsilon_{ij} \nabla\phi_i \nabla\phi_j \right] \mathrm{d}V + \int_V \left[\frac{\epsilon_{ij}^2}{2} \nabla\delta\phi_i \nabla\phi_j \right] \mathrm{d}V. \tag{4.37}$$

The variation $\delta\epsilon_{ij}$ in the first integral in Eq. (4.37) can be modified as

$$\delta\epsilon_{ij} = \frac{(\epsilon_{ij})_{\theta_j}}{|\nabla\phi_i|^2} \left[(\phi_i)_x (\delta\phi_i)_y - (\phi_i)_y (\delta\phi_i)_x \right]. \tag{4.38}$$

In order to get the final form of the anisotropic phase field equation, we should obtain the first integral in Eq. (4.37), obtain the functional derivatives and factor this equation. The final result of the functional derivatives is [see Appendix C]

$$\frac{\partial F_{ij}}{\partial\phi_i} = -\frac{\epsilon_{ij}^2}{2} \nabla^2\phi_j + \frac{1}{2} \epsilon_{ij} \epsilon'_{ij} B_{ij} + \frac{1}{2} \left[(\epsilon'_{ij})^2 + \epsilon_{ij} \epsilon''_{ij} \right] A_{ij} \tag{4.39}$$

with

$$\begin{aligned} A_{ij} &= P_{ij} \left[\nabla^2\phi_i + [(\phi_i)_{yy} - (\phi_i)_{xx}] \cos(2\theta_i) - 2(\phi_i)_{xy} \sin(2\theta_i) \right] \\ &\quad + \frac{1}{8} \left[1 + \cos(2\theta_i)\cos(2\theta_j) + \sin(2\theta_i)\sin(2\theta_j) \right] \nabla^2\phi_j \\ &\quad + \frac{1}{8} \left[\cos(2\theta_i) + \cos(2\theta_j) \right] \left[(\phi_j)_{yy} - (\phi_j)_{xx} \right] \\ &\quad - \frac{1}{4} \left[\sin(2\theta_i) + \sin(2\theta_j) \right] (\phi_j)_{xy} \end{aligned} \tag{4.40}$$

and

$$\begin{aligned} B_{ij} &= (\phi_j)_{xy} \left[\cos(2\theta_j) + \cos(2\theta_i) \right] \\ &\quad + \frac{1}{2} \left[(\phi_j)_{yy} - (\phi_j)_{xx} \right] \left[\sin(2\theta_j) + \sin(2\theta_i) \right] \\ &\quad + W_{ij} \left[\nabla^2\phi_i + [(\phi_i)_{yy} - (\phi_i)_{xx}] \cos(2\theta_i) - 2(\phi_i)_{xy} \sin(2\theta_i) \right], \end{aligned} \tag{4.41}$$

where

$$W_{ij} = \frac{(\phi_j)_y(\phi_i)_x - (\phi_j)_x(\phi_i)_y}{|\nabla\phi_i|^2} \tag{4.42}$$

and

$$P_{ij} = \frac{(\phi_j)_x(\phi_i)_x - (\phi_j)_y(\phi_i)_y}{|\nabla\phi_i|^2}. \tag{4.43}$$

Therefore the anisotropic phase field equation is

$$\frac{\partial\phi_i}{\partial t} = -\frac{2}{N}\sum_{i\neq j} M_{ij}\chi_i\chi_j\left[\frac{\partial F^a}{\partial\phi_i} - \frac{\partial F^a}{\partial\phi_j}\right], \tag{4.44}$$

where

$$\begin{aligned}\frac{\partial F^a}{\partial\phi_i} &= \frac{1}{2}\left[\frac{\epsilon_{ij}^2}{2}\nabla^2\phi_j + \epsilon_{ij}\epsilon'_{ij}B_{ij} + \left[(\epsilon'_{ij})^2 + \epsilon_{ij}\epsilon''_{ij}\right]A_{ij} + 2\omega_{ij}\phi_j\right] \\ &\quad + f^i(c_i) - c_i f_c.\end{aligned} \tag{4.45}$$

5. Thermodynamic terms

In order to apply the thermodynamic data from a eutectic phase diagram into a thermodynamic potential of the model, equilibrium liquidus slopes, equilibrium partition coefficients and eutectic composition near eutectic temperature should be certain values. So, we assume that the linearity of the phase boundaries in the diagram from the temperature dependence of the chemical potentials of pure solvent and pure solute where A is the pure solvent and B is a pure solute and their Gibb's free energy are G_A and G_B, respectively. We can write the chemical potentials of component A and B in the i phase of an ideal dilute solution as

$$\mu_A^i = G_A^i - \frac{RT_e}{v_m}c_i, \tag{4.46}$$

$$\mu_B^i = G_B^i - \frac{RT_e}{v_m}\ln c_i, \tag{4.47}$$

From the chemical potential equilibrium, we can get $\mu_A^\alpha = \mu_A^L$ and $\mu_B^\alpha = \mu_B^L$ in

case of α phase and L phase, so that

$$G_A^\alpha - \frac{RT_e}{v_m} c_{\alpha\{L\}} = G_A^L - \frac{RT_e}{v_m} c_{L\{\alpha\}}, \tag{4.48}$$

$$G_B^\alpha - \frac{RT_e}{v_m} \ln c_{\alpha\{L\}} = G_B^L - \frac{RT_e}{v_m} \ln c_{L\{\alpha\}}, \tag{4.49}$$

which follows

$$c_{\alpha\{L\}} - c_{L\{\alpha\}} = \left(\frac{T_e - T}{m_1} - c \right) (1 - k_\alpha), \tag{4.50}$$

$$\ln \frac{c_{\alpha\{L\}}}{c_{L\{\alpha\}}} = \ln k_\alpha. \tag{4.51}$$

Therefore

$$G_A^L - G_A^\alpha = \frac{RT_e}{v_m} \left(c - \frac{T_e - T}{m_\alpha} \right) (1 - k_\alpha), \tag{4.52}$$

$$G_B^L - G_B^\alpha = \frac{RT_e}{v_m} \ln k_\alpha, \tag{4.53}$$

where R, T_e, v_m, k_α are gas constant, eutectic temperature, moral volume and partition coefficient of α and L phases, respectively. With the same manner, we can get for β and L phases

$$G_A^L - G_A^\beta = \frac{RT_e}{v_m} \left(c - \frac{T_e - T}{m_\beta} \right) (1 - k_\beta), \tag{4.54}$$

$$G_B^L - G_B^\beta = \frac{RT_e}{v_m} \ln k_\beta, \tag{4.55}$$

If we regard $G_A^L = 0$ and $G_B^L = 0$ as a standard state, the chemical potential can be obtained as

for α phase:

$$\mu_A^\alpha = \frac{RT_e}{v_m} \left(c - \frac{T_e - T}{m_\alpha} \right) (1 - k_\alpha) - \frac{RT_e}{v_m} c_\alpha, \tag{4.56}$$

$$\mu_B^\alpha = \frac{RT_e}{v_m} \ln \frac{c_\alpha}{k_\alpha}, \tag{4.57}$$

for β phase:

$$\mu_A^\beta = \frac{RT_e}{v_m}\left(c - \frac{T_e - T}{m_\beta}\right)(1 - k_\beta) - \frac{RT_e}{v_m}c_\beta, \tag{4.58}$$

$$\mu_B^\beta = \frac{RT_e}{v_m}\ln\frac{c_\beta}{k_\beta}, \tag{4.59}$$

and for L phase:

$$\mu_A^L = -\frac{RT_e}{v_m}c_L, \tag{4.60}$$

$$\mu_B^L = \frac{RT_e}{v_m}c_L, \tag{4.61}$$

where we can expect $k_L = 1$ in Eqs. (4.60) and (4.61).

From the chemical potential equilibrium condition ($\mu_A^\alpha - \mu_B^\alpha = \mu_A^\beta - \mu_B^\beta = \mu_A^L - \mu_B^L$) and dilute solute approximation ($c_\alpha/c_L = k_\alpha$ and $c_\beta/c_L = k_\beta$), we can get the thermodynamic terms as

for α and β phases:

$$f^i(c_i) - c_i f_c = -\frac{RT_e}{v_m}\left(c - \frac{T_e - T}{m_i}\right)(1 - k_i) - \frac{RT_e}{v_m}c_i \tag{4.62}$$

and for L phase

$$f^L(c_L) - c_L f_c = -\frac{RT_e}{v_m}c_L, \tag{4.63}$$

where i can be either α or β.

6. Numerical implementation

The phase-field equation and the diffusion equation will be numerically solved by using finite difference method with different size of particle, temperature gradient and solidification front velocity. The calculation domain is 400×2000 for the horizontal and vertical coordinates, respectively. The particle is located at the lower position in the calculation domain. Periodic boundary conditions are applied to the sides of the calculation domain and Neumann boundary condition is applied to the top and

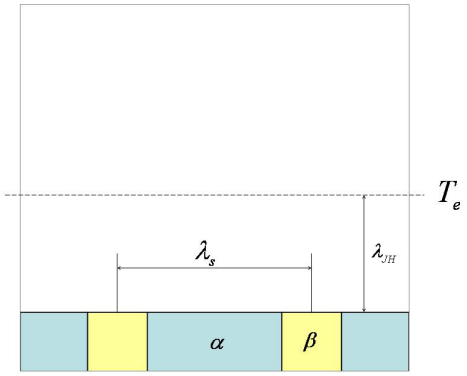

Fig. 20. Lamella spacing with respect to a couple of phases and undercooling spacing with respect to T_e and interface.

bottom of the calculation domain. The initial configuration is shown in Fig. 20.

The physical parameters for the present study will be used as follows [37]; diffusion coefficients of the liquid, solid and particle are respectively $D_L = 5\times10^{-10}(m^2/s)$, $D_\alpha = D_\beta = 5\times10^{-14}(m^2/s)$. Eutectic temperature and composition are $T_e = 357.6$K and $c_e = 0.118$, respectively. The slopes of the liquidus boundary are $m_\alpha = -81$K and $m_\beta = 165$K. Partition coefficients are $k_\alpha = 0.75$ and $k_\beta = 1.6$. Interfacial energies are $\sigma_{\alpha L} = 6.6\times10^{-3}(m^2/s)$, $\sigma_{\beta L} = 5.8\times10^{-3}(m^2/s)$ and $\sigma_{\alpha\beta} = 11.5\times10^{-3}(m^2/s)$. The molar volume is $v_m = 1.12\times10^{-4}(m^3/\text{mol})$. The temperature gradient (G) and the solidification front velocity (V) applied into the system are fixed as $G = 8.0\times10^3(\text{K}/m)$ and $V = 2.0\times10^{-6}(m/s)$, respectively. We apply the interface width for $2\xi = 7\triangle x$ where $\triangle x = 2.0\times10^{-7}m$.

Directional eutectic solidification is set to be isotropic or anisotropic, and the dimensionless lamellar spacing $\overline{\lambda} = \lambda_s/\lambda_{JH}$ is set to be variable. According to Jackson and Hunt [115], the definition of lamella spacing λ_s is given by Fig. 20 where λ_{JH} is the undercooling distance.

7. Results and discussions

Figs. 21(a-b) and Fig. 21(c) are applied with isotropic and anisotropic phase filed equations, respectively. The regular lamella eutectic structure with straight α/β boundaries parallel to the thermal gradient direction appeared to be stable up to $\overline{\lambda}$=2.1 as shown in Fig. 27(b). However, an oscillatory pattern with periodic change in widths of α and β phases appeared at $\overline{\lambda}$=2.3. This pattern ($1\lambda O$ pattern) was observed also at $\overline{\lambda}$=2.5, as shown in Fig. 21(a). By increasing $\overline{\lambda}$ above 2.5, transition of the lamella pattern occurs at the initial stage of growth. At first, the $1\lambda O$-like pattern occurred, but after a transient stages, the lamella pattern transformed into another oscillatory pattern with a wavelength of twice the lamellar spacing, which is called $2\lambda O$ pattern, and experimental observation of this pattern was reported by Mergy *et al.* [37].

This transient stage from $1\lambda O$ pattern to $2\lambda O$ pattern occurred earlier with increasing $\overline{\lambda}$ further. Fig. 21(b) is a computation result obtained with at $\overline{\lambda}$=2.7, showing behavior of typical transition pattern. Thus, it is noted that the regular lamella eutectic structure with straight α/β boundaries can be found at $\overline{\lambda}$ <2.2, $1\lambda O$ pattern can be found at 2.2< $\overline{\lambda}$ <2.5, and The transient stage from $1\lambda O$ pattern to $2\lambda O$ can be found at 2.5< $\overline{\lambda}$. Also, these patterns based on the values of $\overline{\lambda}$ can be reported by Grinbre *et al.* [38].

The experimental results, such as oscillatory lamellar growth in Figs. 21(a) and (b) [38], are realized as follows. At first, a sample is pulled with a pulling velocity V_i (for example, Figs. 21(a) and (b) have different V_i for a sufficiently long time to reach a initial steady state having equilibrium undercooling spacing (λ_{JH}) and lamellar spacing (λ_S). Then the pulling velocity is suddenly increased by a sufficiently small quantity for not triggering creations of lamellae or tilt domains (an upward V jump).

This practically makes the average and the local values of λ_s unchanged. But, because of the V change, we can expect an instability behavior of lamellar growth. Once it happens, the system is likely to restabilize into a different type of lamella growing pattern that is another steady state of lamellar growth according to the V jump without the change of λ_s. This means that experimental run of different V jump, such as Fig. 21(a) and (b), is supposed to give us a series of points representing the various pattern of lamellar growth. Grinbre *et al.* [38] performed many such experiments with various values of the concentration and spacing until the interesting zone of the parameter space was satisfactorily scanned. In practice, numerous difficulties complicate this idealized picture.

Here, I select two cases of the experimental results described above for isotropic lamella growth to reproduce Figs. 21(a) and (b). The simulation of Figs. 21(a1) adapted $\overline{\lambda}$=2.5 and the simulation of Figs. 21(b1) adapted $\overline{\lambda}$=2.7. The simulation results are shown in Figs. 21(a1) and (b1). They provide a good agreement each other. In the consideration of undercooling and lamella spacing as shown Fig. 22, we can expect that the system has lamella growth approaching another steady state that is satisfied with $\lambda_{S,min}$, but the initial lamella spacing (X in Fig. 22) is higher than $\lambda_{S,min}$. Therefore, local decrease of a lamella spacing occurs and local undercooling decreases afterwards. If it happens, the lamella are stabilized by the resulting change in the interface shape. When the stabilization process occurs, the lamella tends to grow normal to the existing local interface. Because the lamella spacing decreases, the neighboring lamella spacing increases simultaneously. Once the neighboring lamella spacing decreases enough, the lamella spacing decreases again based on the re-stabilization behavior.

This increase/decrease of lamella spacing can be explained with Fig. 22. When a lamella spacing moves to Point B, it is certain that the neighbor moves to Point A in

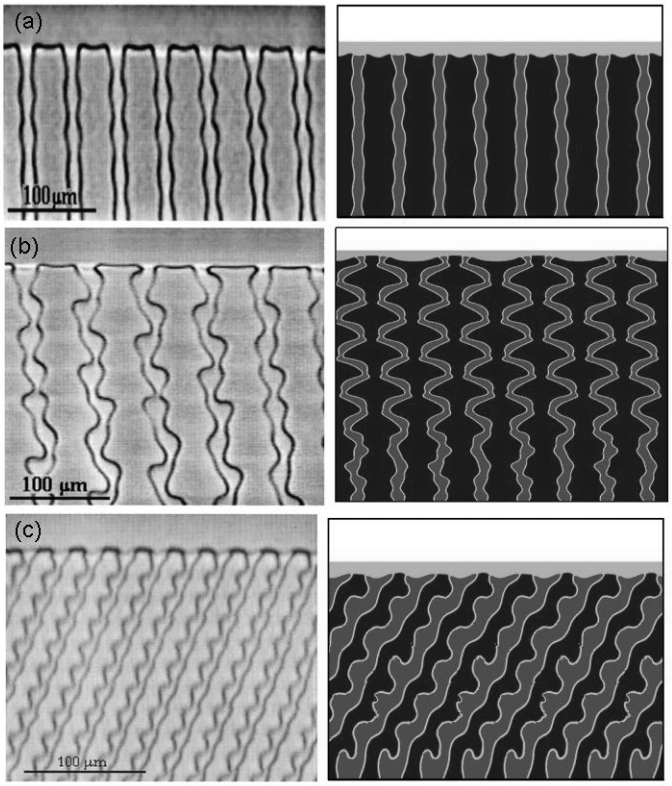

Fig. 21. Phase field simulation for directional eutectic solidification of organic alloy (CBr_4-C_2Cl_6). (a) $\overline{\lambda}$=2.5 and (b) $\overline{\lambda}$=2.7 are simulated under isotropic condition. (c) $\overline{\lambda}$=2.2 with θ=22^o as anisotropic condition. Solidification front velocity and temperature gradient are 2.0×10^{-6}(m/s) and 8.0×10^3(K/s), respectively. The left figures are from experimental results [38] and the right figures are generated by using parameters from [38].(Reprinted with Permission of American Physical Society.)

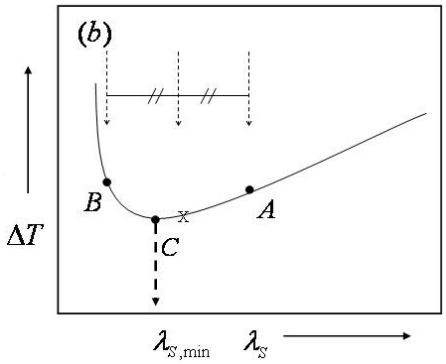

Fig. 22. Schematic drawing of the variation of interface undercooling ($\Delta T = T_e - T_i$) with lamella spacing (λ_s). An important factor from the experimental research in order to reproduce lamellar growth using computational method is the dimensionless lamellar spacing $\overline{\lambda} = \lambda_s/\lambda_{JH}$ that can be set to be variable. According to [38, 115], λ_s is the lamella spacing and λ_{JH} is the undercooling distance.

Fig. 22. The growth condition moves to the left (Point B), a local decrease in lamella spacing results in a narrowing depression of interface (higher ΔT), while a local increase in lamella spacing results in a widening uplift of interface. The depressing lamellar spacing is more unstable, because of higher ΔT, than the uplifting one. The fluctuation that decreases the local lamella spacing (point B) becomes more unstable compared with the right (Point A), and the unstable lamella spacing moves to point C (increase of lamella spacing)in order to be stable, while the other neighboring lamella spacing that moved to Point A moves back to Point C resulting in the decrease of lamella spacing. This indicates the fluctuation of lamella spacing, and this fluctuation is continuously repeated. This behavior presents oscillatory lamella growth, and the degree of the oscillation during lamella growth depends on the lamella spacing corresponding to a initial pulling velocity .

The minimum lamellar spacing ($\lambda_{S,min}$) can be obtained from Gibb-Thompson

relations as [115]

$$\frac{\Delta T}{m} = v\lambda_s Q^L + \frac{a_L}{\lambda_s}, \tag{4.64}$$

where

$$\begin{aligned}
\frac{1}{m} &= \frac{1}{m_\alpha} + \frac{1}{m_\beta} \\
Q^L &= \frac{P(1+\xi)^2 C_0}{\xi_L D}, \\
a^L &= 2(1+\xi)\left(\frac{a_\alpha^L}{m_\alpha} + \frac{a_\beta^L}{\xi m_\beta}\right) \\
a_\alpha^L &= \left(\frac{T_E}{L}\right)_\alpha \sigma_\alpha^L \; sin\theta_\alpha^L \\
a_\beta^L &= \left(\frac{T_E}{L}\right)_\beta \sigma_\beta^L \; sin\theta_\beta^L
\end{aligned} \tag{4.65}$$

and v is the pulling velocity, P is a constant, ξ_L is the ratio of α and β lamella widths, D is the diffusion coefficient, m is the liquidus slop corresponding to phase, L is the latent heat, T_E is the eutectic temperature, σ is the liquid/solid interface energy corresponding to phase, and θ is the angle of the solid/liquid interface at a triple point.

From Eq. (4.64), $\lambda_{S,min}$ at constant pulling velocity can be obtained as [115]

$$\lambda_{S,min} = \frac{2ma^L}{\Delta T\cdot}. \tag{4.66}$$

$\lambda_{S,min}$ depends on a^L that is a interfacial energy as shown in Eq. (4.65), when ΔT, λ_{JH} and m are fixed. Here, we can define $\sigma_\alpha^L \; sin\theta_\alpha^L + \sigma_\beta^L \; sin\theta_\beta^L = \sigma_{\alpha\beta}$, not $= \sigma_{S/L}$, which is called interfacial energy between α and β phases [see Fig. 23]. Therefore, $\overline{\lambda} = 2.7$ in Fig. 21(a) indicates higher $\sigma_{\alpha\beta}$ occupied than $\overline{\lambda} = 2.5$ in Fig. 21(b).

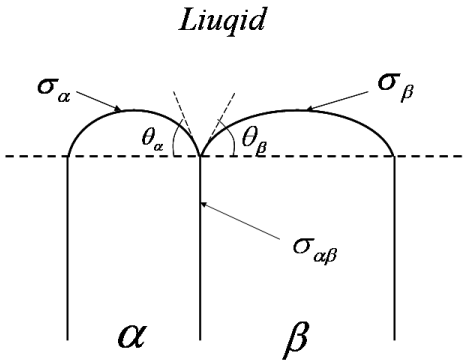

Fig. 23. A sketch of a lamella eutectic with the contact angles θ_α and θ_β and interfacial energies σ_α, σ_β and $\sigma_{\alpha\beta}$.

C. Phase-field simulations of the eutectic solidification of binary alloy containing encapsulated impurities

1. Free energy density and the constraints

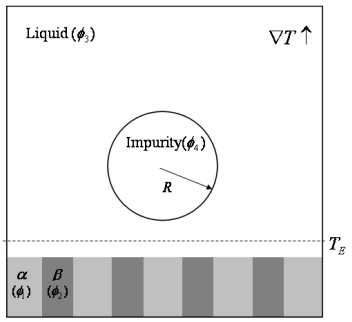

Fig. 24. A particle near a advancing eutectic solidification front in a temperature gradient G. Each phases are identical.

From this section, the term 'impurity' denotes a circular (spherical) particle that is insoluble in both the liquid as well as any of the two solid phases present in the system. Consider that a directional solidification front approaches a particle of radius R located in front of solid-liquid interface which has velocity V and temperature

gradient G as seen in Fig. 24. There is a spontaneous formation composed of two phases (α and β)from the liquid phase (i. e. eutectic solidification). During the eutectic solidification, a system has four phases such as α-phases (ϕ_1) and β-phases (ϕ_2) for solid phase, L-phases (ϕ_3) for liquid and P-phases (ϕ_4) for the particle as seen in Fig. 24. Because the sum of the phases in a point in the system is equal to 1, we can note that

$$\sum_i \phi_i = 1 \quad \text{and} \quad i = 1, ..., 4. \tag{4.67}$$

The presence of the particle can be introduced into a model by adding a positive contribution to the total free energy of the system due to the presence of the insoluble particle, as suggested by [112, 113, 114]. The free energy functional can be defined as

$$F = \int_V [f_P + f_T] \, \mathrm{d}V. \tag{4.68}$$

With f_p being defined regarding the present of the particle as

$$f_P = \sum_{j>i} \sum_i \left[-\frac{\epsilon_{ij}}{2} \nabla\phi_i \cdot \nabla\phi_j + \omega_{ij} \left(\phi_i\phi_j + \Phi \left(\frac{1}{4}\phi_i^2 - \frac{3}{2}\phi_i\phi_j + \frac{1}{4}\phi_j^2 \right) \right) \right], \tag{4.69}$$

where ϵ is the gradient energy coefficient and ω is the double well potential representing the energy barrier separating two phases i, j.

Φ is a spatially dependent parameter which is equal 1 in the particle phase and 0 out of the particle phase. Φ can be considered to be a foreign phase field variable which is static (invariant) in time. Having $\Phi = 0$ leads to a typical double well potential [27]. When $\Phi = 1$, the free energy density as a function of ϕ_i has one minimum at which ϕ is equal to 0.5. For $\Phi = 0$, the free energy density has two minima at $\phi_i = 0$ and $\phi_i = 1$, which represents double-well potential. The shapes of the free energy density as a function of phase field variable for $\Phi = 1$ and $\Phi = 0$ are

shown in the Fig. 25.

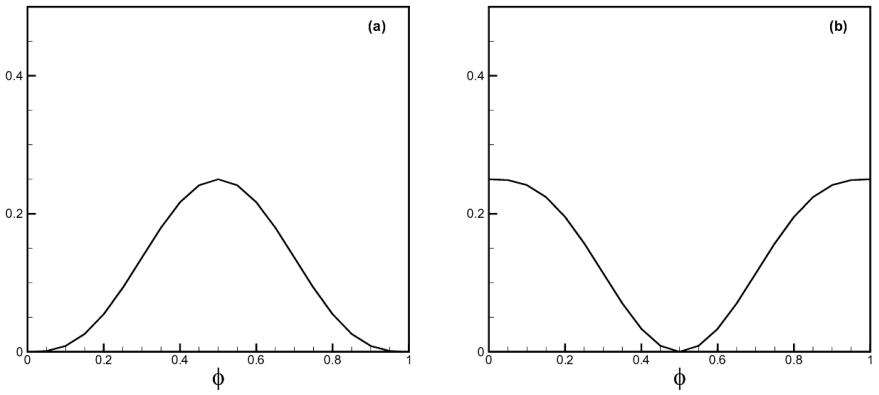

Fig. 25. Free energy density as a function of phase fields. (a) Φ =0: the free energy density has two minima at $\phi_i = 0$ and $\phi_i = 1$, which means that there is a phase separation. (b) Φ =1: the free energy density as a function of ϕ_i and ϕ_j has one minimum at which ϕ equal 0.5. The number of the minima can be determined by Φ.

The thermodynamic potential can be obtained from the mixture rule as

$$f_T = \sum_i \phi_i f^i \left(c_i\right), \tag{4.70}$$

where $f^i\left(c_i\right)$ is the free energy density of i phase as a function of composition c_i. At any point in the computational grid, when multiple phases coexist, heir composition can be determined by assuming a condition of local thermodynamic equilibrium [5], which can be defined as:

$$f^1_{c_1}\left[c_1\right] = f^2_{c_2}\left[c_2\right] = f^3_{c_3}\left[c_3\right] = f^4_{c_4}.\left[c_4\right] \tag{4.71}$$

Local thermodynamic equilibrium enforces continuity in the chemical potential of all the species across the interfaces, eliminating the extra chemical potential that introduces additional interfacial energetic contributions to the total free energy of a

system. This approach in turn relaxes the restrictions on the width of the numerical interfaces during the simulations [6].

The composition can be obtained from a function of ϕ_i and c_i at any point in the computational domain:

$$c(x,t) = \sum_{i=1}^{4} \phi_i c_i. \tag{4.72}$$

2. Phase field and diffusion equations

According to [20] and [6], we can get a phase field description for coexisting phases at interfaces as:

$$\Psi_{ij} = \phi_i - \phi_j. \tag{4.73}$$

With Eq.(4.73) we can obtain a description of the kinetics of the evolution of the phase-field as a function of time through the use of Allen-Cahn evolution equation:

$$\frac{\partial \phi_i}{\partial t} = \frac{1}{N}\left(\sum_{i \neq j} s_i s_j \frac{\partial \Psi_{ij}}{\partial t}\right), \tag{4.74}$$

where s_i is equal 1 when corresponding phase exists, otherwise 0, and N presents the number of the coexisting phases. This equation is only valid on the phase interfaces which tells that the equation is valid on the phase interfaces since the presence of only on phase in any point of the calculation domain would make s_i or s_j zero, resulting in the cancelation of the whole equation.

Eqs. (4.73) and (4.74) lead to the ansatz of the phase field [27] as

$$\frac{\partial \phi_i}{\partial t} - \frac{\partial \phi_j}{\partial t} = -2M_{ij}\left[\frac{\partial F}{\partial \phi_i} - \frac{\partial F}{\partial \phi_j}\right], \tag{4.75}$$

where M_{ij} is the mobility. It is noted that the derivative of the free energy functional $\partial F/\partial \phi_i$ is the sum of $\partial F_P/\partial \phi_i$ and $\partial F_T/\partial \phi_i$.

The functional derivatives can be obtained from Eqs. (4.69) and (4.70) by dif-

ferentiation with respect to ϕ_i as

$$\frac{\partial F}{\partial \phi_i} = \sum_{i \neq j} \left[\frac{\epsilon_{ij}^2}{2} \nabla^2 \phi_j + \omega_{ij} \phi_j + \frac{1}{2} \Phi \omega_{ij} \phi_i - \frac{3}{2} \Phi \omega_{ij} \phi_j \right] + f^i(c_i) - f_c c_i, \tag{4.76}$$

where $\epsilon(\epsilon_{ij} = \epsilon_{ji})$ is gradient energy coefficient and $\omega(\omega_{ij} = \omega_{ji})$ is the height of double well potential. Finding these two parameters will be explained in the next section. Thus the phase field equation can be obtained from the combination of Eqs. (4.74) and (4.75) as

$$\frac{\partial \phi_i}{\partial t} = -\frac{2}{N} \sum_{i \neq j} M_{ij} s_i s_j \left[\frac{\partial F}{\partial \phi_i} - \frac{\partial F}{\partial \phi_j} \right]. \tag{4.77}$$

In order to get a diffusion equation, we can set a formulation consisting of diffusion coefficient and the derivative of free energy functional with respect to composition. The formulation can be modified with a function of free energy density with Eqs. (4.68), (4.71) and (4.72). Because each phase has different diffusion coefficient (D), the formulation can be modified depending on phase field, resulting in an equivalent diffusion equation under dilute solute approximation [5, 27, 39] as

$$\frac{\partial c}{\partial t} = \nabla \cdot \left(D \sum_{i=1}^{4} \phi_i \nabla c_i \right). \tag{4.78}$$

3. Evaluation of model parameters

In order to get model parameters in the phase field equation, we should obtain a stationary solution of the phase field equation in a planar interface. The solution will then be associated with interfacial energy and interfacial width. According to the definition of the interface energy as a function of gradient energy coefficient and phase field with a referred interface width, we can get two relationships between model parameters and material parameters, as shown in [5] and [27]:

$$\xi = \frac{1}{\sqrt{8}} \frac{\pi \epsilon_{ij}}{\sqrt{\omega_{ij}}} \quad \text{and} \quad \sigma_{ij} = \frac{\pi \epsilon_{ij} \sqrt{\omega_{ij}}}{4\sqrt{2}}, \tag{4.79}$$

where ξ is the half width of the interface, and σ_{ij} is the interface energy for the corresponding phases. Based on the approximation of the interface thickness [27], ξ has a fixed value at the solid-liquid interface. However, in order to incorporate the effects of insoluble particles, the value of ξ for particle-solid and particle-liquid interfaces should be different. According to Eq.(4.69), this phase does not undergo any phase transformation (i. e., the phase field is invariant in time). The corresponding interfaces should then be very thin comparing with the solid-liquid interface resulting in a small value of ϵ_{ij}. A small value of ϵ_{i4} in turn requires a large value for the energy barrier between any phase and the insoluble particle, ω_{i4}. It is noted that interface energy between the insoluble particle and any of the two solid eutectic phases or the liquid can be given from the determination of the proper interface width of particle-phase interface as well as from the energy barrier ω_{i4}.

From the phase field diagram of the organic alloy investigated by [38], we can get a simple form of the thermodynamic potential [27]. The linearity of the phase boundaries in the diagram can help to obtain a chemical potential equation which is a function of Gibb's energy of individual composition and the energy of the mixture within the ideal dilute solute approximation. Although the Gibb's energy of individual phases at any given composition is fixed, the total free energy of the mixture varies because it is a function of the corresponding composition.

Since the insoluble particle is incorporated into the model as a fourth phase containing any or both species of the organic alloy, the presence of such a fourth phase could in principle affect the topology of the eutectic phase diagram. Such a fourth phase would then evolve over time according to the proper kinetics as well as

the local thermodynamic conditions established at the interface between this particle and any of the three other phases. Although in principle we could actually designate this particle as being composed of a third species, such a description would only complicate the model without gaining much advantage. In this work, we constrain the composition of the particle to very small amounts of one of the species of the alloy. We restrict the evolution of this insoluble particle by suppressing the mobility of any interface involving this phase as well as any diffusion within the particle phase field. Essentially, what we are doing in this work is to establish this fourth particle as being a metastable phase that, under normal considerations would dissolve but that it is kinetically constrained to do so due to the extremely small interface and atomic mobilities. Full incorporation of this particle within the computational domain and subject to the constraints described above allows us to keep global mass conservation during the simulation.

The thermodynamic potential terms (the last two terms in Eq. (4.76)) for solid, liquid and particle phases can be respectively obtained under the a standard state as

$$\frac{RT}{v_m}\left[\left(c_E-\frac{T_E-T}{m_i}\right)(1-k_i)-c_i\right],\ -\frac{RT}{v_m}c_3\ \text{ and }\ \frac{RT}{v_m}\left[\left(c_E-\frac{T_E-T}{m_i}\right)-c_4\right], \tag{4.80}$$

where R is the gas constant, v_m is the molar volume, m_i is the slope of the liquidus boundary in the phase diagram, T_E is eutectic temperature of the system, k_i is the partition coefficient. When $k_3 = 1$ and $k_4 \approx 0$ are applied into the first thermodynamic potential in Eq. (4.80), we can obtain the last two thermodynamic potentials because partition. Note that the thermodynamic potential for the fourth phase does not have any relation to the actual thermodynamics of the eutectic system. The mathematical functional form in this case is just selected to facilitate the implementation

of the numerical model. Since the particle is kinetically prevented from evolving, its actual thermodynamic description is actually inconsequential.

The mobility (M_{i3}) can be obtained based on the thin interface limit [27] neglecting a kinetic coefficient as

$$M_{i3} = \frac{v_m}{RT}\frac{\sigma_{i3}}{(1-k_i)^2}\frac{\sqrt{2\omega_{i3}}}{c^e_{i3}\epsilon^3_{i3}}\frac{D_{\phi_3}}{\int_1^0 \frac{\sqrt{\phi^2-\phi}}{(\phi-1)(k_i+1)+k_i}\mathrm{d}\phi}. \tag{4.81}$$

However, obtaining mobility (M_{i4}) requires further consideration. Some parameters in Eq. (4.81) should be based on the particle parameters. According to Eq. (4.81), D_{ϕ_3} is referred by M_{i3}, which means that when we consider the mobility based on the particle phase, we can denote D_{ϕ_4} for M_{i4}, and the diffusivity of the particle phases is close to zero due to the insoluble particle. Therefore M_{i4} can be selected with a negligible value as well.

4. Numerical implementation

The phase field equation and the diffusion equation will be numerically solved by using finite difference method with different size of particle, temperature gradient and solidification front velocity. The calculation domain is 400×2000 for the horizontal and vertical coordinates, respectively. The particle is located at the lower position in the calculation domain. Periodic boundary conditions are applied to the sides of the calculation domain and Neumann boundary condition is applied to the top and bottom of the calculation domain. The initial configuration is shown in Fig. 25.

The physical parameters for the present study will be used as the following [37]; diffusion coefficients of the liquid, solid and particle are respectively $D_L = 5 \times 10^{-10}(m^2/s)$, $D_S = 5\times10^{-14}(m^2/s)$ and $D_P = 5\times10^{-24}(m^2/s)$. Eutectic temperature and composition are $T_E = 357.6$ and $c_E = 0.118$, respectively. The slopes of the

liquidus boundary are $m_1 = m_4 = -81$K and $m_2 = 165$K. Partition coefficients are $k_1 = 0.75$, $k_2 = 1.6$ and $k_4 = 0.0001$. $k_4 = 0.0001$ is caused by the small value of particle composition. Interfacial energies are $\sigma_{13} = 6.6 \times 10^{-3}(m^2/s)$, $\sigma_{23} = 5.8 \times 10^{-3}(m^2/s)$, $\sigma_{12} = 11.5 \times 10^{-3}(m^2/s)$ and $\sigma_{i4} = 22.5 \times 10^{-3}(m^2/s)$. The molar volume is $v_m = 1.12 \times 10^{-4}(m^3/\text{mol})$.

Directional eutectic solidification is set to be isotropic, and the lamellar spacing is uniformly $10\mu m$. The radius of the particle varies from $5\mu m$ to $12\mu m$. The distance between the bottom of a particle and solidification front is set to be 30 μm which is enough to grow lamellae stable until the lamellae impinge the particle. The temperature gradient (G) and the solidification front velocity (V) applied into the system also vary from $1.0 \times 10^3(\text{K}/s)$ to $3.2 \times 10^4(\text{K}/s)$ and from $2.0 \times 10^{-7}(m/s)$ to $4. \times 10^{-6}(\text{K}/s)$, respectively. The solidification front velocity is controlled by moving eutectic temperature in the calculation domain, and the temperature gradient is imposed on the system based on the eutectic temperature position. The referred G and V are $8.0 \times 10^3(\text{K}/s)$ and $2.0 \times 10^{-6}(m/s)$, respectively. We applied different interface width between the solid-liquid interface ($2\xi = 7\triangle x$) [27] and the particle-liquid (or particle-solid) interface ($2\xi = 2\triangle x$), where $\triangle x = 2.0 \times 10^{-7}m$.

5. Results and discussions

The eutectic growth pattern containing an encapsulated particle appears to be highly complex due to many mechanisms, caused by the existence of the particle and system parameters which are the size of the particle, the interface energies of phase-coexisting areas, lamella spacing, temperature gradient, solidification front velocity and so on. Understanding of the morphology of eutectic lamellar growth with the effect of the encapsulated particle can be attained by investigating the instability of lamellar growing and the number of the growing lamellae. Here we consider the instability of lamellar

growing and the number of the growing lamellae according to the variation of the size of a particle, the temperature gradient and solidification front velocity.

Eutectic solidification growth patterns with different particle sizes are presented in Fig. 26, where $V = 2.0 \times 10^{-6}$(m/s) and $G = 8.0 \times 10^{3}$(K/s). There are a lot of possible sizes of the particle applied to the calculation, but representative figures for the morphology of solidification are selected with $R = 5\&12\mu m$. In case of simple solidification impinging an insoluble and immobile particle [111], the particle at an early stage does not affect interface shape even though solute trapping has occurred. As the interface moves to the particle, solute diffusion is obstructed by the particle resulting in the concave morphology of the solid/liquid interface. The concentration of solute in the liquid phase between the interface and the particle is gradually higher, and then the particle is encapsulated by the advancing interface front. Instantly, a solute-enriched thin liquid film exists along the surface of the particle, but it becomes solid as the evolution progresses. While passing the particle, the interface near the surface of the particle is likely to slide on the surface of the particle with less velocity due to the higher solute concentration [5], comparing with other areas that have no contact with the particle, which pattern of the interface is likely to render the deep-valley shape of the interface at the top of the particle once the particle is completely engulfed. After that, the interface does not return its original flat configuration, but becomes swallow-dipped shape due to the higher solute concentration even at the late stage, as discussed by [110], in Fig. 27.

The behavior of the interface shape upon particle impingement and engulfing affects the instability and growth of lamellae during solidification. According to the particle size relative to the lamella spacing, there are several cases showing different morphologies of eutectic solidification. For example, in some cases, lamellae keep growing without changing the number of initial lamellae. The behavior in Fig. 26(a)

can be obtained at $R < 6\mu m$, which corresponds to a particle size less than half the lamella spacing. Under these conditions, the lamella seem to be almost unperturbed by the presence of the particle.

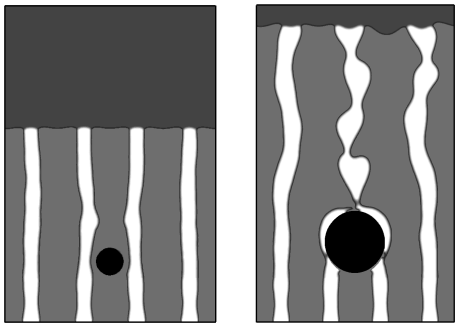

Fig. 26. Eutectic solidification according to various particle sizes ($R = 5\&12\mu m$) with fixed solidification front velocity ($V = 2.0 \times 10^{-6} m/s$) and temperature gradient ($G = 8.0 \times 10^3$ K/s). β is minor phase.

When the particle is comparable in size to the lamella spacing, instabilities in the growth pattern can emerge. For example, Fig. 26(b) shows the interaction between a eutectic solidification front and an insoluble particle of radius of 12 μm. In this case, two inner lamellae grow along surface of the particle, and then they coalesce as the particle is completely engulfed by the solidification front. Because of the reduction of the number of lamellae caused by the change of interface shape, equilibrium condition between lamella spacing and undercooling rate is broken, resulting in unstable growth of lamellae at the later stage. This instability is manifested as morphological perturbations with a wavelength of about the lamella spacing. These sorts of instability patterns can be seen to occur under different conditions, according to the particle size, but the behavior was observed to occur whenever particle size was between one and two times the lamella spacing.

Morphologies of eutectic solidification with smaller solidification front velocity

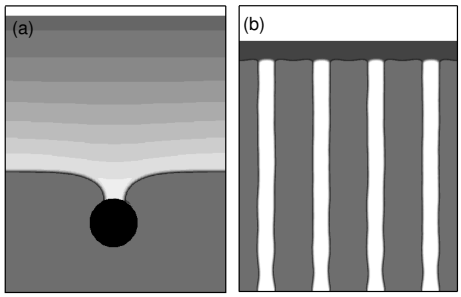

Fig. 27. Interface shape around an insoluble particle from Ode *et al.* [111] and a typical eutectic solidification from Kim *et al.* [27]. (a):$V = 2.0 \times 10^{-7} m/s$ and $G = 8.0 \times 10^3$ K/s in a radius ($R = 5\mu m$). (b):$V = 2.0 \times 10^{-7} m/s$ and $G = 8.0 \times 10^3$ K/s.

($V = 2.0 \times 10^{-7}$(m/s)) and larger solidification velocity ($V = 4.0 \times 10^{-6}$(m/s)) are shown in Figs. 28(a)$\sim$(c) and in Figs. 28(d)$\sim$(e), respectively. Comparing with Fig. 26, lamellae grow stably but their number is decreased under the low solidification front velocity without the transition zone in Figs. 28(a)-(c), while lamellae grow also stable but the number is increased under the large solidification front velocity with the transition zone (Figs. 28(d)-(e)). The lamellae grow stably and slowly at the early stage, but due to the smaller solidification front velocity lamellae passing adjacent the particle grow bending toward the particle as shown in Fig. 28(a)-(c), or lamellae growing toward the bottom of the particle stop growing by particle's blocking as shown in Fig. 28(c). Unlike the cases in Fig. 26, the lamellae grow stably even though they bend toward the surface of the particle because of the low solidification front velocity which distributes insufficient energy for the lamellae to arrive at an out-of-equilibrium state, so that they are likely to grow stably although the lamellar spacing becomes different from that prior interaction with the particle.

Contrary to the cases of the low solidification front velocity, the lamellae growing under the higher solidification front velocity show morphological instabilities in the

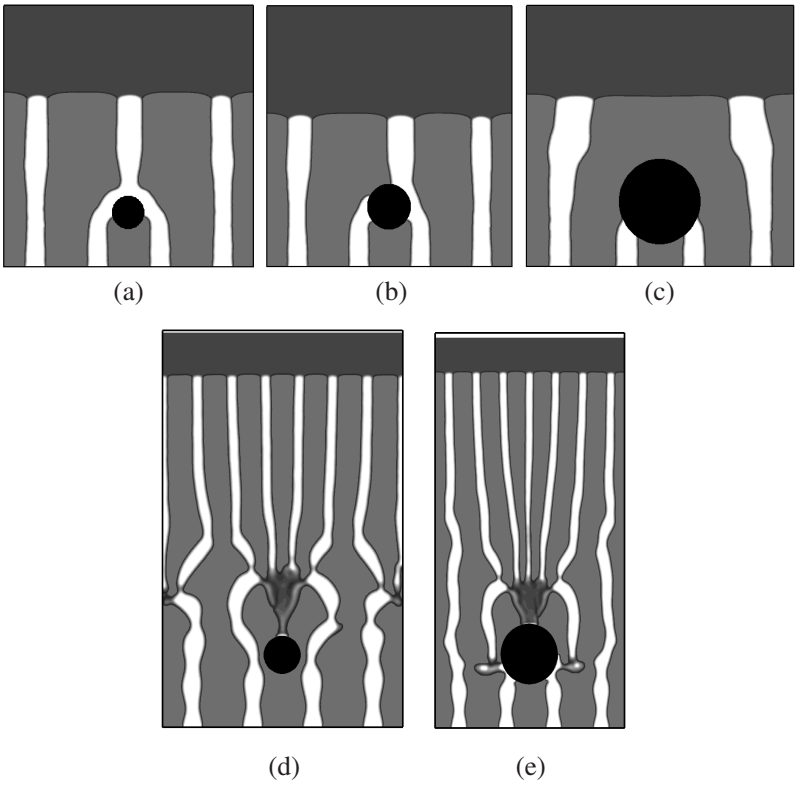

Fig. 28. Eutectic solidification according to various particle sizes with fixed solidification front velocity and temperature gradient. (a)-(c) are applied with $V = 2.0 \times 10^{-7} m/s$ and temperature gradient ($G = 8.0 \times 10^3$ K/s) in each radius ($R = 5, 7, \&12 \mu m$) . (d)-(e) are applied with $V = 4.0 \times 10^{-6} m/s$ and temperature gradient ($G = 8.0 \times 10^3$ K/s) in each radius ($R = 6\&12 \mu m$).

eutectic phases prior their interaction with the insoluble particle. Upon encapsulation, transition zones are formed in all cases investigated, irrespective of the particle size. The number of transition zones formed after particle encapsulation actually decreases as the particle size increases, as shown in Figs. 28(d)-(e). Contrary to the case shown in Fig. 28(c), the two inner lamellae in Fig. 28(e) are not stopped from growing by the particle but actually grow around it, contributing eventually to the formation of the transition zone. It can be found that all cases in Figs. 28(d)-(e) show that the lamellae grow in an stable manner after particle encapsulation. Growth apparently is

stabilized due to the decrease in lamella spacing in accordance with previous numerical investigations [27]. It is interesting to note that the larger size of particle and larger solidification front velocity result in an increase in the number of growing lamella after encapsulation.

Because there are three controllable parameters; size of the particle, solidification front velocity and temperature gradient, numerous cases can be obtained from the numerous combination of three parameters. In order to avoid redundant explanations, the stability maps of the lamella growth according three parameters are required. The stability maps according the solidification front velocity and temperature gradient with some fixed particle's radii are useful to understand physics of the eutectic growth containing a particle because the particle may be regarded as an unnecessary object in the system and the other parameters can be under control in solidification manufacturing. In this work, more than a hundred different cases involving different particle sizes, solidification front velocities as well as temperature gradients were used to construct stability maps for the problem in question.

The temperature gradient (G) and the solidification front velocity (V) applied into the system were varied from 1.0×10^3(K/s) to 3.2×10^4(K/s) and from 2.0×10^{-7}(m/s) to 4.0×10^{-6}(K/s), respectively. Three sizes of the particle are selected. One case (similar to that shown in Fig. 26(a)) should involve a particle should show that the diameter of a particle is smaller than the largest width of the lamella (dark-colored lamellar) among a set of lamella. In this case the lamella (white-colored lamella) will not touch the surface of the particle based on general eutectic lamella growth. In a second case (similar to that shown in Fig. 26(b)), the particle has the same size as the lamella spacing, resulting in the lamella structure definitely touching the particle and 'sliding' on the surface of the particle as it is being engulfed. The third case should involve a particle with size twice that of the lamella spacing. This

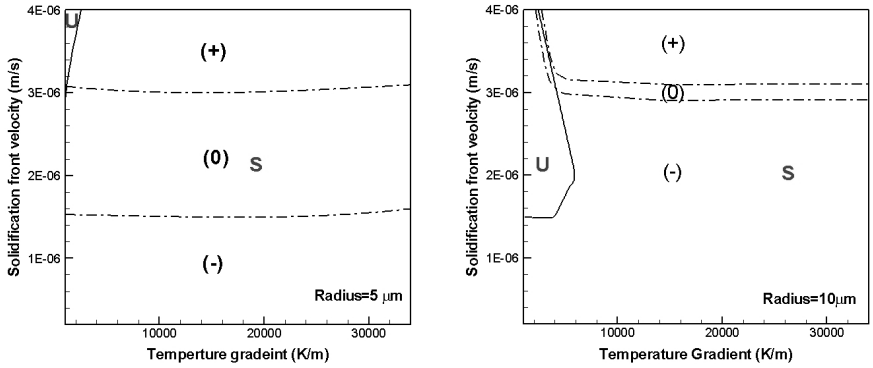

Fig. 29. Instability of eutectic solidifications according to front velocities and temperature gradients with two fixed particle radius, (a)$R = 5\mu m$ and (b)$R = 10\mu m$. The range of the solidification front velocity is $2.0 \times 10^{-7} < V < 4.0 \times 10^{-6}$(m/s) and the range of the temperature gradient is $1.0 \times 10^{3} < G < 3.4 \times 10^{4}$ (K/s). (0), (-) and (+) in the figures indicate that the system has the same number, less number and large number of lamellae after particle impingement compared with initial number of lamellae, respectively.

can result in the interruption of the growth of some of the lamellae. The two radii of particles representing the three different situations just described are 5μm and 10μm.

Fig. 29 shows the resulting maps of stability of eutectic solidification and the number of growing lamella sets after complete encapsulation according to the variation of temperature gradient and solidification front velocity with two different particle sizes. In Fig. 29, (0), (-) and (+) indicate that the system has the same number, less number and large number of lamellae after particle impingement compared with initial number of lamellae, respectively, while the shaded regions indicate the unstable growth of lamellae after engulfment. In general, larger G stabilizes lamellae while smaller G and larger V tend to induce morphological instabilities during solidification. Larger V increases the number of lamellae formed after particle en-

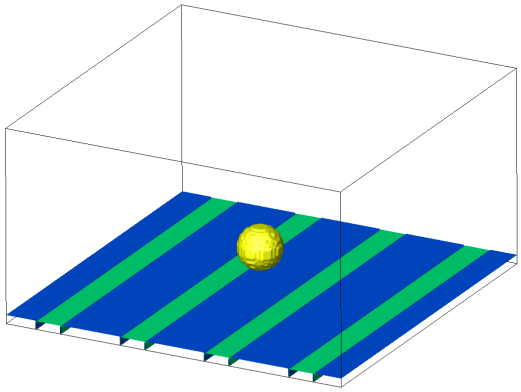

Fig. 30. Configuration of the eutectic solidification containing insoluble impurities in 3D. $400 \times 400 \times 2000$ of calculation domain is used.

capsulation. However due to the two different formation between particle and initial lamella spacing, the results of the instability are slightly different. For unstable regions, $R = 5\mu m$ shows that the unstable zone exists in large V and small G and disappears with $V < 3.0 \times 10^{-6}$(m/s), and $R = 10\mu m$ shows that the unstable zone exists in large V and small G, but occupies large area even in $V \approx 1.5 \times 10^{-6}$(m/s) and $G \approx 5.0 \times 10^{3}$(K/s) because of the positional characteristics between lamella spacing and particle size mentioned above. For the number of the growing lamella set, $R = 5\mu m$ shows four growing lamella sets are widely occupied in the middle of Fig. 29(a). More than four growing lamella sets occur in $V > 3 \times 10^{-6}$(m/s)and mostly grow stably. $R = 10\mu m$ shows that the area of the less than four growing lamella sets becomes wider, and four growing lamella sets becomes narrower. However, the area presenting more than four growing lamella sets in this case is equilibrant to the area of the $R = 5\mu m$ case except low V.

Fig. 31 shows the three different lamella growth after impinging a particle ($R =$

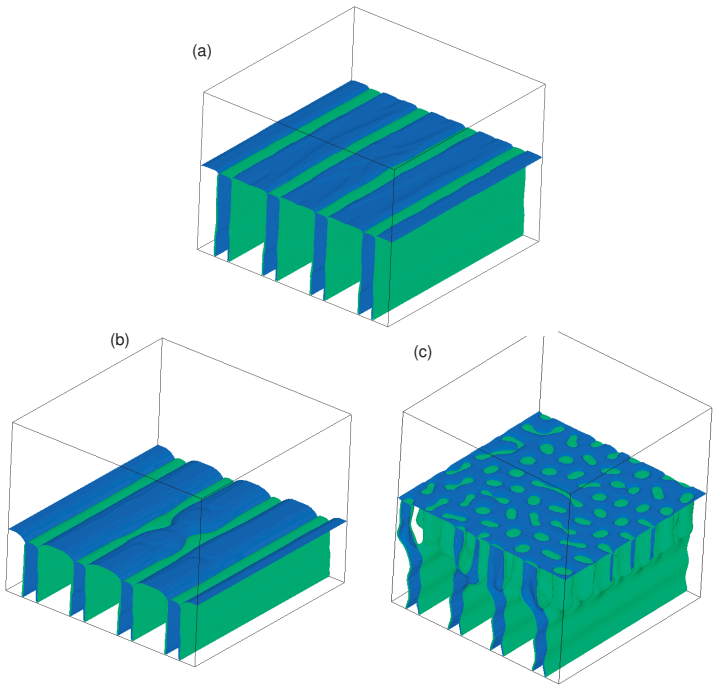

Fig. 31. 3D simulation of eutectic solidifications impinging particle ($R = 5\mu$m) according to (a) $V = 2.0 \times 10^{-6}$(m/s) and $G = 8.0 \times 10^{3}$ (K/s), (b) $V = 2.0 \times 10^{-7}$(m/s) and $G = 8.0 \times 10^{3}$ (K/s) and (c) $V = 4.0 \times 10^{-6}$(m/s) and $G = 16.0 \times 10^{3}$ (K/s).

5μm) from 3D simulation. Initially configuration of the 3D eutectic solidification containing insoluble impurities is adopted in Fig. 30. As we discussed before, we found that there are three different significant features of lamella growth due to the existence of the particle. The first one is the feature that initial number of lamellae is not changed and the lamellae grows stable as shown in Fig. 26(a). According to the position of the particle, the morphology of lamella growth would be different, but the case of Fig. 26(a) shows that the particle does not affect the growth of lamella. The 3D simulation in Fig. 31(a) gives us more realistic evolution of lamella growth including the neighboring ones. The second one is the feature that initial number of lamellae is reduced and the lamellae grows stable as shown in Fig. 28(a). From

fig. 28(a), two inner lamella is merged after impinging a particle, and the thickness of lamella increases. The case of Fig. 26(b) shows that the particle cause the inner lamella merged, but does not affect to stability of lamella growth. The 3D simulation in Fig. 31(b) gives us different evolution of lamella growth near the particle. Because of the existence of the far-away lamellae, contrary to Fig. 28(a) the lamella near the particle is not merged together, but becomes separated and stable. The last one is the feature that initial number of lamellae increases and the lamellae grows stable after impinging a particle as shown in Figs. 28(d)-e. 3D simulation in Fig. 31(c) provides more detail evolution of lamella growth which number increases.

D. Eutectic solidification of binary alloy containing impurities of different conductivity

In this section, we will use the phase field model, diffusion equation, and model parameters from the previous section. We will investigate morphology of eutectic growth adjacent to the encapsulating impurity, that has a different conductivity with system and plot engulfments for each case based on the effects, which results in obtaining instability of the growing lamellar pattern in the CBr_4-C_2Cl_6 system. It is expected that this description will allow the qualitative investigation of stability phenomena as a function of some of the most important factors that can be controlled during actual experimental investigations.

1. Conductivity difference between impurity and system

Because we consider the conductivity difference between a particle and system, the heat equation derived from Fourier's law must be included in the calculation. Obtaining temperature distribution is only for getting model parameter that is involved in

the governing equations. Therefore time-independent heat equation required in the calculation is

$$T_t = k_c \nabla T, \tag{4.82}$$

where k_c is the conductivity which varies with material of particles (k_p) and system (k_m) according to calculation points in this study. While it is true that the system conductivity during eutectic solidification is slightly different because the system has different phases and different compositions, we use a bulk conductivity for the whole system in order to focus on the difference between a impurity and system. Fig. 32 shows that non-dimensional temperature distribution according to the value of $\overline{k} = k_m/k_p$.

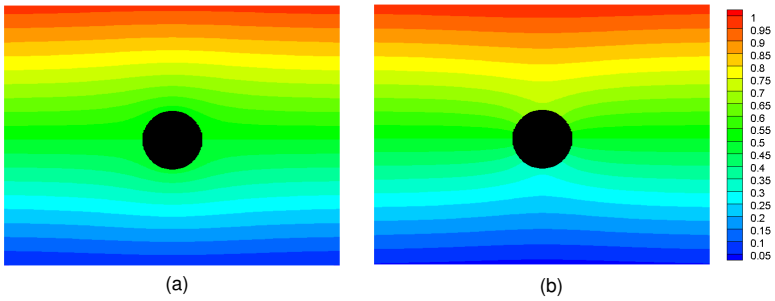

Fig. 32. Temperature distribution with different conductivity of a system and an impurity. The values of the temperature are non-dimensionalized. $\overline{k} = k_m/k_p$=100 and $\overline{k} = k_m/k_p$=0.01 are plotted in Fig. 32(a) and (b), respectively.

2. Numerical implementation

The phase field equation and the diffusion equation will be numerically solved by using finite difference method with different size of particle, temperature gradient and solidification front velocity. The calculation domain is set to be three dimensions ($400 \times 400 \times 2000$). The particle is located at the lower position in the calculation

domain. Periodic boundary conditions are applied to the sides of the calculation domain and Neumann boundary condition is applied to the top and bottom of the calculation domain. The initial configuration is shown in Fig. 30.

The physical parameters and initial system configurations for the present study will be the same as those shown in the previous section. Directional eutectic solidification is set to be isotropic, and the lamellar spacing is uniformly $10\mu m$. The radius of the particle is selected from $5\mu m$ to $10\mu m$. The distance between the bottom of a particle and solidification front is set to be 30 μm which is enough to grow lamellae stable until the lamellae impinge the particle. The temperature gradient (G) and the solidification front velocity (V) applied into the system will be used as the same with the previous section. The ratio of the conductivity between the system and impurity ($\overline{k} = k_m/k_p$) varies from 0.01 to 100. Therefore the temperature distribution on the system and will be varied according to $\overline{k}$ while temperature distribution in the previous section has gradient only for solidification direction. The temperature gradient in this section is imposed on the system based on the eutectic temperature position and results from heat equation. We applied different interface width between the solid-liquid interface ($2\xi = 7\triangle x$) [27] and the particle-liquid (or particle-solid) interface ($2\xi = 2\triangle x$), where $\triangle x = 2.0 \times 10^{-7} m$.

3. Results and discussions

We discussed that the eutectic growth pattern containing an encapsulated particle should be considered with many mechanical factors, such as size of the particle, temperature gradient, solidification front velocity, and discussed the results based on the factor. Conductivity of materials is also one of the important mechanical factors that may change the evolution of lamella growth. Here we additionally include conductivity difference in the system, and show the effect of the conductivity difference on the

instability of lamellar growing.

As discussed in the previous section, we found that the lamella growth pattern after impinging an impurity can be classified into three different cases. The first case is that the number of lamellae is not changed compared with the initial number of lamellae as shown in Fig. 33. The second case is that the number of lamellae is reduced as shown in Fig. 34. In 2D simulation as shown in Fig. 28(a), two lamellae seem to be merged together, but 3D simulation shows a different behavior. The two lamellae near the impurity are merged together resulting in the change of growth pattern of adjacent lamellae. The last case is that the number of lamellae is increased as shown in Fig. 35. In previous section, the solidification interface is performed as a flat surface except the time that the interface engulfs the impurity resulting that the previous cases do not have convex shape of solidification front, but have concave shape of solidification front. Now, we consider the shape of the solidification front by using the conductivity difference between a system and an impurity. Thus, we can find that cases applied with the same V and G may provide the different growth pattern due to the shape of the interface brought by the conductivity in this section.

The first case shown in Fig. 33 shows that the change of the lamellae during the solidification does not happen. The 3D growth pattern in Fig. 33(a) agrees with the result of the previous section [see Fig. 29(a)]. The growth pattern in Fig. 33(b) shows possibility of second cases. If the case of Fig. 33(b) would be simulated without the effect of the conductivity difference, it definitely results that the change of the lamellae pattern at the adjacent the impurity do not happens, and the lamellae grow stably. $\overline{k}$ >1 changes the solidification front into convex shape when the solidification front is located under the impurity. On the other hand, the solidification front becomes concave shape when it is located over the impurity due to heat flux distribution around the impurity. The concave shape of the solidification front would drive two

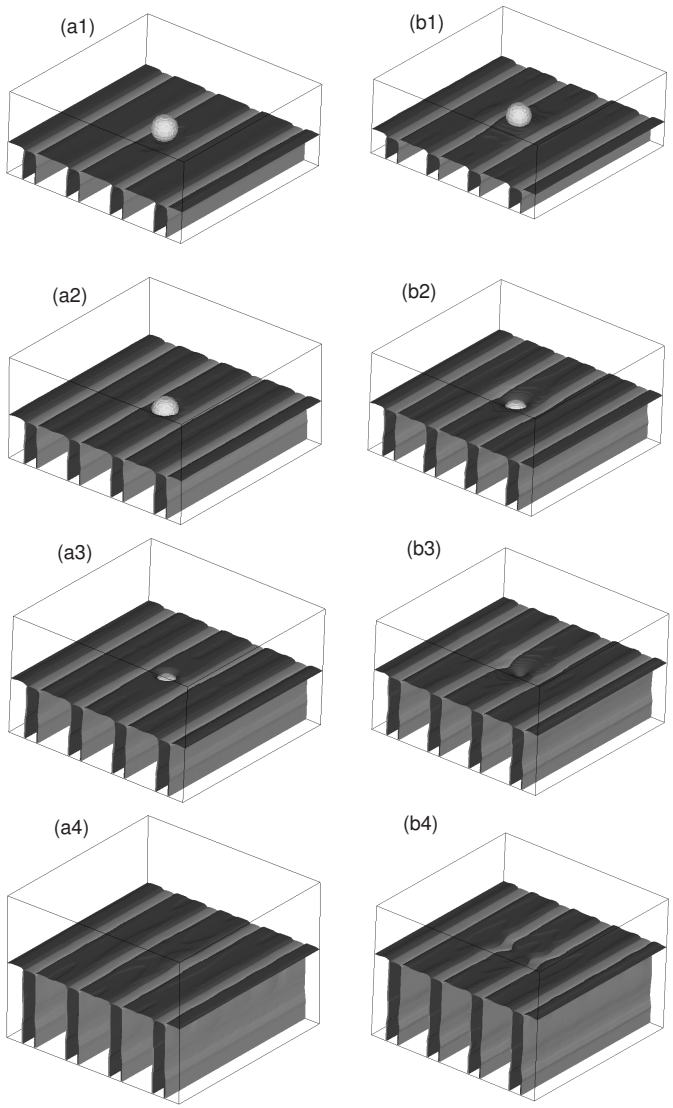

Fig. 33. Growth pattern of eutectic lamellae according to (a) $G = 32.0 \times 10^3$(K/m), $V = 2.5 \times 10^{-6}$(m/s) and $\overline{k} = 0.5$ and (b) $G = 32.0 \times 10^3$(K/m), $V = 2.0 \times 10^{-6}$(m/s) and $\overline{k} = 100$ with $R = 5\mu m$.

lamella to be merged. but, it does not happen afterward. If driving to merge two lamellae together is applied strongly, the lamellae near the impurity will be merged together, and the next growth pattern is well simulated in Fig. 35.

Fig. 34 shows that merging of two lamellae near an impurity. Once the two lamellae are merged together near the impurity, the wavy pattern of the lamella is observed in Fig. 34(a). Moreover, the degree of the mergence of two lamellae near the impurity is observed strongly as shown in Fig. 34(b), then the two lamellae are broken apart, and new lamella forms on top of the impurity. Because the broken lamellae are unstable, other independent lamellae appear by cutting the tail of the broken lamellae. The newborn lamellae will affect the growth pattern of the lamellae in the system according to value of $\overline{k}$, V and G. If the break of the longitudinal set of lamellae happens continuously, the set of lamellae are eventually broken into small pieces of lamellae, and the growth of small pieces turns to be stable [see Fig. 35].

In order to understand the growth pattern of lamellae in detail, the stability maps of the growth pattern should be required as shown in Figs. 36-38. Fig. 36 shows growth pattern map of eutectic solidification according to the conductivity difference ($0.01 < \overline{k} < 100$) and the solidification velocity (4.0×10^7(m/s)$< V < 4.0 \times 10^6$(m/s)) at a fixed temperature gradient ($G = 8.0 \times 10^3$(K/m)) in Fig. 36(a) and the conductivity difference ($0.01< \overline{k} <100$) and the temperature gradients (1.0×10^3(K/m)$< G < 32.0 \times 10^3$(K/m)) at a fixed solidification velocity ($V = 6.0 \times 10^7$(m/s)) in Fig. 36(b). The total areas in Fig. 36(a) shows the stable growth pattern. From Fig. 36 one can find that high solidification front velocity produce mores lamellae pieces after impingement, and small $\overline{k}$ is likely to reduce the number of lamellae unless solidification from velocity is larger than 1.9×10^6(m/s). In Fig. 36(b), one can find that unstable region of growth pattern is observed at low G and high $\overline{k}$. It is expected that high $\overline{k}$ pushes away due to the convex shape of the front. The pushed lamellae

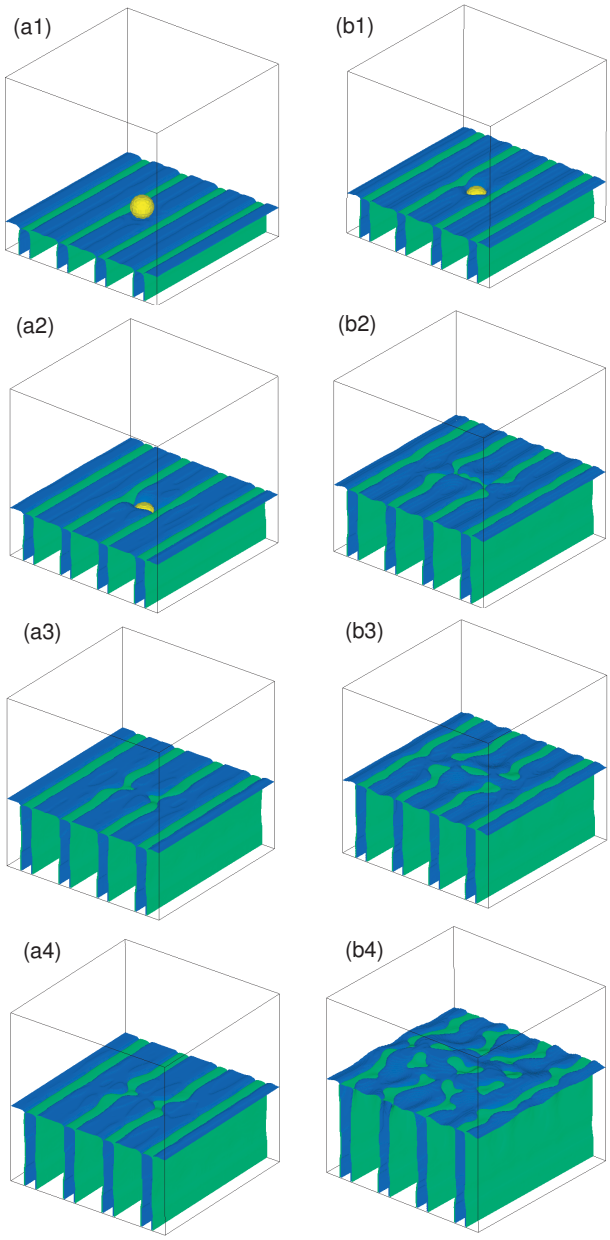

Fig. 34. Growth pattern of eutectic lamellae according to (a) $G = 5.0 \times 10^3$(K/m), $V = 2.0 \times 10^{-6}$(m/s) and $\overline{k} = 100$ and (b) $G = 1.0 \times 10^3$(K/m), $V = 3.5 \times 10^{-6}$(m/s) and $\overline{k} = 10$ with $R = 5\mu m$.

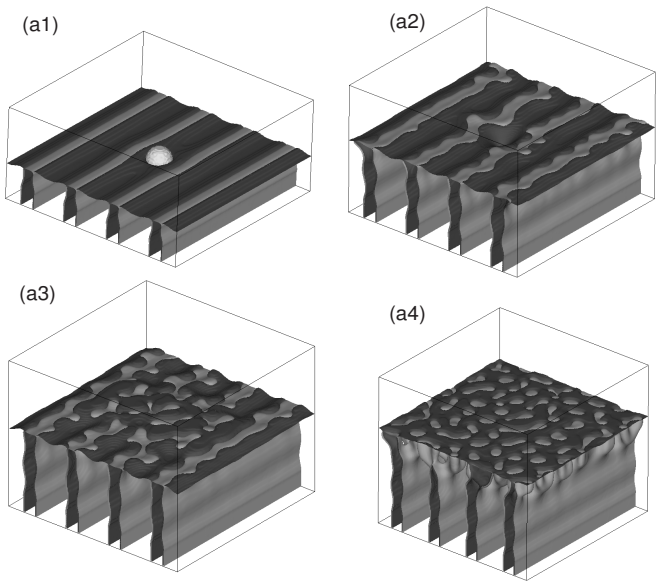

Fig. 35. Growth pattern of eutectic lamellae according to $G = 1.0 \times 10^4$(K/m), $V = 4.0 \times 10^{-6}$(m/s) and $\overline{k} = 100$ with $R = 5\mu m$.

becomes unstable, and the low G stimulate the instability of the lamellae because unstable regions is likely to be formed at low G in the case without the effect of conductivity difference as shown in Fig. 29.

Fig. 37 shows growth pattern map of eutectic solidification according to front velocities and temperature gradients with $R = 5\mu m$, (a) $\overline{k} = 0.01$ and (b) $\overline{k} = 100$. The range of the solidification front velocity is $2.0 \times 10^{-7} < V < 4.0 \times 10^{-6}$(m/s) and the range of the temperature gradient is $1.0 \times 10^3 < G < 3.4 \times 10^4$ (K/s). When conductivity difference was not taken into account in the previous section, larger G stabilizes lamellae while smaller G tends to induce morphological instabilities during solidification and larger V increases the number of lamellae formed after particle encapsulation. Under the consideration of conductivity difference, one can find that the reduction of the lamella's number newly appear at $G > 2.0 \times 10^4$ and $G < 2.0 \times 10^3$,

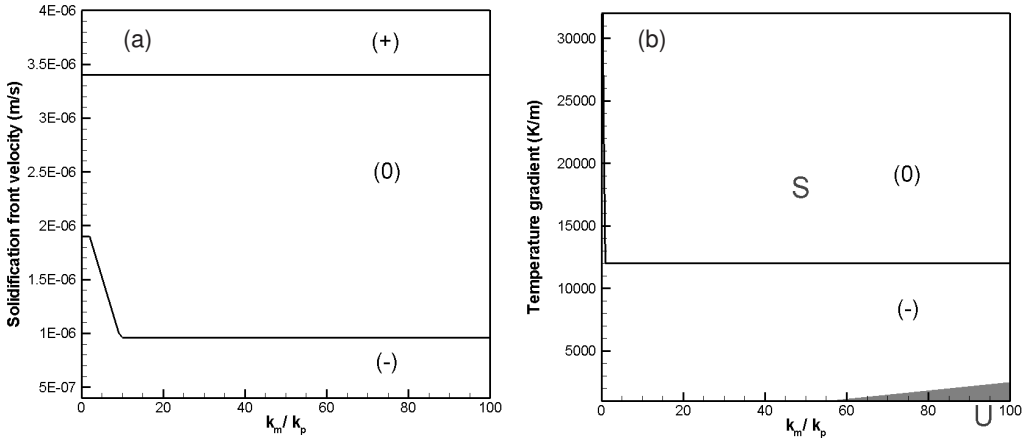

Fig. 36. Growth pattern map of eutectic solidification according to (a) the conductivity difference and the solidification velocity at a fixed temperature gradient ($G = 8.0 \times 10^3$(K/m)) and (b) the conductivity difference and the temperature gradients at a fixed solidification velocity ($V = 6.0 \times 10^{-7}$(m/s)). (0), (-) and (+) in the figures indicate that the system has the same number, less number and large number of lamellae after the particle impingement compared with initial number of lamellae, respectively. It is notes that all area in Fig. 36(a) appears stable for lamellae.

and the unstable region is extended to $V = 2.0 \times 10^{-6}$ in case of $\overline{k} = 0.01$ while the reduction of the lamella's number appears at only $G < 5.0 \times 10^3$, and the unstable region is extended to $V = 6.0 \times 10^{-7}$ in case of $\overline{k} = 100$. Fig. 38 shows growth pattern map of eutectic solidification according to front velocities and temperature gradients with $R = 10\mu$m, (a) $\overline{k} = 0.01$ and (b) $\overline{k} = 100$. The range of the solidification front velocity is $2.0 \times 10^{-7} < V < 4.0 \times 10^{-6}$(m/s) and the range of the temperature gradient is $1.0 \times 10^3 < G < 3.4 \times 10^4$ (K/s). In the case, it is interesting to note that unstable region becomes wider.

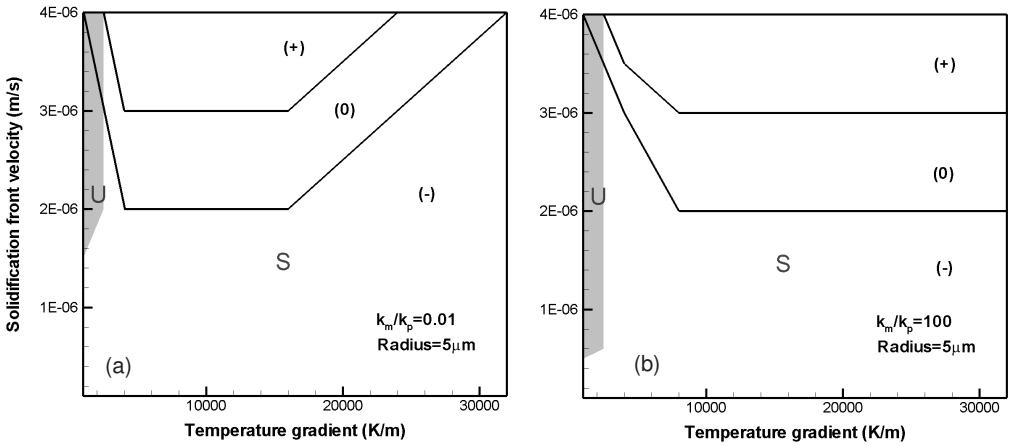

Fig. 37. Growth pattern map of eutectic solidification according to front velocities and temperature gradients with $R = 5\mu m$, (a) $\overline{k} = 0.01$ and (b) $\overline{k} = 100$. The range of the solidification front velocity is $2.0 \times 10^{-7} < V < 4.0 \times 10^{-6}$(m/s) and the range of the temperature gradient is $1.0 \times 10^3 < G < 3.2 \times 10^4$ (K/s). (0), (-) and (+) in the figures indicate that the system has the same number, less number and large number of lamellae after the particle impingement compared with initial number of lamellae, respectively.

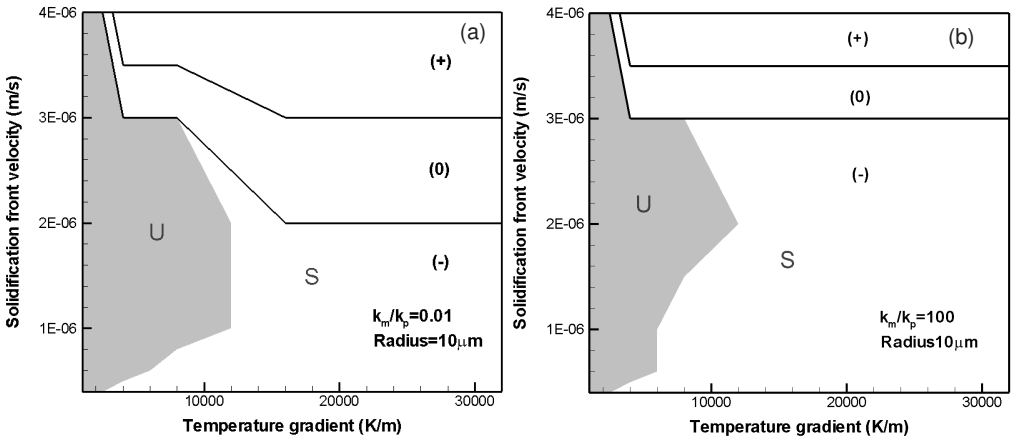

Fig. 38. Growth pattern map of eutectic solidification according to front velocities and temperature gradients with $R = 10\mu m$, (a) $\overline{k} = 0.01$ and (b)$\overline{k} = 100$. The range of the solidification front velocity is $2.0 \times 10^{-7} < V < 4.0 \times 10^{-6}$(m/s) and the range of the temperature gradient is $1.0 \times 10^3 < G < 3.2 \times 10^4$ (K/s). (0), (-) and (+) in the figures indicate that the system has the same number, less number and large number of lamellae after the particle impingement compared with initial number of lamellae, respectively.

E. Conclusions

The multiphase-field model for eutectic solidification was introduced using the diffuse interface method under chemical potential equilibrium between solid and liquid. An anisotropic phase field model considering the behavior of anisotropic materials was also introduced. A phase field model developed to describe the interaction between a eutectic solidification front and an insoluble impurity. A modified phase field model was introduced for the impurities. We found that the morphology of the growing lamellae can vary according to size of the impurity, solidification front velocity and temperature gradient and conductivity difference between the system and the impurity which allows us to investigate various eutectic growth patterns adjacent and behind to the encapsulation of the impurity.

In the treatment of the phase field model of eutectic solidification, we compared with experimental results, and found about good agreement. In the treatment of the phase field model for the existence of the impurities, we put a particle as a second-phase field in the calculation domain, not out of the calculation domain. This treatment requires evaluation of model parameters for the particle phase associated with liquid and solid phases. Based on the variation of the size of the particle, the solidification front velocity and the temperature gradient, we addressed various solidification patterns with some figures and showed the instability and the number of growing lamella sets after complete encapsulation according to the solidification front velocities, the temperature gradients and conductivity difference between a system and a particle with the fixed particle sizes ($R = 5\&10\mu m$). Using real properties of the organic alloy (CBr_4-C_2Cl_6), it is possible to demonstrate simple eutectic solidification phenomena which can be observed experimentally in simple cases, even it can hardly be performed by experiments, such as containing the encapsulated

particles and controlling the front velocity and temperature gradient within physical approaches. According to our results, we found that large G makes the growing lamellae stable while small G makes them unstable, and larger V makes more number of the growing lamella sets than the initial number of the lamella set. That means that if a system contains any size of impurity during solidification manufacturing, it is expected the patterns of growing lamellae will be modified according the size of the impurity, the solidification front velocity and the temperature gradient. In other words, it is possible to control the size of the impurity, the solidification front velocity and the temperature gradient in order to obtain an expected microstructure of an selected alloy according to the instability maps during eutectic solidification as shown in Figs. 29, 37 and 38.

CHAPTER V

MULTIPHASE FIELD SIMULATIONS OF INTERMETALLIC COMPOUND GROWTH DURING SOLDERING REACTIONS

A. Introduction

When a molten solder alloy is put in contact with a substrate, interfacial reactions result in the formation and growth of complex intermetallic compound (IMC) phases at the substrate/solder interface. Due to the imposed chemical potential gradients, the substrate initially dissolves into the molten solder alloy once they come into contact. Dissolution then results in local supersaturation at the solder/substrate interface. The supersaturation in turns makes the precipitation (nucleation) of IMC phases thermodynamically possible. This stage is important for further evolution of the IMCs because initial IMC growth determines the reliability of metallurgical bonding at the solder joint in a soldering process. The nature of the interfacial reactions depends on the individual alloy systems and soldering temperatures [41, 46, 96, 116, 117, 118, 119] and ultimately is a very complex process affected by both thermodynamics and kinetics.

In soldering reactions involving the Cu-Sn binary system, the intermetallic layers typically formed at the substrate/solder interface have been observed to consist mainly of Cu_6Sn_5 and subsequently Cu_3Sn. Understanding the solder/substrate interactions and their microstructural evolution at the interface is important as this can provide valuable insights on the nature of the interfacial evolution from a metallurgical point of view [30, 31, 120, 121, 122] and serve the way of accurate control during these reactions for the optimization of the soldering process [123].

Thermodynamics provides the fundamental information for analyzing reactions

between different components and their phase stability and it also provides the driving forces for chemical reactions and diffusion processes occurring in solder interconnections or thin film structures [124]. However, knowledge of the global equilibrium state of the system is not sufficient to understand the complex phenomena for the solder interaction with the substrate, as the actual path selected for the likely interfacial reactions and structural evolution are highly dependent on the local minimization of the free energy of the system. Recently, it has been shown that phase-field modeling [6, 27] can be used to simulate soldering reactions [28, 125] which in turn provide us with a powerful tool to describe the complex microstructural evolution of IMCs in which significant topological changes in the microstructure take place as the reaction progresses.

Experimental investigations on IMC growth during soldering previously published by other groups have been used to elucidate some of the most important mechanisms responsible for the formation and growth of IMC layers [41, 43, 44, 45, 46, 96]. These investigations have reported that a Cu_6Sn_5 layer is formed as scallop-type grains in contact with liquid solder, while Cu_3Sn is formed as a reactive diffusion layer between Cu_6Sn_5 and the solid substrate. These studies have also investigated the influence of IMC morphology on the solid-state microstructural processes that affect reliability of interconnects during normal operation. Although many groups have observed the morphological change of IMC layers, it is still unclear how kinetics of the soldering process is related to IMC growth. Although only through experimental work it is actually possible to gain a fundamental understanding of the complex phenomena occurring at substrate/solder interfaces, computer simulations can be used, through controlled 'virtual experiments', to elucidate some of the likely mechanisms controlling the observed morphologies.

In this chapter, we will simulate different morphologies of the soldering reaction

as a function of different material parameters involving the presence of Cu_6Sn_5 in Section B and the presence of both Cu_6Sn_5 and Cu_3Sn in Section C. We will briefly introduce the development of a phase-field model to simulate the microstructural evolution of the intermetallic compound layer formed by the interface reaction. The phase-field model accounts for the fast grain boundary diffusion in the intermetallic compound layer and the intermetallic compound grain coarsening. The results will show you the effects of the fast grain boundary diffusion, concurrent coarsening of the intermetallic compound grains and dissolution of Cu from the substrate and intermetallic compound layer. They bring on the growth kinetics of the intermetallic compound layer formed by the soldering reaction between Sn-Cu solders and a Cu substrate with different grain boundary diffusions, the different interfacial energies, and dissolution of Cu from the substrate and intermetallic compound layer based on the different liquid solder compositions with/without Cu_3Sn layer.

B. Intermetallic compound growth during soldering reaction for Cu_6Sn_5

1. Phase field and diffusion equations

We consider an isothermal Cu-Sn binary system. The system is composed of a Sn-rich liquid solder (L), a Cu-rich solid substrate (α), and an intermetallic layer of Cu_6Sn_5 (η). The intermetallic layer forms between the liquid solder and the solid substrate. The intermetallic layer is polycrystalline consisting of many grains and they are differentiated only by the crystallographic orientation. The spatial distribution of the liquid solder, the substrate, and the grains in the intermetallic layer on the system is mathematically expressed by using N arrays of phase fields $\phi_i(x,t)(i = 1, ..., N)$ and can obey a multiphase field model. The phase field variables in this model can be defined with ϕ_1 for solid substrate, $\phi_{2,...,N-1}$ for the grains in the intermetallic

layer and ϕ_N for liquid solder, respectively. $\phi_i = 1$ indicates that a point of the computational domain is occupied exclusively by phase i, while $\phi_i = 0$ indicates that there is no i phase in a particular region of the domain. Additionally $0 < \phi_i < 1$ corresponds to a point within the interface. From the previous works [5, 6, 126] the interface is considered as a finite region consisting of a mixture of different phases or grains and the N phase field variables at any position in the system are subjected to the two constraints as

$$\sum_{i=1}^{N} \phi_i = 1 \tag{5.1}$$

and

$$c(x,t) = \sum_{i=1}^{N} \phi_i c_i. \tag{5.2}$$

The free energy density f can be defined with the summation of potential energy and thermodynamic energy as

$$f = \sum_{j>i} \sum_{i} \left[-\frac{\epsilon_{ij}}{2} \nabla\phi_i \cdot \nabla\phi_j + \omega_{ij}\phi_i\phi_j \right] + \sum_{i} \phi_i f^i(c_i) \tag{5.3}$$

so that the total free energy functional with respect to system volume can be defined [6, 27] as

$$F = \int_V \left[\sum_{j>i} \sum_{i} \left[-\frac{\epsilon_{ij}}{2} \nabla\phi_i \cdot \nabla\phi_j + \omega_{ij}\phi_i\phi_j \right] + \sum_{i} \phi_i f^i(c_i) \right] \mathrm{d}V, \tag{5.4}$$

where f^i is the chemical free energy density of phase i and it depends on the phase composition c_i. ϵ is gradient energy coefficient and ω is double well potential representing the energy barrier separating two phases ϕ_i and ϕ_j. The advantage of using the double well potential helps the temporal evolution of the phase fields to be computed for the finite region of the interface.

At any point in the computational grid, when multiple phases coexist, composi-

tions can be determined by Eq. (5.2) and assuming a condition of local thermodynamic equilibrium [5], which can be defined as

$$f_{c_1}^1 [c_1] = f_{c_2}^2 [c_2] = f_{c_3}^3 . [c_3] = ... = f_{c_N}^N [c_N] . \tag{5.5}$$

This equilibrium allows continuity in the chemical potential of all the species across the interfaces. Elimination of the extra chemical potential in turn relaxes the restrictions on the width of the numerical interfaces during the simulations [6].

The number of phases coexisting in a given point can be obtained as [6]

$$N_p(x,t) = \sum_i^N \chi_i(x,t). \tag{5.6}$$

According to the consideration of a phase-field description for coexisting phases at interfaces, we can obtain the kinetics of the evolution of the phase-field as a function of time as

$$\frac{\partial \phi_i}{\partial t} = \frac{1}{N} \left[\sum_{i \neq j} \chi_i \chi_j \left(\frac{\partial \phi_i}{\partial t} - \frac{\partial \phi_j}{\partial t} \right) \right], \tag{5.7}$$

where χ_i is equal 1 when corresponding phase exists, otherwise 0, and N_p presents the number of the coexisting phases at a given position. This equation is only valid on the phase interfaces since the presence of only on phase in any point of the calculation domain would make χ_i or χ_j zero.

Eq. (5.7) leads to the ansatz of the phase field [27] as [see Appendix B]

$$\frac{\partial \phi_i}{\partial t} - \frac{\partial \phi_j}{\partial t} = -2 M_{ij} \left[\frac{\partial F}{\partial \phi_i} - \frac{\partial F}{\partial \phi_j} \right], \tag{5.8}$$

where M_{ij} is mobility. It is noted that the derivative of the free energy functional $\partial F / \partial \phi_i$ is

$$\frac{\partial F}{\partial \phi_i} = \sum_{i \neq j} \left[\frac{\epsilon_{ij}^2}{2} \nabla^2 \phi_j \right] + f^i(c_i) - f_c c_i. \tag{5.9}$$

Inserting Eq. (5.9) into Eq. (5.7) leads to

$$\begin{aligned}\frac{\partial \phi_i}{\partial t} &= -\frac{2}{N_p}\sum_{i\neq j}^{N}\chi_i\chi_j M_{ij}\left[\frac{\epsilon_{ij}^2}{2}\left(\nabla^2\phi_j-\nabla^2\phi_i\right)+\omega_{ij}\left(\phi_j-\phi_i\right)\right.\\ &\quad+\sum_{k\neq i,j}^{N}\left\{\left(\frac{\epsilon_{ik}^2}{2}-\frac{\epsilon_{jk}^2}{2}\right)\nabla^2\phi_k+(\omega_{ik}-\omega_{jk})\phi_k\right\}\\ &\quad\left.+\left\{(f_i-c_jf')-(f_j-c_jf')\right\}\right],\end{aligned} \tag{5.10}$$

where ϵ ($\epsilon_{ij}=\epsilon_{ji}$) is gradient energy coefficient and ω ($\omega_{ij}=\omega_{ji}$) is the height of double well potential.

For a diffusion equation, we set the flux equation with respect to diffusion coefficient, free energy density and composition gradient for multiphase system. The flux equation can be modified into a diffusion equation by using spatial differentiation with a diffusivity that is a function of the local phase-field variable. The diffusion equation is

$$\frac{\partial c}{\partial t}=\nabla\cdot\left(D(\phi)\sum_{i=1}^{N}\phi_i\nabla c_i\right). \tag{5.11}$$

2. Evaluation of model parameters

In order to get model parameters in the phase-field equation, we should obtain a stationary solution of the phase field equation in a planar interface. The solution will then be associated with interfacial energy and interfacial width. According to the definition of the interface energy as a function of gradient energy coefficient and phase field with a referred interface width, we can get two relationships between model parameters and material parameters, as shown in [5] and [27]:

$$\epsilon=\frac{4\sqrt{\xi\sigma_{ij}}}{\pi}\quad\text{and}\quad\omega_{ij}=\frac{2\sigma_{ij}}{\xi}, \tag{5.12}$$

where ξ is half width of the interface, and σ_{ij} is interface energy for the corresponding phases. Based on the approximation of the interface thickness [5], ξ has a fixed value.

3. Numerical implementation

Two dimensional simulations of phase field equation and the diffusion equation will be numerically solved by using finite difference method on the cross section of the Cu/Sn solder joint at 523K. In all cases, dimensional grid spacing of Δx and the half width of the interface ξ are used for 4.0×10^{-8}(m) and $4\Delta x$, respectively. Fig. 39 shows a schematic configuration for the computational domain. The size of the system is set to be $184\Delta x \times 290\Delta x$. For the initial array of phases, intermetallic grains (η phase) are placed from $20\Delta x$ to $25\Delta x$ between the liquid solder (from $25\Delta x$ to $90\Delta x$) and the solid substrate (from 0 to $20\Delta x$). The intermetallic layer initially consists of 30 rectangular grains that has different widths between $4\Delta x$ and $8\Delta x$. Periodic boundary conditions are applied to the sides of the calculation domain and Neumann boundary condition is applied to the top and bottom of the calculation domain. The calculation will be finished when thickness of the Cu-substrate will be used up.

We put an buffer solder region of $184\Delta x \times 200\Delta x$ at the top ($90\Delta x \times 290\Delta x$) of liquid solder since the fast diffusivity in the liquid phase makes composition gradients far away from the solder/substrate interface negligible. This allows the reduction in size of the computational domain considered in the simulation. The composition of the buffer region is initially the same as that of the solder in the computational solder. The average composition of the buffer region may change with time, depending on the mass flux across the solder/buffer interface. However, the composition assumes a single value throughout the buffer zone.

The free energy densities per unit moral volume of individual phases were ob-

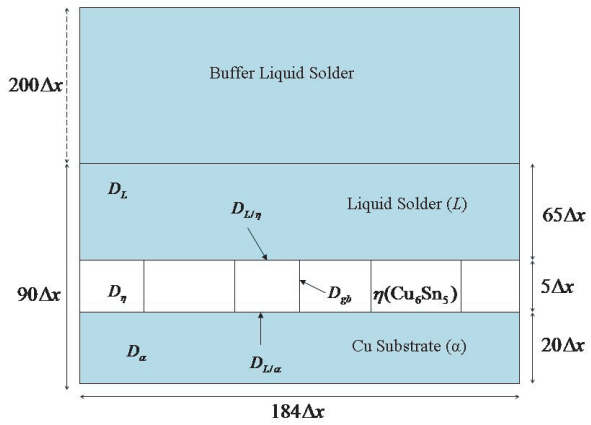

Fig. 39. A schematic configuration for the computational domain.

tained from the CALPHAD method [124] and they are

$$\begin{aligned} f_\alpha &= (1-c)G^\alpha_{Cu} + cG^\alpha_{Sn} + RT\left[(1-c)\ln(1-c) + c\ln c\right] \\ &\quad + c(1-c)\left[L^\alpha_0 + L^\alpha_1(1-2c)\right], \end{aligned} \tag{5.13}$$

$$\begin{aligned} f_\eta &= 2.0\times 10^5(c-0.435)^2 + 0.545G^\alpha_{Cu} + 0.455G^{SER}_{Sn} \\ &\quad - 6869.5 - 0.1589T, \end{aligned} \tag{5.14}$$

$$\begin{aligned} f_L &= 1-c)G^L_{Cu} + cG^L_{Sn} + RT\left[(1-c)\ln(1-c) + c\ln c\right] \\ &\quad + c(1-c)\left[L^L_0 + L^L_1(1-2c) + L^L_2(1-4c-4c^2)\right], \end{aligned} \tag{5.15}$$

where

$$G^{\alpha}_{Cu} = -19073.0, \quad G^{\alpha}_{Sn} = -27280.0,$$
$$G^{SER}_{Sn} = 346160.0, \quad G^{L}_{Cu} = -11083.0, \quad G^{L}_{Sn} = -28963.0,$$
$$L^{\alpha}_{0} = -11448.0, \quad L^{\alpha}_{1} = -11694.0,$$
$$L^{L}_{0} = -10487.0, \quad L^{L}_{1} = -18198.0, \quad L^{L}_{2} = 10528.4$$

We assumed that all phases have the same molar volume ($v_m = 16.29 \times 10^{-6}$), and f_η is formulated as a parabolic function due to allowance of solubility range in the η phase. The equilibrium phase compositions can be solved by using Eqs. (5.13), (5.14) and (5.15) [see Appendix D]. They are

$$c^{\alpha\eta}_{\alpha} = 0.1954, \quad c^{\eta\alpha}_{\eta} = 0.380, \quad c^{\eta L}_{\eta} = 0.441, \quad c^{L\eta}_{L} = 0.9767, \tag{5.16}$$

where $c^{\alpha\eta}_{\alpha}$ is the equilibrium composition of the α phase at the $\alpha - \eta$ interface and the other terms are defined correspondingly. The initial compositions of the substrate and intermetallic layer are taken to be uniform as $c_\alpha = 0.002$ and $c_\eta = 0.4105$, respectively. The initial composition of the liquid solder phase is chosen to be either $c_L = c^{L\eta}_{L}$ corresponding to a Cu-saturated solder, or $c_L = c^{L\eta}_{L} + 0.02$, corresponding to a nearly pure Sn solder.

The diffusivities and other material parameters employed in the numerical calculation are summarized in followings: Diffusion coefficients of the liquid solder, intermetallic layer and cu-substrate are $D_L = 2.0 \times 10^{-12}(m^2/s)$, $D_\eta = 2.0 \times 10^{-5} D_L(m^2/s)$ and $D_\alpha = 1.0 \times 10^{-6} D_L(m^2/s)$, respectively. Diffusion coefficients of the $\eta - L$, $\eta - \alpha$ and $\eta - \eta$ interfaces are $D_{\eta L} = 2.0 \times 10^{-1} D_L(m^2/s)$, $D_{\eta\alpha} = 2.0 \times 10^{-3} D_L(m^2/s)$ and $D_{\eta\eta} = 2.0 \times 10^{-2} D_L(m^2/s)$, respectively. The interfacial energies for $\eta - L$, $\eta - \alpha$ and $\eta - \eta$ interfaces are $\sigma_{\eta L} = 0.1$, $\sigma_{\alpha\eta} = 0.3$ and $\sigma_{\eta\eta} = 0.3(\mathrm{J}/m^2)$, respectively. Mobilities

of $\eta - L$, $\eta - \alpha$ and $\eta - \eta$ interfaces are $M_{\eta L} = 1.0 \times 10^{-6}$, $M_{\alpha\eta} = 7.0 \times 10^{-8}$ and $M_{\eta\eta} = 7.0 \times 10^{-8}$, respectively.

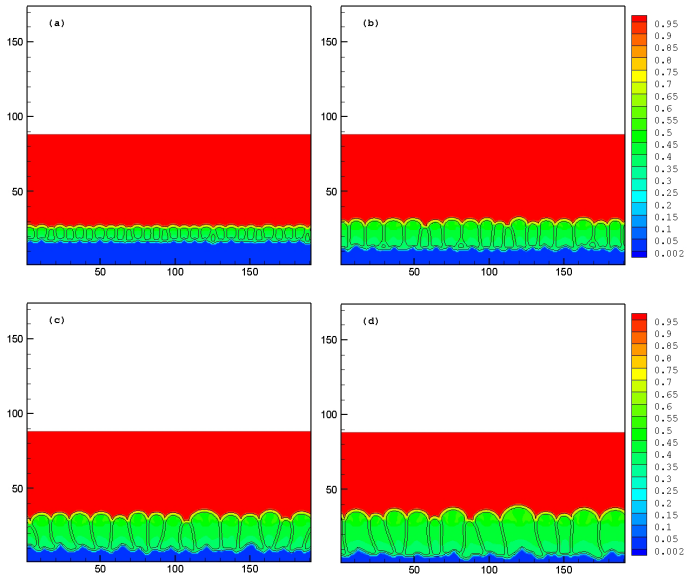

Fig. 40. Microstructural evolution of the intermetallic compound layer for the case of the fast grain boundary diffusion ($D_{\eta\eta} = 2.0\times10^{-2}D_L$ and $D_\eta = 2.0\times10^{-5}D_L$) is depicted for times: (a) t=0.02(sec), (b) t=6(sec), (c) t=14(sec) and (d) t=20(sec). The initial solder composition was the one saturated with Cu ($c_L = c_L^{L\eta}$).

4. Results and discussions

In this work, the evolution of IMC layer morphology as the soldering reaction progresses is investigated through a systematic study of the effects of different material parameters on the kinetics of IMC layer evolution. In order to examine how the growth kinetics of the η phase is affected by diffusion along η grain boundaries, simulations are carried out with three different grain boundary diffusion coefficients.

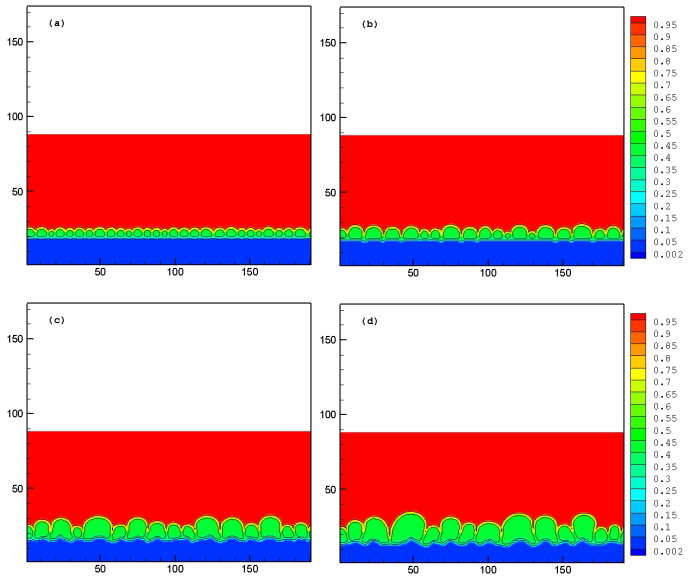

Fig. 41. Microstructural evolution of the intermetallic compound layer for the case of the regular grain boundary diffusion ($D_{\eta\eta} = 2.0 \times 10^{-4} D_L$ and $D_\eta = 2.0 \times 10^{-5} D_L$) is depicted for times: (a) t=0.02(sec), (b) t=6(sec), (c) t=19(sec) and (d) t=21(sec). The initial solder composition was the one saturated with Cu ($c_L = c_L^{L\eta}$).

The first one is for the fast diffusion coefficient where $D_{\eta\eta} = 2.0 \times 10^{-2} D_L$ and $D_\eta = 2.0 \times 10^{-5} D_L$ which shows us that more mass will diffuse through the grain boundaries then through the grains. The second one is for the regular diffusion coefficient where $D_{\eta\eta} = 2.0 \times 10^{-4} D_L$ and $D_\eta = 2.0 \times 10^{-5} D_L$ which can be obtained from the interdiffusion formulations. The last one is for the regular diffusion coefficient where $D_{\eta\eta} = 2.0 \times 10^{-4} D_L$ and $D_\eta = 2.0 \times 10^{-4} D_L$ which tells us that diffusing rate of mass through the grains is the same with the that through the grain boundaries. For the cases, the initial solder composition was equal to the one saturated with Cu, $c_L = c_L^{L\eta}$ and $L - \eta$ interfacial energy is taken to be the value shown in the previous section.

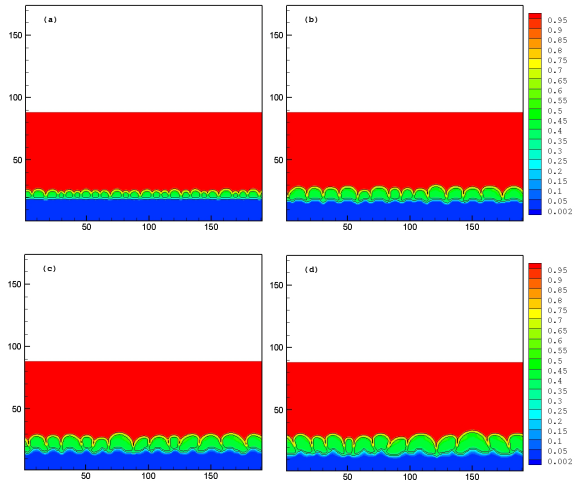

Fig. 42. Microstructural evolution of the intermetallic compound layer for the case of the low grain boundary diffusion ($D_{\eta\eta} = 2.0 \times 10^{-4} D_L$ and $D_\eta = 2.0 \times 10^{-4} D_L$) is depicted for times: (a) t=0.02(sec), (b) t=6(sec), (c) t=19(sec) and (d) t=21(sec). The initial solder composition was the one saturated with Cu ($c_L = c_L^{L\eta}$).

Fig. 40 shows that intermetallic compound growth for the case of fast grain

boundary diffusion ($D_{\eta\eta} = 2.0 \times 10^{-2} D_L$ and $D_\eta = 2.0 \times 10^{-5} D_L$) in time (Case 1); (a) t=0.02(sec), (b) t=6(sec), (c) t=14(sec) and (d) t=20(sec). As the Intermetallic grain layer grows thicker with time, there is a concurrent coarsening of the η grains, resulting in fewer grains remaining in the intermetallic compound layer. Although $\sigma_{\eta\eta} > 2\sigma_{\eta L}$ is assumed, the liquid solder does not wet the grain boundaries entirely through the layer, since the driving force for the η phase formation from the diffusion fluxes through the grain boundary is large enough to overcome the difference between $\sigma_{\eta\eta}$ and $\sigma_{\eta L}$. Fig. 41 shows intermetallic compound growth for the case of the regular grain boundary diffusion ($D_{\eta\eta} = 2.0 \times 10^{-4} D_L$ and $D_\eta = 2.0 \times 10^{-5} D_L$) in time (Case 2); (a) t=0.02(sec), (b) t=6(sec), (c) t=19(sec) and (d) t=21(sec), and Fig. 42 shows intermetallic compound growth for the case of the low grain boundary diffusion ($D_{\eta\eta} = 2.0 \times 10^{-4} D_L$ and $D_\eta = 2.0 \times 10^{-4} D_L$) in time (Case 3); (a) t=0.02 (sec), (b) t=10 (sec), (c) t=20(sec) and (d) t=22(sec). They show the microstructural evolution of the intermetallic compound layer for the case neglecting the fast grain boundary diffusion. Since the diffusion across the intermetallic compound layer is sluggish, the system tends to decrease its energy predominantly by reducing the grain boundary area. Therefore, compared to Case 1 shown, the liquid solder penetrates deeper into the grain boundary and the η grain coarsening occurs much faster.

The microstructural evolution of the intermetallic compound layer may be described in terms of a competition between two diffusion processes: (a) the fast grain boundary diffusion to increase the intermetallic compound layer thickness and (b) the diffusion driven by the interface curvature effect (i.e., Gibbs-Thomson effect) to reduce the interface and grain boundary areas. The former provides the initial mass fluxes necessary for η phase growth: the Cu flux to the grain boundary junction with the liquid solder and the Sn flux to the grain boundary junction with the α substrate. The latter distributes the diffusion fluxes from the grain boundary over the $\eta - L$

and $\alpha - \eta$ interfaces. Competition between the two diffusion processes determines the groove shapes at the grain boundary junctions. The individual η grains have a morphology such that the $\eta - L$ and $\alpha - \eta$ interfaces have opposite signs of curvature. This is due to the fact that the latter diffusion process is sufficiently fast at the $\eta - L$ interface but more sluggish at the $\alpha - \eta$ interface. The η grain coarsening is initiated by a competitive grain growth at the $\eta - L$ interface at which the diffusion process caused by the Gibbs-Thomson effect occurs rapidly.

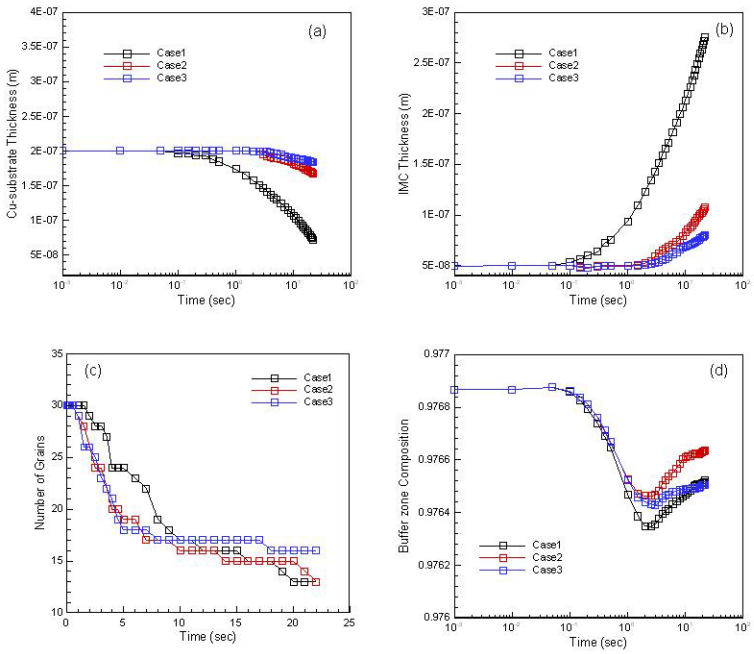

Fig. 43. Evolution of (a) solid substrate thickness, (b) intermetallic compound layer thickness, (c) number of grains and (d) buffer zone composition in time for the three cases that is shown in figures 40–42.

Fig. 43 shows the evolution of solid substrate thickness, intermetallic compound layer thickness, number of grain and buffer zone composition in time for the three cases. Based on the change in the Cu-substrate and intermetallic compound layer

thickness, the evolution of the system from its initial state may be understood by dividing it into three stages, regardless of the presence of the fast grain boundary diffusion. The initial stage of simulation up to 0.1 second, for which the intermetallic compound layer thickness does not change, corresponds to the stage of interface (and grain boundary) broadening. The initial stage is followed by a transient stage in which the grain boundary grooves develop between η grains and the initially flat $\eta - L$ interface becomes rounded. Thus, the liquid composition decreases due to the curvature effect at the $\eta - L$ interface. This is accompanied by the dissolution of η grains into the liquid solder, as shown by the slight decrease in the intermetallic compound layer thickness for Case 2 and Case 3 neglecting the fast grain boundary diffusion comparing with Case 1. At the same time, for the case with the fast grain boundary diffusion, fast diffusion through the broadened grain boundaries takes place so that η grains can grow. Apparently, the grain growth kinetics for the case with the fast grain boundary diffusion is fast enough so that there is a net increase in the intermetallic compound layer thickness during this transient stage. The transient stage is then followed by "normal" stage in which the liquid composition increases slightly as the η grains coarsen. The transient stage ends much earlier for the case with the fast grain boundary diffusion since a part of the Cu flux from the fast grain boundary diffusion enters the liquid solder.

The effects of the concurrent coarsening of the η grains on the intermetallic compound layer growth kinetics in the calculation are carried out with changing the interface energy in Fig. 44 ($\sigma_{\eta L} = 0.05(\mathrm{J}/m^2)$, Case 4) and in Fig. 45 ($\sigma_{\eta L} = 0.15(\mathrm{J}/m^2)$, Case 5). Because of the lower and higher value of $\sigma_{\eta L}$, there is a smaller and larger tendency for competitive grain growth at the $\eta - L$ interface comparing with Case 1. As you compare with Case 5, you can see more grains in Case 4 are alive during the soldering reaction. Thus the coarsening rate of the η grains is reduced,

which results in an increased growth rate of the intermetallic compound layer.

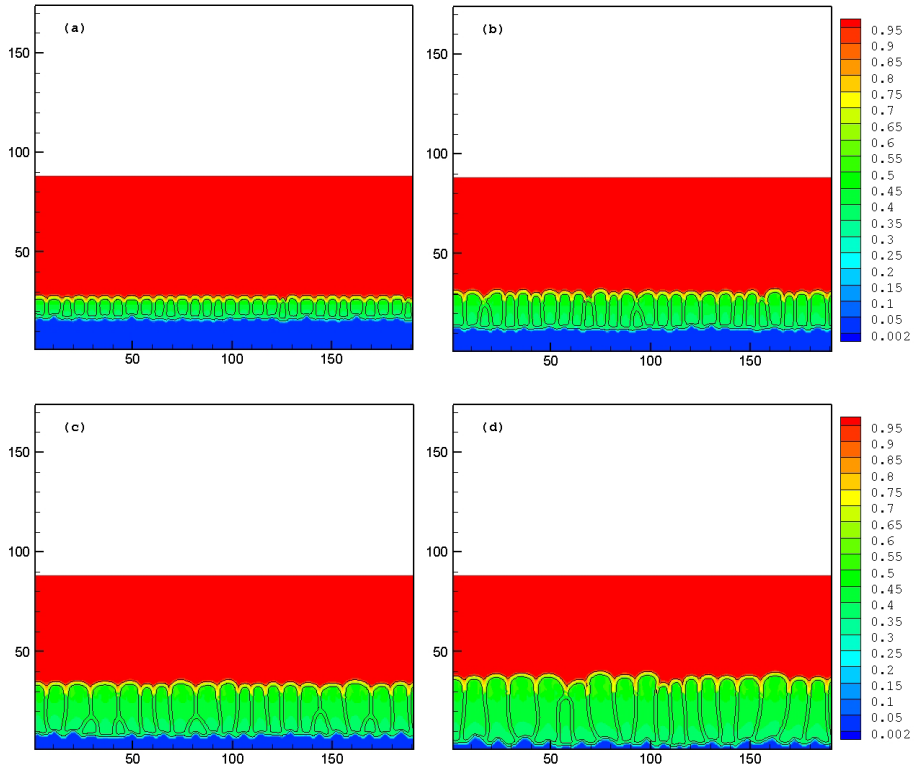

Fig. 44. Microstructural evolution of the intermetallic compound layer for the case of the low interfacial energy ($\sigma_{\eta L} = 0.05(\mathrm{J}/m^2)$ is depicted for times: (a) t=0.02(sec), (b) t=5(sec), (c) t=10(sec) and (d) t=20(sec). The initial solder composition was the one saturated with Cu ($c_L = c_L^{L\eta}$).

Fig. 46 shows the evolution of solid substrate thickness, intermetallic compound layer thickness, number of grain and buffer zone composition in time for the three cases. The changes in the average intermetallic compound layer thickness and the number of η grains with time for Case 4 are compared with those for Case 1. The growth rate of the intermetallic compound layer thickness in the normal stage of simulation is estimated to be 0.42 for Case 4 and 0.33 for Case 1, the increase of

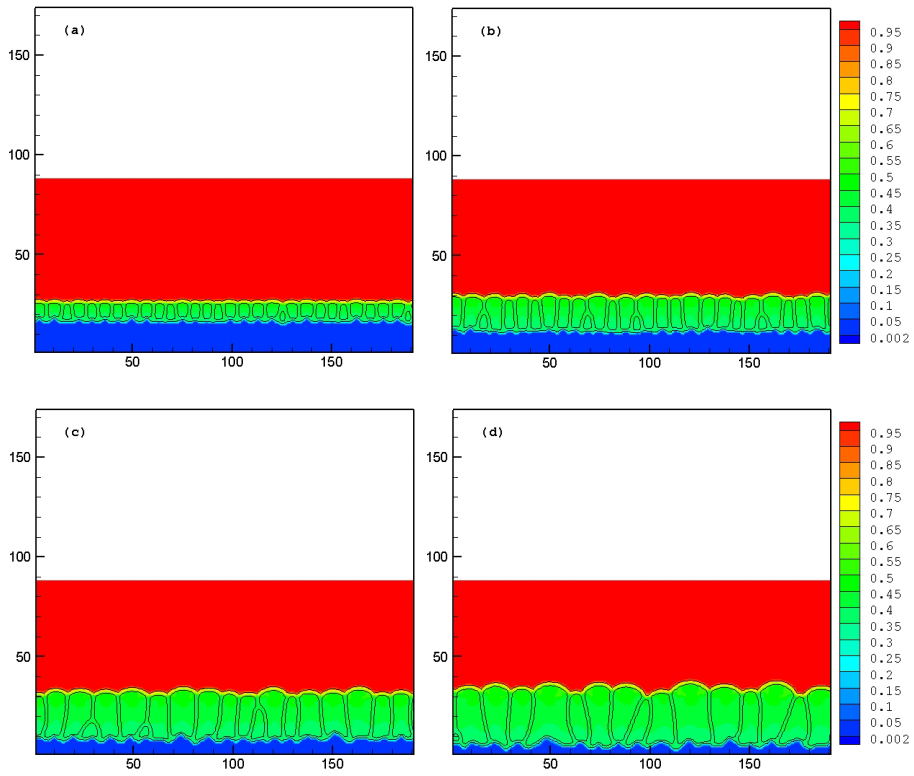

Fig. 45. Microstructural evolution of the intermetallic compound layer for the case of the high interfacial energy ($\sigma_{\eta L} = 0.15(\mathrm{J}/m^2)$ is depicted for times: (a) t=0.02(sec), (b) t=5(sec), (c) t=12(sec) and (d) t=20(sec). The initial solder composition was the one saturated with Cu ($c_L = c_L^{L\eta}$).

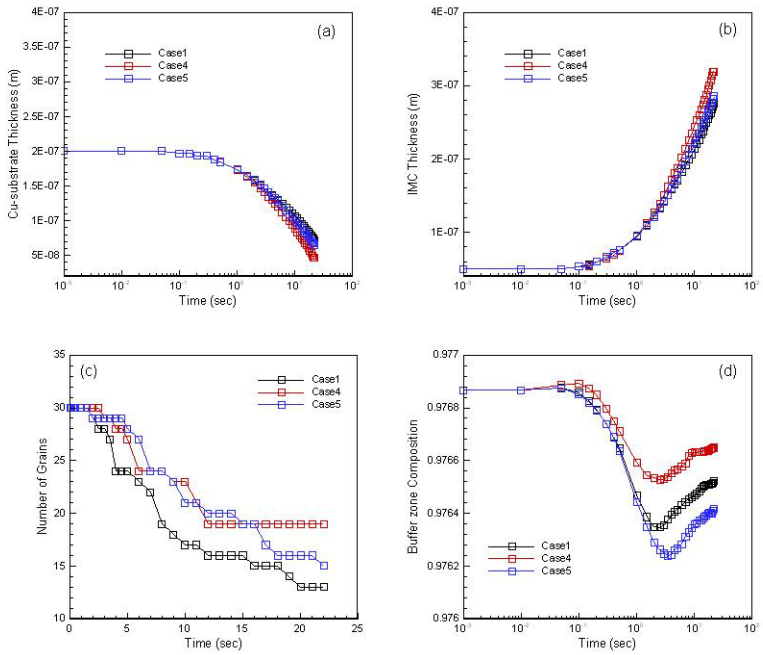

Fig. 46. Evolution of (a) solid substrate thickness, (b) intermetallic compound layer thickness, (c) number of grain and (d) buffer zone composition in time for the three cases; Case 1, Case 4 and Case 5.

growth rate by reducing $\sigma_{\eta L}$ is attributed to the slow coarsening of the η grains. If the η grain coarsening does not occur at all, and thus the number of η grains remains constant until consuming Cu-substrate.

Microstructural evolution of the intermetallic compound are simulated based on the initial solder composition of the system that is changed as $c_L = c_L^{L\eta} + 0.02$ in Fig. 47 (Case 6) and $c_L = c_L^{L\eta} - 0.02$ in Fig. 48 (Case 7) which represent nearly pure Sn and Cu-enriched liquid solder, respectively. The corresponding changes in the Cu-substrate thickness and the intermetallic compound layer thickness and the number of the η grains and the buffer zone composition with time are shown in Fig. 49, respectively.

Since the initial solder is set to be Pure Sn in Case 6, dissolution of Cu from the intermetallic compound layer and Cu-substrate occurs at the early stages of soldering, and the intermetallic compound layer grows at the $\alpha - \eta$ interface due to the Sn flux through the grain boundary in the intermetallic compound layer while the intermetallic compound layer growth at the $\eta - L$ interface hardly occurs due to the lack of Cu flux from liquid solder. Because of the insufficient Cu flux from liquid solder, the intermetallic compound layer thickness decreases, and the concurrent dissolution and growth of the intermetallic compound layers appear downward at the early stages of soldering. As the liquid solder composition becomes Cu enriched in time, the dissolution rate of Cu from the intermetallic compound layer and Cu-substrate slowly increases and the intermetallic compound layer thickness starts to grow at $\alpha - \eta$ interface. When the largeness of the Cu flux by the grain boundary diffusion is involved into the intermetallic compound formation at the $\eta - L$ interface, the intermetallic compound layer also slightly grows at the η_L interface, and the solder composition with time, as measured at the top surface of liquid solder zone, will is reduced, and it touches below $c_L^{L\eta}$, because of the involvement of the Cu flux from Cu-substrate, and

increase until the composition of the top surface of liquid solder zone reaches $c_L^{L\eta}$.

It is noted that the grain coarsening at $\eta - L$ interface is suppressed when the liquid solder is set to be pure Sn, which means that the lower Cu flux from the $\eta - L$ interface into the liquid zone reduces the composition gradient generated by low interfacial curvature of the $\eta - L$ interface. Therefore the coarsening rate of the grains is lowered by using the initially pure Sn. When the liquid solder composition is set to be Cu-supersaturated (Case 7), the dissolution rate is fast and the intermetallic compound layer thickness starts to grow both at $\alpha - \eta$ interface and at $\eta - L$ interface. Furthermore, since diffusion in the liquid solder is stronger, most Cu diffuses into intermetallic compound layer, so that the composition of the top surface initially closes to pure Sn composition, and then decreases. After the initial stage, the soldering in Case 7 shows us the similar process comparing to Case 6. Although the detailed values, such as the number and size distribution of the intermetallic compound grains and the material parameters, depend on the initial condition, the simulation results, after initial stage, follow a generic feature for the effect of the fast grain boundary diffusion on the growth of the intermetallic compound layer during soldering reactions.

Fig. 50 shows Cu flux into the solder liquid at the $\eta - L$ interface with respect to different curvatures of the $\eta - L$ interface for three cases ((a) Case 1, (b) Case 3 and (c) Case 6). Three figures have different curvature of $\eta - L$ interface. The contour in the figures indicates the magnitude of the Cu flux, the black lines are for phase field, and the arrows are for Cu flux direction. The length of the arrows represents the magnitude of the Cu flux. High and low curvature of the $\eta - L$ interface can be obtained by many possible combinations of the material parameter. Among a lot of cases, Case 1, Case 3 and Case 6 can represent the intermediate, high and low curvature cases, respectively. Three figures tell us the Cu flux from the $\eta - L$

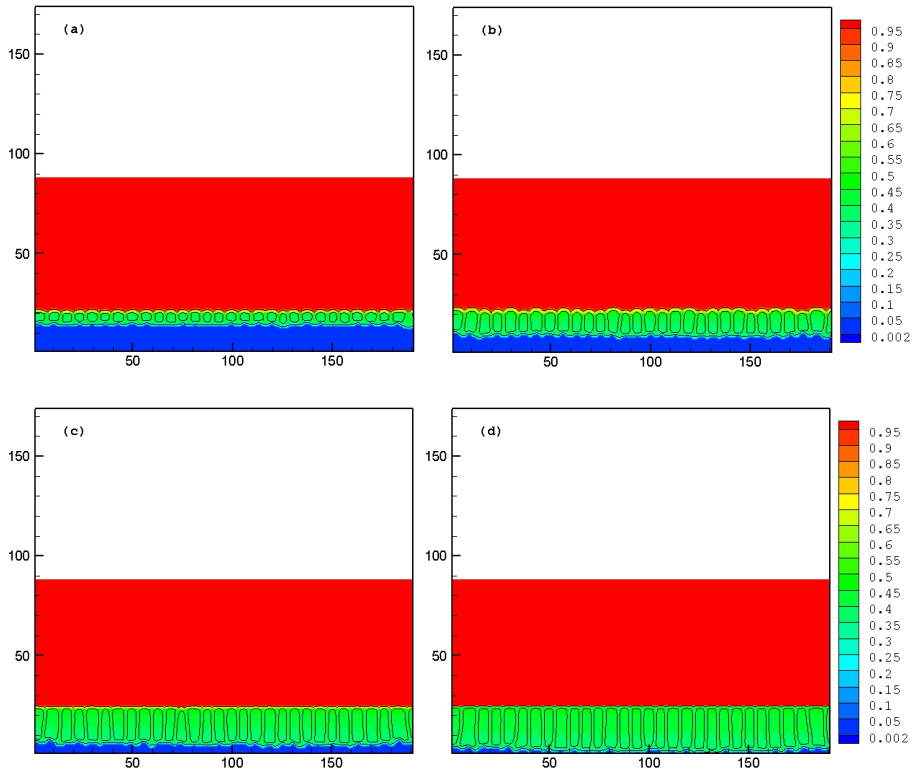

Fig. 47. Microstructural evolution of the intermetallic compound layer for the case of the pure Sn liquid solder ($c_L = c_L^{L\eta}$+0.02 is depicted for times: (a) t=0.02(sec), (b) t=4(sec), (c) t=10(sec) and (d) t=20(sec). The diffusion coefficients are taken as $D_{\eta\eta} = 2.0 \times 10^{-2} D_L$ and $D_\eta = 2.0 \times 10^{-5} D_L$. Interfacial energy is taken as $\sigma_{\eta L} = 0.1(\mathrm{J}/m^2)$.

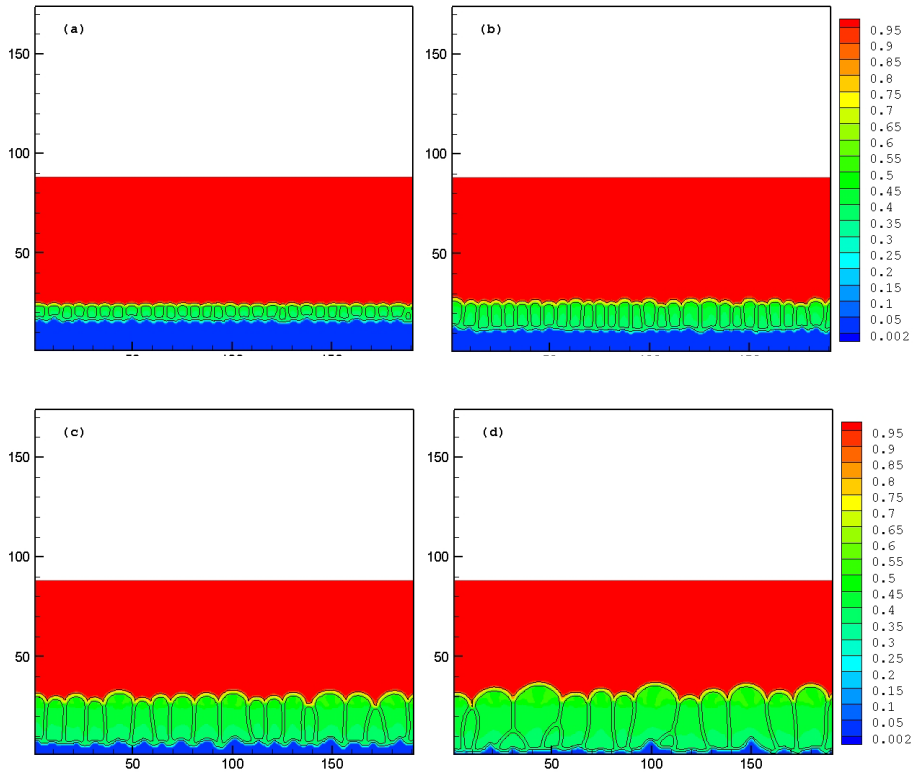

Fig. 48. Microstructural evolution of the intermetallic compound layer for the case of the Cu-supersaturated liquid solder ($c_L = c_L^{L\eta} - 0.02$) is depicted for times: (a) t=0.02(sec), (b) t=4(sec), (c) t=12(sec) and (d) t=20(sec). The diffusion coefficients are taken as $D_{\eta\eta} = 2.0 \times 10^{-2} D_L$ and $D_\eta = 2.0 \times 10^{-5} D_L$. Interfacial energy is taken as $\sigma_{\eta L} = 0.1(\mathrm{J}/m^2)$.

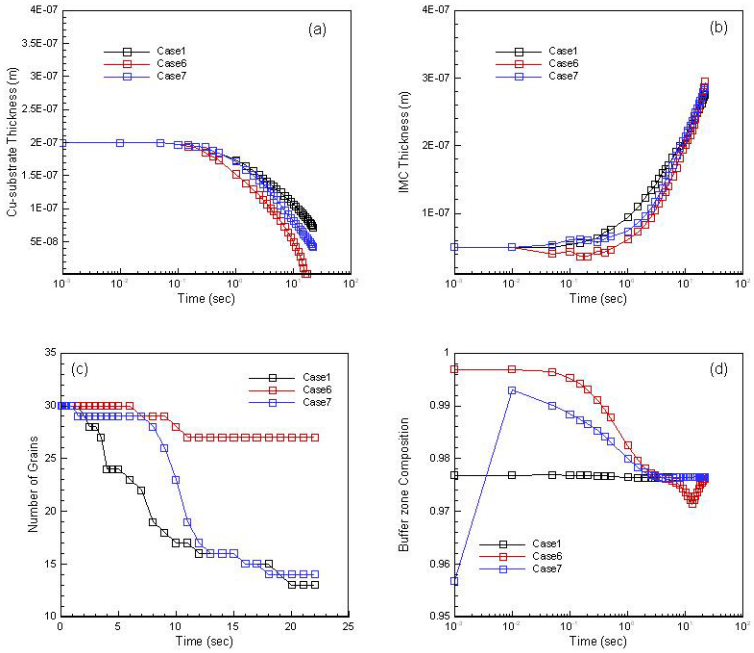

Fig. 49. Evolution of (a) solid substrate thickness, (b) intermetallic compound layer thickness, (c) number of grain and (d) buffer zone composition in time for the three cases; Case 1, Case 6 and Case 7.

interface into the bulk liquid have effect to composition gradient, and the change of the composition gradient is related to interface curvature. We can say that say the change of the interface curvature may change Cu flux from the $\eta - L$ interface. The $\eta - L$

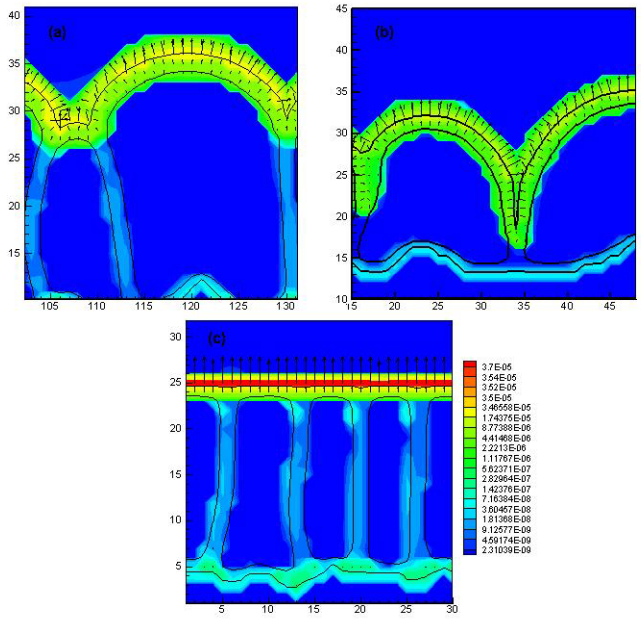

Fig. 50. Cu flux into the solder liquid at the $\eta - L$ interface with respect to different curvatures of the $\eta - L$ interface for three cases ((a) Case 1, (b) Case 3 and (c) Case 6).

interface in each case contains various curvature values according to the temporal and spatial value along the $\eta - L$ interface in Fig. 50(b), but the curvatures of each case are positioned in a group area in Fig. 51(a). The line in Fig. 51(a) is plotted by using trend line. According to the curvature and the corresponding Cu flux, high curvature causes the low Cu flux, which results in that the $\eta - L$ interface can penetrate into the intermetallic compound layer deeply in Fig. 50(b). The increasing penetration depth provides the large difference in curvature between the two positions on the $\eta - L$

interface, and result in that the composition gradient along the liquid solder between the neighboring intermetallic compound grains is reduced, as shown the figure (the 'valley' area of the two grains in Fig. 50(b)), so that the intermetallic compound dissolution rate at the grain boundary junction decreases (when the intermetallic compound dissolution rate is rather low, the growth of intermetallic compound layer is slow because not much Cu will be involved into make grains) and the increasing rate of intermetallic compound layer is reduced, which is proved in Fig. 51(b), comparing with the case of low curvature. Therefore, the high Cu flux from the $\eta - L$ interface into the bulk liquid produces the $\eta - L$ interface plateau (low curvature) while low Cu flux from the $\eta - L$ interface into the bulk liquid produces the $\eta - L$ interface curved (high curvature). In other words, high curvature reduces composition gradient while low curvature increases the composition gradient. It is worth to say that the Cu flux from the $\eta - L$ interface into the liquid solder reduces the composition gradient engendered by the Gibbs-Thomson effect (i.e. interface curvature).

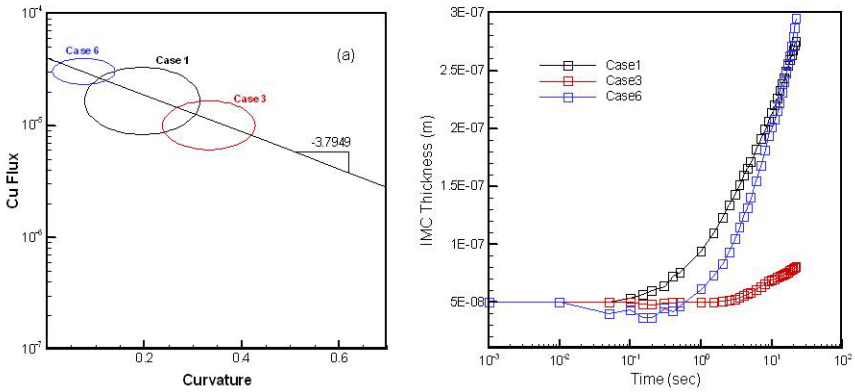

Fig. 51. Comparison of (a) Cu flux due to different curvatures and (b) number of intermetallic compound grains for three cases; (a) Case 1, (b) Case 3 and (c) Case 6.

C. Intermetallic compound growth during soldering reaction for Cu_6Sn_5 and Cu_3Sn

We consider an isothermal Cu-Sn binary system at 523K again. The system is composed of a Sn-rich liquid solder (L), a Cu-rich solid substrate (α), an intermetallic compound layer of Cu_6Sn_5 (η) and an intermetallic compound layer of Cu_3Sn (ε). The IMC layers form between the liquid solder and the Cu substrate, and the η-IMC lies on the ε-IMC.

The IMC layers consist of many grains that are differentiated by non-conserved phase fields [45]. The spatial distribution of the liquid solder, the substrate, and the grains in the intermetallic layer of the system is mathematically expressed by using N arrays of phase fields $\phi_i(x,t)(i = 1, ..., N)$, which can be expressed with multi-phase field variables. The phase field variables in this model can be defined as ϕ_1 for solid substrate, $\phi_{2,...,N-1}$ for the grains in the two IMC layers and ϕ_N for liquid solder. $\phi_i = 1$ indicates that phase i exists in that point of space, while $\phi_i = 0$ indicates that i phase does not exist in the region. Additionally, interfaces are defined in the system whenever $0 < \phi_i < 1$. Within the interface, ϕ_i is considered to change continuously within the $0 < \phi_i < 1$ range. For example, if $0 < \phi_1 < 1$ and $0 < \phi_2 < 1$ at a point in an interface region, the point indicates the presence of the η-IMC layer and a solid substrate. In the same way, we can expect phase information at any point from phase field variables.

All explanations about constraints, total free energy functional, multiphase field model, diffusion model and model parameters were introduced well in the previous section. Multiphase field model, diffusion model , their constraints and model parameters are used as, respectively,

$$\frac{\partial \phi_i}{\partial t} = -\frac{2}{N_p}\sum_{i\neq j}^{N}\chi_i\chi_j M_{ij}\left[\frac{\epsilon_{ij}^2}{2}\left(\nabla^2\phi_j - \nabla^2\phi_i\right) + \omega_{ij}\left(\phi_j - \phi_i\right)\right.$$
$$+\sum_{k\neq i,j}^{N}\left\{\left(\frac{\epsilon_{ik}^2}{2} - \frac{\epsilon_{jk}^2}{2}\right)\nabla^2\phi_k + (\omega_{ik} - \omega_{jk})\phi_k\right\}$$
$$\left. + \left\{(f_i - c_j f') - (f_j - c_j f')\right\}\right], \tag{5.17}$$

$$\frac{\partial c}{\partial t} = \nabla\cdot\left(D(\phi)\sum_{i=1}^{N}\phi_i\nabla c_i\right), \tag{5.18}$$

$$\sum_{i=1}^{N}\phi_i = 1 \quad \text{and} \quad c(x,t) = \sum_{i=1}^{N}\phi_i c_i, \tag{5.19}$$

$$\epsilon = \frac{4\sqrt{\xi\sigma_{ij}}}{\pi} \quad \text{and} \quad \omega_{ij} = \frac{2\sigma_{ij}}{\xi}. \tag{5.20}$$

1. Numerical implementation

Multi-phase field equation and the diffusion equation will be numerically solved by using finite difference method on the cross section of the Cu/Sn solder joint at 523K with two dimensional analysis. In all cases, the values of dimensional grid spacing $h(=\Delta x)$ and the half width of the interface ξ used are 1.0×10^{-8}(m) and $4h$, respectively. It is important to note that in this work we neglect treatment of nucleation at the substrate/solder interface. Although this in principle can be tackled either through thermal noise or by applying classical nucleation theory, this component of the problem is outside the scope of the present work.

Fig. 52 shows a schematic configuration for the computational domain. The size of the system is set to be $158h\times101h$. Cu substrate, ε-IMC layer, η-IMC layer and liquid solder layer are positioned from bottom to top for initial array of phases.

η-IMC layer is 4 or 5 times thicker than ε-IMC layer a grain in η phase is 4

or 5 times wider than a grain in ε phase [45]. ε and η IMC layer are placed from $21h$ to $26h$ and from $27h$ to $41h$, respectively, between the liquid solder (from $42h$ to $101h$) and the solid substrate (from 0 to $20h$). The η-IMC layer initially consists of 12 rectangular grains that have different widths between $10h$ and $15h$, and the ε-IMC layer initially consists of 34 rectangular grains that have different widths between $5h$ and $6h$ [see Fig. 52]. Periodic boundary conditions are applied to the sides of the calculation domain and Neumann boundary condition is applied to the top and bottom of the calculation domain. The calculations are finished when the thickness of the Cu-substrate is close to zero.

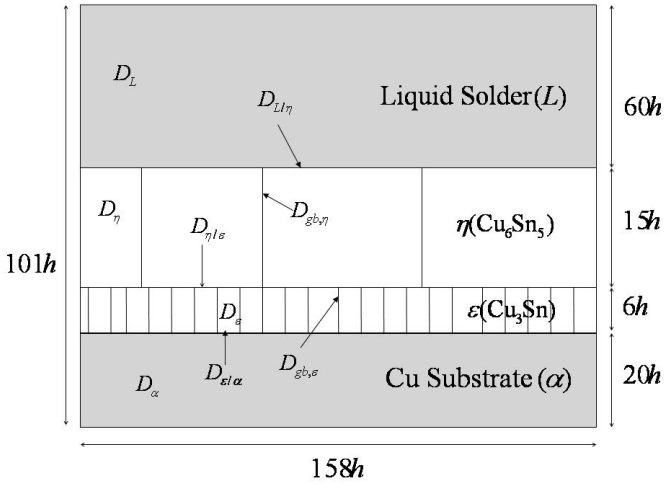

Fig. 52. A schematic configuration for the computational domain.

The free energy densities per unit moral volume of individual phases were obtained from the CALPHAD method [124] and they are

$$\begin{aligned} f_\alpha &= (1-c)G^\alpha_{Cu} + cG^\alpha_{Sn} + RT\left[(1-c)\in(1-c) + c\ln c\right] \\ &\quad + c(1-c)\left[L^\alpha_0 + L^\alpha_1(1-2c)\right], \end{aligned} \tag{5.21}$$

$$\begin{aligned} f_\varepsilon &= 2.0\times10^5(c-0.249)^2+0.75G^\alpha_{Cu}+0.25G^{SER}_{Sn} \\ &\quad -8194.2-0.2043T, \end{aligned} \tag{5.22}$$

$$\begin{aligned} f_\eta &= 2.0\times10^5(c-0.435)^2+0.545G^\alpha_{Cu}+0.455G^{SER}_{Sn} \\ &\quad -6869.5-0.1589T, \end{aligned} \tag{5.23}$$

$$\begin{aligned} f_L &= 1-c)G^L_{Cu}+cG^L_{Sn}+RT\left[(1-c)\ln(1-c)+c\ln c\right] \\ &\quad +c(1-c)\left[L^L_0+L^L_1(1-2c)+L^L_2(1-4c-4c^2)\right], \end{aligned} \tag{5.24}$$

where

$$\begin{aligned} &G^\alpha_{Cu}=-19073.0, \quad G^\alpha_{Sn}=-27280.0, \\ &G^{SER}_{Sn}=346160.0, \quad G^L_{Cu}=-11083.0, \quad G^L_{Sn}=-28963.0, \\ &L^\alpha_0=-11448.0, \quad L^\alpha_1=-11694.0, \\ &L^L_0=-10487.0, \quad L^L_1=-18198.0, \quad L^L_2=10528.4 \end{aligned}$$

We assumed that all phases have the same molar volume [$v_m = 16.29(\mathrm{cm}^3/\mathrm{mole})$], and f_η and f_ε are formulated as a parabolic function in order to allow a limited solubility range in the η and ε phases. The equilibrium phase compositions can be solved by using Eqs. (5.21)-(5.24) [see Appendix D]. They are

$$\begin{aligned} &c^{\alpha\varepsilon}_\alpha=0.027, \quad c^{\varepsilon\alpha}_\varepsilon=0.227, \quad c^{\eta\varepsilon}_\eta=0.433, \\ &c^{\varepsilon\eta}_\varepsilon=0.247, \quad c^{\eta L}_\eta=0.436, \quad c^{L\eta}_L=0.977. \end{aligned} \tag{5.25}$$

where $c^{\alpha\varepsilon}_\alpha$ is the equilibrium composition of the α phase at the $\alpha-\varepsilon$ interface and the other terms are defined correspondingly. The initial compositions of the substrate and ε and η intermetallic compound layers are taken to be uniform as $c_\alpha = 0.002$

$c_\varepsilon = 0.237$ and $c_\eta = 0.435$, respectively. The initial composition of the liquid solder phase is chosen to be either $c_L = c_L^{L\eta}$ corresponding to a Cu-saturated solder, or $c_L = c_L^{L\eta} + 0.02$, corresponding to a nearly pure Sn solder.

The diffusivities and other material parameters employed in the numerical calculation are summarized in followings: Diffusion coefficients of the liquid solder (L), the intermetallic compound layers ($\eta$and ε) and cu-substrate (α) are $D_L = 2.0 \times 10^{-12}(m^2/s)$, $D_\eta = 2.0 \times 10^{-5} D_L(m^2/s)$, $D_\varepsilon = 5.0 \times 10^{-6} D_L(m^2/s)$ and $D_\alpha = 1.0 \times 10^{-6} D_L(m^2/s)$, respectively. Diffusion coefficients of interfaces are $D_{\eta L} = 2.0 \times 10^{-1} D_L(m^2/s)$, $D_{\varepsilon\alpha} = 1.0 \times 10^{-4} D_L(m^2/s)$, $D_{\eta\alpha} = 2.0 \times 10^{-4} D_L(m^2/s)$, $D_{\eta\eta} = 2.0 \times 10^{-2} D_L(m^2/s)$ and $D_{\varepsilon\varepsilon} = 1.0 \times 10^{-4} D_L(m^2/s)$. The interfacial energies are taken as $\sigma_{\eta L} = 0.1$, $\sigma_{\alpha\varepsilon} = \sigma_{\alpha\eta} = 0.3$ and $\sigma_{\eta\eta} = \sigma_{\varepsilon\varepsilon} = 0.3(\mathrm{J}/m^2)$. Mobilities are taken as $M_{\eta L} = 1.0 \times 10^{-6}$, $M_{\alpha\varepsilon} = 7.0 \times 10^{-8}$, $M_{\eta\varepsilon} = 7.0 \times 10^{-8}$, $M_{\varepsilon\varepsilon} = 7.0 \times 10^{-8}$ and $M_{\eta\eta} = 7.0 \times 10^{-8}$.

2. Results and discussions

Determination of material parameters used in the simulation is very difficult (but possible) because material properties of single phases, for example, the material parameters of α, η, ε and L in this study are dependent on theoretical approach based on experimental data [41, 43, 127, 128, 129]. Additionally, in a region of phases mixture, for example interface regions, it is even more difficult to determine the material properties for the simulation. So, the simulation in this study will follow the morphology of IMC grain growth that will be affected by the different material properties, such as changing diffusion coefficient of grain boundary, changing interfacial energy between η-IMC layer and liquid solder and changing initial Cu content in liquid solder.

In order to examine how the kinetics of the η-IMC growth is affected by diffusion in grain boundary, simulations are carried out with three different grain boundary

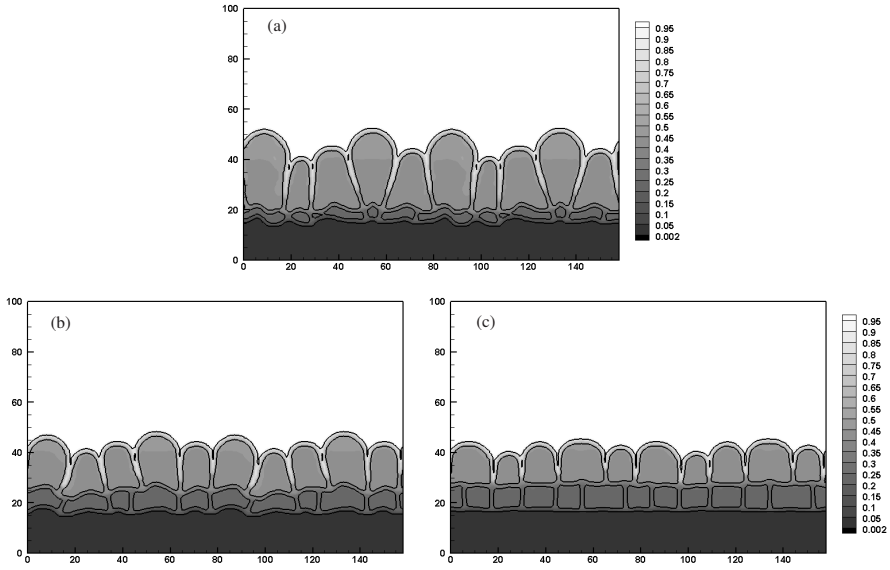

Fig. 53. Microstructural evolution of the intermetallic compound layer for the case of (a) high grain boundary diffusion ($D_{\eta\eta} = 4.0 \times 10^{-14}$), (b) intermediate grain boundary diffusion ($D_{\eta\eta} = 4.0 \times 10^{-15}$) and (c) low grain boundary diffusion ($D_{\eta\eta} = 8.0 \times 10^{-17}$) at t=20(sec).

diffusion coefficients. The first one is for the high diffusion coefficient where $D_{\eta\eta} = 4.0 \times 10^{-14}$ which shows us that more mass likely diffuses through the grain boundaries than through the grains. The second one is for the intermediate diffusion coefficient where $D_{\eta\eta} = 4.0 \times 10^{-15}$, which can be obtained from interdiffusion formulations. The last one is for the low diffusion coefficient where $D_{\eta\eta} = D_{\eta}$, which indicates that the diffusing rate of mass through the grain boundaries is the same as that through the grains. For all three cases, the initial solder composition is set to $c_L = c_L^{L\eta}$ and $L - \eta$ interfacial energy is taken to be the value as shown in the previous section.

Fig. 53 shows intermetallic compound growth for the case with different grain boundary diffusion at t=20(sec). As the intermetallic compound layer grows thicker with time, there is a concurrent coarsening of the η and ε grains resulting in fewer

grains remaining in the intermetallic compound layer. But the number of grains that have survived in both layers are similar. However, the thickness of ε-IMC and η-IMC layer varies according to the different grain boundary diffusion as shown in Fig. 54. We can find that $\eta - L$ and $\varepsilon - \eta$ interfaces have opposite signs of curvature resulting in the scollop shape for η grains and thin film shape for ε grains [28, 45].

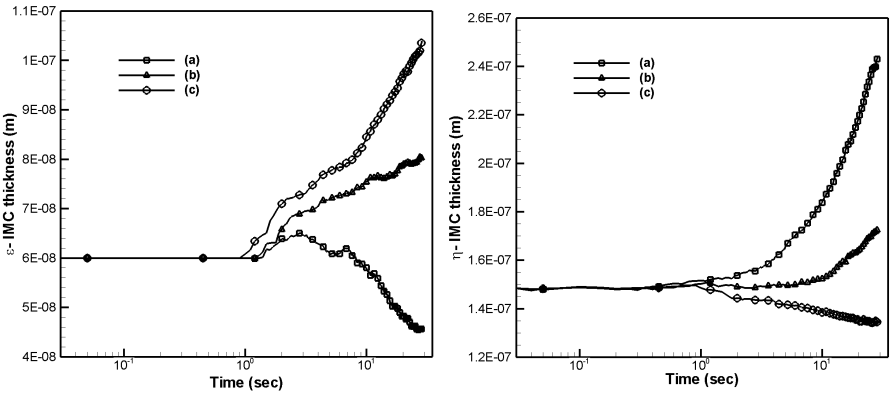

Fig. 54. Evolution of ε-IMC layer and η-IMC layer thickness with respect to time corresponding (a), (b) and (c) in Fig. 53.

In the case of high grain boundary diffusion, we can see that the thickness of η-IMC layer increases at a faster rate than in the other cases, while that of ε-IMC layer decreases. Reduction of Cu substrate thickness occurs at the same rate regardless of different grain boundary diffusion. Precisely speaking, the thickness of ε-IMC layer increases but the η-ε interface moves down faster than α-ε interface, which can be called encroachment, so that the thickness of ε-IMC layer turn out decreases although more Sn flux from the liquid solder through grain boundary is expected. When Sn flows through the grain boundary of η-IMC layer to form η-IMC and ε-IMC, both η-IMC and ε-IMC layer simultaneously increase together. However, excess of Sn flux at the η-ε interface results in the conversion of Cu_3Sn to Cu_6Sn_5 because Cu_6Sn_5 is

the most stable product of the chemical reaction in the Cu-Sn system. The behavior of encroachment has been observed by many experimental researches [78, 116, 130] and explained by using additional chemical reaction between η-IMC and ε-IMC [131].

In the case of intermediate grain boundary diffusion, we can expect that there is a high probability that Sn diffuses from the liquid solder through the grain boundaries resulting in the simultaneous growth of η-IMC and ε-IMC together. This means that there is no more extra Sn supply from the liquid solder for the phase transition from ε-IMC to η-IMC. The growing speed of η-IMC in Fig. 54(b) is likely to be less than that in Fig. 54(a) because no encroachment is expected.

When grain boundary diffusion is the same as that for the grains in the η layer, we can see that the thickness of η-IMC layer decreases while that of ε-IMC layer increases. This behavior can be explained by considering Cu flux from the substrate. Contrary to the two previous cases, we can expect that less Cu flux is delivered to both IMC layers. However, forming Cu_3Sn requires less Cu and Sn compared with Cu_6Sn_5 resulting in the increased thickness of ε-IMC layer and lowering of $\varepsilon - \alpha$.

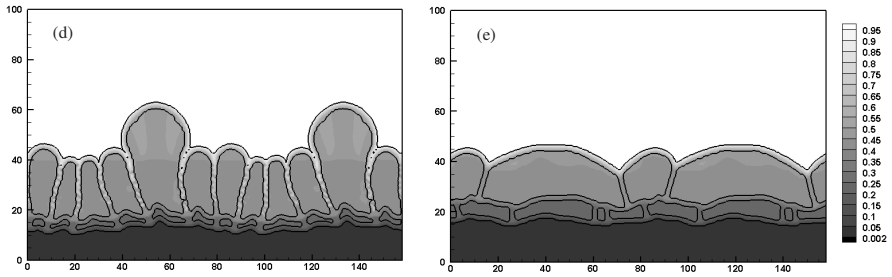

Fig. 55. Microstructural evolution of the IMC layer for the case of (d) the low $\eta - L$ interfacial energy ($\sigma_{\eta L} = 0.05(\mathrm{J}/m^2)$) and (e) high $\eta - L$ interfacial energy ($\sigma_{\eta L} = 0.15(\mathrm{J}/m^2)$) at t=20(sec).

The concurrent coarsening of the η grains on the IMC layer growth in calculations

are carried out by changing the $\eta - L$ interfacial energy as shown in Fig. 55(d) ($\sigma_{\eta L} = 0.05(\mathrm{J}/m^2)$) and in Fig. 55(e) ($\sigma_{\eta L} = 0.15(\mathrm{J}/m^2)$). Other material parameters for Fig. 55 are adopted from the case of Fig. 54(a).

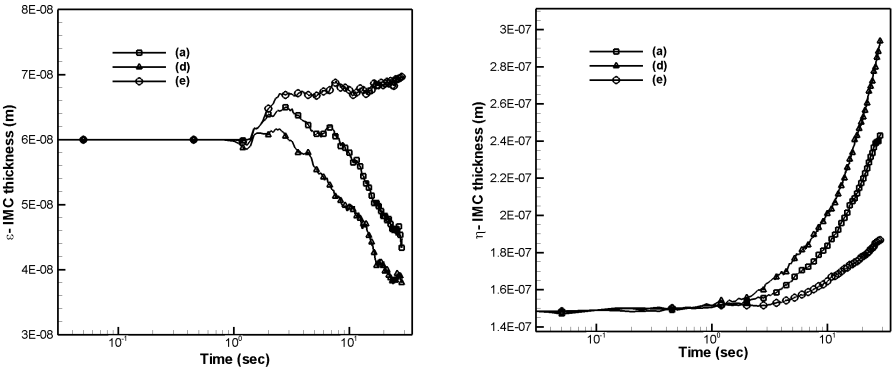

Fig. 56. Evolution of thickness of two IMC layers with respect to time for Figs. 55(d) and (e) compared with Fig. 54(a).

Although high grain boundary diffusion is employed in the η phase, there is a smaller tendency for competitive grain growth at the $\eta - L$ interface compared to the case shown in Fig. 54(a) because of the lower value of $\sigma_{\eta L}$. The coarsening rate is related to the grain boundary diffusion and difference between $\sigma_{\eta L}$ and $\sigma_{\eta\eta}$ [28]. In this case high grain boundary diffusion causes grain growth, but higher difference of two interfacial energies leads to grain boundary wetting, which essentially acts to limit horizontal coarsening of the grains. Thus, the grains grow upward with less coarsening with neighboring grains in η-IMC layer, which is faster than the other case as shown in Fig. 54(a). Because of more Sn flux through the grain boundary, encroachment of the ε-IMC layer in Fig. 55(d) occurs faster than the case shown in Fig. 54(a). On the other hand, if relatively higher interfacial energy is applied at the $\eta - L$ interface, the reversed behavior of grain growth can be expected. This means that high $\sigma_{\eta L}$

stimulates faster spreading of a grain and faster coarsening with neighboring grains, resulting in less-upward grain growth and less grains that survive at any given time. Less Sn flux caused by reduced fast diffusion paths causes a slight increase of ε-IMC layer because of the phenomena we already discussed while explaining Fig. 54(c). High Cu consumption can be expected in the case of low interfacial energy because Cu consumption is affected by total thickness of the two IMC layers. All explanation for morphologies of IMC development can be accompanied with Fig. 56.

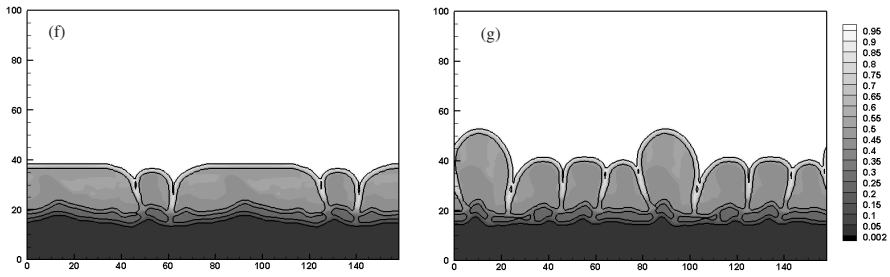

Fig. 57. Microstructural evolution of the IMC layer for the case of (f) the pure Sn liquid solder ($c_L = c_L^{L\eta} + 0.02$) and (g) Cu-supersaturated liquid solder ($c_L = c_L^{L\eta} - 0.02$) at t=20(sec).

Microstructural evolution of the IMC is also simulated based on the initial solder composition that is changed from pure Sn liquid solder ($c_L = c_L^{L\eta} + 0.02$) as shown in Fig. 57(f) and Cu-supersaturated liquid solder ($c_L = c_L^{L\eta} - 0.02$) as shown in Fig. 57(g). Liquid solder composition far from the IMC layers and two IMC layer thickness with respect to time are shown in Fig. 58.

Since the initial liquid solder is set to be pure Sn in Fig. 57(f), dissolution of Cu from the η-IMC layer and Cu-substrate occurs at the early stages of soldering. Because of the dissolution of Cu from the η-IMC layer to liquid solder (caused by liquid solubility), the η-IMC layer shrinks at the $\eta - L$ interface quickly, which causes

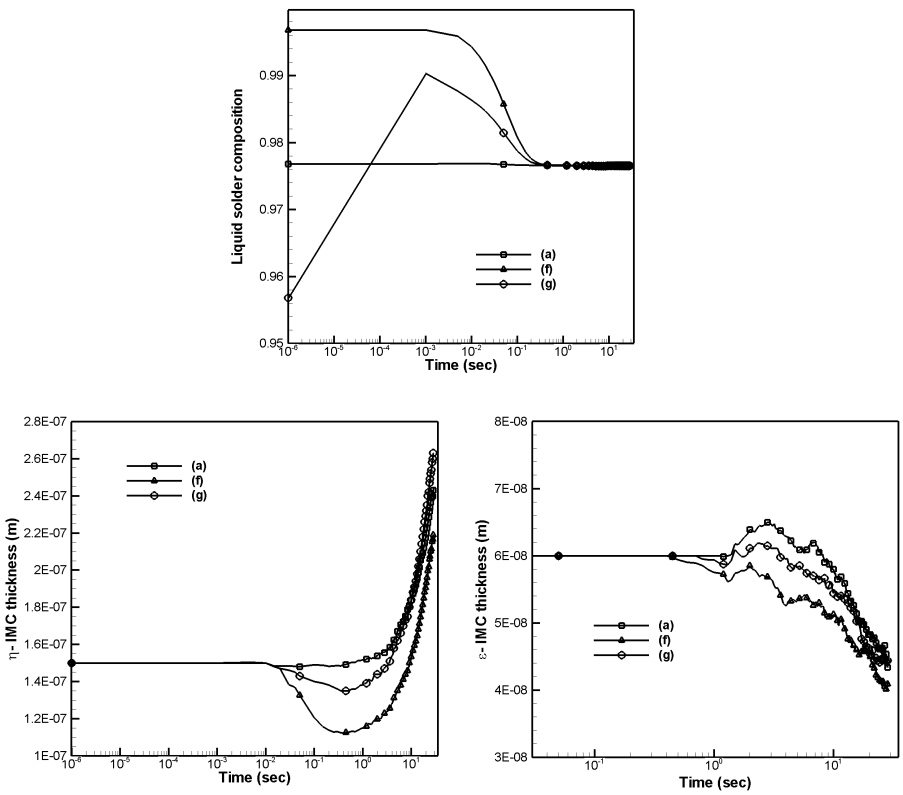

Fig. 58. Evolution of liquid solder composition far from the IMC layers in case of Fig. 57(f) and (g) compared with Fig. 54(a).

faster grain coarsening. After shrinkage of the η-IMC layer with less number of survived grains, we can expect that the liquid solder composition becomes Cu-enriched, the dissolution rate of Cu from the intermetallic compound layer and Cu-substrate decreases and the η-IMC layer thickness starts to grow at the $\eta - \varepsilon$ interface by encroachment behavior. From the point of view of ε-IMC layer, its thickness decreases due to suppression at an early stage as well as encroachment at the late stage from η-IMC layer.

When initial liquid solder is set to be supersaturated with Cu, the composition of the liquid solder is likely to approach equilibrium composition according to liquid

solubility. In order to reach the equilibrium composition, liquid solder requires more Sn from all phases, which causes slight excess of Sn flux on the liquid solder, but not more than the case of the pure Sn liquid solder. After the excess of Sn flux towards the liquid solder area, the thickness change of two IMC layers during soldering reaction follows the same physics of the case in Fig. 54(a).

D. Conclusions

The morphological evolution and growth of the IMC (Cu_6Sn_5) layer during soldering reaction in Cu-Sn alloys on a Cu substrate was investigated by using a multi-phase field model and was computed with two configurations, considering the existence (or absence) of Cu_3Sn. The multi-phase field simulations were performed by using two different grain boundary diffusion coefficients in η-IMC layer and two different interfacial energies of L/η interface causing the concurrent coarsening of the IMC grains. The microstructural evolution of the η-IMC layer appeared more complicated according to either the presence of Cu_3Sn or not, but describable with two controllable parameters (grain boundary diffusion, L/η interfacial energy) that deliver us the following: (a) The presence of Cu_3Sn retards increase of η-IMC layer in spite of high grain boundary diffusion coefficient affecting grain coarsening of η-IMC layer. (b) The growth of Cu_3Sn affects morphological evolution and growth of the η-IMC layer. (c) High L/η interfacial energy leads to decrease of grain boundary wetting effect resulting in increase of grain coarsening.

In view of the interaction between η and ε IMC layers, we found that the change of their thickness is important to understand the morphology of soldering reaction at an early stage because growth ratio of the two IMC layers possibly affects the mechanical properties of solder joints due to the degree of brittleness of IMCs. In

the case of the Cu_3Sn presence, the interaction between η-IMC and ε-IMC layers (or grains) should be studied. Some parts of this chapter are from [58].

CHAPTER VI

EARLY STAGES OF INTERMETALLIC COMPOUND FORMATION AND GROWTH DURING LEAD-FREE SOLDERING

A. Introduction

Further optimization of lead-free soldering alloys and processes requires proper understanding of the interfacial interactions–including intermetallic compounds (IMCs) layers formation and growth–occurring at solder/substrate interfaces. IMC layer formation generally consists of several distinct physical processes, such as nucleation, growth and coarsening. Among these processes, IMC nucleation is one of the most important ones as the particular sequence of IMC formed has a significant effect on the morphology and evolution of IMC layers, consequently affecting the reliability of soldered assemblies [30, 31, 32].

In Cu-Sn systems, two IMCs (Cu_6Sn_5 (η phase) and Cu_3Sn(ε phase)) have been observed to form at the substrate (Cu)/solder (Sn) interface [40, 41, 43, 44, 45, 46, 96, 117, 119, 120, 122, 123, 128, 129, 130]. The actual formation sequence of these phases has been shown to be determined by the local thermodynamic conditions at the Cu/Sn interface. Specifically, the η phase has been shown to precipitate during the earliest stages of solder/substrate interactions due to the fact that its driving force for precipitation under metastable local equilibrium conditions at the solder/substrate interface is much higher than the driving force for the precipitation of the ε phase [98, 132]. Experimentally, it has been observed that the η phase precipitates in a random fashion along the solder/substrate interface. After the precipitation of the η phase, the precipitation of the ε phase at the η/substrate interface becomes thermodynamically possible and it is thus usually observed at later stages of the

soldering reactions [132].

A significant number of experimental investigations had been focused on the late stages of growth and coalescence of η phase [40, 41, 43, 44, 45, 46, 96, 117, 119, 120, 122, 123, 128, 129, 130]. Recently, the formation of η phases during early stages of soldering reaction had been studied by several groups [97, 98, 133]. These recent experimental works have found that individual Cu_6Sn_5 grains appear at random locations along the (metastable) solid-liquid interface within a few milliseconds. After the η grains appear, they have been found to spread along the interface without much growth perpendicular to the solder/substrate interface until they meet with other spreading grains, forming a relatively uniform IMC layer of Cu_6Sn_5. After the initial formation of the IMC layer, its thickness increases at the expense of the underlying substrate, with the individual grains acquiring a scallop-like morphology [45] that continues to grow perpendicularly to the interface.

Very recently, the growth and morphological evolution of IMC layers during soldering reactions have been simulated by using phase-field models [6, 27]. These mathematical models have been proved to be a very useful tool to investigate the microstructural evolution of IMC as a function of factors such as solid/liquid interfacial energies, grain boundary energies, relative mass transport enhancement by grain boundaries and so forth [28, 125]. None of these works have studied the early stages of IMC formation by considering the nucleation of individual IMC grains along the solder/substrate interface.

In this study, we will briefly introduce a nucleation model for the formation of the η phase along a Cu/Sn interface which was derived from previous nucleation models developed within the context of phase-field modeling of solidification phenomena [33, 34, 56]. The proposed nucleation model will be incorporated to a multi-phase field model derived from previous works [6, 27] for the evolution of grains of (Cu_6Sn_5)

under isothermal conditions. We will show different morphologies of IMC grains and layers during lead-free soldering as a function of material parameters. In this work, we will assume that the Cu_6Sn_5 phases are the only ones to precipitate, essentially limiting this investigation to the early stages of the soldering reaction. The rate of growth of the IMC individual grains will be controlled by the diffusion rates while the coarsening of the IMC grains as well as the nucleation kinetics will be controlled by using different solder/IMC interface energies. Investigation of nucleation and microstructural evolution during the solder/substrate interactions will provide a deeper insight into the nature of IMC layer formation and growth in model lead-free solder systems, which in turn can be used to better control of the soldering reactions.

B. Nucleation modeling

Within the context of phase-field modeling, the incorporation of realistic models for the nucleation of a new phase is still a very hard problem. The usual approach to simulate nucleation is to introduce Langevin noise in the phase-field evolution equations with the proper amplitude to ensure that the system samples configurations corresponding to the nucleating phase. For this approach to work, it is usually required that the required perturbations of the local configuration of the system are small enough so they can actually be sampled within the normal running time of the simulation. More sophisticated versions of this approach [36] can be realized by explicitly calculating the barrier for nucleation by explicitly considering the structure of the forming nuclei in terms of thermodynamic driving forces and nuclei/matrix interfacial energies.

An alternative method for incorporating nucleation into phase-field simulations relies on explicitly incorporating nuclei throughout the simulation time by relying on

classical nucleation theory and stochastic approaches [33, 34, 56]. In this approach, the probability for the nucleation of a new phase at an arbitrary point in space and time is determined and the microstructure is 'seeded' accordingly. This approach assumes that the time necessary for the new phase to nucleate is much smaller than the time interval of the simulation. Furthermore, the expectation value of the number of nuclei that form during a time interval Δt corresponds to the nucleation rate, J, which can be calculated from classical nucleation theory. This approach further assumes that once the nuclei forms, it occupies a definite volume of space which in turn yields a "zero event probability" for the formation of subsequent nuclei [33, 34, 56]. The stochastic nucleation process can be thus approximated by unity minus the zero event probability of a Poisson distribution:

$$P_n = 1 - \exp\left[-P\right], \tag{6.1}$$

where $P = J \cdot v \cdot \Delta t$. Δt is the time interval over which the probability of nucleation is to be determined while v represents the volume over which the nucleation probability is calculated. As mentioned above, the nucleation rate J can be obtained from a classical nucleation model, and the parameters in the model can be obtained in principle from experimental data. In this work,, we adopt the model used to simulate nucleation in an undercooled liquid developed by [56]:

$$J = J_0 \exp\left[-\frac{16\pi\sigma_{sl}^3}{3kT(\Delta G_V)^2}\left(\frac{\cos^3\theta - 3\cos\theta + 2}{4}\right)\right], \tag{6.2}$$

where J_0 is a frequency factor with order of magnitude $10^{39\pm1}(m^{-3}s^{-1})$ in volume nucleation and $10^{31\pm1}(m^{-2}s^{-1})$ for surface nucleation. σ_{sl} represents the energy of a solid/liquid interface. k is the Boltzmann constant. θ is the contact angle of a nucleus with respect to the solid substrate. ΔG_V is the driving force between the crystal (η-phase) and the melt.

Nucleation of Cu_6Sn_5 is revealed easily by observing the free energy diagram shown in Fig. 59. Free energy profiles for each of the phases (substrate, solder, and η phase) can be obtained from the CALPHAD thermodynamic assessments by [124]. During the initial stages of the soldering reaction, the only coexisting phases may be the substrate (α) and the liquid (L) solder. The free energy of the α/L interface can be obtained by applying the common tangent construction between these two phases. By comparing this tangent with the position of the free energy curve of the η phase it is clear that the α/L equilibrium is metastable. The formation of the η phase is thus thermodynamically possible. The strength of the thermodynamic driving force (ΔG_V for the nucleation of this phase can be calculated from the difference between the free energy of this phase and the chemical potentials of the system components corresponding to the metastable α/L equilibrium. Although there is another phase (Cu_3Sn, ε) that may nucleate at α/L interface, under normal conditions this is precluded during early stages of the interfacial reaction due to its smaller driving force for precipitation. After the nucleation of η phase, ε has a change to nucleate since now the α/η interface is metastable with respect to its formation [132, 134].

At first, we need the free energies of individual phases that can be obtained from the CALPHAD model by [124]:

$$\begin{aligned} G_\alpha &= (1-c)G^\alpha_{Cu} + cG^\alpha_{Sn} + RT\left[(1-c)\ln(1-c) + c\ln c\right] \\ &\quad + c(1-c)\left[L^\alpha_0 + L^\alpha_1(1-2c)\right], \end{aligned} \tag{6.3}$$

$$\begin{aligned} G_\eta &= 2.0\times 10^5(c-0.435)^2 + 0.545G^\alpha_{Cu} + 0.455G^{SER}_{Sn} \\ &\quad -6869.5 - 0.1589T, \end{aligned} \tag{6.4}$$

$$\begin{aligned} G_L &= (1-c)G^L_{Cu} + cG^L_{Sn} + RT\left[(1-c)\ln(1-c) + c\ln c\right] \\ &\quad + c(1-c)\left[L^L_0 + L^L_1(1-2c) + L^L_2(1-4c-4c^2)\right], \end{aligned} \tag{6.5}$$

where the parameters in Eqs. (6.3)-(6.5) are

$$\begin{aligned} &G^{\alpha}_{Cu} = -19073.0, \quad G^{\alpha}_{Sn} = -27280.0, \\ &G^{SER}_{Sn} = 346160.0, \quad G^{L}_{Cu} = -11083.0, \quad G^{L}_{Sn} = -28963.0, \\ &L^{\alpha}_0 = -11448.0, \quad L^{\alpha}_1 = -11694.0, \\ &L^{L}_0 = -10487.0, \quad L^{L}_1 = -18198.0, \quad L^{L}_2 = 10528.4 \end{aligned}$$

Here, we note that the free energy of the nearly stoichiometric η phase was modified by introducing quadratic terms that allow for a finite degree of non-stoichiometry which facilitate the numerical treatment of the problem.

The driving force for the η phase for nucleation can be calculated from:

$$\Delta G_V = \mu_{\mathrm{Cu/Sn}} - \mu_{\mathrm{Cu_6Sn_5}}, \tag{6.6}$$

where the chemical potentials of the constituents (Cu and Sn) are defined at the metastable equilibrium between the substrate and the liquid solder.

Determination of the driving force thus requires the determination (at any time during the simulation) of the common tangent line connecting the free energy curves of the α and L phases. The compositions of Cu and Sn in the equation above correspond to the equilibrium composition of the η phase which in turns correspond to the composition of the forming Cu_6Sn_5 nucleus. It should be mentioned that in this work, the local metastable equilibrium at any point where the α and L phases coexist are calculated at every time step of the simulation. The resulting driving force for the nucleation of the η phase is thus a dynamical quantity that is not to be determined *a priori*, as done in [33]. The actual implementation of the nucleation of the η phase

is discussed in the section below.

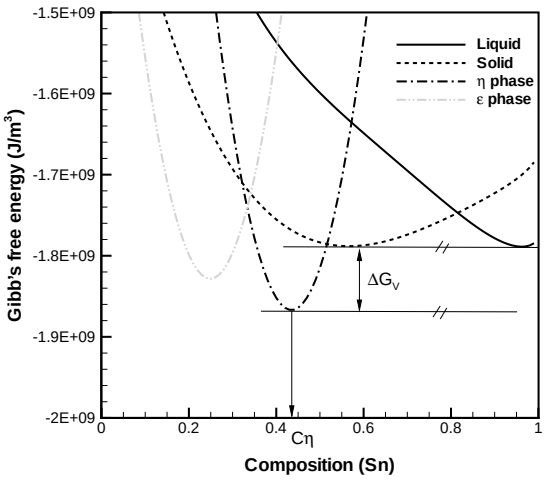

Fig. 59. Gibb's free energy of individual phases (S, L and η) with respect to the composition at 523K. Driving force can be obtained from the free energy profiles.

C. Multi-phase field and diffusion equations

A system initially consists of Sn-based liquid solder (L) and Cu solid substrate (α). When considering the evolution of a two-phase system, a simple phase-field model with a single (with its complement) phase-field variable can be used [5]. However, the introduction of third (and more) phases requires one to introduce additional phase-fields. Moreover, if the third phase is supposed to represent the formation of multiple grains of the same phase, one must introduce either orientation fields that allow the differentiation of individual grains of the same phase [36], or differentiated non-conserved phase fields that represent individual grains [45]. In this work, the spatial distributions of the liquid solder, the substrate, and the nucleated grains in the system

is mathematically expressed by using N arrays of phase fields $\phi_i(x,t)$ $(i = 1, ..., N)$, which can be expressed with multi-phase field variables. The phase-field variables in this model can be defined as ϕ_1 for solid substrate, $\phi_{2,...,N-1}$ for the nucleating grains and ϕ_N for liquid solder. Each of these non-conserved field variables represents the occupation of a given point in the computational domain by the solid substrate, the liquid solder and/or any of $N-2$ individual grains of the η phase.

From previous works [5, 6], the free energy density f of the multi-phase system can be defined as follows:

$$f = \sum_{j>i} \sum_{i} \left[-\frac{\epsilon_{ij}^2}{2} \nabla\phi_i \cdot \nabla\phi_j + \omega_{ij}\phi_i\phi_j \right] + \sum_{i} \phi_i f^i\left(c_i\right), \tag{6.7}$$

where f^i is the chemical free energy density of the $i-th$ phase and it depends on the phase composition c_i. ϵ_{ij} is the gradient energy coefficient which is related to the energy penalty involved in forming an interface and ω_{ij} is a double well potential representing the energy barrier between two phases ϕ_i and ϕ_j. Within the phase-field approach, the structure of the interface can in principle be defined in an arbitrary manner. In some instances, for example, the composition of the different coexisting phases is assumed to correspond to the bulk compositions. In this work, we instead determine the compositions of coexisting phases at any given point of the computational domain by establishing the chemical potential equilibrium condition as suggested by [5]. This approach has the advantage that it somewhat relaxes the maximum interfacial thickness allowable in the numerical implementation of phase-field simulations and avoids the formation of extraneus secondary 'energy barriers' resulting from discontinuities in the chemical potentials of the constitutes across an interface [5].

According to the previous descriptions for coexisting phase fields at interfaces,

we can obtain the evolution of two different field equations as a function of time [27]. They are the phase-field equation:

$$\frac{\partial \phi_i}{\partial t} = -\frac{2}{N_p} \sum_{i \neq j} \chi_i \chi_j M_{ij} \left[\frac{\partial F}{\partial \phi_i} - \frac{\partial F}{\partial \phi_j} \right], \tag{6.8}$$

where

$$\frac{\partial F}{\partial \phi_i} = \sum_{i \neq j} \left[\frac{\epsilon_{ij}^2}{2} \nabla^2 \phi_j + \omega_{ij} \phi_j \right] + f^i(c_i) - f_c c_i \tag{6.9}$$

with a constraint:

$$\sum_{i=1}^{N} \phi_i = 1, \tag{6.10}$$

and diffusion equation:

$$\frac{\partial c}{\partial t} = \nabla \cdot \left(D(\phi_i) \sum_{i=1}^{N} \phi_i \nabla c_i \right) \tag{6.11}$$

with a constraint:

$$c(x,t) = \sum_{i=1}^{N} \phi_i c_i. \tag{6.12}$$

where χ_i is equal to 1 when the corresponding phase exists, otherwise χ_i is 0, and N_p represents the number of the coexisting phases at a calculated position: $N_p(x,t) = \sum_i^N \chi_i(x,t)$. This equation is only valid on the phase interfaces since the presence of only one phase in any point of the calculation domain renders χ_i or χ_j equal to zero. M_{ij} represents the mobility of the interfacial region.

Model parameters can be obtained from a stationary solution of the phase-field equation in a planar interface, which turns out two relationships between model parameters and material parameters based on the definition of the interface energy as a function of gradient energy coefficient and phase-field with a referred interface width [27, 28]:

$$\epsilon_{ij} = \frac{4\sqrt{\xi \sigma_{ij}}}{\pi} \quad \text{and} \quad \omega_{ij} = \frac{2\sigma_{ij}}{\xi}, \tag{6.13}$$

where ξ is the half of the width of the interface, and σ_{ij} is the interface energy for

the corresponding phases.

D. Numerical implementation

A Cu-Sn binary system at 523K will be regarded. The system is initially composed of a Sn-rich liquid solder (L), a Cu-rich solid substrate (α). Meanwhile, IMC grains of Cu_6Sn_5 (η) will are randomly seeded based on nucleation theory discussed above. The phase-field equation and diffusion equation will be numerically computed by using finite difference method for spatial domain and Euler scheme for temporal domain in two dimensions. Mesh size of the calculation domain is fixed as $\Delta x = 4.0 \times 10^{-8}$(m) and the half width of the interface ξ is used $4\Delta x$.

For nucleation, the nucleation probability P_n will be calculated according to the material parameters at each time step and every 4 nodal points in the interface. Meanwhile, a random number is generated. If the generated number is smaller than average P_n from every 4 nodal points, the nodes will be transformed to a single nucleus. Because the nodes is transformed, the composition of the surrounding subdomains must change in order to enforce mass conservation. The amount of residuary composition after the phase transformation should be added into the neighboring liquid nodes. It is reasonable to add the residuary composition into liquid phase due to the fact that diffusion in the liquid phase is much higher than that in the substrate ($D_L >> D_\alpha$). To ensure smooth compositional gradients at the nuclei/matrix interface, the steady state diffusion equation is solved after each of the nuclei are introduced. If P_n is not satisfied with the criteria described above, no nucleus is transformed, and calculation will be continued at the next interface position to be satisfied with the nucleation probability. It is noted that a new born nucleus is not allowed to overlap with other nuclei in the simulation.

The size of the nucleus is determined by the critical radius of nucleus from the classical nucleation theory [97]. From Simmons [34], the typical size of a nucleus was obtained empirically. However, we use the size of a nucleus from the radius of the critical nucleus $r_{cri} = (2\sigma_{L\eta} sin(\theta)/\Delta G_V)$ brought by a classical nucleation theory [97], and it is $4\Delta x \times 4\Delta x$ in the study. The size of the nuclei is also observed in an experimental result [98]. The contact angle (θ) of a nucleus with respect to the substrate is adopted as $\theta = 23$ [97], and frequency factor (J_0) is set to be $10^{32}(m^{-2}s^{-1})$ [56].

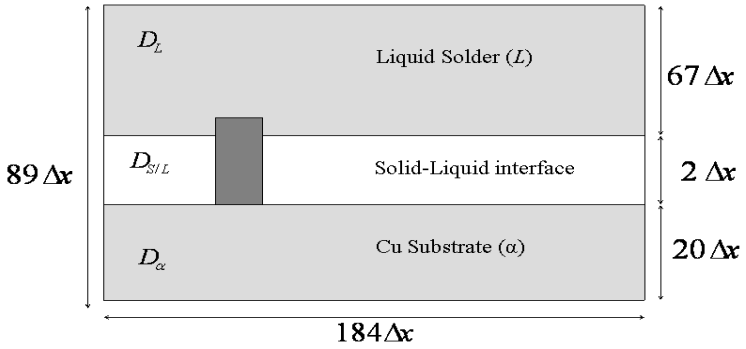

Fig. 60. A schematic configuration for the computational domain. The system is $184\Delta x \times 89\Delta x$. Cu substrate and liquid solder are positioned between 0 and $20\Delta x$ and between $22\Delta x$ and $89\Delta x$. The position between $20\Delta x$ and $22\Delta x$ is set to be the $\alpha - L$ interface. Nuclei (a rectangular in the interface on figure) will be randomly positioned at the interface based on the Poisson distribution function.

Fig. 60 shows a schematic illustration of the computational domain and the position of the nuclei as it appears at the interface. The size of the system is set to be $184\Delta x \times 89\Delta x$. Cu substrate and liquid solder are positioned between 0 and $20\Delta x$ and between $22\Delta x$ and $89\Delta x$. The position between $20\Delta x$ and $22\Delta x$ is set to

Table I. Material parameter values for use in simulating the formation and growth of IMC layer during lead-free soldering.

$D_L = 2.0 \times 10^{-12}(m^2/s)$,	$D_\eta = 2.0 \times 10^{-5} D_L(m^2/s)$
$D_\alpha = 1.0 \times 10^{-6} D_L(m^2/s)$,	$D_{\eta L} = 2.0 \times 10^{-1} D_L(m^2/s)$
$D_{\eta\alpha} = 2.0 \times 10^{-3} D_L(m^2/s)$,	$D_{GB} = 2.0 \times 10^{-2} D_L(m^2/s)$
$\sigma_{\eta L} = 0.1(\mathrm{J}/m^2)$,	$\sigma_{\eta\alpha} = \sigma_{GB} = 0.3(\mathrm{J}/m^2)$
$M_{\eta L} = 1.0 \times 10^6 D_L(m^2/s)$,	$M_{\eta\alpha} = M_{GB} = 7.0 \times 10^4 D_L(m^2/s)$

be the $\alpha - L$ interface. Periodic boundary conditions are applied to the sides of the calculation domain and Neumann boundary conditions are applied to the top and bottom of the calculation domain. The calculations are finished when the thickness of the Cu-substrate is broadly close to zero.

The free energy densities per unit molar volume of individual phases can be obtained from the CALPHAD method [124] as shown in Eqs. (6.3)-(6.6) with molar volume [$v_m = 16.29$ (cm^3/mole)]. The equilibrium phase compositions can be used as $c_L^{\alpha L} = 0.977$ and $c_\alpha^{\alpha L} = 0.1957$ and the equilibrium composition of η phase can be calculated by using free energy equations as shown in the previous section ($c_\eta = 0.435$) where $c_\alpha^{\alpha L}$ is the equilibrium composition of the α phase at the $\alpha - L$ interface and the other terms are defined correspondingly. The initial compositions of the Cu-substrate and liquid solder are set to be $c_\alpha = 0.002$ and $c_L = c_L^{\alpha L}$.

Critical parameters for the simulation, such as interfacial energies and mobilities are notoriously hard to obtain from experimental results. They are thus used as simulation parameters which are carried by theoretical approaches from experimental data [41, 43, 128, 129]. The diffusivities and other material parameters employed in the numerical calculation are summarized in the Table I.

E. Results and discussions

The morphologies of IMC grain growth, including nucleation behavior, will be performed by using the different material properties such as the diffusion coefficient of grain boundary and the interface energy between L/η interface.

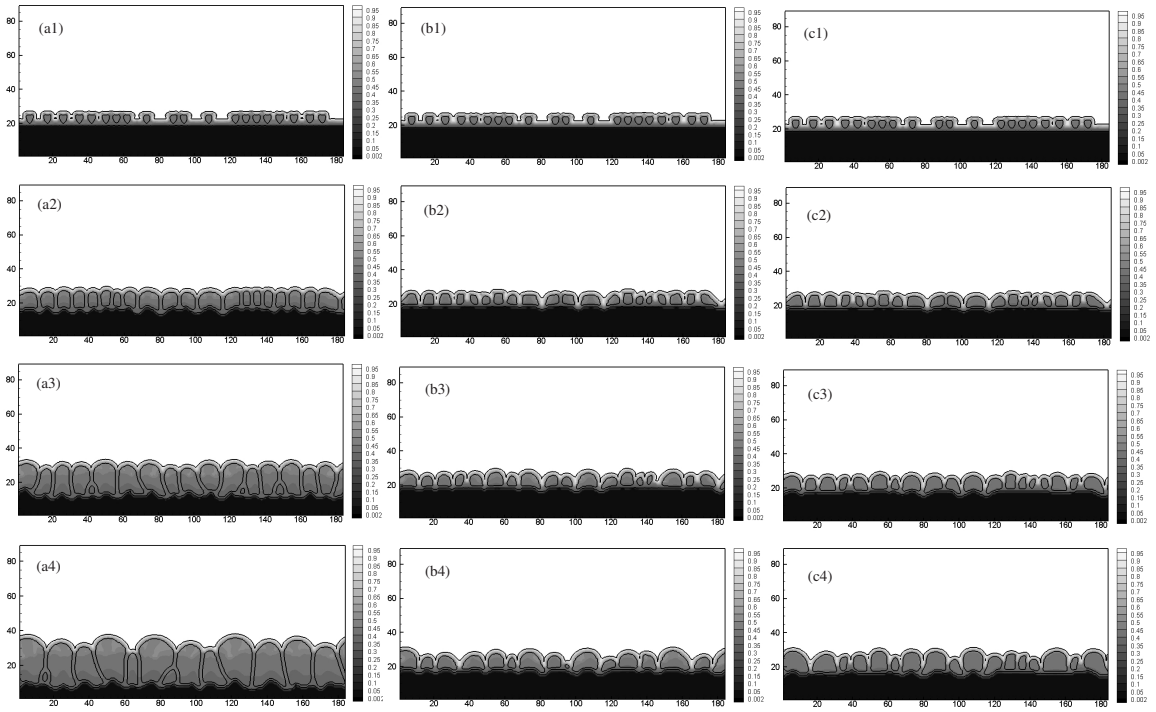

Fig. 61. Microstructural evolution of the IMC grains for the case of (a) high grain boundary diffusion ($D_{GB} = 4.0 \times 10^{-14}(m^2/s)$), (b) intermediate grain boundary diffusion ($D_{GB} = 4.0 \times 10^{-15}(m^2/s)$) and (c) low grain boundary diffusion ($D_{GB} = 8.0 \times 10^{-17}(m^2/s)$) at t= (1) 0.05, (2) 1.8, (3) 6.8 and (4) 17 (sec). We denote that Figures a, b and c corresponds Case 1 and Case 2 and Case 3 for convenience respectively.

Simulations are carried out with three different diffusion coefficients within grain boundaries in order to investigate the kinetics of the η-IMC growth affected by short-

cut diffusion paths. The values of the diffusion coefficients along grain boundary will be defined related to the diffusion coefficient within Cu_6Sn_5 (η) grains. According to the magnitude of the diffusion coefficient difference between the grain boundary and the Cu_6Sn_5 (η) grains, the grain boundaries can play a role of channels of fast mass transport or not.

The fast diffusion through the grain boundaries,rather than through η grains, can be performed by using $D_{GB} = 2.0 \times 10^3 D_\eta$. The low diffusion through the grain boundaries can be performed by using where $D_{GB} = D_\eta = 2.0 \times 10^1 D_\eta$ which tells that the diffusion rate of mass through the grain boundaries and through the η grains are the same. The intermediate diffusion coefficient where $D_{GB} = 2.0 \times 10^2 D_\eta$, which is just set to be the mean value of high and low diffusion coefficients. The value of D_η in the case of low diffusion is chosen different with that in the cases of fast and intermediate diffusion in order to compare with the previous work by [28]. For all three cases, the initial solder composition is set to $c_L = c_L^{L\eta}$ and other simulation parameters in the three cases, such as $L - \eta$ interface energy and so on, are taken to be the value as shown in the Table I.

Fig. 61 shows nucleation of the IMC grains with three different grain boundary diffusion coefficients at t=0.05, 1.8, 6.8 and 17 (sec). IMC grains randomly nucleate in space and time according to the role of nucleation statistic. The number of nuclei at early stages depends on the soldering conditions. 20 nuclei appear in initial times in all three cases, and they grow without an additional nucleus in the interface because overlapped nucleation is prohibited in spite of the agreement of nucleation condition. About 0.05 sec, one can find triple junctions that contains α, η and L phases. Because of the existence of the triple junction of three phases, some nuclei are allowed to grow without coarsening, which is a behavior supported by experimental investigations by [98]. The grains under these conditions likely grow in width rather than in height.

This behavior can be explained in the following. Composing Cu_6Sn_5 phase requires Cu components and Sn components. In the vertical growth of Cu_6Sn_5 phase, Cu should be supplied from the cu-substrate to the $\eta - L$ interface. However, because of the diffusion coefficients, it takes longer time. On the other hand, Cu supply at the triple junction likely occurs easily because the component to make Cu_6Sn_5 are close together, so that forming Cu_6Sn_5 at the edge of the grain occurs faster than forming Cu_6Sn_5 at the top of the grains, which means that grains have a tendency to grow to the horizontal direction, rather than to the vertical direction until neighboring η grains meet each other.

As horizontal growth ensues, the grains start to impinge on each other and coarsening begins. During coarsening, one can see that $\eta - L$ and $\alpha - \eta$ interfaces have curvatures of opposite signs resulting in scallop-like morphology of individual η grains as already reported by a theoretical result [28] and experimental results [45, 98]. The scallop shape can be observed only in the stage of grain coarsening, not in the stage of grain nucleation. Thus, the scallop morphology represents the byproduct of grain competition, and it leads to ongoing of grain coarsening.

Contrary to the evolution of IMC grain in the early stage, one can find that the morphologies of η grain growth in the late stage for the three cases are similar to the results from the previous works [28, 45, 117]. The Cu substrate at intermediate grain boundary diffusion and low grain boundary diffusion is not much dissolved to form Cu_6Sn_5 phase, so that the thickness of IMC phase in the two cases shows a small increase compared with the case of fast grain boundary diffusion, which is a good agreement with the previous work [28]. More detailed information about the similarity between the present work and the previous work can be found in Fig. 62.

At the early stage ($t < 1$ (sec)) during lead-free soldering in Fig. 62, the thickness Cu-substrate remains unchanged, the thickness of IMC increases gradually, and the

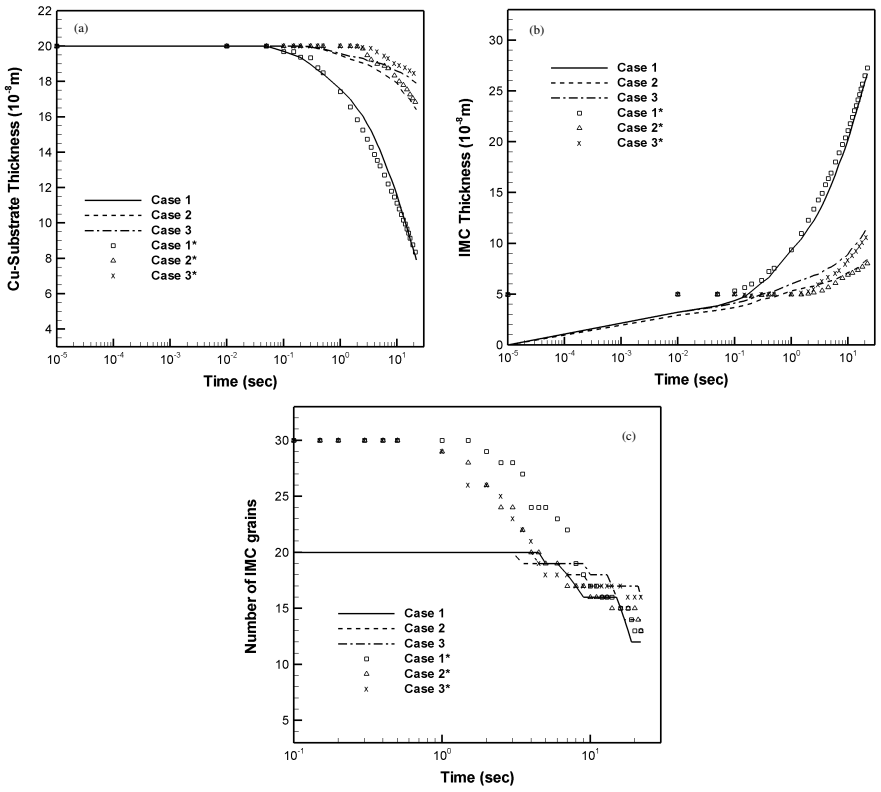

Fig. 62. Evolution of Cu-substrate and η-IMC layer thickness and the number of grains with respect to time corresponding (a), (b) and (c) in Fig. 61. Case 1, 2 and 3 show the current results with high grain boundary diffusion, intermediate grain boundary diffusion and low grain boundary diffusion,respectively. Case 1*, 2* and 3* are obtained from the previous work [28] with the same diffusion conditions. They were computed excluding nucleation. IMC thicknesses are given from division of total η phase area by horizonal axis length for convenience.

number of IMC grains is not changed. Those phenomena is understandable because the grains is likely to grow to horizontal direction. At first, a lot of nuclei are randomly born at the $\alpha - L$ interface according to nucleation conditions, and the newly formed nuclei grow in width until grain coarsening occurs. It is known that nucleation takes place mainly in the interface region, slightly in the liquid phase. So, the change of Cu-substrate thickness will be relatively small, and the number of IMC grains will remain constant in spite of subsequential appearance of nuclei until the nucleated grains coarsens while IMC thickness increases with respect to time [98]. It is important to note that these features of soldering reaction at early stages can be observed in the simulations regardless of the grain boundary diffusion coefficient used.

After the early stage, one can find that the soldering reaction shows behavior already observed computationally and experimentally [28, 45, 98]. The grain boundaries are grooved and partial penetration (wetting) of the η grain boundaries is observed. The initially flat $\eta - L$ interface becomes rounded, and the grain coarsening starts. The degree of grain coarsening depends on the grain boundary diffusion coefficient. If fast grain boundary diffusion is applied, we can expect that the large flux Cu and Sn is delivered through the grain boundary resulting in the fast grain growth and coarsening. It agrees with case 1 in Fig. 61 and Fig. 62. On the other hand, if a grain boundary diffusion coefficient smaller than case 1 is applied, less supply of Cu and Sn lead to a little decrease of Cu-substrate thickness and a little increase of IMC thickness. Eventually, at the late stage, the decrease of Cu-substrate, increase of IMC thickness and number of the survived grains is similar compared with the previous work [28] regardless of the incorporation of nucleation in our model, with only a 2-3 % difference for Cu-substrate and IMC thickness, and 1-2 grains difference is founded for the number of the survived grains.

The different nucleation rate of the η grains on the IMC layer growth in the

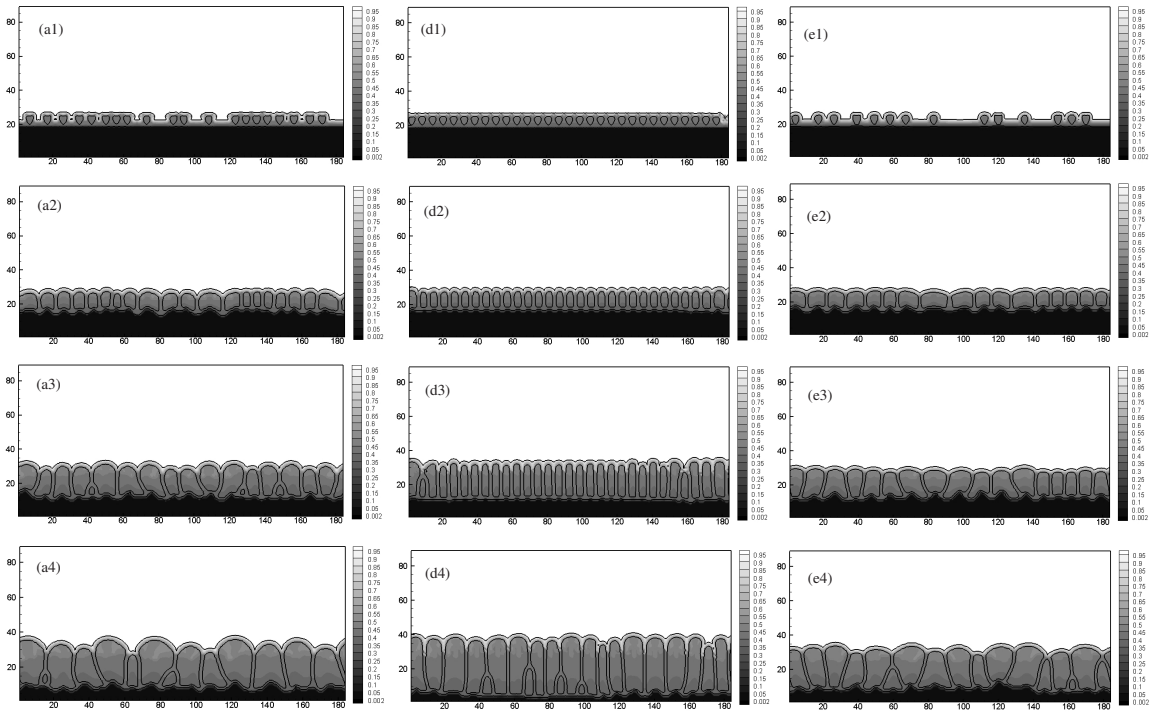

Fig. 63. Microstructural evolution of the IMC grains for the case of (d) the low $\eta - L$ interface energy ($\sigma_{\eta L} = 0.05(\mathrm{J}/m^2)$) and (e) high $\eta - L$ interface energy ($\sigma_{\eta L} = 0.15(\mathrm{J}/m^2)$) at t= (1) 0.05, (2) 1.8, (3) 6.8 and (4) 17 (sec). Figures (a) are the same in Figures 61(a). We denote that Figures (a), (d) and (e) corresponds Case 1 and Case 4 and Case 5 for convenience respectively.

simulations are realized by changing the $\eta - L$ interface energy as shown in Fig. 63(d) ($\sigma_{\eta L} = 0.05(\mathrm{J}/m^2)$) and (e) ($\sigma_{\eta L} = 0.15(\mathrm{J}/m^2)$). Other material parameters for Fig. 63 are adopted from the case of Fig. 61. The change of the interface energy in the simulation is also helpful to understand the concurrent coarsening at a late stage in soldering reaction.

Although fast grain boundary diffusion is employed along η grain boundaries, an early stage of the soldering reaction depends on the nucleation rate that is determined by the $\eta - L$ interface energy. One can find that case 4 and case 5 have the different

nucleation rate at an early stage. In mechanics of nucleation, it is well known that η phases are transformed from α and L phases. Energy is used to form a new phase creating interfaces that have specific energy [98]. The interfacial energy occupied in new interface comes from the energy of the parent phases. Based on the relationship between interface energy of a new phase and energies of parent phases and new born phases, lower $\eta - L$ interface energy of new phases is likely to create more nuclei in a certain time interval than the number of nuclei created in case of higher $\eta - L$ interface energy in the same time interval in the nucleation stage.

As mentioned above, assigning low $\eta/ - L$ interfacial energies results in higher nucleation rates. Our results suggest that despite this larger number of grains nucleated during the early stages of the soldering reaction, grain coarsening is delayed (by about 6.8 seconds in our simulations) when compared to cases in which the interfacial energies are higher. The same result can be found in other theoretical [135] and an experimental investigations [136]. This behavior can be explained by observing that a higher difference between the $\eta - L$ interfacial energy η grain boundary energy leads to grain boundary wetting, which essentially pins the $\eta - L$ interfaces resulting in the slowing of lateral growth of the η grains. Therefore, the grains grow upward and downward with less coarsening with neighboring η grains. The growth rate in case 4 can be observed to be faster than the case 1 shown in Fig. 63.

Our simulations show that a few nuclei are nucleated when high $\alpha - L$ interface energy is used until about 0.3 sec. The number of the nucleated grains gradually increases up to 17. Due to the small nucleation rate, grain coarsening occurs at $t > 10$(sec). However, once grain coarsening happens, the behavior of the IMC grain follows the same behavior observed in the cases that exclude nucleation phenomenon and in which the η grains are assumed to exist at the substrate/solder interface since the beginning of the simulation. Our results show that the Cu-substrate thickness,

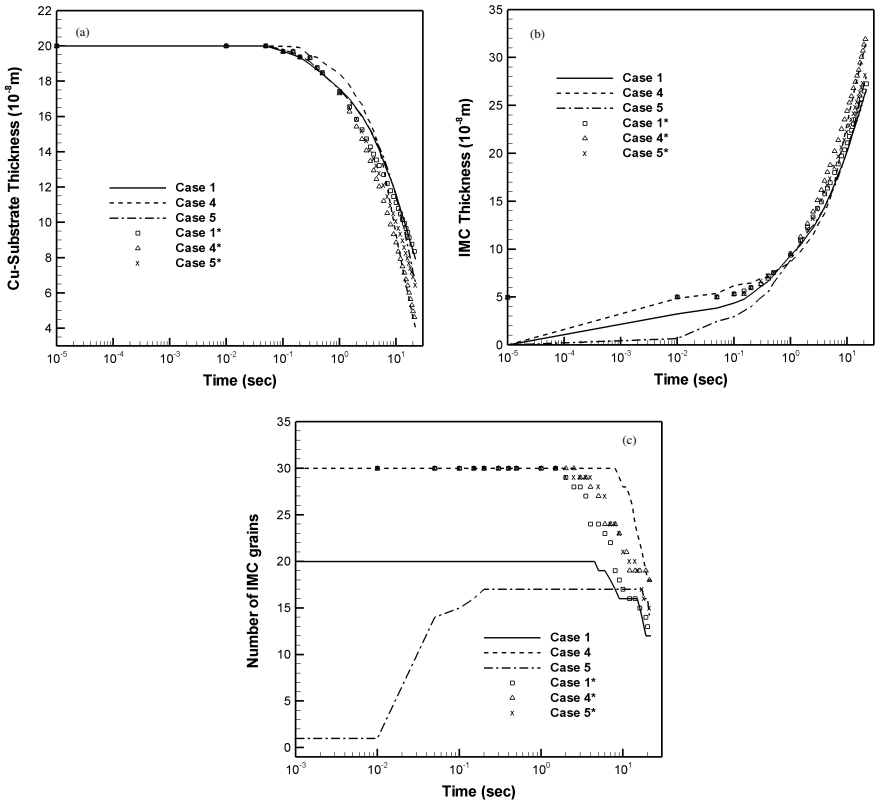

Fig. 64. Evolution of Cu-substrate, η-IMC layer thickness and the number of grains with respect to time corresponding Figs. 63(a), (d) and (e). Case 1, 4 and 5 show the current results with (a) intermediate interface energy, (b) lower interface energy and (c) higher interface energy, respectively. Case 1*, 4* and 5* are obtained from the previous work [28] with the same interface energy. They were computed excluding nucleation. IMC thicknesses are given from division of total η phase area by horizonal axis length for convenience.

the IMC thickness and the number of the grains vary from case to case considered during the early stages of the soldering reaction. However, as soon as coarsening dominates, the behavior of the system converges to that obtained by [28]. This essentially means that once full interface coverage by η grains is achieved, the system 'looses' any memory of the particular differences in the nucleation of the IMC grains. This observation, however, cannot be generalized in cases in which the concurrent nucleation of the ε phase is considered. This latter cases will be the subject of future work.

F. Conclusions

The study provided a phase-field modeling approach in order to investigate intermetallic compound phase transformation with extension of nucleation phenomenon in an early stage in Cu-Sn soldering system. Also, the combination with CALPHAD thermodynamic models offers a fundamental information to analyzes the phase birth related to nucleation phenomenon of Cu_6Sn_5 and the phase death related to coarsening phenomenon of Cu_6Sn_5 grains. The combination of phase-field model with simple, explicit nucleation models allows the investigation of the different material parameters that changes the morphology of IMC grains formed at the early and late stages of the reaction in Cu-Sn alloy system. The nucleation of the IMC (Cu_6Sn_5) grains during lead free soldering was performed using nucleation model that contains Poisson distribution function, and the morphological evolution and growth of the IMC (Cu_6Sn_5) grains after the nucleation stage was performed using a multi-phase-field model.

The simulations were performed by using three different grain boundary diffusion coefficients in η-IMC grains (or layer) and three different interface energies of

$\eta - L$ interface causing the concurrent coarsening of the IMC grains along with the IMC layer growth with applying nucleation probability. From the results, one can found many results from the simulations corresponding to the change of material parameter. However, Several conclusions can be narrowed down overall compared with the previous research [28] as follows: (1) Cu_6Sn_5 easily formed at the edge of the grain occurs faster than at the top of the grains due to high diffusion coefficient of liquid solder until η grains impinges. (2) Contrary to the stage of grain nucleation, the scallop shape of the grains can be observed only in the stage of grain coarsening, which result from the grain coarsening. (3) Although the formation and growth of the IMC grains observed explicitly different from the research [28] in the early stages, The behavior of the IMC grains (or layer) applied with different material parameters (e.g. grain boundary diffusion coefficient and a $\eta - L$ interface energy) at the late stages eventually appears similar to the research [28].

The microstructural evolution of the IMC grains initially appeared more complicated compared with previous works [28, 125]. However, it was found in this study that phase-field simulation of IMC during soldering reaction containing nucleation theory can show the nature of IMC layer formation, which in turn can be used to better control of the soldering reactions. Moreover, it is now possible to qualitatively reproduce many previous experimental researches about nucleation behaviors at early stages, lateral growth of IMC grains prior to coarsening as well as the evolution of a scallop-like morphology of the IMC layer once complete coverage of the substrate/liquid interface is achieved.

CHAPTER VII

CRYSTALLOGRAPHIC PHASE-FIELD SIMULATIONS OF INTERMETALLIC COMPOUND GROWTH DURING LEAD-FREE SOLDERING

A. Introduction

IMC layer formation during soldering reactions generally consists of several distinct physical processes, such as nucleation, growth and coarsening. Individual IMC grains form at the solder/substrate interface before the formation of the IMC layer. In the formation process, it is interesting to know that each grains form containing independent crystalline. During the formation, individual IMC grains with their own crystallographic orientation simply grows reacting with liquid solder and solid substrate. However once the grains impinge together, layer evolution involves grain boundary migration through which a grain with a particular orientation with respect to an external frame of reference grows at the expense of neighboring grains. Grain misorientation may affect both the driving force for grain boundary migration and the grain boundary mobility.

Two IMCs (Cu_6Sn_5 (η phase) and Cu_3Sn(ε phase)) have been observed to form at the substrate (Cu)/solder (Sn) interface in Cu-Sn systems [40, 41, 43, 44, 45, 46, 96, 117, 119, 120, 122, 123, 128, 129, 130]. The sequence of these phases' formation is determined by the local thermodynamic conditions of Cu/Sn interface. In case of nucleation process, one can understand that the η phase , rather than ε phase, has been shown to precipitate during the earliest stages of solder/substrate interactions due to magnitude of driving force of the two phases. However, determining orientation of individual grains can not be obtained from local thermodynamics conditions, but would be chosen by random manners.

In spite of the difficulty of introducing the effect of misorientation in mathematical theories of microstructure evolution, several researches have been coupling phase-field descriptions of phase transformations with crystalline orientational fields by using mathematical and computational methods [7, 21, 22, 56, 137, 138, 139, 140, 141, 142, 143, 144, 145, 146]. Among the researches, Kobayashi [7] and Warren [8] have produced the most rigorous study of the introduction of orientation fields within the context of phase-field modeling. These authors have developed mathematical descriptions of systems where the crystallographic orientation of a particular phase changes, established the new model parameters in terms of grain boundary energies and have implemented these formalisms to the investigation of solidification of polycrystalline materials [8]. Despite this progress, further extension of this approach to the multi-phase field formalism has not been performed as extensively.

A huge number of experimental researches have been done in a lot of different area of research field, and can be also found in the area of soldering processes [147, 148, 149, 150, 151, 152, 153]. These recent experimental works have focused on the effect of crystallographic orientation of grains to the microstructural evolution, orientation relationships between IMC grains and a substrate and growth kinetic of IMC grains with morphologies affected by crystallographic orientations. In spite of many experimental researches, unfortunately, the development of computational researches in the area of soldering processes is behind experimental results.

In this study, we will briefly introduce a phase-field model including crystallographic orientation for the evolution of η phase along a Cu/Sn interface. The proposed model is based on a multi-phase field model derived from previous works [6, 27] for the evolution of grains of Cu_6Sn_5 under isothermal conditions. We will show different morphologies of IMC grains and layers during lead-free soldering as a function of material parameters. In this work, we will assume that the Cu_6Sn_5 phases are set up

at the initial condition as shown in Fig. 65. The rate of growth of the IMC individual grains will be controlled by the diffusion rates while the coarsening of the IMC grains as well as the concurrent coarsening will be controlled by using different solder/IMC interface energies with different gradient coefficients of misorientation. Investigation of microstructural evolution affected by crystallographic orientation during the solder/substrate interactions will provide one with a deeper insight for the nature of IMC layer growth in model lead-free solder systems, which in turn can be used to better control of the soldering reactions.

B. A free energy density of crystalline

The order parameters, ϕ and Θ, represent phase-field and the crystallographic orientation, respectively. For the construction of a physically realistic model of phase boundaries, schematic configuration of two impinged phases is required as shown in Fig. 65.

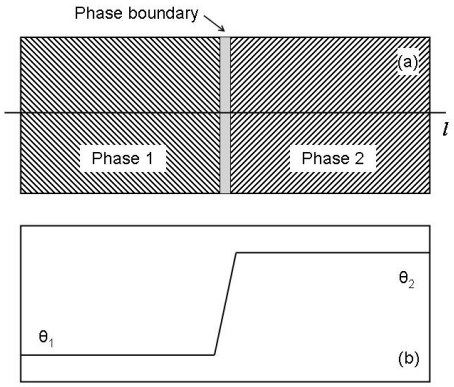

Fig. 65. A schematic configuration for misorientation of two grains. (a) Bicrystal structure (b) Graph of misorientation of two grains along the line l.

For the explanation of ϕ and Θ, a interfacial region of two phases, shown in

Fig. 65, should be considered where the orientation of an atomic bond (lattice vector) with respect to a reference frame should be differentiated by a continuous modular (i.e. cyclic) variable, Θ_i. For the interfacial region, we can simply define the relationship between ϕ and Θ as

$$h(\phi)\Theta = \Theta_i, \tag{7.1}$$

where Θ_i is the orientation of a single phase (liquid solder, solid substrates and individual grain) that is mathematically expressed by using N arrays $\Theta_i(x,t)(i = 1,...,N)$. The orientation variables in this model can be defined as Θ_1 for solid substrate, $\Theta_{2,...,N-1}$ for the grains in the two IMC layers and Θ_N for liquid solder.

Some approaches have considered an additional order parameter to represent the degree of crystallinity of a particular region of the computational domain [7]. Because this parameter and the usual (and non-physical) ϕ parameter have been physically uncoupled [8], the model can be simplified by the selection of ϕ field parameter. The crystalline phase field model now have two order parameter, ϕ and Θ, and now ϕ is associated with the degree of crystalline orientational order (as well as with the chemical identity of a particular region in the domain).

Misorientation ($\Delta\Theta$) is the difference of orientation between two adjacent grains and is a macroscopic quantity. The misorientation of a grain boundary can be defined by spatially integrating $\nabla\Theta$ from a side of a grain into the other side of the grain, and gradient of misorientation is associated with grain boundary properties, particularly grain boundary energy. Once the grain boundary energy can be related to of the gradient in misorientation, it should be characterized as anisotropic [8]. Therefore, free energy density involving the orientational order is postulated as

$$f_O = a_1 h(\phi)|\nabla\Theta|, \tag{7.2}$$

where a_1 is the gradient coefficient of misorientation and $h(\phi) = \phi^3(10 - 15\phi + 6\phi^2)$ is a function of phase-field. A term, $a_2 g(\phi)|\nabla\Theta|^2$, can be included in the free energy density [7, 8]. The term shows the curvature of the misorientation that is associated with the effect of grain boundary motion, but in this study we will not use the term.

C. Models

We consider an isothermal Cu-Sn binary system. The system is composed of a Sn-rich liquid solder (L), a Cu-rich solid substrate (α), and an intermetallic layer of Cu_6Sn_5 (η).

The IMC layers consist of many grains that are differentiated by non-conserved parameters for phase fields [45] and crystalline fields [151]. The spatial distribution of the liquid solder, the substrate, and the grains in the intermetallic layer of the system is mathematically expressed by using N arrays of phase fields $\phi_i(x,t)(i = 1, ..., N)$, which can be expressed with multi-phase field variables. The phase field variables in this model can be defined as ϕ_1 for solid substrate, $\phi_{2,...,N-1}$ for the grains in the two IMC layers and ϕ_N for liquid solder. $\phi_i = 1$ indicates that phase i exists in that point of space, while $\phi_i = 0$ indicates that i phase does not exist in the region. Additionally, interfaces are defined in the system whenever $0 < \phi_i < 1$. Within the interface, ϕ_i is considered to change continuously within the $0 < \phi_i < 1$ range. For example, if $0 < \phi_1 < 1$ and $0 < \phi_2 < 1$ at a point in an interface region, the point indicates the presence of the η-IMC layer and a solid substrate. Moreover, the discrete orientation of a grain can be obtained from Eq. (7.1).

From previous works [5, 6], the free energy density f of the multi-phase system

including crystallographic orientation can be defined as follows:

$$f = \sum_{j>i} \sum_{i} \left[-\frac{\epsilon_{ij}^2}{2} \nabla\phi_i \cdot \nabla\phi_j + \omega_{ij}\phi_i\phi_j \right] + \sum_{i} a_1 h(\phi_i) |\nabla\Theta_i| + \sum_{i} \phi_i f^i\left(c_i\right), \quad (7.3)$$

where f^i is the chemical free energy density of the $i-th$ phase and it depends on the phase composition c_i. ϵ_{ij} is the gradient energy coefficient which is related to the energy penalty involved in forming an interface and ω_{ij} is a double well potential representing the energy barrier between two phases ϕ_i and ϕ_j. We will determine the compositions of coexisting phases at any given point of the computational domain by establishing the chemical potential equilibrium condition as suggested by [5]. This approach has the advantage that it somewhat relaxes the maximum interfacial thickness allowable in the numerical implementation of phase-field simulations and avoids the formation of extraneus secondary 'energy barriers' resulting from discontinuities in the chemical potentials of the constitutes across an interface [5].

According to the previous descriptions for coexisting phase fields at interfaces and crystallographic orientations, we can obtain the evolution of three different field equations as a function of time [8, 27]. They are the phase field equation:

$$\frac{\partial\phi_i}{\partial t} = -\frac{2}{N_p} \sum_{i\neq j} \chi_i\chi_j M_\phi \left[\frac{\partial F}{\partial\phi_i} - \frac{\partial F}{\partial\phi_j} \right], \quad (7.4)$$

where

$$\frac{\partial F}{\partial\phi_i} = \sum_{i\neq j} \left[\frac{\epsilon_{ij}^2}{2} \nabla^2\phi_j + \omega_{ij}\phi_j \right] + a_1 h'(\phi_i) |\nabla\Theta_i| + f^i(c_i) - f_c c_i, \quad (7.5)$$

crystallographic field equation:

$$\frac{\partial\Theta}{\partial t} = M_\Theta \nabla \cdot \left(a_1 \sum_{i=1}^{N} h(\phi) \frac{\nabla\Theta_i}{|\nabla\Theta_i|} \right), \quad (7.6)$$

and diffusion equation:

$$\frac{\partial c}{\partial t} = \nabla \cdot \left(D(\phi_i) \sum_{i=1}^{N} \phi_i \nabla c_i \right). \tag{7.7}$$

where χ_i is equal to 1 when the corresponding phase exists, otherwise χ_i is 0, and N_p represents the number of the coexisting phases at a calculated position: $N_p(x,t) = \sum_i^N \chi_i(x,t)$. This equation is only valid on the phase interfaces since the presence of only one phase in any point of the calculation domain renders χ_i or χ_j equal to zero. M_ϕ and M_Θ represent the phase mobility and orientation mobility of the interfacial region, respectively.

The constraint for phase field equation and diffusion equation are

$$\sum_{i=1}^{N} \phi_i = 1 \quad \text{and} \quad c(x,t) = \sum_{i=1}^{N} \phi_i c_i. \tag{7.8}$$

It is noted that the constraint for crystallographic field equation is used as Eq. (7.1).

Model parameters can be obtained from a stationary solution of the phase field equation in a planar interface, which turns out two relationships between model parameters and material parameters based on the definition of the interface energy as a function of gradient energy coefficient and phase field with a referred interface width [27, 28]:

$$\epsilon_{ij} = \frac{4\sqrt{\xi \sigma_{ij}}}{\pi} \quad \text{and} \quad \omega_{ij} = \frac{2\sigma_{ij}}{\xi}, \tag{7.9}$$

where ξ is the half of the width of the interface, and σ_{ij} is the interface energy for the corresponding phases.

D. Numerical implementation

A Cu-Sn binary system at 523K will be regarded. The system is initially composed of a Sn-rich liquid solder (L), a Cu-rich solid substrate (α). Meanwhile, IMC grains of

Cu_6Sn_5 (η) will are randomly seeded based on nucleation theory discussed above. The phase field equation and diffusion equation will be numerically computed by using finite difference method for spatial domain and Euler scheme for temporal domain in two dimensions. Mesh size of the calculation domain is fixed as $\Delta x = 4.0 \times 10^{-8}$(m) and the half width of the interface ξ is used $4\Delta x$.

Fig. 66 shows a schematic configuration for the computational domain. The size of the system is set to be $184\Delta x \times 290\Delta x$. For the initial array of phases, intermetallic grains (η phase) are placed from $25\Delta x$ to $30\Delta x$ between the liquid solder (from $30\Delta x$ to $90\Delta x$) and the solid substrate (from 0 to $25\Delta x$). The intermetallic layer initially consists of 30 rectangular grains that has different widths between $4\Delta x$ and $8\Delta x$. Orientational values for liquid solder and solid substrate are set to be 0 and 1, respectively, and the orientational values of each grain are randomly chosen ($0< \Theta <1$). Periodic boundary conditions are applied to the sides of the calculation domain and Neumann boundary condition is applied to the top and bottom of the calculation domain. The calculation will be finished when thickness of the Cu-substrate will be used up.

We put an buffer solder region at the top of liquid solder ($90\Delta x \times 290\Delta x$) because the liquid solder is composed of the liquid metal in which no phase change appears so that the composition change in region far from the soldering reaction can be negligible. Therefore it can be defined that the composition of the buffer region is initially the same as that of the solder in calculation.

The free energy densities per unit moral volume of individual phases were obtained from the CALPHAD method [124] and they are

$$\begin{aligned} f_\alpha &= (1-c)G^\alpha_{Cu} + cG^\alpha_{Sn} + RT\left[(1-c)\ln(1-c) + c\ln c\right] \\ &\quad + c(1-c)\left[L^\alpha_0 + L^\alpha_1(1-2c)\right], \end{aligned} \tag{7.10}$$

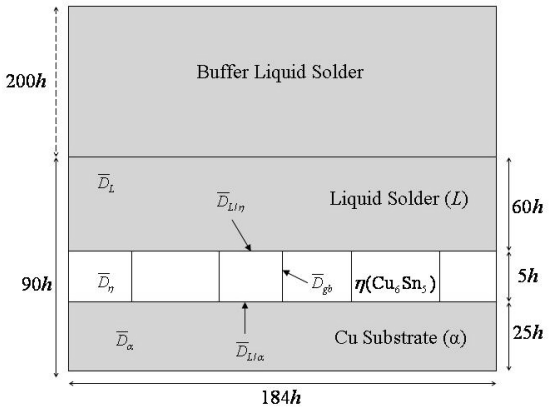

Fig. 66. A schematic configuration for the computational domain.

$$\begin{aligned} f_\eta &= 2.0\times 10^5(c-0.435)^2 + 0.545G^\alpha_{Cu} + 0.455G^{SER}_{Sn} \\ &\quad -6869.5 - 0.1589T, \end{aligned} \tag{7.11}$$

$$\begin{aligned} f_L &= 1-c)G^L_{Cu} + cG^L_{Sn} + RT\left[(1-c)\ln(1-c) + c\ln c\right] \\ &\quad +c(1-c)\left[L^L_0 + L^L_1(1-2c) + L^L_2(1-4c-4c^2)\right], \end{aligned} \tag{7.12}$$

where

$$\begin{aligned} &G^\alpha_{Cu} = -19073.0, \quad G^\alpha_{Sn} = -27280.0, \\ &G^{SER}_{Sn} = 346160.0, \quad G^L_{Cu} = -11083.0, \quad G^L_{Sn} = -28963.0, \\ &L^\alpha_0 = -11448.0, \quad L^\alpha_1 = -11694.0, \\ &L^L_0 = -10487.0, \quad L^L_1 = -18198.0, \quad L^L_2 = 10528.4 \end{aligned}$$

The free energy densities per unit molar volume of individual phases can be obtained from the CALPHAD method [124] as shown in Eqs. (7.10)-(7.12) with molar volume [$v_m = 16.29$ (cm^3/mole)]. The equilibrium phase compositions can be used

Table II. Material parameter values for use in simulating the growth of IMC layer during lead-free soldering

$D_L = 2.0 \times 10^{-12}(m^2/s)$,	$D_\eta = 2.0 \times 10^{-5} D_L(m^2/s)$
$D_\alpha = 1.0 \times 10^{-6} D_L(m^2/s)$,	$D_{\eta L} = 2.0 \times 10^{-1} D_L(m^2/s)$
$D_{\eta\alpha} = 2.0 \times 10^{-3} D_L(m^2/s)$,	$D_{GB} = 2.0 \times 10^{-3} D_L(m^2/s)$
$\sigma_{\eta L} = 0.1(\mathrm{J}/m^2)$,	$\sigma_{\eta\alpha} = \sigma_{GB} = 0.3(\mathrm{J}/m^2)$
$M_{\phi,\eta L} = 1.0 \times 10^6 D_L(m^2/s)$,	$M_{\phi,\eta\alpha} = M_{\phi,GB} = 7.0 \times 10^4 D_L(m^2/s)$
$M_\Theta = 1.0 \times 10^{-6} M_{\phi,\eta L}$	

as $c_L^{\alpha L} = 0.977$ and $c_\alpha^{\alpha L} = 0.1957$ and the equilibrium composition of η phase can be calculated by using free energy equations as shown in the previous section ($c_\eta = 0.435$) where $c_\alpha^{\alpha L}$ is the equilibrium composition of the α phase at the $\alpha - L$ interface and the other terms are defined correspondingly. The initial compositions of the Cu-substrate and liquid solder are set to be $c_\alpha = 0.002$ and $c_L = c_L^{\alpha L}$.

Critical parameters for the simulation, such as interfacial energies and mobilities are notoriously hard to obtain from experimental results. They are thus used as simulation parameters which are carried by theoretical approaches from experimental data [41, 43, 128, 129]. The diffusivities and other material parameters employed in the numerical calculation are summarized in Table II.

E. Results and Discussions

It is difficult to determination of material parameters used in the simulation because material properties of single phases, for example, the material parameters of α, η and L in this study are dependent on theoretical approach based on experimental data, and gradient coefficient of misorientation a_1 is not well established yet. But the

material parameters except a_1 are obtainable [41, 43, 127, 128, 129] while a_1 can be predictable, and can be related to interface energies [8, 144].

In a region of phases mixture, for example interface regions, it is even more difficult to determine the material properties for the simulation (e.g. $\sigma_{\eta L}$ and D_{GB}). So, the simulation in this study will follow the morphology of IMC grain growth that will be affected by the different material properties, such as changing diffusion coefficient of grain boundary, changing interfacial energy between η-IMC layer and liquid solder and changing gradient coefficient of misorientation.

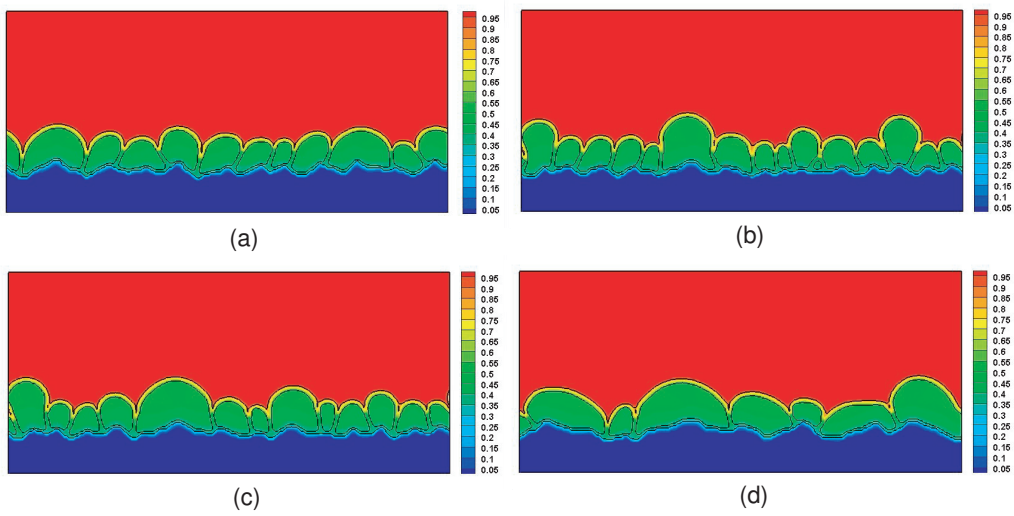

Fig. 67. Microstructure evolution of the intermetallic compound layer for the case of (a) a_1=0.0, (b) a_1=0.001, (c) a_1=0.01 and (d) a_1=0.1 at t = 28(sec). The other material parameters are referred from Table II.

In order to examine how the kinetics of the η-IMC growth is affected by a_1, simulations are carried out with four different a_1 are used as a_1 = 0.0, a_1 = 0.001, a_1 = 0.01 and a_1 = 0.1.For all four cases, the other material properties are used shown in Table II.

Fig. 67 shows intermetallic compound growth for the case with different a_1 at

$t = 28$(sec). Fig. 67(a) shows the intermetallic compound grain growth that was, in a previous chapter, explained as followings. As the intermetallic compound grain grows thicker with time, there is a concurrent coarsening of the η grains, resulting in fewer grains remained in the intermetallic compound layer. The liquid solder seems not to wet the grain boundaries entirely through the layer, since the driving force for the η phase formation from the diffusion fluxes through the grain boundary is large enough to overcome the difference between σ_{GB} and $\sigma_{\eta L}$. However, once the effect of misorientation is included like Figs. 67(b)-(d), the intermetallic compound growth appears to be different.

a_1 is associated with the degree of orientation transformation. Supposes that there are two phases that has different orientations. Competition of phases occurs at a phase boundary, and the phase boundary moves, which are affected by the difference of local free energy density of each phases and the the misorientation of two phases. Once phase transformation associated with a local misorientation eventually occurs, and a point of abutting orientation is transformed into the other orientation, which requires energetic cost [7, 22]. Therefore, the existence of misorientation in the multi-phase field changes the mobility of phase transformation.

For the misorientation, it is a general note that large misorientation causes the increase of grain boundary energy [8, 7]. The increase of grain boundary energy indicated that the solid/liquid interface energy is relatively smaller than grain boundary energy, so that small competition of grains occurs. Thus, coarsening rate of the grains is reduced and the thickness of intermetallic compound increases compared with the case ($a_1 = 0.0$). As a_1 increases we can find that grain coarsening is accelerated. As we mentioned above, a_1 is the degree of the orientation transformation in a given misorientation. Thus, large a_1 accelerates the grain coarsening, and due to the grain coarsening, more grain boundaries are eliminated compared with the case

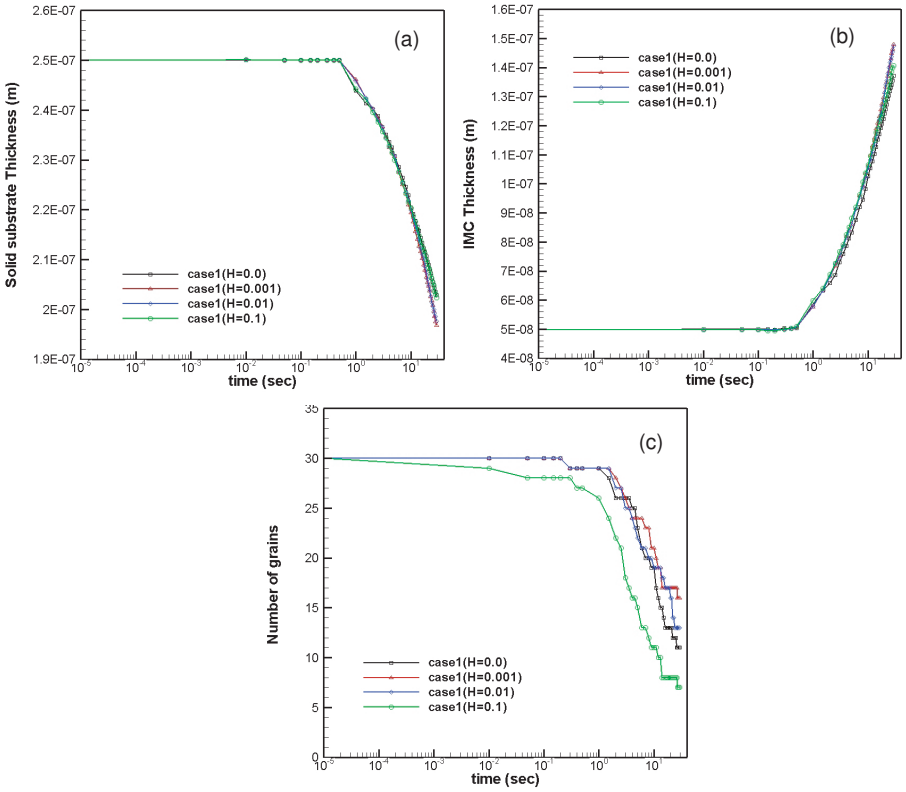

Fig. 68. Evolution of (a) solid substrate thickness, (b) η-IMC layer thickness and (c) number of grains with respect to time corresponding the different a_1=(0.0, 0.001, 0.01 and 0.1). Profiles correspond Fig. 67.

($a_1 = 0.001$). The existence of less grain boundaries prohibits the IMC growth of the lack of Cu supply [28]. This morphological behaviors of the IMC growth can be evaluated by Fig. 68. It seems to be conflict because the increase of the grain boundary energy retards the grain coarsening and increase the thickness of IMC thickness, but the increase of a_1 causes increase of the wetting effects. We expect that grain boundary energy would be rather dominated in the phase transformation comparing with the wetting effect because of the small value of $a_1 = 0.001$. It is interesting to note that $\eta - L$ and $\alpha - \eta$ interfaces have opposite signs of curvature resulting in the scollop shape for η grains with the inclusion of misorientation effect, which is experimentally observed [151].

As we mentioned above, a_1 should be likely chosen with similar values of solid/liquid interface energy; that is $a_1 = 0.1$ IMC growth by the variation of D_{GB} is good to investigate morphological change of IMC. We select a high D_{GB} as $D_{GB} = 2.0 \times 10^{-3} D_L$ (Fig. 69(a)) and a low D_{GB} as $D_{GB} = 2.0 \times 10^{-5} D_L$ (Fig. 69(b)) with $t = 0.4, 8, 15$ and 26(sec).

As intermetallic compound layer grows thicker with time, there is a fast coarsening of the η grains in both cases, resulting in fewer grains remained in the intermetallic compound layer. Both cases are applied the effect of the misorientation. Essentially, the system tends to decrease its energy predominantly by reducing the grain boundary area [28], which expect that the fast coarsening of Fig. 69(b) would be accelerated due to the inclusion of misorientation effect. However, Fig. 69(b) reveals less coarsening resulting in more eliminated grains. We expect that the phenomenon is caused by low D_{GB}. Low D_{GB} leads to less survived grains, and less flux of composition through the grain boundaries decreases the effect of misorientation. Contrary to the number of grains, solid substrate and IMC thicknesses of Fig. 69(a) compared with Fig. 69(b) appears normally increased due to the D_{GB} that supply more flux of compositions

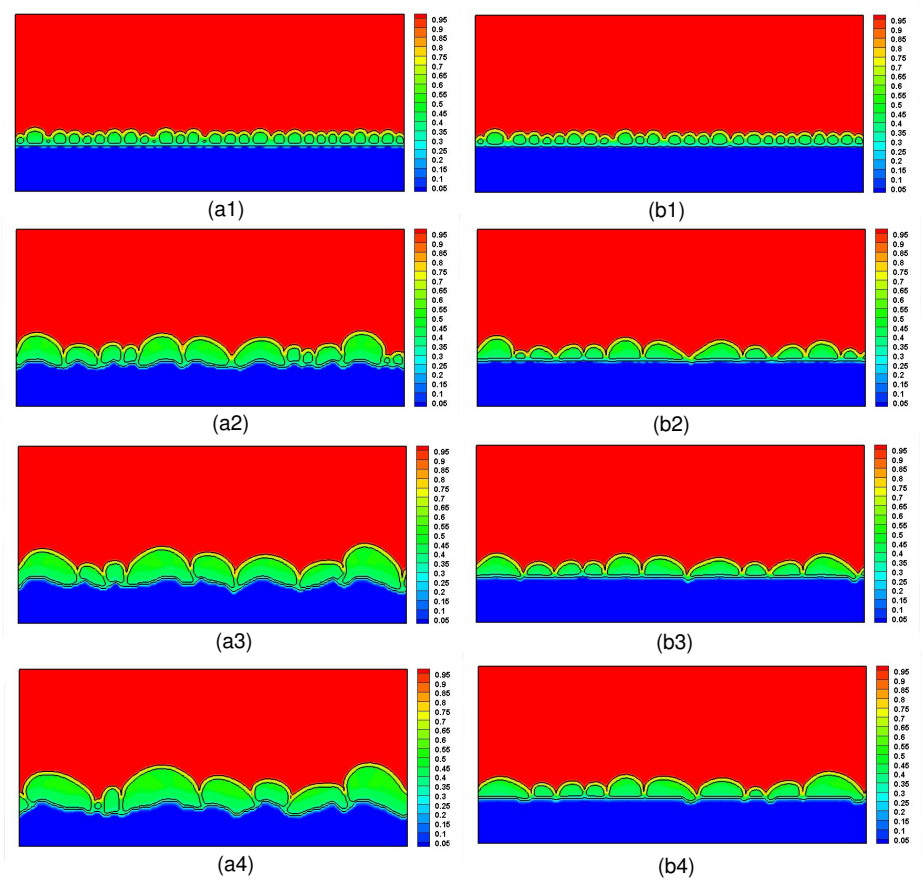

Fig. 69. Microstructure evolution of the intermetallic compound layer for the case of (a) high D_{GB} ($D_{GB} = 4.0 \times 10^{-15}$) and (b) low D_{GB} ($D_{GB} = 4.0 \times 10^{-17}$) at $t = 28$(sec) with $t = 0.4, 8, 15$ and 26(sec). a_1=0.1. The other material parameters are referred from Table II.

[see in Fig. 71].

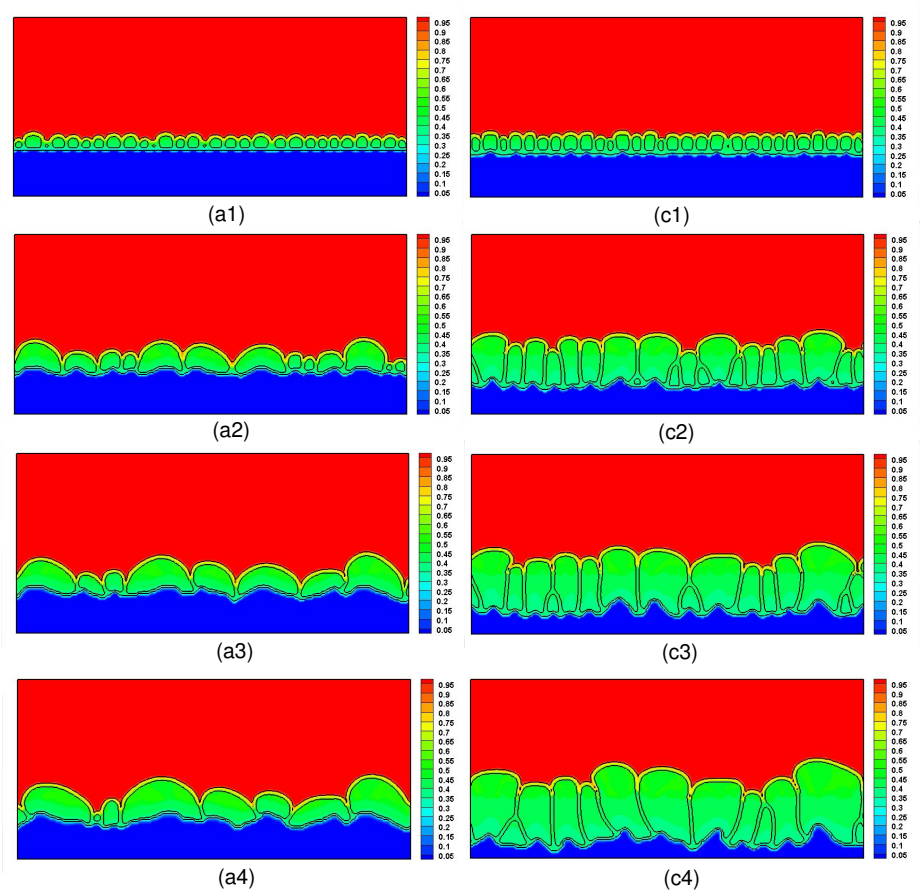

Fig. 70. Microstructure evolution of the intermetallic compound layer for the case of (a) high $\eta - L$ interfacial energy ($\sigma_{\eta L} = 0.1(\mathrm{J}/m^2)$) and low $\eta - L$ interfacial energy ($\sigma_{\eta L} = 0.05(\mathrm{J}/m^2)$) at with $t = 0.4, 8, 15$ and $26(\mathrm{sec})$. $a_1 = 0.1$. The other material parameters are referred from Table II.

Although high D_{GB} is employed in η phase in Fig. 70, there is a different tendency for competitive grain growth at the $\eta - L$ interface compared to the cases shown in Fig. 70(a) because of the lower value of $\sigma_{\eta L}$. The coarsening rate is related to the D_{GB} and difference between $\sigma_{\eta L}$ and σ_{GB} [28].

Without the effect of misorientation, high D_{GB} causes grain growth, but higher

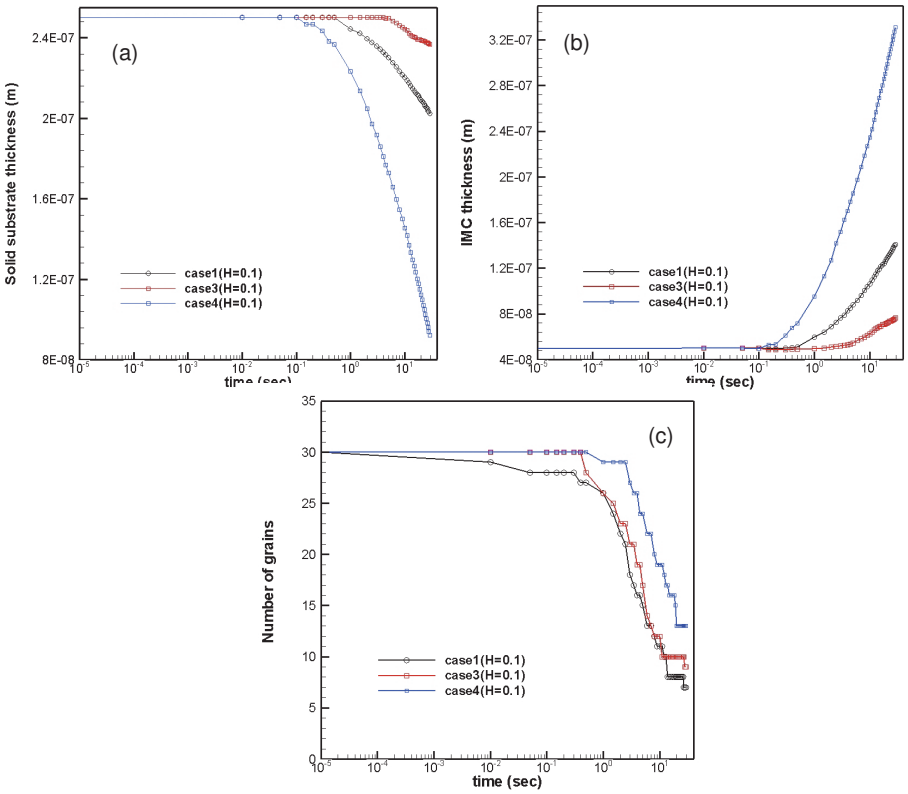

Fig. 71. Evolution of (a) solid substrate thickness, (b) η-IMC layer thickness and (c) number of grains with respect to time corresponding case 1, case 3 and case 4 a_1=0.1. The case 1, 3 and 4 corresponds Figs. 69(a), (b) and Fig. 70(c).

difference of two interfacial energies leads to grain boundary wetting, which essentially acts to limit horizontal coarsening of the grains. Thus, the grains grow upward with less coarsening with neighboring grains in η-IMC layer, which is faster than the other case as shown in Fig. 40. Less coarsening with neighboring grains similarly happens in both cases of Fig. 40 and Fig. 70(a). So, the solid substrate thickness decreases and IMC thicknesses increase. However, due to the effect of misorientation grain coarsening occurs. Therefore, contrary to the solid substrate and IMC thicknesses, number of survived grains during lead-free soldering become less than the case in Fig. 43. Evolution of solid substrate thickness, IMC layer thickness and number of survived grains with respect to time are provided Fig. 71.

F. Conclusions

A multi-phase field model including crystallographic orientation [8] was used in order to the evolution of η phase along a Cu/Sn interface. Different coefficient of grain boundaries, solid/liquid interface energies and gradient coefficients of misorientation were varied to understand the characteristics of each parameter on the behavior of IMC layer. With the results, we addressed the characteristics of each parameter from the simulations, and we will expect that the investigation of microstructural evolution affected by crystallographic orientation during the lead-free soldering will hopefully provide one with the nature of IMC layer growth and possibility of better control of the soldering reactions.

The simulations were performed by using two different grain boundary diffusion coefficients and two different $\eta - L$ interface energies causing the concurrent coarsening of the IMC grains along with the IMC layer growth. From the results, one can find useful results from the simulations corresponding to the change of material

parameter. However, several conclusions can be narrowed down compared with the previous research [8, 28] as follows: (1) grain boundary energy would be rather dominated in the phase transformation comparing with the wetting effect if a_1 is small enough. (2) As gradient coefficient of misorientation increases, grain coarsening is accelerated resulting that number of grains was changed but the solid substrate and IMC thicknesses was barely changed but small increase of IMC thickness is observed [Fig. 68]. (3) The effect of misorientation is more dominated when the high diffusion coefficient of grain boundary is applied. (4) If solid/liquid interface energy would be small, the effect of misorientation becomes less [see Fig. 71].

The inclusion of a physical characteristics of microstructure provides one with complexity with respect to computational and experimental works. Especially, the computational works appear more difficulty because of verification and acquisition of series of model parameters, for example diffusion coefficient, interface energy and gradient coefficient of misorientation, from experimental investigation. However, it is realized in this study that a multi-phase field simulation is applicable with respect to additional features, such as crystallographic orientation. Moreover, it is now possible to qualitatively reproduce many previous experimental researches about nucleation behaviors at early stages, lateral growth of IMC grains prior to coarsening as well as the evolution of a scallop-like morphology of the IMC layer once complete coverage of the substrate/liquid interface is achieved.

CHAPTER VIII

SUMMARY

The objective of this work is to investigate solidification phenomena of solid-liquid interactions, such as dendritic growth in pure and binary materials, eutectic solidification in a binary alloy and intermetallic compounds growth during soldering reaction in electronic material by using phase field models. After reviews of phase field models, free energy density theory, thermodynamic potential and theory of crystallographic orientation, I presented several simulation results of solidification comparing with experimental results showing the details of my works.

At first I presented a single phase field model developed by [5] adopting chemical potential equilibrium at interface region. His model appears to be equivalent to the model [3] introduced in the several years ago, but this approach adopts a different definition of the free energy density and assumption in interface region compared with the previous model [3] that has extra potential originated from the free energy density definition, but this approach makes the extra potential disappear by using the chemical potential equilibrium in the interface region. With the model [5] I simulated phase transition for isothermal solidification in binary alloys in 1D and introduced an anisotropic phase field model to simulate dendrite solidification in 2D.

Secondly, I introduced a multi-phase field model developed by [6, 20] for solidification modeling by using phase field approaches. Coexisting phases are postulated as pairwise energy difference between the coexisting phases under the guarantee of the minimum of free energy. The multiphase field equation was reformed by summing contributions of each existing phase field at the interface. With the multi-phase field model I simulated eutectic solidification problems based on the experimental results [37], and addressed good agreements with them. For the extension of the eutectic so-

lidification, I simulated eutectic solidification of binary alloy containing encapsulated impurities with/without the effect of conductivity resulting in morphological changes of lamellae, which expects better characteristics of microstructure with respect to desired performances.

I also presented the possibilities of the multi-phase field model in use of intermetallic compound formation and growth during soldering reactions in electronic materials. I simulated the morphological evolution and growth of the IMC (Cu_6Sn_5 only or Cu_6Sn_5 and Cu_3Sn) layers during lead-free soldering with Sn-Cu solder alloys on a Cu substrate. The multi-phase field simulations were performed by using three different grain boundary diffusion coefficients in η-IMC layer, three different interfacial energies of $\eta - L$ interface causing the concurrent coarsening of the IMC grains along with the IMC layer growth, and three different initial liquid solder compositions inducing dissolution of Cu from the substrate and IMCs, and the results were compared with previous works [28, 125]. Three controllable parameters (grain boundary diffusion, $\eta - L$ interfacial energy and initial liquid solder) delivered that (1) High grain boundary diffusion leads to increase of η-IMC layer thickness and decrease of ε-IMC layer thickness. (2) High $\eta - L$ interfacial energy leads to decrease of grain boundary wetting effect resulting in increase of grain coarsening. (3) As a net result of the concurrent dissolution and growth of the η-IMC layers in the case of poor Sn liquid solder, the η-IMC layer thickness decreases at the early stages of soldering. (iv) ε-IMC is affected by the behavior of η-IMC layer and Sn flux from liquid solder.

For the extension of the multi-phase field modeling in lead-free soldering system, I adopted nucleation phenomenon in an early stage in Cu-Sn soldering. For the theory of the nucleation, I supplemented Poisson distribution function for the explanation of nucleation of intermetallic compound gains during lead-free soldering, and compared my current results and experimental results [**?**, 45, 97]. I found out that Cu_6Sn_5 easily

formed at the edge of the grain occurs faster than at the top of the grains due to high diffusion coefficient of liquid solder until η grains impinges and the behavior of the IMC grains (or layer) applied with different material parameters (e.g. grain boundary diffusion coefficient and a $\eta - L$ interface energy) at the late stages eventually appears similar to the research [28] although the formation and growth of the IMC grains observed explicitly different from the research [28] in the early stages.

Finally, I included crystallographic orientation effect [8] in the multi-phase field model in order to investigate the evolution of intermetallic compound phase along a Cu/Sn interface. Different diffusion coefficients of grain boundaries, solid/liquid interface energies and gradient coefficients of misorientation, provided one with understanding of the characteristics of each parameters according to the behavior of IMC layer. With the results, I addressed the characteristics of each parameter from the simulations, which expects that the investigation of microstructural evolution affected by crystallographic misorientation during the lead-free soldering will hopefully give one the nature of IMC layer growth and possibility of better control of the soldering reactions.

The inclusion of a physical characteristics of microstructure provides complexity of computational and experimental works. Especially, the computational works appear more difficult to establish because constitutive equations obtained from mathematical methods is required to be good for experimental investigations. Although the constitutive equations are approximated, it is realized in this study that phase field models and their supplemental model parameters are applicable with respect to advanced solidification problems, and it is now possible to qualitatively reproduce many previous experimental researches. This steps in my study look tiny, but significant steps in both the advancement of phase field modeling of microstructure and the development of the next generation in material sciences are surly prospective.

REFERENCES

[1] G. Caginalp and X. Chen, "Phase field equations in the singular limit of sharp interface problems," *On the Evolution of Phase Boundaries*, vol. 43, pp. 1, 1992.

[2] J. W. Cahn and J. E. Hilliard, "Free energy of a nonuniform system. 1. interfacial free energy," *J.Chem. Phys.*, vol. 28, pp. 258–267, 1958.

[3] A. A. Wheeler, W.J. Boettinger, and G. B. McFadden, "Phase-field model for isothermal phase transition in binary alloys," *Phys. Rev. A*, vol. 45, pp. 7424–7439, 1992.

[4] A. Karma , "Phase-field model of eutectic growth," *Phys. Rev. E*, vol. 49, pp. 2245-2250, 1994.

[5] S. G. Kim, W. T. Kim, and T. Suzuki, "Phase-field model for binary alloys," *Phys. Rev. E*, vol. 60, pp. 7186–7197, 1999.

[6] I. Steinbach and F. Pezzolla, "A generalized field method for multiphase transformations using interface fields," *Physica D*, vol. 134, pp. 385–393, 1999.

[7] R. Kobayashi, J. A. Warren, and C. Carter, "A continuum model of grain boundaries," *Physica D*, vol. 140, pp. 141–150, 2000.

[8] J. A. Warren, R. Kobayashi, A. E. Lobkovsky, and W. G. Carter, "Extending phase field models of solidification to polycrystalline materials," *Acta Mater.*, vol. 51, pp. 6035–6053, 2003.

[9] R. Kobayashi, "A numericla approach to three-diemntional dendrite solidification," *Exp. Math.*, vol. 3, pp. 59–81, 1994.

[10] A. A. Wheeler, W.J. Boettinger, and G. B. McFadden, "Computation of dendrites using a phase field model," *Physica D*, vol. 66, pp. 243–262, 1993.

[11] S. L. Wang and R. F. Sekerka, "Computation of the dendritic operating state at large supercoolings by the phase field model," *Phys. Rev. E*, vol. 53, pp. 3760–3776, 1996.

[12] J. A. Warren and W. J. Boettinger, "Prediction of dendritic growth and microsegration patterns in a binary alloy using the phase-filed model," *Acta Metall. Mater.*, vol. 43, pp. 689–703, 1995.

[13] W. T. Kim, S. G. Kim, J. S. Lee and T. Suzuki, "Equilibrium at stationary solid-liquid interface during phase-field modeling of alloy solidification," *Metall. Mater. Trans. A*, vol. 32, pp. 961–969, 2001.

[14] I. Steinbach, F. Pezzolla , B. Nestler, M. Sesselberg, R. Prieler, G. J. Schmitz, and J. L. L. Rezende, "A phase field concept for multiphase systems," *Physica D*, vol. 94, pp. 135–147, 1996.

[15] B. Nestler and A. A. Wheeler, "A multi-phase-field model of eutectic and peritectic alloys: numerical simulation of growth structures," *Physica D*, vol. 138, pp. 114–133, 2000.

[16] J. Tiaden, "Phase field simulations of the peritectic solidification of Fe-C," *J. Cryst. Growth*, vol. 199, pp. 1275–1280, 1999.

[17] G. Caginalp and W. Xie, "Phase-field and sharp-interface alloy models," *Phys. Rev. E.*, vol. 48, pp. 1897–1909, 1993.

[18] A. Karma, "Phase-field method for computationally efficient modeling of solidification with arbitrary interface kinetics," *Phys. Rev. E*, vol. 53, pp. 3017–3020,

1996.

[19] J. S. Langer, "Models of pattern formation in first-order phase transitions" *Directions in Condensed Matter Physics*. World Scientific Pub. Co. Inc., New York, 1986, pp. 165–186.

[20] J. Tiaden, B. Nestler, H. J. Diepers, and I. Steinbach, "The multiphase-field model with an integrated concept for modelling solute diffusion," *Physica D*, vol. 115, pp. 73–86, 1998.

[21] R. Kobayashi, J. A. Warren, and W. C. Carter, "Vector-valued phase field model for crystallization and grain boundary formation," *Physica D*, vol. 119, pp. 415–423, 1998.

[22] M. T. Lusk, "A phase-field paradigm for grain growth and recrystallization," *Proc R Soc Lond A*, vol. 455, pp. 677–700, 1999.

[23] A. Lobkovsky and J. A. Warren, "Sharp interface limit of a phase field model of crystal grains," *Phy. Rev. E*, vol. 63, pp. 051605–051614, 2001.

[24] J. B. Collins and H. Levine, "Diffuse interface model of diffusion-limited crystal-growth," *Phys. Rev. B*, vol. 31, pp. 6119–6122, 1985.

[25] G. B. McFadden, A. A. Wheeler, R. J. Braun, S. R. Coriell, and R. F. Sekerka, "Phase-field models for anisotropic interfaces" *Phys. Rev. E*, vol. 48, pp. 2016–2024, 1993.

[26] T. Suzuki, M. Ode, S. G. Kim, and W. T. Kim, "Phase-field model of dendrite growth," *J. Crystal Growth*, vol. 237, pp. 125–131, 2002.

[27] S. G. Kim , W. T. Kim, T. Suzuki, and M. Ode, "Phase-field modeling of eutectic solidification," *J. Crystal Growth* vol. 261, pp. 135–158, 2004.

[28] J. Y. Huh, K. K. Hong, Y. B. Kim, and K. T. Kim, "Phase field simulations of intermetallic compound growth during soldering reactions," *J. Electron. Mater.*, vol. 33, pp. 1161–1170, 2004.

[29] K. K. Hong and J. Y. Huh, "Phase field simulations of morphological evolution and growth kinetics of solder reaction products," *J. Electron. Mater.*, vol. 35, pp. 56–64, 2006.

[30] M. Abtew and G. Selvaduray, "Lead-free solder in microelectronics," *Mater. Sci. Eng. R*, vol. 27, pp. 95–141, 2000.

[31] K. N. Tu and K. Zeng, "Tin-lead (SnPb) solder reaction in flip chip technology," *Mater. Sci. Eng. R*, vol. 27, pp. 1–58, 2001.

[32] T. Laurila, V. Vuorinen, and J. K. kivilahti, "Interfacial reactions between lead-free solders and common base materials," *Mater. Sci. Eng. R*, vol. 49, pp. 1–60, 2005.

[33] J. P. Simmon, C. Shen, and Y. Wang, "Phase field modeling of simultaneous nucleation and growth by explicitly incorporating nucleation events," *Scripta Mater.*, vol. 43, pp. 935–942, 2000.

[34] J. P. Simmon, Y. Wen, C. Shen, and Y. Z. Wang, "Microstructural development involving nucleation and growth phenomena simulated with the phase field method," *Mater. Sci. Eng. A*, vol. 365, pp. 136–143, 2004.

[35] B. Li, H. D. Brody and A. Kazimirov, "Real time Synchrotron microradiography of dendrite coarsening in Sn-13 Wt Pct Bi alloy" *Metall. Mater. Trans. A*, vol. 38, pp. 599-605, 2007.

[36] J. Warren, T. Pusztai, L Környei, and L. Gránásy, "Phase field approach to heterogeneous crystal nucleation in alloys," *Phy. Rev. B*, vol. 79, 014204, 2009.

[37] J. Mergy, G. Faivre, C. Guthmann, and R. Mellet, "Quantitative determination of the physical parameters relevant to the thin-film directional solidification of the CBr_4-C_2Cl_6 eutectic alloy," *J. Crystal Growth*, vol. 133, pp. 353–368, 1993.

[38] M. Ginibre, S. Akamatsu, and G. Faivre, "Experimental determination of the stability diagram of a lamellar eutectic growth front," *Phys. Rev. E*, vol. 56, pp. 780–796, 1997.

[39] M. Zanotello, M. C. C. Cunha, and R. Caram, "Evaluation of lamellar spacing selection in eutectic alloys using phase field model," *Comput. Mater. Sci.*, vol. 44, pp. 695–701, 2008.

[40] P. L. Tu, Y. C. Chan, K. C. Hung, and J. K. L. Lai, "Growth kinetics of intermetallic compounds in chip scale package solder joint," *Scripta Mater.*, vol. 44, pp. 317–323, 2001.

[41] W. K. Choi and H. M. Lee, "Effect of soldering and aging time on interfacial microstructure and growth of intermetallic compounds between Sn-3.5Ag solder alloy and Cu substrate," *J. Electron. Mater.*, vol. 29, pp. 1207–1213, 2000.

[42] H. K. Kim, H. K. Liou, and K. N. Tu, "Three-dimensional morphology of a very rough interface formed in the soldering reaction between eutectic SnPb and Cu," *Appl. Phys. Lett.*, vol. 66, pp. 2337–2339, 1995.

[43] H. K. Kim and K. N. Tu, "Kinetic analysis of the soldering reaction between eutectic SnPb alloy and Cu accompanied by ripening," *Phys. Rev. B*, vol. 53, pp. 16027–16304, 1996.

[44] M. Schaefer, R. A. Fournelle, and J. Liang, "Theory for intermetallic phase growth between Cu and liquid Sn-Pb solder based on grain boundary diffusion control," *J. Electron. Mater.*, vol. 27, pp. 1167–1176, 1998.

[45] J. Gorlich and G. Schmitza, "On the mechanism of the binary Cu/Sn solder reaction," *Appl. Phys. Lett.*, vol. 86 pp. 053106, 2005.

[46] K. S. Kim, S. H. Huh, and K. Suganuma, "Effects of intermetallic compounds on properties of Sn.Ag.Cu lead-free soldered joints," *J. Alloys Compounds*, vol. 352, pp. 226–236, 2003.

[47] Z. Bi and R. Sekerka, "Phase-field model of solidification of a binary alloy," *Physica A*, vol. 261 pp. 95–106, 1998.

[48] G. J. Fix, *Free Boundary Problems: Theory and Applications*. Chapman & Hall/CRC. New York, 1983.

[49] M. C. Flemmings, *Solidification Processing*, New York, McGraw-Hill, 1974.

[50] R. W Balluffi, S.M. Allen, and W. C. Carter *Kinetics of Materials*, New York, John Wiley & Sons Inc, 2005.

[51] G. Caginalp, "Stefac and Hele-shew models as asymptotic limits of the phaee field equations," *Phy. Rev. A*, vol. 39, pp. 5887–7896, 1989.

[52] S. -L. Wang, R. F. Sekerka, A. A. Wheeler, B. T. Murray, S. R. Coriell, R. J. Braun, and G. B. McFadden, "Thermodynamically-consistent phase-field models for solidification," *Physica D*, vol. 69, pp. 189–200, 1993.

[53] A. Ekhlakov, S. Dimitrov, T.-A. Langhoff, and E. Schnack "Phase-field model for deposition of pyrolytic carbon," *Comm. in Num. Methods in Eng.*, vol. 24, pp. 2139, 2008.

[54] M. Ohno and K. Matsuura, "Quantitative phase-field modeling for dilute alloy solidification involving diffusion in the solid," *Phy. Rev. E*, vol. 79, pp. 031603, 2009.

[55] P. R. Cha, D. H. Yeon, and K. K. Yoon, "A phase field model for isothermal solidification of multicomponent alloys," *Acta Mater.*, vol. 49, pp. 3295–3307, 2001.

[56] J. Li, J. Wang and G. Yang, "Phase-field simulation of microstructure development involving nucleation and crystallographic orientations in alloy solidification," *J. Ctystal Growth*, vol. 309, pp. 65–69, 2007.

[57] N. Moelans, B. Blanpain, and P. Wollants "Quantitative analysis of grain boundary properties in a generalized phase field model for grain growth in anisotropic systems," *Phy. Rev. B*, vol. 78, pp. 024113, 2008.

[58] M. S. Park and R. Arroayve, "Multiphase field simulations of intermetallic compound growth during lead-free soldering," *J. Electron. Mater.*, DOI. 10.1007/s11664-009-0849-5, 2009.

[59] P. R. Harrowell and D. W. Oxtoby, "On the interaction between order and a moving interface-dynamic disordering and anisotropic growth-rate," *J. Chem. Phys.*, vol. 86, pp. 2932–2942, 1987.

[60] L. Q. Chen and Y. Z. Wang, "Computer-simulation of the domain dynamics of a quenched system with a large number of nonconserved order parameters: The grain growth kinetics," *Phys. Rev. B*, vol. 50, pp. 15752–15756, 1994.

[61] A. Karma, D. A. Kessler, and H. Levine, "Phase-field model of mode III dynamic fracture," *Phys. Rev. Lett.*, vol. 87, pp. 045501, 2001.

[62] M. Plapp. and A. Karma, "Eutectic colony formation: A stability analysis," *Phys. Rev. E*, vol. 60, pp. 6865–6889, 1999.

[63] C. Beckermann, H. J. Diepers, I. Steinbach, A. Karma, and X. Tong, "Modeling melt convection in phase-field simulations of solidification," *J. Comp. Phys.*, vol. 154, pp. 468–496, 1999.

[64] R. Tonhardt and G. Amberg, "Simulation of natural convection effects on succinonitrile crystals," *Phy. Rev. E*, vol. 62, pp. 828–836, 2000.

[65] J. Jeong, N. Goldenfeld, and J. A. Dantzig, "Phase field model for three-dimensional dendritic growth with fluid flow," *Phy. Rev. E*, vol. 64, pp. 041602, 2000.

[66] B. Nestler, H. Garcke, and B. Stinner, "Multicomponent alloy solidification: Phase-field modeling and simulations," *Phy. Rev. E*, vol. 71, pp. 041609, 2005.

[67] I. Steinbach, "Phase-field models in materials science," *Modelling Simul. Mater. Sci. Eng.*, vol. 17, pp. 073001, 2009.

[68] S. G. Kim, "A phase-field model with antitrapping current for multicomponent alloys with arbitrary thermodynamic properties," *Acta Mater.*, vol. 55, pp. 4391–4399, 2007.

[69] A. A. Wheeler, W.J. Boettinger, and G. B. McFadden, "Phase-field model of solute trapping during solidification," *Phys. Rev. E*, vol. 47, pp. 1893–1909, 1993.

[70] T. Suzuki, M. Ode, S. G. Kim, and W. T. Kim, "Phase-field model of dendritic growth," *J. Crystal Growth*, vol. 237-239, pp. 125–131, 2002.

[71] R. Kobayashi, "Modeling and numerical simulations of dendrite crystal growth," *Physica D*, vol. 63, pp. 410-423, 1993.

[72] W. L. George and J. A. Warren, "A parallel 3D dendritic growth simulator using the phase-field method," *J. Comp. Phys.*, vol. 177, pp. 264–283, 2002.

[73] S. G. Kim and W. T. Kim, "Phase-field modeling of rapid solidification," *Mater. Sci. Eng. A*, vol. 304, pp. 281–286, 2001.

[74] D. Lewis, J. Warren, W. Boettinger, T. Pusztai, and L. Granasy, "Phase-field models for eutectic solidification," *JOM*, vol. 56, pp. 34–39, 2004.

[75] A. Parisi and M. Plapp, "Stability of lamellar eutectic growth," *Acta Mater.*, vol. 56, pp. 1348–1357, 2008.

[76] S. Akamatsu , G. Faivre, M. Plapp, and A. Karma, "Overstability of lamellar eutectic growth below the minimum-undercooling spacing," *Met. Mater. Trans. A*, vol. 35, pp. 1815–1828, 2004.

[77] T. Borzsonyi, T. Toth-Katona, A. Buka, and L. Granasy, "Regular dendritic patterns induced by nonlocal time-periodic forcing," *Phy. Rev. E*, vol. 62, pp. 7817–7827, 2000.

[78] D. C. Lin, S. Liu, T. M. Guo, G.-X. Wang, T. S. Srivatsan, and M. Petraroli, "An investigation of nanoparticles addition on solidification kinetics and microstructure development of tin/lead solder," *Mater. Sci. Eng. A*, vol. 360, pp. 285–292, 2003.

[79] E. P. Wood and K. L. Nimmo, "In search of new lead-free electronic solders," *J. Electron. Mater.*, vol. 23, pp. 709–713, 1994.

[80] E. R. Monsalve, "Lead ingestion hazard in hand soldering environments," *Proceedings of the 8th Annual Soldering Technology and Product Assurance Seminar*, Naval Weapons Center, China Lake, CA., February 1984.

[81] D. Napp, "Lead-free interconnect materials for the electronics industry," in *Proceedings of the 27th International SAMPE Technical Conference*, Austin TX. USA, October 1995, pp. 338–244.

[82] B. R. Allenby, J. P. Ciccarclli, I. Artaki, R. J. Fisher, D. Schoenthaler, *et al.* "An assessment of the use of lead in electronics assembly," *Circuit World*, vol. 19(2), pp. 1–28, 1993.

[83] J. O. Nriagu and J. M. Pacyna, "Quantitative assessment of worldwide contamination of air, water and soils by trace metals," *Nature* vol. 333(6169), pp. 134–139, 1988.

[84] Environmental Protection Agency, National Air Quality and Emission Trend Report, 1989, EPA-450/4-91-003,Research Triangle Park, NC, 1991.

[85] NCMS Lead-free solder project finial report, NCMS, National Center for Manufacturing Science, 3025 Boardwalk, Ann Arbor, Michigan 48108-3266, Report 0401RE96. 1999.

[86] J. Glazer, "Metallurgy of low temperature Pb-free solders for electronic assembly," *Int. Mater. Rev.* vol. 40(2), pp. 67-93, 1995.

[87] C. Lea, "A Scientific Guide to Surface Mount Technology", Electrochemical Publications Ltd. GB-Port Erin, British Isles, pp. 378–379, 1988.

[88] ASM International, Electronic Material Handbook, Vol. 1, CRC, Materials Park, OH, pp. 1161–1162, 1989.

[89] J. W. Morris, J.L.F. Goldstein Jr., and Z. Mei, "Microstructure and mechanical properties of Sn-In and Sn-Bi solders," *J. Electron. Mater.*, vol. 45, pp. 25–28, 1993.

[90] R. W. Wild, "Properties of some low melting fusible alloys," New York, Technical Report, IBM Federal Systems Division Laboratory, 1971.

[91] M. Hansen and K. Anderko, *Constitution of Binary Alloys*, New York, McGraw-Hill, pp. 1218, 1958.

[92] M. McCormack, S. Jin, and G. W. Kammlott, "The design of new Pb-free solder alloys with improved properties," *IEEE* 0-7803-2137-5/95, 1995.

[93] K. N. Tu, "Interdiffusion and reaction in bimetallic Cu-Sn thin films," *Mat. Chem. and Physics*, vol. 46, pp. 217–223, 1996.

[94] P. J. Kay and C. A. Mackay, "The growth of intermetallic compounds on common base materials coated with tin and tin-lead alloys," *Trans. Instit. Metal Finish.*, vol. 54, pp. 68–74, 1976.

[95] D. S. Dunn, T. F. Marinis, W. M. Sherry and C. J. Williams, "Dependence of Cu/Sn and Cu/Sn/Pb solder joint strength on diffusion controlled growth of Cu3Sn and Cu6Sn5," *Mater. Res. Soc. Symp. Proc.*, vol. 40, pp. 129–138, 1985.

[96] H. K. Kim and K. N. Tu, "Rate of consumption of Cu in soldering accompanied by ripening," *Appl. Phys. Lett.*, vol. 67, pp. 2002–2004, 1995.

[97] R. A. Gagliano, G. Ghosh, and M. E. Find, "Nucleation kinetics of Cu6Sn5 by reaction of molten tin with a copper substrate," *J. Electron. Mater.*, vol. 31, pp. 1195–1202, 2002.

[98] R. A. Lord and A. Umantsev, "Early stages of soldering reactions," *J. App. Phys.*, vol. 98, pp. 063525, 2005.

[99] W. J. Boettinger and J. A. Warren, "The phase-field method: simulation of alloy dendritic solidification during recalescence," *Met. Trans. A*, vol. 27A, pp. 657–669, 1996.

[100] M. Ode, J. S. Lee, S. G. Kim, W. T. Kim, and T. Suzuki, "Phase-field model for solidification of ternary alloys," *ISIJ Int.*, vol. 40, pp. 870–876, 2000.

[101] M. Kahlweit, "One the ageing of dendrites," *Scr. Metall.*, vol. 2, pp. 251–254, 1968.

[102] B. Li, H. D. Brody, and A. Kazimirov, "Real-time observation of dendrite coarsening in Sn-13%Bi alloy by synchrotron microradiography," *Phys. Rev. E*, vol. 70, pp. 062602-062605, 2004.

[103] J. L. Marshall, J. Calderon, J. Sees, G. Lucey, and J. S. Hwang, "Composite solder," *IEEE Trans. Components, Hybrids, Manufacturing Technol.*, vol. 14 pp. 698–702, 1991.

[104] S. K. Das, A. Sharif, and Y. C. Chan, "Effect of Ag micro-particles content on the mechanical strength of the interface formed between Sn-Zn binary solder and Au/Ni/Cu bond pads," *Microelec. Eng.*, vol. 86 pp. 2086–2093, 2009.

[105] B. Liu, F. Tai, F Guo, Z. Xia, and Y. Shi, "Mechanical properties of lead-free solder joint containing nano-structured reinforcements," *Acta Materiae Compositae Sinica*, vol. 26 pp. 11–17, 2009.

[106] A. A. Chernov, D. E. Temkin, and A. M. Mel'nikova, "Theory of the capture of solid inclusions during the growth of crystals from the melt," *Sov. Phys.*

Crystallogr., vol. 21, pp. 369–373, 1976.

[107] D. R. Uhlmann, B. Chalmers, and K. A. Jackson, "Interaction between particles and a solid-liquid interface," *J. Appl. Phys.* vol. 35(10), pp. 2986–2993, 1964.

[108] A. W. Rempel and M. G. Worster, "The interaction between a particle and an advancing solidification front" *J. Crystal Growth*, vol. 205, pp. 427–440, 1999.

[109] M. S. Park, A. A. Golovin, and S. H. Davis, "The encapsulation of particles and bubbles by an advancing solidification front," *J. Fluid Mech.*, vol. 560, pp. 415–436, 2006.

[110] D. M. Stefanescu, R. V. Phalnikar, H. Pang, A. Ahuja, and B. K. Dhindaw, "A coupled force field-thermal field analytical model for the evaluation of the critical velocity for particle engulfment," *ISIJ* International, vol. 35, pp. 700–707, 1995.

[111] M. Ode, J. S. Lee, T. Suzuki, S. G. Kim, and W. T. Kim, "Phase-field model for solidification of Fe-C alloys," *ISIJ* International, vol. 39, pp. 149–153, 1999.

[112] N. Moelans, B. Blanpain, and P. Wollants, "A phase field model for the simulation of grain growth in materials containing finely dispersed incoherent second-phase particles," *Acta Mater.*, vol. 53, pp. 1771–1781, 2005.

[113] N. Moelans, B. Blanpain, and P. Wollants, "Phase field simulations of grain growth in two-dimensional systems containing finely dispersed second-phase particles," *Acta Mater.*, vol. 54, pp. 1175–1184, 2006.

[114] N. Moelans, B. Blanpain, and P. Wollants, "Pinning effect of second-phase particles on grain growth in polycrystalline films studied by 3-D phase field simulations," *Acta Mater.*, vol. 55, pp. 2173–2182, 2007.

[115] K. A. Jackson and J. D. Hunt, "Lamellar and rod eutectic growth," *Trans. Metall. Soc.* AIME, vol. 236, pp. 1129–1142, 1966.

[116] A. A. Liu, H. K. Kim, K. N. Tu, and P. A. Totta, "Spalling of Cu6Sn5 spheroids in the soldering reaction of eutectic SnPb on Cr/Cu/Au thin films," *J. Appl. Phys.*, vol. 80, pp. 2774–2780, 1996.

[117] S. K. Kang, R. S. Rai, and S. Purushothaman, "Interfacial reactions during soldering with lead-tin eutectic and lead (Pb)-free, tin-rich solders," *J. Electron. Mater.*, vol. 25, pp. 1113–1120, 1997.

[118] A. J. Sunwoo, J. W. Morris Jr., and G. K. Lucey Jr., "The growth of Cu-Sn intermetallics at a pretinned copper-solder interface," *Metall. Trans. A*, vol. 23A, pp. 1323–1332, 1992.

[119] C. H. Zhong and S. Yi, "Solder joint reliability of plastic ball grid array packages," *Soldering & Surface Mount Tech.*, vol. 11, pp. 44–48, 1999.

[120] D. R. Frear and P. T. Vianco, "Intermetallic growth and mechanical behavior of low and high melting temperature solder alloys," *Metall. Mater. Trans. A*, vol. 25A, pp. 1509–1523, 1994.

[121] D. Yao and J. K. Shang, "Effect of aging on fatigue crack growth at Sn-Pb/Cu interfaces," *Metall. Mater. Trans. A*, vol. 26A, pp. 2677–2685, 1995.

[122] C. K. Shin, Y. J. Baik, and J. Y. Huh, "Effects of microstructural evolution and intermetallic layer growth on shear strength of ball-grid-array Sn-Cu solder joints," *J. Electron. Mater.*, vol. 30, pp. 1323–1331, 2001.

[123] S. Bader, W. Gust, and H. Hieber, "Rapid formation of intermetallic compounds by interdiffusion in the Cu-Sn and Ni-Sn systems," *Acta Metall. Mater.*, vol. 43,

pp. 329–337, 1995.

[124] J. H. Shim, C. S. Oh, B. J. Lee, and D. N. Lee, "Thermodynamic assessment of the Cu-Sn system," *Z. Metallkd.*, vol. 87, pp. 205-212, 1996.

[125] M. Ode, T. Koyama, H. Onodera, and T. Suzuki, "Phase-field modeling for Sn-Bi soldering," *J. Electron. Mater.*, vol. 32, pp. 1534–1539, 2003.

[126] S. G. Kim, W. T. Kim, and T. Suzuki, "Interfacial compositions of solid and liquid in a phase-field model with finite interface thickness for isothermal solidification in binary alloys," *Phys. Rev. E*, vol. 58, pp. 3316–3323, 1998.

[127] M. Onishi and H. Fujibuchi, "Reaction-diffusion in the Cu-Sn system," *Trans. JIM*, vol. 16, pp. 539–547, 1975.

[128] Z. Mei, A. J. Sunwoo, and J. W. Morris Jr., "Analysis of low-temperature intermetallic growth in copper-tin diffusion couples," *Metall. Trans. A*, vol. 23A, pp. 857, 1992.

[129] Y. G. Lee and J. G. Duh, "Characterizing the formation and growth of intermetallic compound in the solder joint," *J. Mater. Sci.*, vol. 33, pp. 5567–5572, 1998.

[130] Y, Wu, J. A. Sees, C. Pouraghabagher, L. A. Foster, J. L. Marshall, E. G. Jacobs, and R. F. Pinizzotto, "The formation and growth of intermetallics in composite solder," *J. Electron. Mater.*, vol. 7, pp. 769–777, 1993.

[131] A. A. Liu, K. N. Tu, T. T. Sheng, C. H. Tung, and D. R. Frear, "Electron microscopy study of interfacial reaction between eutectic SnPb and Cu/Ni(V)/Al thin film metallization," *J. Appl. Phys.*, vol. 87, pp. 750–754, 2000.

[132] B. J. Lee, N. M Hwang, and H. M. Lee, "Prediction of interface reaction products between Cu and various solder alloys by thermodynamic calculation," *Acta Mater.*, vol. 45, pp. 1867–1874, 1997.

[133] C. Pan, C. Yu, and K. Lin, "The amorphous origin and the nucleation of intermetallic compounds formed at the interface during the soldering of Sn.3.0Ag.0.5Cu on a Cu substrate," *App. Phys. Lett.*, vol. 93, pp. 061912, 2008.

[134] R. S. Qin and E. R. Wallach, "A phase-field model coupled with a thermodynamic database," *Acta Mater.*, vol. 51, pp. 6199–6210, 2003.

[135] J. D. Robson, "Modelling the overlap of nucleation, growth and coarsening during precipitation," *Acta Mater.*, vol. 52, pp. 4669–4676, 2004.

[136] H. Zhang, "Theoretical analysis of spreading and solidification of molten droplet during thermal spray deposition," *Intl' J. Heat and Mass Trans.*, vol. 47, pp. 2191–2203, 2003.

[137] W. T. Read and W. Shockley, "Dislocation models of crystal grain boundaries," *Phy. Rev.*, vol. 78, pp. 275–289, 1950.

[138] B. Morin, K. R. Elder, M. Sutton, and M. Grant, "Model of the kinetics of polymorphous crystallization," *Phy. Rev. Lett.*, vol. 75, pp. 2156–2159, 1995.

[139] L. Granasy, T. Pusztai, and J. A. Warren, "Modelling polycrystalline solidification using phase field theory," *J. Phys.: Condens. Matter*, vol. 16, pp. R1205–R1235, 2004.

[140] W. C. Cater, J. E. Taylor, and J. W. Cahn, "Variational methods for microstructureal evolution" *JOM*, vol. 49, pp. 30–48, 1997.

[141] J. A. Warren, R. Kobayashi, and W. G. Carter, "Modeling grain boudaries using a phase-field technique," *J. Crystal Growth*, vol. 211, pp. 18–20, 2000.

[142] J. A. Warren, W. G. Carter, and R. Kobayashi, "A phase field model of the impingement of solidifying particles," *Phyica A*, vol. 261, pp. 159–166, 1998.

[143] T. Takaki, A Yamanaka, Y. Higa, and Y Tomita, "Phase-field model during recrystallization based on crystal-plasticity theory," *J. Computer-Adided Mater. Des.*, vol. 14, pp. 75–84, 2007.

[144] J. Li, J. Wang, and G. Yang, "Investigration into microsegregation during solidification of a bindary alloy by phase-field simulation," *J. Crystal Growth*, vol. 311, pp. 1217–12222, 2009.

[145] J. Li, J. Wang, Q. Xu, and G. Yang, "Comparison of Johnson-Mehl-Avami-Kologromov (JMAK) kinetics with a phase simulation for polycrystalline solidification," *Acta Mater.*, vol. 55, pp. 825–832, 2007.

[146] A. Yamanaka, T. Takaki, and Y. Tomita, "Multi-phase-field modeling of diffusive solid phase transition in carbon steel during continuous cooling transformation," *J. Crystal Growth*, vol. 310, pp. 1337–1342, 2008.

[147] K. H. Prakash and T. Sritharan, "Interface reaction between copper and molten tin-lead solders," *Acta Mater.*, vol. 49, pp. 2481–2489, 2001.

[148] N. S. Bosco and F. W. Zok, "Critical interlayer thickness for transient liquid phase bonding in the Cu/Sn system," *Acta Mater.*, vol. 52, pp. 2965–2972, 2004.

[149] D. Yu, C. Wu, C. Law, L. Wang, and J. Lai, "Intermetallic compounds growth between Sn-3.5Ag lead-free solder and Cu substrate by dipping method," *J.*

Alloys and Compounds, vol. 392, pp. 192–199, 2005.

[150] T. Lee, S. Zhang, C. Wong, A. Tan, and D. Hadikusuma, "Interfacial microstructures and kinetics of Au/SnAgCu," *Thin Solid Film*, vol. 504, pp. 441–445, 2006.

[151] H. F. Zou, H. J. Yang, and Z. F. Zhang, "Morphologies, orientation relationships and evolution of Cu6Sn5 grains formed between molten Sn and Cu single crystals," *Acta Mater.*, vol. 56, pp. 2649–2662, 2008.

[152] M. Lu, D. Shih, P. Lauro, C. Goldsmith, and D. W. Henderson, "Effect of Sn grain orientation on electromigration degradation mechanism in high Sn-based Pb-free solders," *Appl. Phys. Lett.*, vol. 92, pp. 211909, 2008.

[153] H. Tsukamoto, Z. Dong, H. Huang, T. Nishimura, and K. Nogita, "Nanoindentation characterization of intermetallic compounds formed between Sn-Cu(-Ni) ball grid arrays and Cu substrates," *Mater. Sci. Eng. B*, vol. 164, pp. 44–50, 2009.

APPENDIX A

PHASE FIELD MODEL FOR BINARY ALLOYS

Free energy density is given as

$$f(\phi(x), c(x)) = f^S(c_S)h(\phi) + f^S(c_L)\left[1 - h(\phi)\right] + wg(\phi), \tag{A.1}$$

where

$$c(x) = h(\phi)c_S + \left[1 - h(\phi)\right]c_L \tag{A.2}$$

and

$$\frac{\mathrm{d}f^S(c_S)}{\mathrm{d}c_S} = \frac{\mathrm{d}f^L(c_L)}{\mathrm{d}c_L}. \tag{A.3}$$

Governing equations are given as

$$\frac{\partial \phi}{\partial t} = M\left(\epsilon^2 \nabla^2 \phi - f_\phi\right), \tag{A.4}$$

and

$$\frac{\partial c}{\partial t} = \nabla\left(\frac{D(\phi)}{f_{cc}}\nabla f_c\right). \tag{A.5}$$

The explicit forms of governing equations can be obtained from equations (A.2) and (A.3). They are

$$h(\phi)\frac{\partial c_S}{\partial c} + \left[1 - h(\phi)\right]\frac{\partial c_L}{\partial c} = 1, \tag{A.6}$$

$$h(\phi)\frac{\partial c_S}{\partial \phi} + \left[1 - h(\phi)\right]\frac{\partial c_L}{\partial \phi} + \frac{\mathrm{d}h(\phi)}{\mathrm{d}\phi}(c_S - c_L) = 0, \tag{A.7}$$

$$\frac{\mathrm{d}^2 f^S(c_S)}{\mathrm{d}c_S^2}\frac{\partial c_S}{\partial c} = \frac{\mathrm{d}^2 f^L(c_L)}{\mathrm{d}c_L^2}\frac{\partial c_L}{\partial \phi}, \tag{A.8}$$

and

$$\frac{\mathrm{d}^2 f^S(c_S)}{\mathrm{d}c_S^2}\frac{\partial c_S}{\partial \phi} = \frac{\mathrm{d}^2 f^L(c_L)}{\mathrm{d}c_L^2}\frac{\partial c_L}{\partial \phi}. \tag{A.9}$$

Equations (A.6) and (A.8) yield

$$\frac{\partial c_L}{\partial c} = \frac{\frac{\mathrm{d}^2 f^S(c_S)}{\mathrm{d}c_S^2}}{h(\phi)\frac{\mathrm{d}^2 f^L}{\mathrm{d}c_L^2} + [1-h(\phi)]\frac{\mathrm{d}^2 f^S}{\mathrm{d}c_S^2}} \tag{A.10}$$

and

$$\frac{\partial c_S}{\partial c} = \frac{\frac{\mathrm{d}^2 f^L(c_S)}{\mathrm{d}c_L^2}}{h(\phi)\frac{\mathrm{d}^2 f^L}{\mathrm{d}c_L^2} + [1-h(\phi)]\frac{\mathrm{d}^2 f^S}{\mathrm{d}c_S^2}}. \tag{A.11}$$

Equations (A.7) and (A.9) yield

$$\frac{\partial c_L}{\partial \phi} = \frac{h(\phi)(c_L - c_S)\frac{\mathrm{d}^2 f^S(c_S)}{\mathrm{d}c_S^2}}{h(\phi)\frac{\mathrm{d}^2 f^L}{\mathrm{d}c_L^2} + [1-h(\phi)]\frac{\mathrm{d}^2 f^S}{\mathrm{d}c_S^2}} \tag{A.12}$$

and

$$\frac{\partial c_S}{\partial \phi} = \frac{h(\phi)(c_L - c_S)\frac{\mathrm{d}^2 f^L(c_L)}{\mathrm{d}c_L^2}}{h(\phi)\frac{\mathrm{d}^2 f^L}{\mathrm{d}c_L^2} + [1-h(\phi)]\frac{\mathrm{d}^2 f^S}{\mathrm{d}c_S^2}}. \tag{A.13}$$

These eight relationships are very useful in deriving the explicit forms of the governing equations (A.3) and (A.4). From now on we use the notations

$$\begin{aligned} f_{cc}^L &\equiv \frac{\mathrm{d}^2 f^L(c_L)}{\mathrm{d}c_L^2}, \\ f_{cc}^S &\equiv \frac{\mathrm{d}^2 f^S(c_L)}{\mathrm{d}c_S^2}. \end{aligned}$$

At first we find the explicit form for f_ϕ as

$$\begin{aligned} f_\phi &= \frac{\partial f^S}{\partial \phi}h(\phi) + \frac{\partial f^S}{\partial \phi}[1-h(\phi)] + \frac{\mathrm{d}h(\phi)}{\mathrm{d}\phi}\left[f^S - f^L\right] + w\frac{\mathrm{d}g}{\mathrm{d}\phi} \\ &= \frac{\mathrm{d}f^S}{\mathrm{d}c_S}\frac{\partial c_S}{\partial \phi}h(\phi) + \frac{\mathrm{d}f^L}{\mathrm{d}c_L}\frac{\partial c_L}{\partial \phi}[1-h(\phi)] + h\prime\left[f^S - f^L\right] + wg\prime. \end{aligned}$$

By using equations (A.3) and (A.7), f_ϕ can be obtained as

$$\begin{aligned} f_\phi &= \frac{\mathrm{d}f^L}{\mathrm{d}c_L}\left[\frac{\partial c_S}{\partial \phi}h(\phi) + \frac{\partial c_L}{\partial \phi}[1-h(\phi)]\right] + h\prime\left[f^S - f^L\right] + wg\prime \\ &= -h(\phi)\prime\left[f^L - f^S - \frac{\mathrm{d}f^L}{\mathrm{d}c_L}(c_L - c_S)\right] + wg\prime. \end{aligned} \tag{A.14}$$

Next we find the explicit form of f_c as

$$\begin{aligned} f_c &= \frac{\partial f^S}{\partial c} h(\phi) + \frac{\partial f^L}{\partial c} \left[1 - h(\phi)\right] \\ &= h(\phi) \frac{\mathrm{d}f^S}{\mathrm{d}c_S} \frac{\partial c_S}{\partial c} + \left[1 - h(\phi)\right] \frac{\mathrm{d}f^L}{\mathrm{d}c_L} \frac{\partial c_L}{\partial c}. \end{aligned} \tag{A.15}$$

By using equations (A.3) and (A.6), equation (A.15) can be shown as

$$\begin{aligned} f_c &= \frac{\partial f^L}{\partial c_L} \left[h(\phi) \frac{\partial c_S}{\partial c} + \left[1 - h(\phi)\right] \frac{\partial c_L}{\partial c} \right] \\ &= \frac{\mathrm{d}f^L(c_L)}{\mathrm{d}c_L} = \frac{\mathrm{d}f^S(c_S)}{\mathrm{d}c_S}. \end{aligned} \tag{A.16}$$

Finally, we find the explicit form of f_{cc} and $f_{c\phi}$. From equation (A.16), we can see

$$f_{cc} = \frac{\mathrm{d}^2 f^L(c_L)}{\mathrm{d}c_L^2} \frac{\partial c_L}{\partial c} = \frac{\mathrm{d}^2 f^S(c_S)}{\mathrm{d}c_S^2} \frac{\partial c_S}{\partial c}. \tag{A.17}$$

After inserting equations (A.10) or (A.11) into equation (A.17), we can get

$$f_{cc} = \frac{f_{cc}^S(c_S) f_{cc}^L(c_L)}{\left[1 - h\right] f_{cc}^S(c_S) + h f_{cc}^L(c_L)}. \tag{A.18}$$

From equation (A.16), we can see

$$f_{c\phi} = \frac{\mathrm{d}^2 f^L(c_L)}{\mathrm{d}c_L^2} \frac{\partial c_L}{\partial \phi} = \frac{\mathrm{d}^2 f^S(c_S)}{\mathrm{d}c_S^2} \frac{\partial c_S}{\partial \phi}. \tag{A.19}$$

Also after inserting equations (A.12) or (A.13) into equation (A.19), we can get

$$f_{c\phi} = \frac{h'(c_L - c_S) f_{cc}^S(c_S) f_{cc}^L(c_L)}{\left[1 - h\right] f_{cc}^S(c_S) + h f_{cc}^L(c_L)}. \tag{A.20}$$

Therefore, we can get

$$\frac{f_{c\phi}}{f_{cc}} = h'\left(c_L - c_S\right). \tag{A.21}$$

Inserting equations (A.14), (A.16) and (A.18) into equations (A.4) and (A.5), we cans

get the finial forms of governing equations as

$$\frac{1}{M}\frac{\partial \phi}{\partial t} = \nabla \cdot \epsilon^2 \nabla \phi + h' \left[f^L - f^S - (c_L - c_S) f^L_{c_L}(c_L) \right] - w g' \tag{A.22}$$

and

$$\frac{\partial c}{\partial t} = \nabla \left[D(\phi) \frac{[1-h]\, f^S_{cc}(c_S) + h f^L_{cc}(c_L)}{f^S_{cc}(c_S) f^L_{cc}(c_L)} \nabla f_c \right] \tag{A.23}$$

with

$$c = h(\phi) c_S + [1 - h(\phi)] c_L \quad \text{and} \quad f^S_{c_S} = f^L_{c_L}.$$

The diffusion equation (A.5) may be written as the other form:

$$\begin{aligned} \frac{\partial c}{\partial t} &= \nabla \left[D(\phi) \nabla c \right] + \nabla \left[D(\phi) \frac{f_{c\phi}}{f_{cc}} \nabla \phi \right] \\ &= \nabla \left[D(\phi) \nabla c \right] + \nabla \left[D(\phi) h'(c_L - c_S) \nabla \phi \right], \end{aligned} \tag{A.24}$$

where we used equation (A.21).

At one dimensional stationary state, it must be

$$f^S_{c_S} = f^L_{c_L} = f^e_c \tag{A.25}$$

and

$$\epsilon^2 \frac{\mathrm{d}^2 \phi}{\mathrm{d}x^2} + h' \left[f^L - f^S - (c_L - c_S) f^L_{c_L}(c_L) \right] - w g' = 0. \tag{A.26}$$

Equation (A.25) yield $c_L = c^e_L$ and $c_S = c^e_S$, and so the bracket in equation (A.26) must be independent of position x. After multiplying $\mathrm{d}\phi/\mathrm{d}x$ on both side of equation (A.26), integrating equation (A.26) from $-\infty$ to $+\infty$ results in

$$f^L(c^e_L) - f^S(c^e_S) - (c^e_L - c^e_S) f^L_{c_L}(c^e_L) = 0. \tag{A.27}$$

Equations (A.25) and (A.27) gives the well known equilibrium condition like

$$f^e_c = f^S_{c^e_S} = f^L_{c^e_L} = \frac{f^L(c^e_L) - f^S(c^e_S)}{c^e_L - c^e_S}. \tag{A.28}$$

Because equation (A.27) must be hold at equilibrium state the phase field equation (A.26) becomes

$$\epsilon^2 \frac{\mathrm{d}^2\phi_0}{\mathrm{d}x^2} = -w\frac{\mathrm{d}g(\phi_0)}{\mathrm{d}\phi_0}. \tag{A.29}$$

When we take $g = \phi^2(1-\phi)^2$ under the condition $\phi_0 = 1$(solid) at $x = -\infty$ and $\phi_0 = 0$(liquid) at $x = +\infty$, the solution of the equation is

$$\phi_0(x) = \frac{1}{2}\left[1 - \tanh\left(\frac{\sqrt{w}}{\sqrt{2}\epsilon}\right)\right]. \tag{A.30}$$

Therefore the equilibrium average composition is

$$c_0(x) = h(\phi_0)c_S^e + [1 - h(\phi_0)]c_L^e. \tag{A.31}$$

When the phase-field equation is given by equation (A.4), the total free energy of the inhomogeneous system at one dimensional stationary state is

$$f_{total} = \int_{-\infty}^{+\infty}\left[f(c_0,\phi_0) + \frac{\epsilon^2}{2}\left(\frac{\mathrm{d}\phi_0}{\mathrm{d}x}\right)\right]\mathrm{d}x. \tag{A.32}$$

The excess free energy of the interface f_x is

$$f_x = \int_{-\infty}^{+\infty}\left[f(c_0,\phi_0) + \frac{\epsilon^2}{2}\left(\frac{\mathrm{d}\phi_0}{\mathrm{d}x}\right)\right]\mathrm{d}x - \int_{-\infty}^{0} f^S\mathrm{d}x - \int_{0}^{+\infty} f^L\mathrm{d}x, \tag{A.33}$$

and the surface excess solute $v_m\Gamma_B$ is

$$v_m\Gamma_B = \int_{-\infty}^{+\infty} c_0\mathrm{d}x - \int_{-\infty}^{0} c_S^e\mathrm{d}x - \int_{0}^{+\infty} c_L^e\mathrm{d}x. \tag{A.34}$$

The interface energy is

$$\begin{aligned}
\sigma &= f_x - f_c^e v_m \Gamma_B \\
&= \int_{-\infty}^{+\infty} \left[f(c_0, \phi_0) + \frac{\epsilon^2}{2} \left(\frac{\mathrm{d}\phi_0}{\mathrm{d}x} \right) \right] \mathrm{d}x - \int_{-\infty}^{0} f^S \mathrm{d}x - \int_{0}^{+\infty} f^L \mathrm{d}x \\
&\quad -f_c^e \left[\int_{-\infty}^{+\infty} c_0 \mathrm{d}x - \int_{-\infty}^{0} c_S^e \mathrm{d}x - \int_{0}^{+\infty} c_L^e \mathrm{d}x \right] \\
&= \int_{-\infty}^{0} \left[f(c_0, \phi_0) - f^S(c_S^e) - f_{c_L}^L c_0 + f_{c_L^e}^L c_S^e \right] \mathrm{d}x \\
&\quad + \int_{0}^{\infty} \left[f(c_0, \phi_0) - f^L(c_L^e) - f_{c_L}^L c_0 + f_{c_L^e}^L c_L^e \right] \mathrm{d}x \\
&\quad + \frac{\epsilon^2}{2} \int_{-\infty}^{\infty} \left(\frac{\mathrm{d}\phi_0}{\mathrm{d}x} \right)^2 \mathrm{d}x. \qquad \text{(A.35)}
\end{aligned}$$

According to

$$\begin{aligned}
f(c_0, \phi_0) &= h(\phi_0) f^S(c_S^e) + [1 - h(\phi_0)] f^L(c_L^e) + w g(\phi_0), \\
c_0 &= h(\phi_0) c_S^e + [1 - h(\phi_0)] c_L^e, \\
f_{c_L}^L(c_L^e) &= \frac{f^L(c_L^e) - f^S(c_S^e)}{c_L^e - c_S^e},
\end{aligned}$$

equation (A.35) becomes

$$\sigma = w \int_{-\infty}^{+\infty} g(\phi_0) \mathrm{d}x + \frac{\epsilon^2}{2} \int_{-\infty}^{+\infty} \left(\frac{\mathrm{d}\phi_0}{\mathrm{d}x} \right)^2 \mathrm{d}x. \qquad \text{(A.36)}$$

Here we integrate equation (A.29) from $x = -\infty$ to $x = x$ after multiplying $\mathrm{d}\phi/\mathrm{d}x$ on both sides, which yields

$$w g(\phi_0) = \frac{\epsilon^2}{2} \left(\frac{\mathrm{d}\phi_0}{\mathrm{d}x} \right)^2, \qquad \text{(A.37)}$$

which can be obtained by direct differentiation of equation (A.30). Thus we can find

$$\sigma = \epsilon^2 \int_{\infty}^{\infty} \left(\frac{\mathrm{d}\phi_0}{\mathrm{d}x} \right)^2 \mathrm{d}x. \qquad \text{(A.38)}$$

Using equation (A.30), direct evaluation of the interface energy gives

$$\sigma = \frac{\epsilon\sqrt{w}}{\sqrt{18}}. \tag{A.39}$$

From equation (A.30), we can see that a measure of the interface thickness 2λ, over which ϕ_0 changes from 0.1 to 0.9, is given by

$$2\lambda = 2.2\sqrt{2}\frac{\epsilon}{\sqrt{w}}. \tag{A.40}$$

We rewrite the governing equation at one dimensional steady state

$$-\frac{v_n}{M}\frac{\partial\phi}{\partial x} = \nabla\cdot\epsilon^2\nabla\phi + h^{'}\left[f^L - f^S - (c_L - c_S)f^L_{c_L}(c_L)\right] - wg^{'} \tag{A.41}$$

and

$$-v_n\frac{\partial c}{\partial x} = \frac{\mathrm{d}}{\mathrm{d}x}\left[\frac{D(\phi)}{f_{cc}}\frac{\mathrm{d}f^L_{c_L}}{\mathrm{d}x}\right]. \tag{A.42}$$

When the diffusivity in solid can be negligible, from equation (A.23) we can get the chemical potential

$$f_c(x) = f^L_{c_L}(c_L) = f^L_{c_S}(c^i_S) - v_n int^{\lambda}_{-\lambda}\frac{f_{cc}}{D(\phi)}(c(x) - c^i_S)\mathrm{d}x, \tag{A.43}$$

where c^i_S is the composition at the solid side of the interface, and f_{cc} is given in equation (A.18). For the first order in the Peclet number (Pe$= 2\lambda v_n/D$), the chemical potential profile f_c can be written as

$$f_c(x) = f^L_{c_L}(c_L) = f^L_{c_S}(c^i_S) - v_n\int^{x}_{-\lambda}\frac{f^e_{cc}}{D(\phi)}(c^e(x) - c^e_S)\mathrm{d}x, \tag{A.44}$$

where the superscript e denote the values that correspond to the case of $v_n = 0$, that is, the equilibrium state. Also for the fist order in the peclet number, we can expand c_L and c_S as $c_L = c^e_L + \delta c_L$ and $c_S = c^e_S + \delta c_S$. Thus the term in the bracket of the

phase field equation of the first order becomes

$$f^L(c_L) - f^S(c_S) - (c_L - c_S) f^L_{c_L}(c_L) = f^L(c^e_L) - f^S(c^e_S)$$
$$-(c^e_L - c^e_S) f^S_{c_S}(c^i_S) + v_n(c^e_L - c^e_S) \int_{-\lambda}^{x} \frac{f^e_{cc}}{D(\phi)} (c^e(x) - c^e_S) \mathrm{d}x. \qquad \text{(A.45)}$$

We insert equation (A.45) into (A.41), and after multiplying $\mathrm{d}\phi/\mathrm{d}x$ on both sides of (A.41) we integrate from $x = -\lambda$ to $x = +\lambda$, which yields

$$-\frac{v_n}{M} \int_{-\lambda}^{+\lambda} \left(\frac{\mathrm{d}\phi_0}{\mathrm{d}x} \right)^2 \mathrm{d}x = -f^L(c^e_L) + f^S(c^e_S) + (c^e_L - c^e_S) f^S_{c_S}(c^i_S) + I. \qquad \text{(A.46)}$$

where

$$\begin{aligned} I &= v_n(c^e_L - c^e_S) \int_1^0 \left[\int_{-\lambda}^{x} \frac{f^e_{cc}}{D(\phi)} (c^e(x\prime) - c^e_S) \mathrm{d}x\prime \right] h'(\phi_0) \mathrm{d}\phi_0 \\ &= -v_n(c^e_L - c^e_S) \int_1^0 h(\phi_0) \frac{f^e_{cc}}{D(\phi)} (c^e(x) - c^e_S) \frac{\mathrm{d}x}{\mathrm{d}\phi_0} \mathrm{d}\phi_0. \end{aligned}$$

From equations (A.18), (A.30) and (A.31) we can get

$$I = -\frac{\epsilon}{\sqrt{2w}D} \zeta^e, \qquad \text{(A.47)}$$

where

$$\begin{aligned} \zeta^e &= f^S_{cc}(c^e_S) f^L_{cc}(c^e_L)(c^e_L - c^e_S)^2 \\ &\quad \times \int_0^1 \frac{h(\phi_0)\,[1 - h(\phi_0)]}{[1 - h(\phi_0)]\, f^S_{cc}(c^e_S) + h(\phi_0) f^L_{cc}(c^e_L)} \frac{\mathrm{d}\phi_0}{\phi_0(1 - \phi_0)}. \end{aligned} \qquad \text{(A.48)}$$

For example, if $h = \phi^2(3 - 2\phi)$ under the dilute solute approximation, we can get

$$f^S_{cc}(c^e_S) = \frac{RT}{v_m} \frac{1}{c^e_S} \quad \text{and} \quad f^L_{cc}(c^e_L) = \frac{RT}{v_m} \frac{1}{c^e_L}, \qquad \text{(A.49)}$$

and then ζ^e becomes

$$\zeta^e = \frac{RT}{v_m} (c^e_L - c^e_S)^2 \int_0^1 \frac{\phi_0(1 - \phi_0)(3 - 2\phi_0)(2\phi_0 + 1)}{c^e_L(1 - \phi_0)^2(2\phi_0 + 1) + c^e_S \phi_0^2 (3 - 2\phi_0)} \mathrm{d}\phi_0. \qquad \text{(A.50)}$$

Therefore equation (A.46) becomes

$$f^L(c_L^e) - f^S(c_S^e) - (c_L^e - c_S^e) f_{c_S}^S(c_S^i) = v_n \left[\frac{\sigma}{M\epsilon^2} - \frac{\epsilon}{D\sqrt{2w}} \zeta^e \right]. \tag{A.51}$$

The idea of Karma and Rappel is that the correct chemical potential of the liquid at the interface should be taken as the extrapolated value $f_{c_L}^L(c_L)$, instead of $f_{c_L}^L(c_L^i)$, to the artificial sharp interface. When the diffusivity in solid is negligible, this value should be the same with $f_{c_S}^S(c_S^i)$. Therefore from equation (A.52) can be rewritten as

$$(c_L^e - c_S^e) \left[f_c^e - f_{c_S}^S \right] = \alpha v_n, \tag{A.52}$$

where $\alpha = \frac{\sigma}{M\epsilon} - \frac{\epsilon\zeta^e}{D\sqrt{2w}}$, and f_c^e is the equilibrium chemical potential given by Equation (A.28). With the express of

$$f_c^e - f_{c_S}^S \approx \frac{RT}{v_m} \left(1 - \frac{c_S^i}{c_S^e} \right) \tag{A.53}$$

for a dilute solution, we can write

$$\begin{aligned} v_n \frac{v_m}{RT} \frac{m^e \alpha}{1 - k_e} &= (T_m - T_i) \left(1 - \frac{c_S^i}{c_S^e} \right) \\ &= T_m - T_i - m^e c_S^i. \end{aligned} \tag{A.54}$$

Thus we can obtain

$$T = T_m - m^e \frac{c_S^i}{k_e} - v_n \frac{v_m}{RT} \frac{m^e \alpha}{1 - k^e}, \tag{A.55}$$

which is the well-known relationship between the interface temperature and the interfacial composition of liquid, and we can define the interface kinetic coefficient as

$$\beta \equiv \frac{v_m}{RT} \frac{m^e \alpha}{1 - k^e} = \frac{v_m}{RT} \frac{m^e}{1 - k^e} \left[\frac{\sigma}{M\epsilon^2} - \frac{\epsilon}{D\sqrt{2w}} \zeta^e \right]. \tag{A.56}$$

Note that equation (A.56) is the same form with that derived by Karma and Rappel for solidification of pure materials, and the relationship is correct only at the condition

with a vanishing interface Peclet number. As shown by them, equation (A.56) permits zero-interface kinetic coefficient by adjusting the parameters.

APPENDIX B

MULTIPHASE TRANSFORMATIONS OF A PHASE FIELD METHOD USING INTERFACE FIELDS

The description of first order phase transformations for multiphase contains different phases ϕ_α, ϕ_β,...,ϕ_N and different phase gradient $\nabla\phi_\alpha$, $\nabla\phi_\beta$,...,$\nabla\phi_N$. The time-dependent equation for ϕ_α with resect to minimization of the free energy functional F is can be derived as

$$\tau\dot{\phi_\alpha} = \left(\nabla\frac{\partial}{\partial\nabla\phi_\alpha} - \frac{\partial}{\partial\phi_\alpha}\right) f, \tag{B.1}$$

where f indicates the free energy density of a phase and τ is a relaxation constant.

There is a constraint for phase fields as

$$\sum_{\alpha=1}^{N}\phi_\alpha = 1. \tag{B.2}$$

Adding Lagrange multiplier λ into equation (B.1) with consideration of the phase field constraint leads to

$$\begin{aligned}\tau\dot{\phi_\alpha} &= \left(\nabla\frac{\partial}{\partial\nabla\phi_\alpha} - \frac{\partial}{\partial\phi_\alpha}\right)\left(f + \lambda\left(\sum_{\alpha=1}^{N}\phi_\alpha - 1\right)\right) \\ &= \left(\nabla\frac{\partial}{\partial\nabla\phi_\alpha} - \frac{\partial}{\partial\phi_\alpha}\right) f + \lambda. \end{aligned} \tag{B.3}$$

ϕ may be identified with the solid density. It varies continuously from 1 (solid) to 0 (liquid) at the interface region. The liquid density is then given by $1-\phi$. The multiphase system can be denoted with a set of N phase field variables $\phi_\alpha(\alpha$=1,,2,...,N). Each phase field is associated with the local density of a different phase and they are connected by phase field constraint equation (B.2). We then define the open spaces

$\tilde{Q}_\alpha$ in Q where $0 < \phi_\alpha < 1$ on $\tilde{Q}$ and the step function χ_α:

$$\chi_\alpha = \begin{cases} 1 & \text{on } \overline{Q}_\alpha, \\ 0 & \text{elsewhere,} \end{cases} \tag{B.4}$$

where $\overline{Q}_\alpha$ is the open space $\tilde{Q}_\alpha$ plus its boundary. The closed space $\overline{Q}_\alpha$ can be separated or overlapping and is changeable with respect to the evolution of ϕ_α. We then set the number of locally existing phases $\tilde{N}(x,t)$ as

$$\tilde{N} = \sum_{\alpha=1}^{N} \chi_\alpha(x,t), \tag{B.5}$$

and then the phase field constraint can be changed as

$$\sum_{\alpha=1}^{\tilde{N}} \phi_\alpha(x,t) = 1, \tag{B.6}$$

where the number of locally existing phases $\tilde{N}$ is 2 on dual interfaces, 3 on triple interfaces. It is considered to be essential for a multiphase method that the transition regions $0 < \phi_{\alpha \mathrm{or} \beta} < 0$ between the phases are finite on $\overline{Q}_{\alpha \mathrm{or} \beta} < Q$. Otherwise, all phases would overlap and the multiple point of order N would extend over the whole domain Q as seen in Fig. 72.

As can be seen from the constraint equation (B.2) with respect to equation (B.6), the set of ϕ_α (α=1,,2,...,N) are dependent of set of phase field variables of the multiphase system. They are defined on a $\tilde{N} - 1$ dimension.

For $\tilde{N}$ phase ${}_{\tilde{N}}C_2$ interface between two phases α and β can be denoted, where C is combination function. We define a set of ${}_{\tilde{N}}C_2$ antisymmetric interface fields Ψ. For example, the antisymmetric interface field can be denoted on the two phases (ϕ_α and ϕ_β) coexisting region as

$$\Psi_{\alpha\beta} = \phi_\alpha - \phi_\beta. \tag{B.7}$$

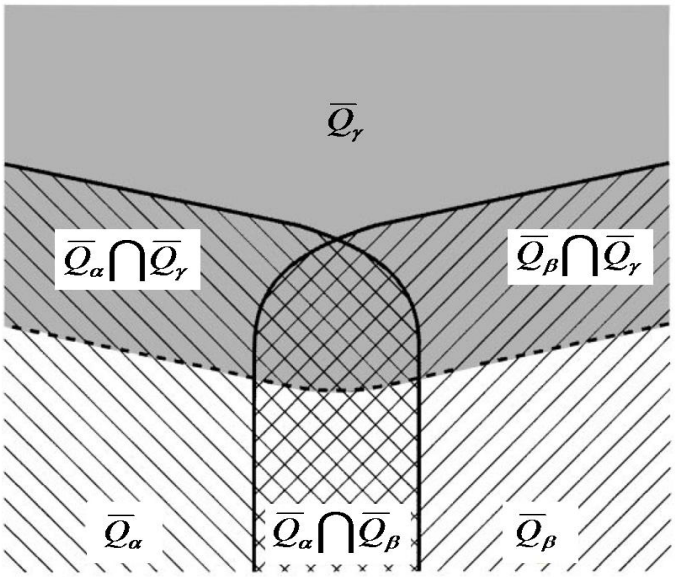

Fig. 72. Simple configuration of three phases coexisting field (ϕ_α, ϕ_β and ϕ_γ), where $\phi_\alpha \cap \phi_\beta$, $\phi_\alpha \cap \phi_\gamma$ and $\phi_\gamma \cap \phi_\beta$ indicate two phases interface each and $\phi_\alpha \cap \phi_\beta \cap \phi_\gamma$ indicates three phases interface.

Application of equation (B.7) for $\tilde{N} > 2$ projects the phase field distribution ϕ_α (α=1,,2,.. .,N) into a $N-1$ dimensional subspace of the $\Psi_{\alpha\beta}$ that again is connected by the constraint equation (B.2) as equation (B.7) is a linear transformation. The reverse transformation is

$$\phi_\alpha = \frac{1}{\tilde{N}} \left[\sum_{\beta=1}^{\tilde{N}} \Psi_{\alpha\beta} - 1 \right], \tag{B.8}$$

and Lagrange energy density l also defined from the phase field constraint as

$$l = f + \lambda \left[\sum_{\alpha=1}^{\tilde{N}} \phi_\alpha - 1 \right]. \tag{B.9}$$

The minimum of the free energy functional F with respect to local phase fields can be obtained by using the integrated Lagrange functional $\mathcal{L}$ that is the volume

integration of l in Q space. It is obtained as

$$0 = -\frac{\partial \mathcal{L}}{\partial \phi_\alpha} = \left(\nabla \frac{\partial}{\partial \nabla \phi_\alpha} - \frac{\partial}{\partial \phi_\alpha} \right) l, \tag{B.10}$$

and phase fields ϕ_α can be independently treated with Kronecker delta as

$$\frac{\partial \phi_\alpha}{\partial \phi_\beta} = \delta_{\alpha\beta}. \tag{B.11}$$

We then rewrite the relaxation formulation as

$$\begin{aligned} \overset{\circ}{\phi}_\alpha &= -\frac{\partial \mathcal{L}}{\partial \phi_\alpha} = -\frac{\partial}{\partial \phi_\alpha} \left(\int_Q \left(f + \lambda \left[\sum_{\alpha=1}^{\tilde{N}} \phi_\alpha - 1 \right] \right) \right) \\ &= -\frac{\partial}{\partial \phi_\alpha} \left(F + \lambda \int_Q \left[\sum_{\alpha=1}^{\tilde{N}} \phi_\alpha - 1 \right] \right) = -\frac{\partial F}{\partial \phi_\alpha} - \lambda, \end{aligned} \tag{B.12}$$

where $\overset{\circ}{\phi}_\alpha$ denotes the motion of the ϕ_α towards the minimum of F without specifying a timescale. Then it is also clear that

$$\overset{\circ}{\Psi}_{\alpha\beta} = \overset{\circ}{\phi}_\alpha - \overset{\circ}{\phi}_\beta = -\frac{\partial F}{\partial \phi_\alpha} + \frac{\partial F}{\partial \phi_\beta} - \lambda + \lambda = -\frac{\partial F}{\partial \phi_\alpha} + \frac{\partial F}{\partial \phi_\beta}. \tag{B.13}$$

The motion $\overset{\otimes}{\Psi}_{\alpha\beta}$ can be obtained from equation (B.7) and equation (B.12) as

$$\begin{aligned} \overset{\otimes}{\Psi}_{\alpha\beta} &\equiv \frac{\partial \mathcal{L}}{\partial \Psi_{\alpha\beta}} \\ &= \frac{1}{\tilde{N}} \left[-\frac{\partial F}{\partial \phi_\alpha} + \frac{\partial F}{\partial \phi_\beta} \right]. \end{aligned} \tag{B.14}$$

Comparing equation (B.14) with equation (B.12) we find that $\overset{\circ}{\Psi}_{\alpha\beta}$ and $\overset{\otimes}{\Psi}_{\alpha\beta}$ scales by a factor $1/\tilde{N}$ as

$$\overset{\circ}{\Psi}_{\alpha\beta} = \left(\frac{\partial}{\partial \phi_\alpha} - \frac{\partial}{\partial \phi_\beta} \right) F \tag{B.15}$$

and

$$\overset{\otimes}{\Psi}_{\alpha\beta} = \frac{\partial F}{\partial \Psi_{\alpha\beta}}. \tag{B.16}$$

Combining (B.13) and (B.15) leads to

$$\overset{\otimes}{\Psi}_{\alpha\beta} = \frac{1}{\tilde{N}} \overset{\circ}{\Psi}_{\alpha\beta}. \tag{B.17}$$

The standard multiphase field model can be obtained from equation (B.13) using equation (B.8) or from equation (B.14) using equations (B.8) and (B.17) as

$$\dot{\phi}_\alpha = -\frac{\partial}{\partial \phi_{alpha}} F + \lambda, \tag{B.18}$$

$$\lambda = \frac{1}{\tilde{N}} \sum_{\beta=1}^{\tilde{N}} \frac{\partial}{\partial \phi_{beta}} F \tag{B.19}$$

and

$$\begin{aligned} \tau \dot{\phi}_\alpha &= -\frac{\partial}{\partial \phi_\alpha} F + \frac{1}{\tilde{N}} \sum_{\beta=1}^{\tilde{N}} \frac{\partial}{\partial \phi_\beta} F \\ &= -\frac{\tilde{N}-1}{\tilde{N}} \frac{\partial}{\partial \phi_\alpha} F + \frac{1}{\tilde{N}} \sum_{\alpha \neq \beta} \frac{\partial}{\partial \phi_\beta} F \\ &= -\frac{1}{\tilde{N}} \sum_{\alpha \neq \beta} \left(\frac{\partial}{\partial \phi_\alpha} - \frac{\partial}{\partial \phi_\beta} \right) F. \end{aligned} \tag{B.20}$$

APPENDIX C

AN ANISOTROPIC PHASE FIELD EQUATION

We extend the model to the anisotropic case in the interface energy σ_{ij} and kinetic coefficient β_{ij}, that is, $\sigma_{ij} = \sigma(\theta_i, \theta_j)$ and $\beta_{ij} = \beta(\theta_i, \theta_j)$, where θ_i and θ_j are the angles of the direction normal to ϕ_i line and ϕ_j line from a reference axis, respectively, that is,

$$\theta = \tan^{-1} \frac{(\phi_i)_y}{(\phi_i)_x}. \tag{C.1}$$

Throughout this section, the subscripts under the parentheses represents the partial derivative by the subscripts. As in the previous method, we put $\epsilon_{ij} = \epsilon(\theta_i, \theta_j)$ and $M_{ij} = M(\theta_i, \theta_j)$. Because the orientation dependence of the phase-field mobility can be easily treated, we here focus on the gradient coefficient $\epsilon_{ij} = \epsilon(\theta_i, \theta_j)$. For convenience, we introduce an average orientation

$$\theta_{ij} = \frac{1}{2} (\theta_i + \theta_j) . \tag{C.2}$$

In a boundary between the two phases with $\phi_i + \phi_j = 1$, we see $\theta_{ij} = \theta_i = \theta_j$ according to equation (C.1). We then take

$$\epsilon_{ij} = \epsilon(\theta_i, \theta_j) = \epsilon(\theta_{ij}), \tag{C.3}$$

$$M_{ij} = M(\theta_i, \theta_j) = M(\theta_{ij}). \tag{C.4}$$

One should note that by equations (C.2) and (C.3) it follows

$$
\begin{aligned}
(\epsilon_{ij})_{\theta_i} = (\epsilon(\theta_{ij}))_{\theta_{ij}}(\theta_{ij})_{\theta_{ij}} &= \frac{1}{2}\frac{\mathrm{d}\epsilon(\theta_{ij})}{\mathrm{d}\theta_{ij}} = \frac{1}{2}\epsilon'_{ij},\\
(\epsilon_{ij})_{\theta_i\theta_i} = \frac{1}{2}(\epsilon'(\theta_{ij}))_{\theta_i} &= \frac{1}{4}\frac{\mathrm{d}^2\epsilon(\theta_{ij})}{\mathrm{d}\theta_{ij}^2} = \frac{1}{4}\epsilon''_{ij},\\
((\epsilon_{ij})_{\theta_i})^2 + (\epsilon_{ij})_{\theta_i\theta_i}\epsilon_{ij} &= \frac{1}{4}\left[(\epsilon'_{ij})^2 + \epsilon_{ij}\epsilon''_{ij}\right],\\
(\epsilon_{ij})_{\theta_j} = \frac{1}{2}\frac{\mathrm{d}\epsilon(\theta_{ij})}{\mathrm{d}\theta_{ij}} &= \frac{1}{2}\epsilon'_{ij},\\
(\epsilon_{ij})_{\theta_j\theta_j} = \frac{1}{4}\frac{\mathrm{d}^2\epsilon(\theta_{ij})}{\mathrm{d}\theta_{ij}^2} &= \frac{1}{4}\epsilon''_{ij},\\
((\epsilon_{ij})_{\theta_j})^2 + (\epsilon_{ij})_{\theta_j\theta_j}\epsilon_{ij} &= \frac{1}{4}\left[(\epsilon'_{ij})^2 + \epsilon_{ij}\epsilon''_{ij}\right],\\
(\epsilon_{ij})_{\theta_i\theta_j} = \frac{1}{4}\frac{\mathrm{d}^2\epsilon(\theta_{ij})}{\mathrm{d}\theta_{ij}^2} &= \frac{1}{4}\epsilon''_{ij}.
\end{aligned}
$$

For simplicity, we consider the free energy functional

$$
F = \int_V \left[-\frac{\epsilon_{ij}^2(\theta_{ij})}{2}\nabla\phi_i\nabla\phi_j\right]\mathrm{d}V. \tag{C.5}
$$

The variation $\delta\phi_i$ in ϕ_i results in the variation of the functional

$$
\begin{aligned}
\delta F &= -\delta\int_V \left[\frac{\epsilon_{ij}^2(\theta_{ij})}{2}\nabla\phi_i\nabla\phi_j\right]\mathrm{d}V\\
&= -\int_V [\epsilon_{ij}\delta\epsilon_{ij}\nabla\phi_i\nabla\phi_j]\,\mathrm{d}V - \int_V \left[\frac{\epsilon_{ij}^2}{2}\nabla\delta\phi_i\nabla\phi_j\right]\mathrm{d}V.
\end{aligned} \tag{C.6}
$$

The last integral in equation (C.6) becomes

$$
\int_V \left[\frac{\epsilon_{ij}^2}{2}\nabla\delta\phi_i\nabla\phi_j\right]\mathrm{d}V = -\frac{1}{2}\int_V \delta\phi_i\nabla\cdot\left(\epsilon_{ij}^2\nabla\phi_j\right)\mathrm{d}V, \tag{C.7}
$$

where we used Gauss theorem. The variation $\delta\epsilon_{ij}$ in the first integral in equation

(C.6) can be modified as

$$\begin{aligned}\delta\epsilon_{ij} &= (\epsilon_{ij})_{\theta_j}\,\delta\theta_j = (\epsilon_{ij})_{\theta_j}\,\delta\left[\tan^{-1}\frac{(\phi_i)_y}{(\phi_i)_x}\right] \\ &= \frac{(\epsilon_{ij})_{\theta_j}}{|\nabla\phi_i|^2}\left[(\phi_i)_x(\delta\phi_i)_y - (\phi_i)_y(\delta\phi_i)_x\right]. \qquad \text{(C.8)}\end{aligned}$$

The first integral in equation (C.6) then can be written into

$$\begin{aligned}\int_V \left[\epsilon_{ij}\delta\epsilon_{ij}\nabla\phi_i\nabla\phi_j\right]\mathrm{d}V &= \int_V \epsilon_{ij}\,(\epsilon_{ij})_{\theta_j}\,\frac{\nabla\phi_i\cdot\nabla\phi_j}{|\nabla\phi_i|^2}\left[(\phi_i)_x(\delta\phi_i)_y - (\phi_i)_y(\delta\phi_i)_x\right]\mathrm{d}V \\ &= -\int_V \frac{\partial}{\partial y}\left[\epsilon_{ij}\,(\epsilon_{ij})_{\theta_j}\,\frac{\nabla\phi_i\cdot\nabla\phi_j}{|\nabla\phi_i|^2}(\phi_i)_x\right]\delta\phi_i\mathrm{d}V \\ &\quad + \int_V \frac{\partial}{\partial x}\left[\epsilon_{ij}\,(\epsilon_{ij})_{\theta_j}\,\frac{\nabla\phi_i\cdot\nabla\phi_j}{|\nabla\phi_i|^2}(\phi_i)_y\right]\delta\phi_i\mathrm{d}V, \qquad \text{(C.9)}\end{aligned}$$

where we used Green theorem. We then obtain the functional derivative like

$$\begin{aligned}\frac{\delta F}{\delta\phi_i} &= \nabla\cdot\left(\frac{\epsilon_{ij}^2}{2}\nabla\phi_i\right) + \frac{\partial}{\partial y}\left[\epsilon_{ij}\,(\epsilon_{ij})_{\theta_j}\,(\phi_i)_x P_{ij}\right] - \frac{\partial}{\partial x}\left[\epsilon_{ij}\,(\epsilon_{ij})_{\theta_j}\,(\phi_i)_y P_{ij}\right] \\ &= \nabla\cdot\left(\frac{\epsilon_{ij}^2}{2}\nabla\phi_i\right) + \frac{1}{2}\frac{\partial}{\partial y}\left[\epsilon_{ij}\epsilon'_{ij}(\phi_i)_x P_{ij}\right] - \frac{1}{2}\frac{\partial}{\partial x}\left[\epsilon_{ij}\epsilon'_{ij}(\phi_i)_y P_{ij}\right], \qquad \text{(C.10)}\end{aligned}$$

where

$$P_{ij} = \frac{\nabla\phi_i\cdot\nabla\phi_j}{|\nabla\phi_i|^2}. \qquad \text{(C.11)}$$

In order to modify the derivative into the more convenient form, we use

$$\begin{aligned}\nabla\cdot\left(\frac{\epsilon_{ij}^2}{2}\nabla\phi_i\right) &= \frac{\epsilon_{ij}^2}{2}\nabla^2\phi_j + \epsilon_{ij}\nabla\epsilon_{ij}\cdot\nabla\phi_j \\ &= \frac{\epsilon_{ij}^2}{2}\nabla^2\phi_j + \epsilon_{ij}\,(\epsilon_{ij})_{\theta_i}\,\nabla\theta_i\cdot\nabla\phi_j + \epsilon_{ij}\,(\epsilon_{ij})_{\theta_j}\,\nabla\theta_j\cdot\nabla\phi_j \\ &= \frac{\epsilon_{ij}^2}{2}\nabla^2\phi_j + \epsilon_{ij}\epsilon'_{ij}\nabla\theta_{ij}\cdot\nabla\phi_j, \qquad \text{(C.12)}\end{aligned}$$

then equation (C.10) becomes

$$\begin{aligned}\frac{\delta F}{\delta \phi_i} &= \frac{\epsilon_{ij}^2}{2}\nabla^2\phi_j + \epsilon_{ij}\epsilon'_{ij}\left[\nabla\theta_{ij}\cdot\nabla\phi_j + \frac{1}{2}(\phi_i)_x(P_{ij})_y - \frac{1}{2}(\phi_i)_y(P_{ij})_x\right] \\ &\quad + \frac{1}{2}\left[(\epsilon'_{ij})^2 + \epsilon_{ij}\epsilon''_{ij}\right]P_{ij}\left[(\theta_{ij})_y(\phi_i)_x - (\theta_{ij})_x(\phi_i)_y\right] \\ &= \frac{\epsilon_{ij}^2}{2}\nabla^2\phi_j + \frac{1}{2}\epsilon_{ij}\epsilon'_{ij}\left[\nabla(\theta_i+\theta_j)\cdot\nabla\phi_j + (\phi_i)_x(P_{ij})_y - (\phi_i)_y(P_{ij})_x\right] \\ &\quad + \frac{1}{2}\left[(\epsilon'_{ij})^2 + \epsilon_{ij}\epsilon''_{ij}\right]P_{ij}\left[(\theta_{ij})_y(\phi_i)_x - (\theta_{ij})_x(\phi_i)_y\right]. \qquad \text{(C.13)}\end{aligned}$$

In simulations one may use the difference equation corresponding to equation (C.10) or (C.13) directly. In such case, however, we can not maintain the same second order accuracy for all the terms in the right side of equation (C.10) or (C.13) because of the partial derivatives of P_{ij} and θ_{ij}. Therefore it is necessary to expand explicitly the partial derivatives of P_{ij} and θ_{ij} in order to maintain the second order accuracy in the difference equation. (The expansion procedure appeared to be very tedious. For your kind checking of the possible mistakes, we wrote the procedure in detail.) At first, by using equation (C.1), we can write

$$\nabla\theta_i\cdot\nabla\phi_j = \frac{1}{|\nabla\phi_i|^2}\left[(\phi_i)_x\nabla(\phi_i)_y\cdot\nabla\phi_j - (\phi_i)_y\nabla(\phi_i)_x\cdot\nabla\phi_j\right] \qquad \text{(C.14)}$$

and

$$\nabla\theta_j\cdot\nabla\phi_i = \frac{1}{|\nabla\phi_j|^2}\left[(\phi_j)_x\nabla(\phi_{ij})_y\cdot\nabla\phi_j - (\phi_j)_y\nabla(\phi_j)_x\cdot\nabla\phi_j\right]. \qquad \text{(C.15)}$$

Also with the definition from the equation (C.11), we can write

$$
\begin{aligned}
&(\phi_i)_x(P_{ij})_y - (\phi_i)_y(P_{ij})_x \\
&\quad = (\phi_i)_x \frac{1}{|\nabla\phi_i|^4}\left[|\nabla\phi_i|^2\left(\nabla\phi_i\cdot\nabla\phi_j\right)_y - 2\left(\nabla\phi_i\cdot\nabla\phi_j\right)\nabla\phi_i\cdot\nabla(\phi_i)_y\right] \\
&\quad -(\phi_i)_y \frac{1}{|\nabla\phi_i|^4}\left[|\nabla\phi_i|^2\left(\nabla\phi_i\cdot\nabla\phi_j\right)_x - 2\left(\nabla\phi_i\cdot\nabla\phi_j\right)\nabla\phi_i\cdot\nabla(\phi_i)_x\right] \\
&\quad = \frac{1}{|\nabla\phi_i||^2}\left[(\phi_i)_x(\nabla\phi_i\cdot\nabla\phi_j)_y - (\phi_i)_y(\nabla\phi_i\cdot\nabla\phi_j)_x\right] \\
&\quad -\frac{2(\nabla\phi_i\cdot\nabla\phi_j)}{|\nabla\phi_i|^4}\left[(\phi_i)_x\nabla\phi_i\cdot\nabla(\phi_i)_y - (\phi_i)_y\nabla\phi_i\cdot\nabla(\phi_i)_x\right]. \qquad \text{(C.16)}
\end{aligned}
$$

Combining equations (C.14) and (C.16) yields

$$
\begin{aligned}
&(\phi_i)_x(P_{ij})_y - (\phi_i)_y(P_{ij})_x + \nabla\theta_i\cdot\nabla\phi_j \\
&\quad = \frac{1}{|\nabla\phi_i|^2}[(\phi_i)_x(\nabla\phi_i\cdot\nabla\phi_j)_y - (\phi_i)_y(\nabla\phi_i\cdot\nabla\phi_j)_x \\
&\quad +(\phi_i)_x\nabla(\phi_i)_y\cdot\nabla\phi_j - (\phi_i)_y\nabla(\phi_i)_x\cdot\nabla\phi_j] \\
&\quad -\frac{2(\nabla\phi_i\cdot\nabla\phi_j)}{|\nabla\phi_i|^4}\left[(\phi_i)_x\nabla\phi_i\cdot\nabla(\phi_i)_y - (\phi_i)_y\nabla\phi_i\cdot\nabla(\phi_i)_x\right] \\
&\quad = \frac{\nabla\phi_i\cdot\nabla\phi_i}{|\nabla\phi_i|^4}\left[(\phi_i)_x\nabla\phi_i\cdot\nabla(\phi_j)_y - (\phi_i)_y\nabla\phi_i\cdot\nabla(\phi_j)_x\right] \\
&\quad +\frac{2\nabla\phi_i\cdot\nabla\phi_i}{|\nabla\phi_i|^4}\left[(\phi_i)_x\nabla(\phi_i)_y\cdot\nabla\phi_j - (\phi_i)_y\nabla(\phi_i)_x\cdot\nabla\phi_j\right] \\
&\quad -\frac{2\nabla\phi_i\cdot\nabla\phi_j}{|\nabla\phi_i|^4}\left[(\phi_i)_x\nabla\phi_i\cdot\nabla(\phi_i)_y - (\phi_i)_y\nabla\phi_i\cdot\nabla(\phi_i)_x\right] \\
&\quad = R + \frac{2}{|\nabla\phi_i|^4}\left[(\phi_i)_x S - (\phi_i)_y T\right], \qquad \text{(C.17)}
\end{aligned}
$$

where R S and T are given by

$$\begin{aligned}
R &\equiv \frac{\nabla\phi_i \cdot \nabla\phi_i}{|\nabla\phi_i|^4}\left[(\phi_i)_x \nabla\phi_i \cdot \nabla(\phi_j)_y - (\phi_i)_y \nabla\phi_i \cdot \nabla(\phi_j)_x\right] \\
&= \frac{1}{|\nabla\phi_i|^2}\left[(\phi_i)_x\left[(\phi_i)_x(\phi_j)_{xy} + (\phi_i)_y(\phi_j)_y y\right] - (\phi_i)_y\left[(\phi_i)_x(\phi_j)_{xx} + (\phi_i)_y(\phi_j)_{xy}\right]\right] \\
&= \frac{1}{|\nabla\phi_i|^2}\left[(\phi_i)_x^2(\phi_j)_{xy} + (\phi_i)_x(\phi_i)_y(\phi_j)_y y - (\phi_i)_x(\phi_i)_y(\phi_j)_{xx} - (\phi_i)_y^2(\phi_j)_{xy}\right] \\
&= \frac{1}{|\nabla\phi_i|^2}\left[\left[(\phi_i)_x^2 - (\phi_i)_y^2\right](\phi_j)_{xy} + (\phi_i)_x(\phi_i)_y\left[(\phi_j)_{yy} - (\phi_j)_{xx}\right]\right], \qquad \text{(C.18)}
\end{aligned}$$

$$\begin{aligned}
S &\equiv \left[\nabla\phi_i \cdot \nabla\phi_i\right]\left[\nabla(\phi_i)_y \cdot \nabla\phi_j\right] - \left[\nabla\phi_i \cdot \nabla\phi_j\right]\left[\nabla\phi_i \cdot \nabla(\phi_i)_y\right] \\
&= \left[(\phi_i)_x(\phi_i)_x + (\phi_i)_y(\phi_i)_y\right]\left[(\phi_i)_{xy}(\phi_j)_x + (\phi_i)_{yy}(\phi_j)_y\right] \\
&\quad - \left[(\phi_i)_x(\phi_j)_x + (\phi_i)_y(\phi_j)_y\right]\left[(\phi_i)_x(\phi_i)_{xy} + (\phi_i)_y(\phi_i)_{yy}\right] \\
&= \left[(\phi_i)_x^2 + (\phi_i)_y^2\right](\phi_i)_{xy}(\phi_j)_x + \left[(\phi_i)_x^2 + (\phi_i)_y^2\right](\phi_i)_{yy}(\phi_j)_y \\
&\quad - \left[(\phi_i)_x^2(\phi_i)_{xy} + (\phi_i)_x(\phi_i)_y(\phi_i)_{yy}\right](\phi_j)_x - \left[(\phi_i)_x(\phi_i)_y(\phi_i)_{xy} + (\phi_i)_y^2(\phi_i)_{yy}\right](\phi_j)_y \\
&= (\phi_i)_y^2(\phi_i)_{xy}(\phi_j)_x + (\phi_i)_x^2(\phi_i)_{yy}(\phi_j)_y \\
&\quad -(\phi_i)_x(\phi_i)_y(\phi_i)_{yy}(\phi_j)_x - (\phi_i)_x(\phi_i)_y(\phi_i)_{xy}(\phi_j)_y \\
&= \left[(\phi_i)_y^2(\phi_i)_{xy} - (\phi_i)_x(\phi_i)_y(\phi_i)_{yy}\right](\phi_j)_x \\
&\quad + \left[(\phi_i)_x^2(\phi_i)_{yy} - (\phi_i)_x(\phi_i)_y(\phi_i)_{xy}\right](\phi_j)_y \qquad \text{(C.19)}
\end{aligned}$$

and

$$
\begin{aligned}
T &\equiv [\nabla\phi_i \cdot \nabla\phi_i]\,[\nabla(\phi_i)_x \cdot \nabla\phi_j] - [\nabla\phi_i \cdot \nabla\phi_j]\,[\nabla\phi_i \cdot \nabla(\phi_i)_x] \\
&= [(\phi_i)_x(\phi_i)_x + (\phi_i)_y(\phi_i)_y]\,[(\phi_i)_{xx}(\phi_j)_x + (\phi_i)_{xy}(\phi_j)_y] \\
&\quad - [(\phi_i)_x(\phi_j)_x + (\phi_i)_y(\phi_j)_y]\,[(\phi_i)_x(\phi_i)_{xx} + (\phi_i)_y(\phi_i)_{xy}] \\
&= \left[(\phi_i)_x^2 + (\phi_i)_y^2\right](\phi_i)_{xx}(\phi_j)_x + \left[(\phi_i)_x^2 + (\phi_i)_y^2\right](\phi_i)_{xy}(\phi_j)_y \\
&\quad - \left[(\phi_i)_x^2(\phi_i)_{xx} + (\phi_i)_x(\phi_i)_y(\phi_i)_{xy}\right](\phi_j)_x \\
&\quad - \left[(\phi_i)_x(\phi_i)_y(\phi_i)_{xx} + (\phi_i)_y^2(\phi_i)_{xy}\right](\phi_j)_y \\
&= \left[(\phi_i)_y^2(\phi_i)_{xx} - (\phi_i)_x(\phi_i)_y(\phi_i)_{xy}\right](\phi_j)_x \\
&\quad + \left[(\phi_i)_x^2(\phi_i)_{xy} - (\phi_i)_x(\phi_i)_y(\phi_i)_{xx}\right](\phi_j)_y. \qquad \text{(C.20)}
\end{aligned}
$$

We then obtain

$$
\begin{aligned}
&(\phi_i)_x S - (\phi_i)_y T \\
&\quad = (\phi_i)_x \left[(\phi_i)_y^2 (\phi_i)_{xy} - (\phi_i)_x (\phi_i)_y (\phi_i)_{yy}\right] (\phi_j)_x \\
&\qquad + (\phi_i)_x \left[(\phi_i)_x^2 (\phi_i)_{yy} - (\phi_i)_x (\phi_i)_y (\phi_i)_{xy}\right] (\phi_j)_y \\
&\qquad - (\phi_i)_y \left[(\phi_i)_y^2 (\phi_i)_{xx} - (\phi_i)_x (\phi_i)_y (\phi_i)_{xy}\right] (\phi_j)_x \\
&\qquad - (\phi_i)_y \left[(\phi_i)_x^2 (\phi_i)_{xy} - (\phi_i)_x (\phi_i)_y (\phi_i)_{xx}\right] (\phi_j)_y \\
&\quad = (\phi_i)_x \left[2(\phi_i)_y^2 (\phi_i)_{xy} - (\phi_i)_x (\phi_i)_y (\phi_i)_{yy}\right] (\phi_j)_x \\
&\qquad + (\phi_i)_x \left[(\phi_i)_x^2 (\phi_i)_{yy} - 2(\phi_i)_x (\phi_i)_y (\phi_i)_{xy}\right] (\phi_j)_y \\
&\qquad - (\phi_i)_y (\phi_i)_y^2 (\phi_i)_{xx} (\phi_j)_x + (\phi_i)_y \left[(\phi_i)_x (\phi_i)_y (\phi_i)_{xx}\right] (\phi_j)_y \\
&\quad = (\phi_i)_x \left[2(\phi_i)_y^2 (\phi_i)_{xy} - (\phi_i)_x (\phi_i)_y (\phi_i)_{yy}\right] (\phi_j)_x \\
&\qquad - (\phi_i)_y (\phi_i)_y^2 (\phi_i)_{xx} (\phi_j)_x + (\phi_i)_y \left[(\phi_i)_x (\phi_i)_y (\phi_i)_{xx}\right] (\phi_j)_y \\
&\qquad + (\phi_i)_x \left[(\phi_i)_x^2 (\phi_i)_{yy} - 2(\phi_i)_x (\phi_i)_y (\phi_i)_{xy}\right] (\phi_j)_y \\
&\quad = \left[2(\phi_i)_x (\phi_i)_y (\phi_i)_{xy} - (\phi_i)_x^2 (\phi_i)_{yy}\right] (\phi_j)_x (\phi_i)_y - (\phi_i)_y^2 (\phi_i)_{xx} (\phi_j)_x (\phi_i)_y \\
&\qquad + (\phi_i)_y \left[(\phi_i)_y (\phi_i)_{xx}\right] (\phi_j)_y (\phi_i)_x + \left[(\phi_i)_x^2 (\phi_i)_{yy} - 2(\phi_i)_x (\phi_i)_y (\phi_i)_{xy}\right] (\phi_j)_y (\phi_i)_x \\
&\quad = \left[2(\phi_i)_x (\phi_i)_y (\phi_i)_{xy} - (\phi_i)_x^2 (\phi_i)_{yy} - (\phi_i)_y^2 (\phi_i)_{xx}\right] (\phi_j)_x (\phi_i)_y \\
&\qquad + \left[(\phi_i)_y^2 (\phi_i)_{xx} + (\phi_i)_x^2 (\phi_i)_{yy} - 2(\phi_i)_x (\phi_i)_y (\phi_i)_{xy}\right] (\phi_j)_y (\phi_i)_x \\
&\quad = \left[(\phi_j)_y (\phi_i)_x - (\phi_j)_x (\phi_i)_y\right] \\
&\qquad \times \left[(\phi_i)_y^2 (\phi_i)_{xx} + (\phi_i)_x^2 (\phi_i)_{yy} - 2(\phi_i)_x (\phi_i)_y (\phi_i)_{xy}\right] . \qquad \text{(C.21)}
\end{aligned}
$$

Therefore we get

$$
\begin{aligned}
&(\phi_i)_x(P_{ij})_y - (\phi_i)_y(P_{ij})_x + \nabla\theta_i \cdot \nabla\phi_j \\
&\quad = \frac{1}{|\nabla\phi_i|^2}\left[\left[(\phi_i)_x^2 - (\phi_i)_y^2\right](\phi_j)_{xy} + (\phi_i)_x(\phi_i)_y\left[(\phi_j)_{yy} - (\phi_j)_{xx}\right]\right] \\
&\qquad + \frac{2\left[(\phi_j)_y(\phi_i)_x - (\phi_j)_x(\phi_i)_y\right]}{|\nabla\phi_i|^4} \\
&\qquad\quad \times \left[(\phi_i)_y^2(\phi_i)_{xx} + (\phi_i)_x^2(\phi_i)_{yy} - 2(\phi_i)_x(\phi_i)_y(\phi_i)_{xy}\right]
\end{aligned} \tag{C.22}
$$

and

$$
\begin{aligned}
&\nabla\theta_j \cdot \nabla\phi_j \\
&\quad = \frac{1}{|\nabla\phi_j|^2}\left[(\phi_j)_x\nabla(\phi_j)_y \cdot \nabla\phi_j - (\phi_j)_y\nabla(\phi_j)_x \cdot \nabla\phi_j\right] \\
&\quad = \frac{1}{|\nabla\phi_j|^2}\left[(\phi_j)_x\left[(\phi_j)_{xy}(\phi_j)_x + (\phi_j)_{yy}(\phi_j)_y\right] - (\phi_j)_y\left[(\phi_j)_{xx}(\phi_j)_x + (\phi_j)_{xy}(\phi_j)_y\right]\right] \\
&\quad = \frac{1}{|\nabla\phi_j|^2}\left[(\phi_j)_{xy}\left[(\phi_j)_x^2 - (\phi_j)_y^2\right] + \left[(\phi_j)_{yy} - (\phi_j)_{xx}\right](\phi_j)_x(\phi_j)_y\right].
\end{aligned} \tag{C.23}
$$

Adding equations (C.22) and (C.23) yields

$$
\begin{aligned}
&\nabla(\theta_i + \theta_j) \cdot \nabla\phi_j + (\phi_i)_x(P_{ij})_y - (\phi_i)_y(P_{ij})_x \\
&\quad = \nabla\theta_j \cdot \nabla\phi_j + \nabla\theta_i \cdot \nabla\phi_j + (\phi_i)_x(P_{ij})_y - (\phi_i)_y(P_{ij})_x \\
&\quad = \frac{1}{|\nabla\phi_j|^2}\left[(\phi_j)_{xy}\left[(\phi_j)_x^2 - (\phi_j)_y^2\right] + \left[(\phi_j)_{yy} - (\phi_j)_{xx}\right](\phi_j)_x(\phi_j)_y\right] \\
&\qquad + \frac{1}{|\nabla\phi_i|^2}\left[\left[(\phi_i)_x^2 - (\phi_i)_y^2\right](\phi_j)_{xy} + (\phi_i)_x(\phi_i)_y\left[(\phi_j)_{yy} - (\phi_j)_{xx}\right]\right] \\
&\qquad + \frac{2\left[(\phi_j)_y(\phi_i)_x - (\phi_j)_x(\phi_i)_y\right]}{|\nabla\phi_i|^4} \\
&\qquad\quad \times \left[(\phi_i)_y^2(\phi_i)_{xx} + (\phi_i)_x^2(\phi_i)_{yy} - 2(\phi_i)_x(\phi_i)_y(\phi_i)_{xy}\right].
\end{aligned} \tag{C.24}
$$

Now we use

$$
\cos(\theta_i) = \frac{(\phi_i)_x}{|\nabla\phi_i|}, \;\; \sin(\theta_i) = \frac{(\phi_i)_y}{|\nabla\phi_i|} \tag{C.25}
$$

and

$$\cos(\theta_j) = \frac{(\phi_j)_x}{|\nabla\phi_j|}, \;\; \sin(\theta_j) = \frac{(\phi_j)_y}{|\nabla\phi_j|}, \tag{C.26}$$

which are obtained from equation (C.1). then equation (C.24) can be written as

$$\begin{aligned}
&\nabla(\theta_i+\theta_j)\cdot\nabla\phi_j + (\phi_i)_x(P_{ij})_y - (\phi_i)_y(P_{ij})_x \\
&\quad = (\phi_j)_{xy}\cos(2\theta_j) + \frac{1}{2}\left[(\phi_j)_{yy} - (\phi_j)_{xx}\right]\sin(2\theta_j) \\
&\qquad + (\phi_j)_{xy}\cos(2\theta_i) + \frac{1}{2}\left[(\phi_j)_{yy} - (\phi_j)_{xx}\right]\sin(2\theta_i) \\
&\qquad + \frac{2\left[(\phi_j)_y(\phi_i)_x - (\phi_j)_x(\phi_i)_y\right]}{|\nabla\phi_i|^2} \\
&\qquad\quad \times \left[(\phi_i)_{xx}\sin^2(\theta_i) + (\phi_i)_{yy}\cos^2(\theta_i) - (\phi_i)_{xy}\sin(2\theta_i)\right].
\end{aligned} \tag{C.27}$$

With the definition

$$W_{ij} \equiv \frac{(\phi_j)_y(\phi_i)_x - (\phi_j)_x(\phi_i)_y}{|\nabla\phi_i|^2}, \tag{C.28}$$

Equation C.27 becomes

$$\begin{aligned}
&\nabla(\theta_i+\theta_j)\cdot\nabla\phi_j + (\phi_i)_x(P_{ij})_y - (\phi_i)_y(P_{ij})_x \\
&\quad = (\phi_j)_{xy}\cos(2\theta_j) + \frac{1}{2}\left[(\phi_j)_{yy} - (\phi_j)_{xx}\right]\sin(2\theta_j) \\
&\qquad + (\phi_j)_{xy}\cos(2\theta_i) + \frac{1}{2}\left[(\phi_j)_{yy} - (\phi_j)_{xx}\right]\sin(2\theta_i) \\
&\qquad + 2W_{ij}\left[(\phi_i)_{xx}\frac{1-\cos(2\theta_i)}{2} + (\phi_i)_{yy}\frac{1+\cos(2\theta_i)}{2} - (\phi_i)_{xy}\sin(2\theta_i)\right] \\
&\quad = (\phi_j)_{xy}\cos(2\theta_j) + \frac{1}{2}\left[(\phi_j)_{yy} - (\phi_j)_{xx}\right]\sin(2\theta_j) \\
&\qquad + (\phi_j)_{xy}\cos(2\theta_i) + \frac{1}{2}\left[(\phi_j)_{yy} - (\phi_j)_{xx}\right]\sin(2\theta_i) \\
&\qquad + 2W_{ij}\left[\frac{1}{2}\left[(\phi_i)_{xx} + (\phi_i)_{yy}\right] + \frac{1}{2}\left[(\phi_i)_{yy} - (\phi_i)_{xx}\right]\cos(2\theta_i) - (\phi_i)_{xy}\sin(2\theta_i)\right]
\end{aligned}$$

Therefore we find

$$\begin{aligned} B_{ij} &\equiv \nabla(\theta_i+\theta_j)\cdot\nabla\phi_j + (\phi_i)_x(P_{ij})_y - (\phi_i)_y(P_{ij})_x \\ &= (\phi_j)_{xy}\left[\cos(2\theta_j)+\cos(2\theta_i)\right] \\ &\quad + \frac{1}{2}\left[(\phi_j)_{yy}-(\phi_j)_{xx}\right]\left[\sin(2\theta_j)+\sin(2\theta_i)\right] \\ &\quad + W_{ij}\left[\nabla^2\phi_i + \left[(\phi_i)_{yy}-(\phi_i)_{xx}\right]\cos(2\theta_i) - 2(\phi_i)_{xy}\sin(2\theta_i)\right] \end{aligned} \tag{C.29}$$

which is the term of the first bracket in the right side of equation (C.13). By similar ways, we expand the second bracket in the right side of equation (C.13). The term can be written as

$$\begin{aligned} &P_{ij}\left[(\theta_{ij})_y(\phi_i)_x - (\theta_{ij})_x(\phi_i)_y\right] \\ &\quad = \frac{P_{ij}}{2}\left[(\theta_i+\theta_j)_y(\phi_i)_x - (\theta_i+\theta_j)_x(\phi_i)_y\right] \\ &\quad = \frac{P_{ij}}{2}\left[(\theta_i)_y(\phi_i)_x - (\theta_i)_x(\phi_i)_y\right] + \frac{P_{ij}}{2}\left[(\theta_j)_y(\phi_i)_x - (\theta_j)_x(\phi_i)_y\right], \end{aligned} \tag{C.30}$$

where

$$\begin{aligned} &(\theta_i)_y(\phi_i)_x - (\theta_i)_x(\phi_i)_y \\ &\quad = (\phi_i)_x\frac{(\phi_i)_x(\phi_i)_{yy}-(\phi_i)_y(\phi_i)_{xy}}{|\nabla\phi_i|^2} - (\phi_i)_y\frac{(\phi_i)_x(\phi_i)_{xy}-(\phi_i)_y(\phi_i)_{xx}}{|\nabla\phi_i|^2} \\ &\quad = \frac{(\phi_i)_x^2(\phi_i)_{yy} - 2(\phi_i)_x(\phi_i)_y(\phi_i)_{xy} + (\phi_i)_y^2(\phi_i)_{xx}}{|\nabla\phi_i|^2} \\ &\quad = (\phi_i)_{yy}\cos^2(\theta_i) - (\phi_i)_{xy}\sin(2\theta_i) + (\phi_i)_{xx}\sin^2(\theta_i) \\ &\quad = (\phi_i)_{yy}\frac{1+\cos(2\theta_i)}{2} - (\phi_i)_{xy}\sin(2\theta_i) + (\phi_i)_{xx}\frac{1-\cos(2\theta_i)}{2} \\ &\quad = \frac{1}{2}\nabla^2\phi_i + \frac{1}{2}\left[(\phi_i)_{yy}-(\phi_i)_{xx}\right]\cos(2\theta_i) - (\phi_i)_{xy}\sin(2\theta_i) \end{aligned} \tag{C.31}$$

and

$$
\begin{aligned}
&P_{ij}\left[(\theta_j)_y(\phi_i)_x-(\theta_j)_x(\phi_i)_y\right]\\
&\quad=\frac{\left[(\phi_i)_x^2(\phi_j)_x+(\phi_i)_x(\phi_i)_y(\phi_j)_y\right](\phi_j)_x(\phi_j)_{yy}}{|\nabla\phi_i|^2|\nabla\phi_j|^2}\\
&\qquad-\frac{\left[(\phi_i)_x^2(\phi_j)_x+(\phi_i)_x(\phi_i)_y(\phi_j)_y\right](\phi_j)_y(\phi_j)_{xy}}{|\nabla\phi_i|^2|\nabla\phi_j|^2}\\
&\qquad-\frac{\left[(\phi_i)_x(\phi_i)_y(\phi_j)_x+(\phi_i)_y^2(\phi_j)_y\right](\phi_j)_x(\phi_j)_{xy}}{|\nabla\phi_i|^2|\nabla\phi_j|^2}\\
&\qquad+\frac{\left[(\phi_i)_x(\phi_i)_y(\phi_j)_x+(\phi_i)_y^2(\phi_j)_y\right](\phi_j)_y(\phi_j)_{xx}}{|\nabla\phi_i|^2|\nabla\phi_j|^2}\\
&\quad=\left[\cos^2(\theta_j)\cos^2(\theta_i)+\frac{1}{4}\sin(2\theta_i)\sin(2\theta_j)\right](\phi_j)_{yy}\\
&\qquad-\left[\frac{1}{2}\cos^2(\theta_i)\sin(2\theta_j)+\frac{1}{2}\sin(2\theta_i)\sin^2(\theta_j)\right](\phi_j)_{xy}\\
&\qquad-\left[\frac{1}{2}\sin(2\theta_i)\cos^2(\theta_j)+\frac{1}{2}\sin^2(\theta_i)\sin(2\theta_j)\right](\phi_j)_{xy}\\
&\qquad+\left[\frac{1}{4}\sin(2\theta_i)\sin(2\theta_j)+\sin^2(\theta_i)\sin^2(\theta_j)\right](\phi_j)_{xx}\\
&\quad=\frac{1}{4}\left[1+\cos(2\theta_i)\cos(2\theta_j)+\sin(2\theta_i)\sin(2\theta_j)\right]\nabla^2\phi_j\\
&\qquad+\frac{1}{4}\left[\cos(2\theta_i)+\cos(2\theta_j)\right]\left[(\phi_j)_{yy}-(\phi_j)_{xx}\right]\\
&\qquad-\frac{1}{2}\left[\sin(2\theta_i)+\sin(2\theta_j)\right](\phi_j)_{xy}. \qquad \text{(C.32)}
\end{aligned}
$$

Combining (C.31) and (C.32) gives

$$
\begin{aligned}
A_{ij}&\equiv P_{ij}\left[(\theta_{ij})_y(\phi_i)_x-(\theta_{ij})_x(\phi_i)_y\right]\\
&=\frac{P_{ij}}{2}\left[(\theta_i)_y(\phi_i)_x-(\theta_i)_x(\phi_i)_y\right]+\frac{P_{ij}}{2}\left[(\theta_j)_y(\phi_i)_x-(\theta_j)_x(\phi_i)_y\right]\\
&=\frac{P_{ij}}{4}\left[\left[(\phi_i)_{yy}+(\phi_i)_{xx}\right]+\left[(\phi_i)_{yy}-(\phi_i)_{xx}\right]\cos(2\theta_i)-2(\phi_i)_{xy}\sin(2\theta_i)\right]\\
&\quad+\frac{1}{8}\left[1+\cos(2\theta_i)\cos(2\theta_j)+\sin(2\theta_i)\sin(2\theta_j)\right]\nabla^2\phi_j\\
&\quad+\frac{1}{8}\left[\cos(2\theta_i)+\cos(2\theta_j)\right]\left[(\phi_j)_{yy}-(\phi_j)_{xx}\right]\\
&\quad-\frac{1}{4}\left[\sin(2\theta_i)+\sin(2\theta_j)\right](\phi_j)_{xy}. \qquad \text{(C.33)}
\end{aligned}
$$

For summary, we have a total free energy as

$$F_{ij} = \int_V \left[-\frac{\epsilon_{ij}^2(\theta_{ij})}{2} \nabla\phi_i \nabla\phi_j \right] \mathrm{d}V. \tag{C.34}$$

The functional derivative for ϕ_i is

$$\frac{\partial F_{ij}}{\partial \phi_i} = -\frac{\epsilon_{ij}^2}{2}\nabla^2\phi_j + \frac{1}{2}\epsilon_{ij}\epsilon'_{ij}B_{ij} + \frac{1}{2}\left[(\epsilon'_{ij})^2 + \epsilon_{ij}\epsilon''_{ij}\right] A_{ij} \tag{C.35}$$

with

$$\begin{aligned} A_{ij} &= P_{ij}\left[\nabla^2\phi_i + [(\phi_i)_{yy} - (\phi_i)_{xx}]\cos(2\theta_i) - 2(\phi_i)_{xy}\sin(2\theta_i)\right] \\ &\quad + \frac{1}{8}\left[1 + \cos(2\theta_i)\cos(2\theta_j) + \sin(2\theta_i)\sin(2\theta_j)\right]\nabla^2\phi_j \\ &\quad + \frac{1}{8}\left[\cos(2\theta_i) + \cos(2\theta_j)\right]\left[(\phi_j)_{yy} - (\phi_j)_{xx}\right] \\ &\quad - \frac{1}{4}\left[\sin(2\theta_i) + \sin(2\theta_j)\right](\phi_j)_{xy} \end{aligned} \tag{C.36}$$

and

$$\begin{aligned} B_{ij} &= (\phi_j)_{xy}\left[\cos(2\theta_j) + \cos(2\theta_i)\right] \\ &\quad + \frac{1}{2}\left[(\phi_j)_{yy} - (\phi_j)_{xx}\right]\left[\sin(2\theta_j) + \sin(2\theta_i)\right] \\ &\quad + W_{ij}\left[\nabla^2\phi_i + [(\phi_i)_{yy} - (\phi_i)_{xx}]\cos(2\theta_i) - 2(\phi_i)_{xy}\sin(2\theta_i)\right], \end{aligned} \tag{C.37}$$

where

$$W_{ij} = \frac{(\phi_j)_y(\phi_i)_x - (\phi_j)_x(\phi_i)_y}{|\nabla\phi_i|^2} \tag{C.38}$$

and

$$P_{ij} = \frac{(\phi_j)_x(\phi_i)_x - (\phi_j)_y(\phi_i)_y}{|\nabla\phi_i|^2}. \tag{C.39}$$

APPENDIX D

CONSTRUCTION OF A BINARY PHASE DIAGRAM

Knowledge of the free energy of each phase of a solution allows for the construction of its phase diagram. As an example, we choose an A-B binary system and assume that it exhibits ideal solution behavior. Thus the free energies of the liquid and solid solutions are given by

$$G^l(T,x) = (1-x)G^l_A(T) + xG^l_B(T) + RT\left[x\ln x + (1-x)\ln(1-x)\right] \tag{D.1}$$

and

$$G^s(T,x) = (1-x)G^s_A(T) + xG^s_B(T) + RT\left[x\ln x + (1-x)\ln(1-x)\right], \tag{D.2}$$

where x is the mole fraction of B and G^l_A, G^s_A, G^l_B and G^s_B are the standard free energies for liquid A, solid A, liquid B and solid B, respectively. The heats of fusion and melting points of A and B, for example, are $\Delta S^f_A = \Delta S^f_B = 10 J/mole \cdot K$, $T_{m,A} = 800K$ and $T_{m,B} = 1200K$, respectively.

Conditions for equilibrium between the liquid and solid phases at fixed T and P are

$$\mu^l_A = \mu^s_A = \mu_A \tag{D.3}$$

and

$$\mu^l_B = \mu^s_B = \mu_B, \tag{D.4}$$

which just states that the chemical potential of each given element is equal in each of the phases.

For some given temperature T , the free energies of the liquid and solid phases as given by equations (D.1) and (D.2) can be plotted as functions of their all density

variables (x is the only density variable in the present case) for the common tangent construction.

The unknown points x^l and x^s are the compositions of the phases that are in equilibrium and must be calculated as the boundaries for the solid-liquid two-phase region in the T-x phase diagram. Simultaneous expressions for x^l and x^s can be obtained from geometrical construction. For the given T,

$$\mu_A^l(x^l) = G^l(x^l) - x^l \left(\frac{\mathrm{d}G^l}{\mathrm{d}x}\right)_{x=x^l}, \tag{D.5}$$

$$\mu_A^s(x^s) = G^l(x^s) - x^s \left(\frac{\mathrm{d}G^s}{\mathrm{d}x}\right)_{x=x^s}, \tag{D.6}$$

$$\mu_B^l(x^l) = G^l(x^l) - \left(1 - x^l\right) \left(\frac{\mathrm{d}G^l}{\mathrm{d}x}\right)_{x=x^l}, \tag{D.7}$$

$$\mu_B^s(x^s) = G^s(x^s) - (1 - x^s) \left(\frac{\mathrm{d}G^s}{\mathrm{d}x}\right)_{x=x^s}, \tag{D.8}$$

where

$$\frac{\mathrm{d}G^l}{\mathrm{d}x} = G_B^l - G_A^l + RT\ln\frac{x}{1-x}, \tag{D.9}$$

$$\frac{\mathrm{d}G^s}{\mathrm{d}x} = G_B^s - G_A^s + RT\ln\frac{x}{1-x}. \tag{D.10}$$

The conditions for equilibrium Equation (D.3) and (D.4) using Equation (D.5)-(D.10) give, upon arrangement,

$$G_A^l - G_A^s + RT\ln\frac{1-x^l}{1-x^s} = 0, \tag{D.11}$$

$$G_B^l - G_B^s + RT\ln\frac{x^l}{x^s} = 0. \tag{D.12}$$

If it is assumed that enthalpy H is not a function of temperature, then from the data, we can write

$$G_A^l - G_A^s = \Delta H_A^f - T\Delta S_A^f = \Delta S_A^f \left(T_{m,A} - T\right) = 10(800 - T) \text{ J/mole}, \tag{D.13}$$

$$G_B^l - G_B^s = \Delta H_B^f - T\Delta S_B^f = \Delta S_B^f \left(T_{m,B} - T\right) = 10(800 - T) \text{ J/mole.} \tag{D.14}$$

Substitution of Equations (D.13) and (D.14) into Equations (D.11) and (D.12) gives two simultaneous expression x^l and x^s:

$$10(800 - T) + RT\ln\frac{1 - x^l}{1 - x^s} = 0, \tag{D.15}$$

$$10(1200 - T) + RT\ln\frac{x^l}{x^s} = 0. \tag{D.16}$$

Equations (D.15) and (D.16) are two nonlinear equations of two unknowns x^l and x^s. Thus, the two unknowns x^l and x^s for a given temperature T can be numerically solved by the Newton-Raphson method using Jacobian:

$$\mathbf{J}(\mathbf{x^l}, \mathbf{x^s}) = \begin{pmatrix} -\frac{RT}{1-x^l} & \frac{RT}{1-x^s} \\ \\ \frac{RT}{x^l} & -\frac{RT}{x^l} \end{pmatrix}.$$

For the construction of the temperature-chemical potential phase diagram, one may perform a Legendre transformation of $G(T, x)$ as

$$G(T,x) - x\left(\frac{\partial G}{\partial x}\right)_T = G(T,x) - (\mu_B - \mu_A)\, x = \mu\left(T, \mu_B - \mu_A\right). \tag{D.17}$$

Therefore, in principle, a liquid-solid two-phase coexistence line in the $T - \mu_B$ phase diagram can be calculated by finding the intersection line of μ_A^l and μ_B^l surfaces in $\mu_A - T - (\mu_B - \mu_A)$ space, which guarantees the equilibrium conditions: $T^l = T^s$, $\mu_A^l = \mu_A^s$ and $\mu_B^l = \mu_B^s$. If one has a program to calculate a $T - x$ phase diagram, one can readily convert the $T - x$ phase diagram to the corresponding $T - \mu_B$ phase diagram simply by calculating μ_B for two-phase equilibria at a given temperature T.

Algorithm to construct phase diagram is following:

(1) Find the set of equations such as (D.15) and (D.16) based on equilibrium condition.

(2) Select a temperature.

(3) Solve them for x^l and x^s.

(4) Change the temperature and repeat the algorithm.

VITA

Min Soo Park completed degree of Bachelor of Engineering and Master of Science in department of mechanical engineering with Sang W. Joo at Yeungnam University, Korea. Meanwhile, he worked with Stephen H. Davis as a research scholar in department of engineering science and applied mathematics at Northwestern University. He received the degree of Doctor of Philosophy in mechanical engineering at Texas A&M University in College Station, TX. While at Texas A&M he has performed research in the field of computational materials science, specifically phase field modeling for solidification. Min Soo Park may be reached at Department of Mechanical Engineering, 3132 TAMU, College Station, Texas, 77843-3123, c/o Raymundo Arróyave or via email at j2220373@gmail.com.

The typist for this thesis was Min Soo Park.